

Current Research in
ANIMAL PHYSIOLOGY

Current Research in
ANIMAL PHYSIOLOGY

Edited By

Victor S. Lamoureux, PhD

Adjunct Professor of Biology, Broome Community College,
State University of New York, Binghamton, U.S.A.



Apple Academic Press

TORONTO NEW YORK

© 2012 by
Apple Academic Press Inc.
3333 Mistwell Crescent
Oakville, ON L6L 0A2
Canada

Apple Academic Press Inc.
1613 Beaver Dam Road, Suite # 104
Point Pleasant, NJ 08742
USA

Exclusive worldwide distribution by CRC Press, a Taylor & Francis Group

International Standard Book Number: 978-1-926692-79-1 (Hardback)

Printed in the United States of America on acid-free paper

This book contains information obtained from authentic and highly regarded sources. Reprinted material is quoted with permission and sources are indicated. Copyright for individual articles remains with the authors as indicated. A wide variety of references are listed. Reasonable efforts have been made to publish reliable data and information, but the authors, editors, and the publisher cannot assume responsibility for the validity of all materials or the consequences of their use. The authors, editors, and the publisher have attempted to trace the copyright holders of all material reproduced in this publication and apologize to copyright holders if permission to publish in this form has not been obtained. If any copyright material has not been acknowledged, please write and let us know so we may rectify in any future reprint.

Library and Archives Canada Cataloguing in Publication

Current research in animal physiology/edited by
Victor S. Lamoureux.

Includes index.
ISBN 978-1-926692-79-1
1. Physiology. I. Lamoureux, Victor S., 1970-

QP31.2.C87 2011 571.1 C2011-905374-8

Trademark Notice: Registered trademark of products or corporate names are used only for explanation and identification without intent to infringe.

Apple Academic Press also publishes its books in a variety of electronic formats. Some content that appears in print may not be available in electronic format. For information about Apple Academic Press products, visit our website at www.appleacademicpress.com

Preface

Animal physiology is based on how simply an animal functions. How does an animal eat, breathe, generate energy, reproduce, develop, and coordinate and control all its activities? Physiology follows the nutrients in a piece of food as it is ingested, digested, absorbed, circulated, and incorporated through the body. It is all the things an organism does just to keep alive. And it answers the “Why?” questions also—Why do organisms have the mechanisms they do and why are they adaptively significant? But examining how an animal functions is anything but “simple.”

The breadth of animal physiology can be staggering, and it has become impossible for any one person to know the entire scope of the subject. The study encompasses the molecular, cellular, tissue, organ, and organ system levels and through to the whole organism. This leaves a broad array of interest areas for an investigator, and one can specialize in cell and molecular physiology, organ and system physiology, anatomy, behavioral physiology, developmental biology, and pathology.

A great deal of research is being conducted on the role of genes in regulating physiological processes, as well as how the genes themselves are regulated. Genes code for proteins and proteins themselves are the functional molecules of the body. With the complete mapping of the human genome, we now face the enormous task of fully determining the role of each gene in cellular functioning—a rapidly emerging field of physiological genomics and proteomics.

With an emphasis on laboratory studies and foci on the molecular and cellular levels, it is important to be reminded that animals did not evolve their physiological mechanisms in a vacuum but with the constant pressure of their environment and the shaping mechanism of natural selection. It is important to study animals in their environment, or with at least a clear understanding of the environmental challenges that a species faces. Animal physiology should always be viewed in the context of the animal’s evolutionary past and the current environmental conditions they face.

Placing the animal in its correct environment, with the conditions it actually faces in that environment, is critical. For example, in my work with frogs it was assumed they overwintered in hypoxic pond bottoms and therefore must have physiological mechanisms to tolerate anoxia. Tests were conducted to determine the physiological basis for frogs surviving anoxia, only to find that frogs did not tolerate anoxia and would die. It was discovered that frogs do not have physiological mechanisms to survive anoxia, but behavioral adaptations. They leave their breeding ponds and overwinter in flowing waters such as streams, a very different and better oxygenated microclimate than that of a pond bottom. The relationship between behavior and physiology is powerfully reciprocal, as understanding the frogs’ physiology greatly aided in interpreting behavioral observations, while not understanding the behavior and environment of an animal will likely lead to fruitless physiological investigations.

The relevance of animal physiology is obvious. Furthering our understanding of the physiology of a wide variety of animals will aid us in all aspects of human health

and disease. Functional attributes of many human structures were first uncovered using other animals. When we first study and understand normal physiological functioning, we can then turn our attention to “what goes wrong” when we see abnormal physiology. This can then be applied to developing new methodologies for treating disease.

The future of the field is strong, with a diversity of careers. Physiologists with PhDs will go on to careers in medicine, veterinary medicine, and research. Many of them will work in higher education as instructors and researchers. Employment can also be found in government laboratories, hospitals, and other clinical settings. Private sector jobs would include artificial insemination services, public relations firms, publishing houses, museums, consulting, and pharmaceutical companies. With the broad array of topics to be studied in animal physiology today, it would seem there is plenty of variety to add spice to the study of life.

— **Victor S. Lamoureux, PhD**

List of Contributors

Ricardo Albay III

Department of Psychology, University of California, Santa Barbara, California, USA.

George M. Anderson

Yale University Child Study Center, New Haven, Connecticut, USA.

Michael J. Angilletta, Jr.

Department of Ecology and Organismal Biology, Indiana State University, Terre Haute, Indiana, USA.

Edson Antunes

Department of Pharmacology, Faculty of Medical Sciences, University of Campinas, Campinas (SP), Brazil.

Kristin L. Bishop

Section of Ecology and Evolution, University of California Davis, Davis, California, USA.

Luca Bonfanti

Department of Veterinary Morphophysiology, University of Turin, Grugliasco, Italy.

Neuroscience Institute of Turin (NIT), Turin, Italy.

National Institute of Neuroscience, Turin, Italy.

Angela Chen

Department of Psychology, University of California, Santa Barbara, California, USA.

Archie C. Clutter

Newsham Choice Genetics, West Des Moines, Iowa, USA.

Tiffany Cragin

Department of Physiology and Pharmacology, Medical School, University of Minnesota-Duluth, 1035 University Dr, Duluth, MN 55812, USA.

Vicktoria Danilova

Department of Physiology and Pharmacology, Medical School, University of Minnesota-Duluth, 1035 University Dr, Duluth, MN 55812, USA.

Ana Paula Couto Davel

Department of Physiology and Biophysics, Institute of Biomedical Sciences (ICB-I), University of São Paulo, São Paulo (SP), Brazil.

Camila de Moraes

Biological Science and Health, Faculty of Physical Education, Cruzeiro do Sul University, São Paulo (SP), Brazil.

Zhi-Qiang Du

Department of Animal Science and Center for Integrated Animal Genomics, Iowa State University, Ames, Iowa, USA.

Raphaëlle Dubruille

Department of Neurobiology, University of Massachusetts Medical School, Worcester, Massachusetts, USA.

Patrick Emery

Department of Neurobiology, University of Massachusetts Medical School, Worcester, Massachusetts, USA.

Program in Neuroscience, University of Massachusetts Medical School, Worcester, Massachusetts, USA.

Christina M. Grozinger

Department of Entomology, North Carolina State University, Raleigh, North Carolina, USA. Department of Genetics, North Carolina State University, Raleigh, North Carolina, USA. W. M. Keck Center for Behavioural Biology, North Carolina State University, Raleigh, North Carolina, USA.

Göran Hellekant

Department of Physiology and Pharmacology, Medical School, University of Minnesota-Duluth, 1035 University Dr, Duluth, MN 55812, USA.

Zoë Ipiña

Département de biomédecine vétérinaire, Faculté de médecine vétérinaire, Université de Montréal, CP 5000, St-Hyacinthe, Québec, J2S 7C6, Canada.

Skirmantas Janušonis

Department of Psychology, University of California, Santa Barbara, California, USA.

Alexey Kopusov

Department of Physiology and Pharmacology, Medical School, University of Minnesota-Duluth, 1035 University Dr, Duluth, MN 55812, USA.

Wah-Keat Lee

X-ray Science Division, Argonne National Laboratory, 9700 S. Cass Avenue, Argonne, IL 60439, USA.

Josiane Lefebvre-Lavoie

Département de biomédecine vétérinaire, Faculté de médecine vétérinaire, Université de Montréal, CP 5000, St-Hyacinthe, Québec, J2S 7C6, Canada.

Jacques G. Lussier

Département de biomédecine vétérinaire, Faculté de médecine vétérinaire, Université de Montréal, CP 5000, St-Hyacinthe, Québec, J2S 7C6, Canada.

Alan MacInnes

Department of Cardiovascular Research, Pfizer Global R&D, St. Louis, MO63017, USA.
Department of Physiology and Pharmacology, Karolinska Institute, Stockholm, Sweden.

Vincenzo Miragliotta

Département de Veterinary Anatomy, Biochemistry and Physiology, University of Pisa, Viale dellePiagge 2 56100 Pisa, Italy.

Alejandro Murad

Department of Neurobiology, University of Massachusetts Medical School, Worcester, Massachusetts, USA.
Program in Neuroscience, University of Massachusetts Medical School, Worcester, Massachusetts, USA.

Carlos A. Navas

Department of Physiology, Institute of Biosciences, University of São Paulo, São Paulo, Brazil.

Amanda C. Niehaus

School of Integrative Biology, University of Queensland, St Lucia, Queensland, Australia.

Maaïke C. Nieveen

Integrative Zoology, Institute of Biology, Leiden University (IBL), van der Klauw Laboratory, Kaiserstraat 63, 2311 GP Leiden, The Netherlands.

David C. O'Carroll

Discipline of Physiology, School of Molecular and Biomedical Science, The University of Adelaide, Adelaide, Australia.

Anita K. Pai

Department of Biological Anthropology and Anatomy, Duke University, Durham, North Carolina, USA.

Arjan P. Palstra

Integrative Zoology, Institute of Biology, Leiden University (IBL), van der Klauw Laboratory, Kaiserstraat 63, 2311 GP Leiden, The Netherlands.

Paolo Peretto

Department of Animal and Human Biology, University of Turin, Turin, Italy.
Neuroscience Institute of Turin (NIT), Turin, Italy.

Giovanna Ponti

Department of Veterinary Morphophysiology, University of Turin, Grugliasco, Italy.

Pedro L. Ribeiro

Department of Physiology, Institute of Biosciences, University of São Paulo, São Paulo, Brazil.

Freddie-Jeanne Richard

Department of Entomology, North Carolina State University, Raleigh, North Carolina, USA. Department of Genetics, North Carolina State University, Raleigh, North Carolina, USA. W. M. Keck Center for Behavioural Biology, North Carolina State University, Raleigh, North Carolina, USA.

Thomas W. Roberts

Department of Physiology and Pharmacology, Medical School, University of Minnesota-Duluth, 1035 University Dr, Duluth, MN 55812, USA.

Fernanda Rodriguez

Monsanto Company, Saint Louis, Missouri, USA Ellen A. A. Nollen, *Editor*
University Medical Center Groningen, The Netherlands

Michael Rosbash

Howard Hughes Medical Institute, National Center for Behavioral Genetics and Department of Biology, Waltham, Massachusetts, USA.

Luciana Venturini Rossoni

Department of Physiology and Biophysics, Institute of Biomedical Sciences (ICB-1), University of São Paulo, São Paulo (SP), Brazil.

Max F. Rothschild

Department of Animal Science and Center for Integrated Animal Genomics, Iowa State University, Ames, Iowa, USA.

Daniel Schmitt

Department of Biological Anthropology and Anatomy, Duke University, Durham, North Carolina, USA.

Denhi Schnabel

Molecular Cell Biology, Institute of Biology, Leiden University (IBL), Clusius Laboratory, 2333 AL Leiden, The Netherlands.

Michael W. Sears

Department of Zoology and Center for Ecology, Southern Illinois University, Carbondale, Illinois, USA.

Fira Shapiro

Biology of Lactation Laboratory, Institute of Animal Sciences, Agricultural Research Organization, PO Box 6, Bet Dagan 50250, Israel.

Dima Shinder

Biology of Lactation Laboratory, Institute of Animal Sciences, Agricultural Research Organization, PO Box 6, Bet Dagan 50250, Israel.

Patrick A. Shoemaker

Tanner Research Inc., Monrovia, California, USA Huibert D. Mansvelder, *Editor*
Vrije Universiteit Amsterdam, The Netherlands.

Nissim Silanikove

Biology of Lactation Laboratory, Institute of Animal Sciences, Agricultural Research Organization, PO Box 6, Bet Dagan 50250, Israel.

John J. Socha

X-ray Science Division, Argonne National Laboratory, 9700 S. Cass Avenue, Argonne, IL 60439, USA.
Current address: Department of Engineering Science and Mechanics, Virginia Polytechnic Institute and State University, Blacksburg, VA, 24061, USA.

Herman P. Spaink

Molecular Cell Biology, Institute of Biology, Leiden University (IBL), Clusius Laboratory, 2333 AL Leiden, The Netherlands.

David R. Tarpy

Department of Entomology, North Carolina State University, Raleigh, North Carolina, USA. W. M. Keck Center for Behavioural Biology, North Carolina State University, Raleigh, North Carolina, USA.

Maggie Tatevosyan

Department of Psychology, University of California, Santa Barbara, California, USA.

Christine L. Theoret

Département de biomédecine vétérinaire, Faculté de médecine vétérinaire, Université de Montréal, CP 5000, St-Hyacinthe, Québec, J2S 7C6, Canada.

Guido E. E. J. M. van den Thillart

Integrative Zoology, Institute of Biology, Leiden University (IBL), van der Klauw Laboratory, Kaiserstraat 63, 2311 GP Leiden, The Netherlands.

James A. Timmons

Department of Cardiovascular Research, Pfizer Global R&D, St. Louis, MO63017, USA.
Department of Physiology and Pharmacology, Karolinska Institute, Stockholm, Sweden.

Natascha Vukasinovic

Newsham Choice Genetics, West Des Moines, Iowa, USA.

Yiwen Wang

Department of Physiology and Pharmacology, Medical School, University of Minnesota-Duluth, 1035 University Dr, Duluth, MN 55812, USA.

Steven D. Wiederman

Discipline of Physiology, School of Molecular and Biomedical Science, The University of Adelaide, Adelaide, Australia.

Robbie S. Wilson

School of Integrative Biology, University of Queensland, St Lucia, Queensland, Australia.

Angelina ZanESCO

Department of Physical Education, Institute of Bioscience, University of Sao Paulo State, Rio Claro (SP), Brazil.

Xia Zhao

Department of Animal Science and Center for Integrated Animal Genomics, Iowa State University, Ames, Iowa, USA.

List of Abbreviations

5-HT	5-Hydroxytryptamine
5-HTP	5-Hydroxytryptophan
9-HAD	9-Hydroxy-(E)-2-decenoic acid
Ach	Acetylcholine
AF	Amplified fragment
AJ	Adherens junction
AMP	Adenosine monophosphate
ASDs	Autism spectrum disorders
ATP	Adenosine triphosphate
BBB	Blood brain barrier
BLBP	Brain lipid binding protein
bm	Body mass
BrdU	5-Bromo-2'-deoxyuridine
BSTFA	Bis(trimethylsilyl)trifluoroacetamide
CAT	Catalase gene
CLK	Clock
CNS	Central nervous system
COLIII	Collagen type III
CRMP-4	Collapsin response mediator protein-4
CRY	Cryptochrome
CT	Chorda tympani
CTSF	Cathepsin F
CYC	Cycle
DAB	3,3'-diaminobenzidine
DCX	Couplecortin
DD	Constant darkness
DN	Dorsal neurons
DW	DurbinWatson test
ECL	Enhanced chemiluminescence
ECM	Extracellular matrix
EGL	External granule cell layer
EGT	Exuberant granulation tissue
EMT	Epithelial-mesenchymal transition
ESTMD	Elementary small target motion detector model
ETHOM	Event-recording software

f	Fragment
FFPE	Formalin-fixed and paraffin-embedded
FN	Fibronectin
FPC	Fingerprint contigs
fps	Frames per second
FSH	Follicle-stimulating hormone
FW	Freshwater
GA	Gymnemic acid
GL	Granule layer
GLM	General linear model
GN	Glossopharyngeal
GnRHa	Gonadotropin-releasing hormone agonist
GS	Glutamine synthetase
GSI	Gonadosomatic index
GWA	Genome-wide association
Hb	Hemoglobin
HIPK3	Homeodomain interacting protein kinase 3
HOB	Methyl p-hydroxybenzoate
HOMA	Homeostasis model assessment
HPF3	High-pass filtering
HPLC	High-performance liquid chromatography
HS	Heat stress
HSD	Highest significant difference test
HVA	4-Hydroxy-3-methoxyphenylethanol
HW-R	Half wave rectification
IC	Intermittent claudication
IIB4	Isolectin B4
IMP	Inosine monophosphate
IR	Insulin receptor
JET	Jetlag
KE	Kinetic energy
KIS	KISMET
LD	Linkage disequilibrium
LH	Luteinising hormone
LH β	Luteinising hormone β
LL	Constant light
LMC	Large monopolar cells
LNds	Dorsal lateral neurons
LNvs	Ventral lateral neurons

LONP1	LON peptidase 1
LPF5	Low-pass filter
MAF	Minor allele frequency
MDI	Multi-drone inseminated
ML	Molecular
MMP7	Matrix metalloproteinase 7
MRI	Magnetic resonance imaging
MY	Milk yield
NMS	N-Methylserotonin
NO	Nitric oxide
NO _x	Nitrite/nitrate
NPTX1	Neuronal pentraxin I
OCT	Optical coherence tomography
ORF	Open reading frame
PA	Plasminogen activator
PBS	Phosphate-buffered saline
PCr	Phosphocreatine
PCR	Polymerase chain reaction
PCR-RFLP	Polymerase chain reaction restriction fragment length polymorphism
PD	Postnatal day
PE	Potential energy
PER	Period
PG	Plasminogen
PKG	Protein kinase
PL	Plasmin
PS	Pericardial sinus
PSA-NCAM	Polysialylated neural cell adhesion molecule
PSL	Proliferative superficial layer
PYCR1	Pyrraline-5-carboxylate reductase 1
Qeq	Queen equivalents
QMP	Queen mandibular pheromone
Q-RT	Quantitative reverse transcriptase
qRT-PCR	Quantitative real-time polymerase chain reaction
QTL	Quantitative trait loci
RM	Repeated-measures
ROC	Receiver operating characteristic
ROS	Reactive oxygen species
RT	Room temperature

RTC	Rectifying transient cell
SD	Sedentary control
SDD	Sedentary diet
SDI	Single-drone inseminated
SEM	Standard error mean
SERT	Serotonin transporter
SMV	Skim-milk-derived vesicles
SNP	Sodium nitroprusside
SNPs	Single nucleotide polymorphisms
SOD	Superoxide dismutase
SPL	Subpial layer
SSC	Sus scrofa chromosomes
SSH	Suppression subtractive hybridization
STMD	Small target motion detectors
SVZ	Subventricular zone
SW	Seawater
TAE	Tris-acetate-EDTA
TBP	Two-bottle preference
Tcf/Lef	T cell factor/lymphoid enhancer factor
TDT	Transmission disequilibrium tests
TE	Tris-EDTA
THI	Temperature humidity index
TI	Time intensity
TIM	Timeless
TMD	Trans-membrane domain
TME	Total mechanical energy
TR	Trained control
TRC	Taste receptor cell
TRD	Trained diet
UTR	5'-Untranslated region
Wnt	Wingless
α -SMA	α -Smooth muscle actin
β -CN	β -Casein

Contents

- 1. Animal Physiology and Circadian Photoresponses 1**
Raphaëlle Dubruille, Alejandro Murad, Michael Rosbash, and Patrick Emery
- 2. Complications in High Caloric Diet-Fed Rats 23**
Camila de Moraes, Ana Paula Couto Davel, Luciana Venturini Rossoni,
Edson Antunes, and Angelina Zanesco
- 3. Young Wild-Type Mice and Serotonin-Related Variables 33**
Ricardo Albay III, Angela Chen, George M. Anderson, Maggie Tatevosyan,
and Skirmantas Janušonis
- 4. Neurogenesis of Peripuberal and Adult Rabbits 47**
Giovanna Ponti, Paolo Peretto, and Luca Bonfanti
- 5. Monkeys and Taste Development..... 72**
Yiwen Wang, Viktoriya Danilova, Tiffany Cragin, Thomas W. Roberts,
Alexey Kopusov, and Göran Hellekant
- 6. Intermittent Claudication in Canines 89**
Alan MacInnes and James A. Timmons
- 7. Body Mechanics of Moving Cats..... 99**
Kristin L. Bishop, Anita K. Pai, and Daniel Schmitt
- 8. Wound Repair on Horses with Equine CPNNB1 and PECAM1110**
Zoë Ipiña, Vincenzo Miragliotta, Josiane Lefebvre-Lavoie, Jacques G. Lussier,
and Christine L. Theoret
- 9. Genetic Factors of Scrotal Hernia in Commercial Pigs 125**
Zhi-Qiang Du, Xia Zhao, Natascha Vukasinovic, Fernanda Rodriguez,
Archie C. Clutter, and Max F. Rothschild
- 10. Acute Heat Stress Effect on Milk Serotonin of Cows 135**
Nissim Silanikove, Fira Shapiro, and Dima Shinder
- 11. Insect Physiology and Detection of Moving Targets..... 148**
Steven D. Wiederman, Patrick A. Shoemaker, and David C. O'Carroll
- 12. Honey Bee Queen Physiology and Insemination 168**
Freddie-Jeanne Richard, David R. Tarpy, and Christina M. Grozinger
- 13. High Heat Effect on City Ants 183**
Michael J. Angilletta, Jr. Robbie S. Wilson, Amanda C. Niehaus, Michael W. Sears,
Carlos A. Navas, and Pedro L. Ribeiro
- 14. Hemolymph Flow in Grasshoppers' (*Schistocerca americana*) Hearts..... 191**
Wah-Keat Lee and John J. Socha

15. Sexual Maturity and Swimming in Male Silver Eels.....	203
Arjan P. Palstra, Denhi Schnabel, Maaïke C. Nieveen, Herman P. Spaïnk, and Guido E.E.J.M. van den Thillart	
Permissions.....	208
References.....	210
Index	247

Chapter 1

Animal Physiology and Circadian Photoresponses

Raphaëlle Dubruille, Alejandro Murad, Michael Rosbash,
and Patrick Emery

INTRODUCTION

Circadian pacemakers are essential to synchronize animal physiology and behavior with the day:night cycle. They are self-sustained, but the phase of their oscillations is determined by environmental cues, particularly light intensity and temperature cycles. In *Drosophila*, light is primarily detected by a dedicated blue-light photoreceptor: Cryptochrome (CRY). Upon light activation, CRY binds to the pacemaker protein Timeless (TIM) and triggers its proteasomal degradation, thus resetting the circadian pacemaker. To understand further the CRY input pathway, we conducted a mis-expression screen under constant light based on the observation that flies with a disruption in the CRY input pathway remain robustly rhythmic instead of becoming behaviorally arrhythmic. We report the identification of more than 20 potential regulators of CRY-dependent light responses. We demonstrate that one of them, the chromatin-remodeling enzyme KISMET (KIS), is necessary for normal circadian photo responses, but does not affect the circadian pacemaker. KIS genetically interacts with CRY and functions in PDF-negative circadian neurons, which play an important role in circadian light responses. It also affects daily CRY-dependent.

The rotation of the Earth on its axis is responsible for the mild temperatures found in most regions of the globe, which allow for a complex biosphere to thrive. However, this rotation is accompanied by important variations in light intensity and temperature, which are challenges for most organisms. Since the day:night cycle has a stable period, the physical and ecological changes it induces in the environment can be temporally predicted. This anticipation is made possible in most organisms by circadian clocks. In *Drosophila*, the molecular circadian pacemaker is a transcriptional feedback loop: two proteins - Period (PER) and Timeless (TIM) - repress their own gene transcription by interfering with the activity of the transcription factors Clock (CLK) and Cycle (CYC) [1-4]. PER and TIM stability, their translocation into the nucleus, and their repressive activity are tightly regulated by kinases (DBT, CKII, and SGG) and phosphatases (PP2A and PP1) [5-14]. Importantly, while this molecular clock free-runs - i.e. its oscillations persist in the absence of environmental cues - its period only approximates 24 hrs and must thus be re-set every day to be in phase with the day:night cycle. This is the role of light and temperature input pathways.

The blue-light photoreceptor cryptochrome (CRY) is the main *Drosophila* circadian photoreceptor [15-17]. After absorbing a photon, CRY undergoes a conformational change involving its C-terminal domain and binds to TIM [18, 19]. TIM is then

tagged for ubiquitination and proteasomal degradation [20, 21]. The mechanisms by which CRY initiates the cascade of events that leads to TIM degradation remain unclear. However, Jetlag (JET) plays an important role in targeting TIM for proteasomal degradation [22, 23]. JET is part of an SCF E3 ubiquitin ligase complex responsible for TIM ubiquitination. Interestingly, JET also regulates CRY's own light-dependent degradation [24]. The COP9 signalosome sub-units CSN4 and CSN5 are also required for circadian behavioral photo responses [25]. The CSN complex regulates the activity of SCF E3 ubiquitin ligases and might thus be functioning upstream of JET in circadian neurons. Another protein known to regulate the CRY input pathway is the kinase SGG [26]. The SGG interacts with CRY, and its over expression inhibits CRY activity, through as yet unclear mechanisms. Little is known about the regulation of the expression and stability of the proteins involved in CRY photoreception. This is an important question, because the level of expression of these proteins needs to be tightly regulated so that circadian rhythms are tuned to the proper range of light intensities. They should be able to respond to subtle and progressive changes in light intensities at dawn or dusk, without being excessively sensitive to light and responds inappropriately to moonlight levels of illumination.

We therefore, undertook a mis-expression screen, which identified more than 20 genes that might affect circadian photoreception. We focused on one gene in particular, which encodes the chromatin remodeling protein KISMET. Indeed, by down regulating its expression with RNA interference, we found that KISMET is essential for CRY-dependent light responses.

MATERIALS AND METHODS

Drosophila Stocks

The EP line collection was previously described [28]. The following strains were used: y w, Canton-S, y w; tim-GAL4/CyO [17], y w; pdf-GAL4 [66]; y w; cry^b ss [16]; y w; cry^m [18]; y w ; tim-GAL4 pdf-GAL80/CyO; pdf-Gal80/TM6B [29]; y w; UAS-cry #12 [17]. The second chromosomes bearing tim-GAL4 and pdf-GAL4 insertions were independently and meiotically re-combined with a chromosome containing the UAS-dcr2 insertion [56]. The presence of the two transgenes on the same chromosome was verified by PCR. To localize the circadian neurons in *Drosophila* brain, the previously described enhancer trap line R32 was used [58]. We also used the following mutant strains: sda^{iso7.8} [51], Akap200^{Δ7} [81], lk6¹ and lk6² [52], Df(3R)exel9019, GstS1^{M38-3} and GstS1^{M29-13} (Benes *et al.*, unpublished GstS1 null mutants), morgue^{Δ457} (Schreuder and Nambu, unpublished deletion strain).

To induce RNAi of the candidate genes, the following lines were used from the NIG-Fly stock and the VDRC. NIG-Fly lines: 30152R-1 (cg30152), 30152R-2 (cg30152), 10459R-1 (cg10459), 3412R-1 (slimb), 3412R-2 (slimb), 15437R-1 (morgue), 15437R-2 (morgue), 15507R-2 (kay), 15507R-4 (kay). VDRC lines: 4024 (cg8735), 4025 (cg8735), 5647 (akap200), 11763 (elB), 42813 (elB), 14385 (cpo), 14691 (cg1621), 14692 (cg1621), 22144 (sda), 22145 (sda), 23037 (calpB), 46241 (calpB), 25033 (cg31123), 25034 (cg31123), 31674 (cg1273), 31676 (cg1273), 32885 (lk6), 38326 (cg10082), 38327 (cg10082), 38848 (cg30152), 41451 (cg10459), 41623

(wech), 35794 (HSPC300). The KISMET RNAi was induced using either the line 3696R-1 (NIG-Fly) or 46685 (VDRC). The UAS-ubcd1 was described in [82], and AGO over expression was obtained with EP (3)1135 [49].

Two alleles of TIM can be found in lab stocks: ls-TIM and s-TIM [22]. The s-TIM is more sensitive to light than ls-TIM. Our y w stock carries the s-TIM allele, while w¹¹¹⁸ and Canton-S carry the less sensitive ls-TIM. The second chromosome with the TIM-GAL4 insertion carries ls-TIM, as well as the second chromosomes of UAS-cry (line #12), UAS-dcr2, EP (3)3041, EP (3)714, VDRC46685, y w; cry^b, y w; cry^m stocks and y w; pdf-GAL4 UAS-dcr2 (rec4)/CyO NIG-Fly3696R-1 and the TIM-GAL4 UAS-myc cry recombinant chromosome carry s-TIM. We also generated a VDRC46685 stock with an s-TIM allele, and a recombinant TIM-GAL4 VDRC46685 chromosome carrying the ls-TIM allele. All these lines are wild-type for jet. Appropriate controls were included in all tables and figures to verify that the decrease in light sensitivity observed with KIS down regulation or with miR-282 over expression was not due to TIM variants.

Behavioral Analysis

Locomotor Activity

The 1–5 day old single males were monitored for locomotion activity in Trikinetics Activity Monitors (Waltham, M. A.) for 3 full days under 12 hr:12 hr light:dark cycle followed by 6 full days of either constant light or constant darkness at 25°C in I-36 LL Percival incubators (Percival Scientific, Perry IA). For the EP line screen, the light intensity was about 1000 lux; all other experiments were done at about 200 lux. Data was analyzed using FaasX software [61]. Rhythmic flies were defined by x^2 periodogram analysis with the following criteria: power ≥ 10 and width ≥ 2 [83]. Actograms were generated using a signal processing toolbox for Matlab (Math Works, Natick, MA) [84].

Ep line Screen

Four flies for each line were initially screened at 1000 lux of constant light. Since even control flies sometime show weak residual behavioral rhythms in LL, we selected only lines for which at least two flies were rhythmic, with a robust rhythm for at least one (i.e. a power over 20, see Ewer and *et al.* [83] for power definition). Each selected line was then re-tested under constant light (LL) at least twice, usually three times, with a minimum of eight flies per experiment.

Phase-Responses

For each experiment, 16 flies per genotype were entrained for 3 full days in 12hr:12hr LD. They were exposed to light (1000lux) at ZT15 or ZT21 (ZT0 corresponds to light on and ZT12 corresponds to light off) and returned in constant darkness for 5 full days. At the end of the experiment, all the flies that had survived the entire run and were scored as rhythmic using FaasX were analyzed. The phase was calculated for each group of flies in Matlab using the “peakphaseplot” function (the non-evening peaks were removed manually), as described in [18].

Western Blot

Twenty fly heads were homogenized in extraction buffer (20mM HEPES pH7.9, 100mM KCl, 5% Glycerol, 0.1% Triton X100, 0.1mM DTT and 1× protease inhibitor [Roche]), 5× SDS-PAGE loading buffer was then added, and samples denatured at 100°C for 10 min. After centrifugation, protein extracts were loaded on 5% and 6% 29.6:0.4 acrylamide:bisacrylamide gels for KIS and TIM, respectively, and a 9 percent 29:1 acrylamide:bisacrylamide gel (for Tubulin). Proteins were transferred on nitrocellulose and blots were incubated with primary antibody (1:1000 for anti-KIS-L [43], 1:5000 for anti-TIM [57] and 1:10,000 for anti-Tubulin [Sigma]) and HRP-conjugated secondary antibodies (Jackson Immuno Research). Films were imaged with the Fujifilm LAS-1000 and band intensities were quantified using the ImageGaugev4.22 software. KIS or TIM protein levels were normalized with Tubulin.

Whole-Mount Brain Immunostaining and Quantification

Brains from adult flies were dissected in 1× PBS, 0.1% Triton (PBT), fixed in 4 percent paraformaldehyde in PBT and blocked in 10 percent Normal Goat Serum (Jackson Immuno Research) in PBT. They were then washed and incubated overnight at 4°C with primary antibodies. After several washes in PBT, they were incubated with secondary antibodies (Jackson Immuno Research) coupled to FITC, Rhodamine, Cy3 or Cy5 for 2–3 hrs at room temperature at a concentration of 1:200. Brains were mounted in Antifade reagent (Biorad or Vectashield).

The anti-KIS-L (generous gift from J. Tamkun) and anti-PDF antibodies were previously described [43], [85] and both used at a 1:400 dilution. For β -Gal immunostaining, we used a mouse anti- β -Gal antibody (Promega) at a concentration of 1:1,000 as previously described in [58] and CRY antibody was used at a concentration of 1:200. Levels of KIS protein expression in circadian neurons were quantified using ImageJ v1.42q (<http://rsb.info.nih.gov/ij>). For each genotype, 5 to 12 neurons from at least three different brains were quantified. For each circadian neuron, the nuclear fluorescence corresponding to KIS staining was measured and normalized, after subtraction of background signal, to the fluorescence of two neighbor neurons on the same focal slice. An average of the two normalized values was then calculated for each circadian neuron.

Real-Time Quantitative PCR

Total RNAs from about 60 fly heads collected at ZT 4 and ZT16 were prepared using Trizol (Invitrogen) according to the manufacturer's instructions. The 2 μ g of total RNAs was then treated with RQ1 DNase (Promega) for 2 hrs and subsequently reverse transcribed using random hexamer primers (Promega) and Superscript II (Invitrogen), following manufacturer's instructions. Real-time PCR analysis was performed using SYBR Green fluorescent dye (Biorad) in an ABI SDS 7000 instrument (Applied Biosystems). For each set of primers, we generated a standard and a melting curve, using RNAs extracted from wild-type fly heads, to verify amplification efficiency and specificity, respectively. For each transcript, data were normalized to rp32 using the $2^{-\Delta\Delta C_t}$ method. The concentration of PER, TIM, CRY, CSN4, CSN5, SGG and JET

was measured in flies expressing KIS dsRNAs (*tim*-GAL4 UAS-*dcr2*/VDRC46685) and in two control genotypes (*tim*-GAL4 UAS-*dcr2*/+ and VDRC46685/+). Primers used: *rp32*-forward ATGCTAAGCTGTGCACAAA; *rp32*-reverse GTTCGATC-CGTAACCGATGT; *TIM*-forward TGAACGAGGACGACAAAGCC; *TIM*-reverse GATTGAAACGCCTCAGCAGAAG; *per*-forward TCATCCAGAACGGTTGC-TACG; *per*-reverse CCTGAAAGACGCGATGGTGT; *cry*-forward CCGCTGAC-CTACCAAATGTT; *cry*-reverse GGTGGCGTCTTCTAGTTCGAG; *csn4*-forward AGCAAGTTGCCTGACGATCT; *csn4*-reverse GAAACGTATGCCAGCCACTT; *csn5*-forward ACCCAGATGCTCAACCAGAC; *csn5*-reverse CTTTTGGATACGT-GCGGAAT; *sgg*-forward TGCTGCTCGAGTATACGCCC; *sgg*-reverse TCCAT-GCGTAGCTCATCGAAG; *jet*-forward CTGCTGCAGTCACTGATGGT; *jet*-reverse ATGTTGCACAGTTGGCATGT.

RNase Protections

The RNase protections were performed and quantified with an *rp49* loading control as described in [17]. The *lk6* probe covered nucleotide 919–1055 of transcript *lk6*-RA. It generated two major bands. The larger one corresponds to transcript *IK6*-RA, and the smaller one most likely to *lk6*-RB. The smaller band cycled with a similar phase and amplitude (data not shown).

DISCUSSION

Our constant light screen has identified a novel important regulator of circadian photo responses: KISMET (KIS). Our results show that KIS is essential for a well-characterized CRY-dependent circadian photo response: LL induced behavioral arrhythmicity. This arrhythmic behavior is caused by the persistent activation of CRY by blue-light photons. CRY thus binds constantly TIM and tags it for JET-mediated proteasomal degradation. This leaves PER unprotected from being itself targeted to proteasomal degradation, and leads to the disruption of the molecular pacemaker in neurons controlling circadian behavior. Consistent with previous studies in which the CRY input pathway was partially disrupted [18, 23], we observed that among CRY-dependent light responses, LL arrhythmicity is much more sensitive to reduction in KIS expression. Our results further suggest that CRY levels are limiting in circadian neurons that can generate LL behavior. It is becoming clear that CRY level varies significantly between circadian neurons [69, 70], and it is therefore likely that those with lower CRY levels are more prone to become rhythmic in LL when the CRY input pathway is partially disrupted (this study and [26, 29]). We presume that this reflects the very fine photosensitive tuning needed for CRY photo responses. The circadian input pathway has to be able to respond to photoperiod length and to progressive light intensity changes at dawn and dusk, but at the same time should not respond inappropriately to moonlight.

The KIS role as a regulator of the CRY input pathway is not limited to circadian neurons. It also influences circadian photo responses in peripheral circadian tissues such as the eyes, since we observed a significant reduction in diurnal CRY-dependent TIM protein oscillations in *cry^m* flies expressing KIS dsRNAs. Whether KIS is actually

essential for light responses in every circadian tissue is not yet clear. Indeed, we were limited to use RNA interference which usually does not completely abolish gene expression to study KIS function in adult flies, because KIS null mutants are lethal. Incomplete KIS knockdown might explain why we could not detect any defects in the phase response to short light the pulses (data not shown). The neurons controlling this circadian photoresponse are at least partially distinct from those controlling LL behavioral responses [59]; they may have retained sufficient residual KIS or may have had high CRY levels. Alternatively, KIS might not be essential in these circadian neurons.

The KIS is a chromatin-remodeling enzyme that was initially discovered in a screen for extragenic suppressor of Polycomb mutations [71]. It was thus categorized as a Trithorax protein, a group of transcriptional activators of homeotic genes that counteracts Polycomb negative regulators. Recent evidence obtained with larval salivary glands has suggested that KIS might be a general regulator of transcription [43]. Indeed, KIS is associated with most, but not all, transcriptionally active sites of larval salivary gland polytenic chromosomes. In KIS mutants, RNA Polymerase II is associated with these sites, but remains hypophosphorylated, which indicates that it is unable to initiate mRNA elongation. In addition, elongation factors are not recruited at transcriptionally active sites. It was therefore proposed that KIS is necessary for the recruitment of these elongation factors and for reorganizing chromatin downstream of the transcriptional start site [43, 72]. However, while we observed strong effects on circadian light responses, we did not detect any significant effects on the period of the circadian oscillator. Our results therefore indicate that KIS is specifically involved in the control of circadian light input genes in neurons controlling circadian light responses. Since we have used RNA interference to disrupt KIS expression, we cannot entirely exclude that residual KIS expression is sufficient for maintaining normal transcription of pacemaker and non-circadian genes. We also cannot exclude the possibility that other chromatin remodeling enzymes could substitute for KIS in the control of these genes. There is however, very clear experimental evidence that supports the idea that KIS regulates the expression of specific genes. The KISMET loss-of-function results in specific segmentation defects and homeotic transformation during development [44]. Moreover, a recent study demonstrates that KIS plays a central and specific role in the regulation of *atonal*, a pro-neural gene, in the fly retina [73]. We therefore strongly favor the hypothesis that KIS is dedicated to the control of circadian light input genes in *Drosophila* circadian clock neurons. We do not know yet the identity of these genes. We have measured by Real-Time quantitative PCR the expression of the known components of the CRY input pathway (*cry*, *sgg*, *jet*, *tim*, *csn4*, *csn5*) but did not detect any significant change in their mRNA levels when KIS is knocked-down (data not shown). This indicates that important elements of the CRY input pathway remain to be identified. These proteins either function downstream of CRY or regulate CRY activity, but they apparently do not affect CRY abundance. Indeed, we could not detect any changes in the CRY levels by Western Blots or brain immunostainings in flies expressing KIS dsRNAs (data not shown).

The demonstration that KIS is essential for circadian light responses validates our screen for circadian light input genes, which has identified over 20 additional genes

that might regulate circadian light responses. As most of these genes were over expressed in the screen, a significant fraction of them might be negative regulators of the CRY input pathway. It is thus entirely possible that a reduction in their expression levels or a complete loss-of-function would result in an increase in light sensitivity, rather than a loss of CRY responses. Our loss-of-function sub-screen was aimed at genes essential for the CRY input pathway and would not have detected genes that increase light sensitivity. It is therefore not surprising that we confirmed a gene (*kis*) that was predicted to be down regulated in our initial screen as essential for circadian photo responses.

Future studies will determine whether other candidate genes are negative regulators of CRY signaling. They will also be aimed at determining whether some of the candidate genes might be part of the circadian pacemaker, rather than regulators of CRY signaling. This is entirely possible, since over expression of circadian pacemaker genes such as PER or TIM results in LL rhythms [26, 29]. Actually, we identified one other pacemaker gene in our screen: *slimb* [48, 49]. The isolation of this gene is unexpected however. The *slimb* over expression would be predicted to reduce PER levels, since it promotes PER ubiquitination and proteasomal degradation. A possibility is that *slimb* over expression is toxic to the PER degradation pathway, and thus results in an increase, rather than a decrease, in PER levels. This idea is supported by the fact that strong *slimb* over expression results in the same circadian phenotype as *slimb* loss-of-function mutations: arrhythmic behavior in DD [48, 49]. Moreover, we observed that over expressing *jet* which is involved in proteasome-dependent protein turnover, like *slimb* [23] disrupts circadian photo responses in LL. This could also be explained by a dominant-negative effect of *jet* over expression on TIM proteasomal degradation. However, recent results demonstrating that JET also promotes CRY proteasomal degradation [24] point at another potential explanation: CRY levels might be reduced when JET is over expressed. In any case, the negative effect of JET over expression on circadian light responses might explain why using the GAL4/UAS system to try to correct the photoreceptive defects of JET mutants resulted only in a partial rescue [23].

In addition to *slimb*, several other genes have been connected to circadian rhythms: *lk6*, *akap200*, *calpB* and *morgue*. The mRNAs of the last three genes were shown to cycle in the fly head in a DNA microarray study [74], while *lk6* was shown to oscillate in fly bodies [75]. RNase protection and Northern Blot assays revealed that *lk6* expression also undergoes circadian oscillations in heads, with a cycling phase and amplitude of oscillation similar to those of CRY. Thus *lk6* and CRY may be co-regulated. It might however be the presence of microRNAs in our screen that is most intriguing. MicroRNAs are known to play an important regulatory role in a variety of biological processes, which include development and neuronal function. In mouse, two miRNAs, miR-219 and miR-132, have recently been shown to be under circadian regulation in the suprachiasmatic nucleus, and miR-132 may be important in the regulation of photic responses [76]. In *Drosophila*, a role for miRNAs in the control of circadian rhythms has recently been demonstrated. In particular, *bantam* was shown to regulate CLK expression and thus to affect the amplitude of circadian rhythms [77]. In addition, a few miRNAs have been shown to be under circadian regulation [78], although

their importance for circadian rhythms is currently unclear. None of the miRNAs we isolated are described to cycle in fly heads. However, two of them are expressed in circadian tissues: miR-282 and miR-8 [77]. This strongly supports the idea that these miRNAs are important for the regulation of circadian rhythms. MiR-282 appears particularly likely to be an important regulator of circadian photo responses, since its over expression profoundly affects both the behavior of the flies in LL and their response to short light pulse. Moreover, a predicted target of miR-282 is jetlag (TargetScanFly, release4.2; Yong and Emery, unpublished observations), which is crucial for CRY signaling and TIM degradation. We are currently determining whether miR-282 is indeed a regulator of the CRY input pathway.

In summary, our work has identified new candidate circadian genes. They might control or modulate circadian light responses and photosensitivity, or they might regulate circadian pacemaker function. Importantly, we have assigned a function to the chromatin-remodeling factor KIS in adult flies: KIS control the photosensitivity of the circadian clock. The function of most chromatin-remodeling proteins is well documented during *Drosophila* development, but their function in the adult fly is not well studied, because null mutants for these genes are frequently lethal. The adult function of KIS was completely unknown, although we showed here its expression in both the circadian and non-circadian fly brain neurons. The CHD7 is a human KIS homolog associated with CHARGE syndrome, a genetic disorder characterized by developmental retardation and complex abnormalities affecting several organs, including the brain and sensory systems [79, 80]. The partial loss of CRY signaling should be a powerful tool for a genetic screen aimed at finding KIS-interacting genes that contribute to transcriptional regulation. This might in turn reveal how CHD7 functions, and helps illuminate the causes of CHARGE syndrome.

RESULTS

A Circadian Mis-expression Screen under Constant Light

The circadian behavior of wild-type flies is dramatically affected by the presence of constant light (LL) at an intensity of 10 lux or more [27]. They become totally arrhythmic, while under constant darkness they would remain rhythmic for weeks. This circadian response to constant light is dependent on the circadian photoreceptor CRY. *cry^b* flies, which carry a severely hypomorphic *cry* mutation (a quasi-null mutation), remain behaviorally rhythmic under constant light, with a periodicity of 24 hrs, as if they were under constant darkness [15] (Fig. 1A). To identify new components of the CRY light input pathway, we decided to screen the P. Rørth collection of EP lines under LL. These EP lines carry randomly inserted P-elements in their genome (Fig. 1B) [28], which contain UAS binding sites. By crossing these EP lines to flies expressing GAL4 under the control of the timeless promoter (TIM-GAL4 flies), we over expressed or in rare cases down regulated [28] the genes targeted by the EP element specifically in tissues with circadian clocks. Whether the targeted genes were up- or down-regulated depended on the orientation of the EP element insertion. A sense RNA is usually produced, which results in over expression of the targeted gene (Fig. 1B). Sometimes however, the EP element generates an antisense RNA. Thus, at least four mechanisms could explain how EP lines might be rhythmic in LL when crossed to TIM-GAL4.

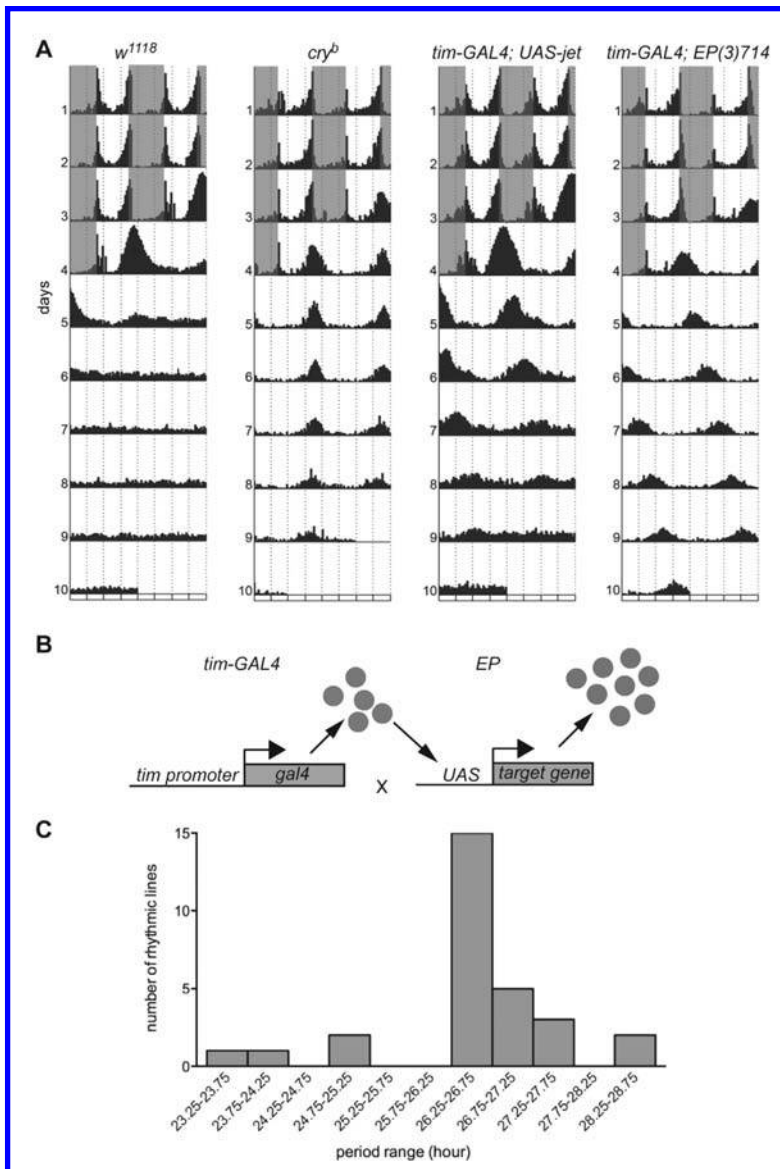


Figure 1: The mis-expression screen in LL.

(A) Average double-plotted actograms of control (*w¹¹¹⁸*), *y w*; *cry^b* (*cry^b*), jet overexpressing (*y w*; *tim-GAL4; UAS-jet*) and miR-282 over expressing flies (*y w*; *tim-GAL4; EP(3)714*). Flies were entrained for 3 days in a 12hr:12hr light:dark cycle (gray shadings indicate the dark phase) and then released in LL. While control flies become arrhythmic in LL, *cry^b* flies and jet and miR-282 over expressing flies remain rhythmic. All genotypes are homozygous for the *ls-TIM* variant [22],[86],[87] (see also Materials and Methods). *n* = 15–16 flies/genotype. (B) The strategy of the mis-expression screen. Each EP line bearing a pseudo-randomly inserted P-element, containing UAS binding sites was crossed to TIM-GAL4 flies. Males from the progeny were tested for rhythmicity in LL. (C) Period range of the rhythmic EP lines (when crossed to TIM-GAL4) in LL. Histograms show the number of rhythmic lines for each period ranging between 23.25 hrs and 28.75 hrs.

First, we might over express a negative regulator of the CRY input pathway, such as SGG. Indeed, when SGG is over expressed, flies are robustly rhythmic in LL [26]. Second, we might down regulate, with the few EP lines that generate antisense RNAs, genes crucial to CRY signaling. Third, the over expression of a gene crucial to CRY signaling might be toxic for the CRY input pathway. Fourth, we might affect PER regulation, since it is over expression results in LL rhythms [26, 29]. Supporting our strategy, we found that over expressing JET, which promotes light-dependent TIM degradation and hence circadian photo responses [22, 23], also results in rhythmic behavior in LL (Fig. 1A), although the long period length we observed indicates that these flies are not entirely blind to constant light [27, 29].

We screened ~1800 EP lines located on the second and third chromosomes, which target ~1350 genes [30] or about 10 percent of the genome, 30 of these lines showed consistent rhythms in LL (>50 percent rhythmic flies, Table 1). This is a hit rate of 1.7 percent, which is in the range of other mis-expression screens [28, 30]. In constant darkness (DD), none of these lines showed any obvious defect. They were all robustly rhythmic, with a period length close to that of control flies. In LL however, the period length was usually not that of control flies in DD, or of *cry^b* flies in LL. Periods were in most cases long, with most lines (20/30) showing a period range that was centered around 26.5–27 hr (Fig. 1A and 1C and Table 1). Power was also weaker than under DD conditions, and the variability of period within lines was higher. This shows that the robustness of circadian rhythmicity is affected; this is not surprising since LL is disruptive to circadian rhythms. In sum, the selected lines clearly are not insensitive to LL, while *cry^b* are virtually blind to constant light [15, 31]. Of note is that 10 lines did not fall into the 26.5–27 hr range. Three lines with a very long period (27.5–28.5 hrs) affected the same gene, miR-282. However, as mentioned above, all these lines showed normal period length in DD. Thus, these differences in LL period length are not due to pacemaker dysfunction, i.e., over expression of specific genes results in specific LL phenotypes.

In some lines, we occasionally observed one or two flies with complex behavior. Most of them displayed two components in their circadian behavior, one with a periodicity of 24 hr, and the other with 26.5 hr. This complex behavior was very rare and probably occurred randomly. However, one line (EP (2)2356/miR-310-311-312-313) was strikingly different: about one quarter to a third of rhythmic flies showed a complex behavior when crossed to TIM-GAL4. The short component had a periodicity that varied between 18 and 22 hrs, while the long component varied from 2629 hrs, or more rarely was around 24 hr. The other rhythmic flies from this line showed only one component, mostly 18–22 hrs, with a few individuals around 24 hrs or 26–29 hrs. This behavior is unique to our knowledge. Complex behavior has been observed in *cry⁰* flies, as well as in *cry^b* and wild-type flies under specific light conditions, but the short period component had a period of approximately 23 hrs [32-34].

Function of the Candidate Genes

Virtually all EP insertions of the collection have been mapped to the genome (see Flybase, <http://www.flybase.org>). We verified the insertion location for eight lines, which were all identical to the insertion sites given in Flybase. For two genes (Ik6 and

morgue), we also verified that they were indeed over expressed as predicted (data not shown). We can therefore predict which genes are misexpressed in the selected lines (Table 1).

Table 1. Behavior of the Selected EP Lines Crossed to TIM-GAL4 under Constant Light (1,000 lux).

Genotype (each EP lines is crossed to <i>tim-GAL4</i>)	Gene predicted to be affected	n	% of rhythmic files	Period average (±SD)	Power average (±SD)
EP(2)2367	<i>morgue</i>	30	87	26.4±0.6	37.5±22.8
EP(3)714	<i>miR-282</i>	43	83	27.5±0.7	54.8±26.5
EP(3)3718	<i>miR-282</i>	31	78	27.5±1	37.8±23
EP(2)670	<i>Gst1</i>	33	73	26.5±1	49.1±23.2
EP(3)703	<i>cg8165/8176</i>	74	71	26.6±1.8	32.5±17.9
EP(3)3041	<i>miR-282</i>	33	70	28.5±1.1	37.3±21.3
EP(2)965	<i>elB</i>	49	67	27.7±2	31.3±20.5
EP(3)972	<i>calpB</i>	31	65	26.5±1.2	33.3±15.6
EP(3)902	<i>kay (as) or cg1973 (as)</i>	34	64	25.1±1.8	25.3±12.2
EP(3)614	<i>cg12173</i>	51	63	27.2±1.3	25.5±17.4
EP(2)506	<i>HSPC300</i>	51	61	26.6±1.2	27.4±14.8
EP(3)3617	<i>miR-282</i>	36	61	27±1.4	32.7±17
EP(2)323	<i>cg8735</i>	35	61	26.7±1.1	24.7±11.3
EP(3)662	<i>slimb</i>	45	60	26.6±1.2	31.8±13.2
EP(2)2345	<i>dap (as) or cg10459 (as)</i>	44	59	27±1	26±17
EP(3)3084	<i>kay</i>	29	59	23.9±1.2	28±14.3
EP(2)2319	<i>cg10082</i>	46	59	26.3±1.1	44±28.3
EP(2)575	<i>Rapgap 1 (as) or cg13791 (as)</i>	36	58	26.3±1.2	27±14.7
EP(2)813	<i>wech (as) or cg1621 (as)</i>	24	58	27.2±1	31.2±13.2
EP(3)1141	<i>sda</i>	35	57	26.4±1.4	25.4±14.9
EP(3)1110	<i>cg9801</i>	27	56	26.7±1.9	26.7±9.3
EP(2)2241	<i>Dg</i>	23	56	26.4±0.7	30.3±10.8
EP(3)661	<i>cpo</i>	34	56	27±1.2	41.8±20.9
EP(2)2469	<i>kis (as)</i>	36	56	24.9±3.1	34.9±16.4
EP(2)2554	<i>akap200</i>	43	55	26.4±1.1	27.1±14.2
EP(3)996	<i>cg31184/cg33108</i>	36	53	26.5±1.5	29.3±14.3
EP(2)2356	<i>miR-310/311/312/313</i>	34	53	complex	
EP(2)2098	<i>cg30152</i>	35	51	26.6±1	29.5±16
EP(2)2402	<i>miR-8</i>	35	51	23.5±0.8	27.8±14.3
EP(3)3094	<i>lk6</i>	20	50	28.5±2.2	22.9±8.9
Controls					
<i>y w; tim-GAL4/+</i>		59	1.7	25.1	17
<i>cry^b</i>		76	83	24.1±0.7	40.2±21

(as=antisense orientation).

Among the candidate genes identified in our screen, we found seven genes that regulate gene expression (Table 2). Among them were three transcription factors. *elB* is known for its role in trachea and appendage development [35, 36]. The *KAY* is the *Drosophila* homologue of *FOS* and is implicated in several signal transduction pathways.

KAY is, for example, essential during embryonic development, for the differentiation of R3/R4 photoreceptors and in immune responses [37-42]. The KIS encodes a chromatin-remodeling protein of the Trithorax family [43, 44]. The CPO was also identified in our screen (EP (3)661). A second EP line affecting CPO (EP (3)3611) was also detected initially, but its phenotype was weaker and thus not listed in Table 1. CPO is an RNA binding protein that regulates different aspects of *Drosophila* behavior (flight, phototaxis, negative geotactic behavior for example) [45].

An interesting set of lines that resulted in LL rhythmicity affected microRNA genes (EP (3)3041/miR-282, EP (3)714/miR-282, EP(3)3718/miR-282, EP(3)3617/miR-282, EP(2)2402/miR-8, EP(2)2356/miR-310-311-312-313). Strikingly, among the six lines with the strongest phenotype were three lines (EP (3)3041, EP (3)714 and EP (3)3718) that are predicted to over express miR-282. A fourth line (EP (3)3617) affects the same gene, and also showed a robust phenotype.

Table 2. Candidate Genes Sorted by Biological Function.

Biological function	Genes	Molecular activity
Regulation of gene expression	<i>elB</i>	Transcription factor
	<i>kay</i>	Transcription factor
	<i>kis</i>	Transcription factor
	<i>cpo</i>	RNA binding protein
	<i>miR-282</i>	MicroRNA
	<i>miR-310-313</i>	MicroRNA
Protein degradation	<i>miR-8</i>	MicroRNA
	<i>morgue</i>	E2 ubiquitin conjuguase
	<i>slimb</i>	E3 ubiquitin ligase
	<i>calpB</i>	Calcium activated protease
Protein modification	<i>sda</i>	Protease
	<i>lk6</i>	Serine/threonine kinase
	<i>cg9801</i>	Serine/threonine phosphatase
Cytoskeleton regulation	<i>HSPC300</i>	
	<i>Dg</i>	
Protein localization	<i>Akap200</i>	PKA interacting protein, actin binding
Metabolism	<i>Gst-S1</i>	Glutathione-S-transferase
	<i>cg12173</i>	Aminoacid metabolism
	<i>cg10082</i>	Inositol metabolism
No putative function	<i>cg30152</i>	
	<i>cg8735</i>	

A second category of interesting candidate genes regulates protein stability. Two genes are implicated in proteasomal degradation (*morgue* and *slimb*). The *Morgue* has an E2 ubiquitin conjugate domain [46], and *SLIMB* is an E3 ubiquitin ligase implicated in the control of PER levels [47-49]. In addition, over expressing the E3 ubiquitin ligase complex sub-unit JET also results in LL rhythms (Fig. 1A). Since these three proteins carry an F-box, we wondered whether the over expression of any protein with an F-box or being involved in proteasomal degradation could render flies resistant to LL. This was not the case: over expressing the ubiquitin conjugate

UBCD1 or the F-box containing E3 ligase AGO did not result in LL rhythmicity. This demonstrates the specificity of the constant light phenotype to MORGUE, SLIMB and JETLAG. Two additional candidate genes encode proteases. CALPB is calcium activated protease of the calpain family [50], whereas another protease, SDA, is known to be important for normal nervous system function: SDA mutants are prone to seizures [51]. A kinase (lk6) involved in the control of growth through its action on the translation initiation factor 4E [52, 53] and a putative protein phosphates (cg9801) were also isolated.

For several lines, the identity of the targeted gene was unclear. Two lines were located in front or within a genomic region, with two overlapping genes. One of them (EP (3)703) was among the lines with the strongest behavior. The two overlapping genes encode a putative metalloprotease (cg8176) and a putative transcription factor of the Jumanji family (cg8165).

Finally, for five EP lines (EP (2)575, EP (3)902, EP (2)2345, EP (2)813 and EP (2)2469) the targeted genes are not up-regulated, but probably down-regulated, since the P-element is predicted to produce an antisense RNA. For EP (2)575, EP (3)902, EP (2)2345 and EP (2)813, the identity of the gene which might be down-regulated is uncertain, because these EP-elements are located near the very 5' end of the *Rapgap1*, *kay*, *dap* and *wech* genes, respectively. They might thus affect the genes located 5' of these three genes. The EP (2)2469 is inserted in the 12th intron of the *kis* gene. It could also potentially over express cg13693, which is nested 10 kb downstream of the EP-element, within *kis* 4th intron. Evidence presented below will demonstrate that *kis* down regulation is sufficient to explain the LL phenotype obtained with EP (2)2469, although we cannot entirely exclude a contribution of cg13693 over expression to this phenotype.

Phase Responses to Short Light Pulses are Disrupted with a Small Sub-set of EP Lines

To determine how profoundly mis-expression of the candidate genes disrupts the CRY input pathway, we tested the response to short light pulses, which is entirely CRY-dependent [16]. In wild-type flies, a 5-min light pulse induces a phase delay when administered at the beginning of the night and a phase advance when administered at the end of the night [54, 55]. All EP lines selected from the primary screen were challenged with 5 min light pulses at ZT15 and ZT21. Three EP lines responded poorly to light pulses at high intensity (1000 lux): EP (2)2367/morgue, as described previously [29], EP (3)3041/miR-282 and EP (3)714/miR-282 (Fig. 2 and data not shown). For EP (3)3041/miR-282 we observed a clear reduction of the response to light at ZT15 compared to all controls. At ZT21, we also observed a reduction, although the magnitude of the phase shift was not significantly different from one of control (Canton-S). A similar phenotype was observed with EP (3)714/miR-282 (data not shown). The other EP lines responded normally to short light pulses. Previous studies have shown that among CRY dependent photo responses, the behavioral responses to constant light are far more sensitive to partial disruption of the CRY input pathway [18, 23]. Thus, it appears that morgue and miR-282 over expression have the most profound effect on CRY signaling, while over expression

of the other candidate genes affect the CRY input pathway more moderately. As mentioned above, most of the EP lines show a long period phenotype and a weak power, which demonstrate that their circadian clock is not insensitive to light. Strikingly, the three lines that disrupt phase responses to short light pulses are among those with the strongest phenotype in LL.

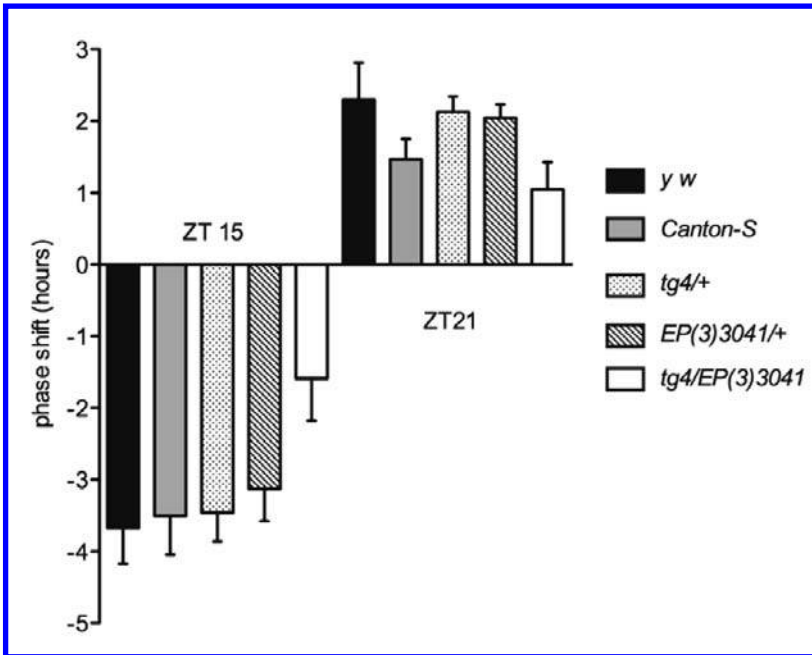


Figure 2. Flies over expressing miR-282 respond poorly to short light pulses.

Phase responses to short light pulses in control flies (*y w*, *Canton-S*, *y w*; *tim-GAL4*; + [*tg4/+*] and *y w*; +; *EP(3)3041* [*EP(3)3041/+*]) and flies over expressing the microRNA miR-282 (*y w*; *tim-GAL4/+*; *EP(3)3041/+* [*tg4/EP(3)3041*]). Flies were entrained for 4 days to a 12hrs:12hrs light:dark cycle. During the fourth night, they were light-pulsed for 5 min at 1,000 lux at ZT15 and ZT21 and then left in constant darkness. Phase changes were calculated by comparing the phase of the evening peak in light-pulsed versus non-pulsed flies of the same genotype. Phase changes are plotted on the y axis; phase delays and advances are shown by negative and positive values, respectively. The histogram represents the average of three independent experiments (16 flies per experiment); the error bars represent standard deviations. *TIM* variants: *y w* is homozygous for *s-tim*; *Canton-S* and *tg4/EP(3)3041* are homozygous for *ls-tim*; *tg4/+* and *EP(3)3041/+* are *ls-tim/s-tim* heterozygotes.

KIS is Essential for Normal Circadian Photoresponses to Constant Light

To identify positive regulators of CRY signaling among our candidate genes, we screened loss-of-function mutants under constant light (200 lux). For five candidate genes, we tested severe loss-of-function alleles that were homozygous viable and healthy (*lk6*, *morgue*, *akap200*, *GstS1* and *sda*). They were all completely arrhythmic in LL (data not shown). For most candidate genes however, severe loss-of-function mutations were either lethal or not available. We therefore, decided to use RNA interference, targeted specifically to circadian tissues, which should in most cases down regulate candidate gene expression and avoid lethality. We crossed *TIM-GAL4* flies to transgenic

flies from the VDRC and NIG-Fly RNAi collections, which carry transgenes encoding gene-specific double-stranded RNAs (dsRNAs). Lethality was only observed with three candidates: KAY, CPO and with one of the RNAi line targeting *elB*. Most viable TIM-GAL4/dsRNA flies were arrhythmic in LL. However, two lines targeting the chromatin remodeling gene KISMET (NIG-Fly3696R-1 and VDRC46685) were 50–60% rhythmic, with a power of about 35 (Table 3). These results are strikingly similar to those obtained with EP (2)2469/KISMET, which as mentioned above is inserted in an antisense orientation within KIS' 12th intron, and is thus predicted to generate a KIS antisense RNA. The only noticeable difference in the behavior between the two RNAi lines was that NIG-Fly3696R-1 shows a period close to 24 hrs, whereas VDRC46685 and the EP line have a ca. 26 hrs period rhythm. This could indicate that the NIG-Fly line is more efficient at repressing KIS expression. In DD, both KIS RNAi lines were rhythmic with a period close to that of control flies.

Table 3. Behavior of Flies Expressing KISMET dsRNAs in Constant Light.

Genotype	<i>tim</i> alleles	% of rhythmic flies	period average \pm SD	Power average \pm SD	n
<i>y w</i>	<i>s-tim/s-tim</i>	0.00%			106
<i>y w; NIG-Fly3696R-1/+</i>	<i>s-tim/s-tim</i>	5.45%	22.12 \pm 1.48	16.52 \pm 242	110
<i>y w; tim-GAL4/+</i>	<i>ls-tim/s-tim</i>	12.73%	25.31 \pm 5.11	20.28 \pm 6.39	110
<i>y w; tim-GAL4/+; NIG-Fly 3696-1/+</i>	<i>ls-tim/s-tim</i>	59.57%	24.16 \pm 1.66	35.08 \pm 18.95	94
<i>y w; VDRC46685/+</i>	<i>ls-tim/s-tim</i>	6.25%	21.93 \pm 1.29	17.57 \pm 7.15	48
<i>y w; VDRC46685/+</i>	<i>ls-tim/ls-tim</i>	6.25%	21.0	18.25	16
<i>y w; tim-GAL4/+</i>	<i>ls-tim/ls-tim</i>	17.39%	21.93 \pm 1.29	17.57 \pm 7.15	23
<i>y w; tim-GAL4/VDRC46685</i>	<i>ls-tim/ls-tim</i>	65.96%	26.18 \pm 1.24	25.43 \pm 6.29	47
<i>y w; tim-GAL4/VDRC46685</i>	<i>ls-tim/s-tim</i>	50.00%	24.96 \pm 1.22	24.28 \pm 13.17	16
<i>w¹¹¹⁸; tim-GAL4, UAS-dcr2/+</i>	<i>ls-tim/ls-tim</i>	9.38%	26.47 \pm 0.40	26.30 \pm 8.61	32
<i>w¹¹¹⁸; tim-GAL4, UAS-dcr2/VDRC46685</i>	<i>ls-tim/ls-tim</i>	82.76%	25.14 \pm 0.97	51.02 \pm 29.27	29
<i>w¹¹¹⁸; tim-GAL4, UAS-dcr2/NIG-Fly3696R-1</i>	<i>ls-tim/s-tim</i>	62.50%	24.25 \pm 0.93	35.35 \pm 17.90	32
<i>y w; cry^b/cry^b</i>	<i>ls-tim/ls-tim</i>	76.58%	24 \pm 0.53	62.04 \pm 26.92	111

Since KIS RNAi flies are clearly less robustly rhythmic than *cry^b* flies, we co-expressed *dicer2* along with the KIS dsRNAs, to increase the RNAi effects [56]. This approach proved successful, as flies expressing the VDRC dsRNAs directed against KIS were almost as robustly rhythmic as *cry^b* flies (Table 3, Fig. 3). The period was also similar to that observed in DD, further indicating that these flies are virtually insensitive to constant illumination and that KIS is essential for normal circadian photo responses. As the period length and amplitude of DD rhythms are not affected by KIS down regulation, KIS specifically regulates circadian photo responses.

A major potential caveat with expression of dsRNAs is off-target effects: dsRNAs sometimes target other genes than the one they were designed to down regulate. With KIS, we have observed a similar phenotype with two independent RNAi transgenes that target two different regions of the KIS RNA. In addition, EP (2)2469/KISMET targets a third region of the *kis* gene specific to the KIS-L isoform, which contains most domains necessary for KIS function in chromatin remodeling [43]. Thus, the

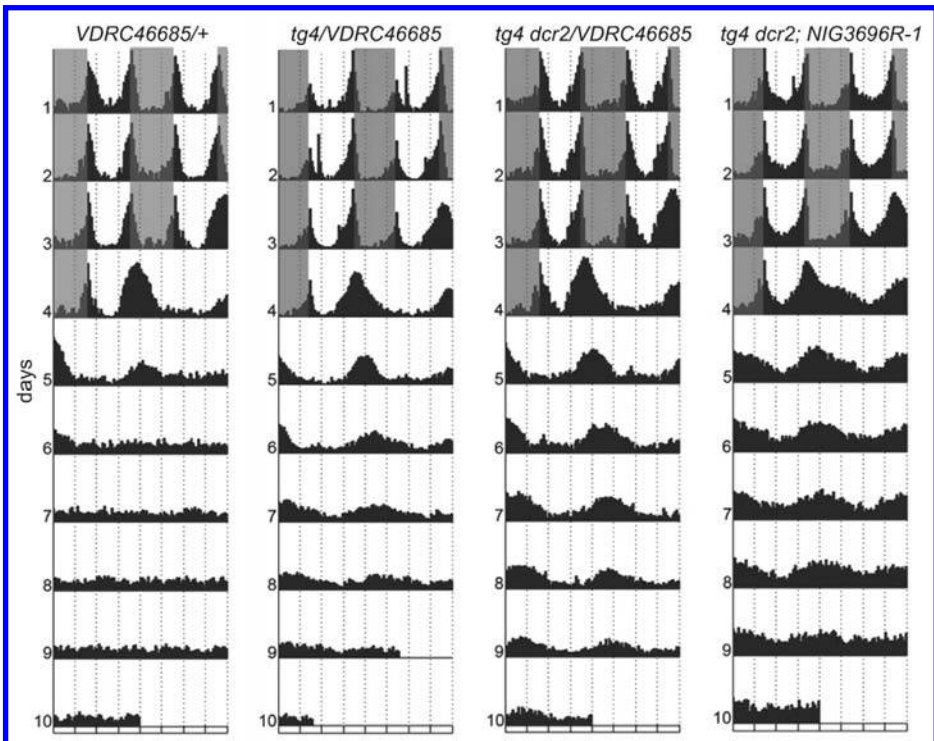


Figure 3. Flies expressing double-stranded RNAs directed against KISMET (KIS) in circadian neurons are rhythmic in LL.

The actograms show the average locomotor behavior of control flies (w1118; VDR46685/+ [VDR46685/+]) and flies expressing KIS dsRNAs under the control of *tim*-GAL4 without (*y w*; *tim*-GAL4/VDR46685 [*tg4*/VDR46685]) or with *dicer2* (w1118; *tim*-GAL4 UAS-*dcr2*/VDR46685 [*tg4 dcr2*/VDR46685]) and w1118; *tim*-GAL4 UAS-*dcr2*; NIG-Fly3696R-1 [*tg4 dcr2*; NIG3696R-1]). Flies were entrained for 3 days in LD and then released in LL. Note that rhythms are more robust when *dicer2* is co-expressed with the VDR46685 KIS dsRNAs. All genotypes are homozygous for *ls*-TIM, except *tg4 dcr2*; NIG3696R-1 (*ls*-*tim*/*s*-*tim*). *n* = 15–16 flies/genotype.

risks of off-target effects are virtually non-existent. In addition, no potential off-targets are predicted for VDR46685 (<http://stockcenter.vdrc.at/control/main>). Nonetheless, we verified that the RNAi lines we used indeed down regulate KIS expression. We first measured KIS expression in whole heads by Western Blot using the TIM-GAL4 driver to induce KIS RNAi, and found KIS levels to be reduced by 30 percent with both RNAi lines (Fig. 4A and 4B). Since the dsRNAs were expressed with TIM-GAL4, this highly reproducible reduction in KIS expression should reflect the down regulation occurring specifically in circadian tissues, in particular the eyes which are by far the largest contributors of circadian tissues in whole heads [57]. The KIS should not be down-regulated in non-circadian tissues.

There are ~150 circadian neurons in the *Drosophila* brains that are organized in 5 clusters in each hemisphere: the large and the small ventral lateral neurons (l-LNVs and s-LNVs), which express the neuropeptide PDF, the dorsal lateral neurons (LNDs) and three

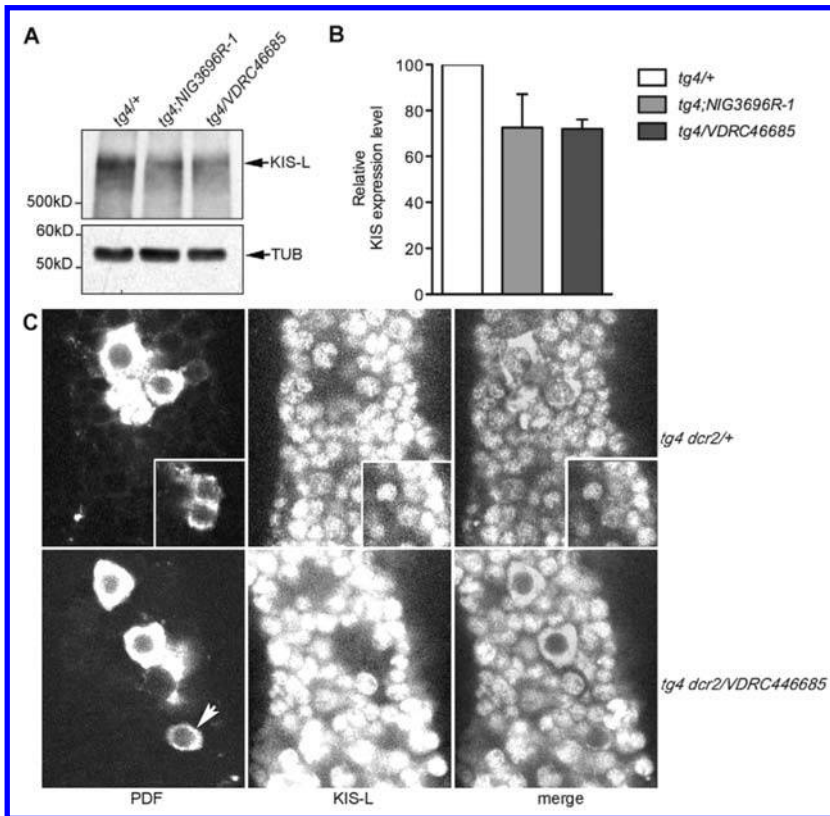


Figure 4. KISMET is down regulated in flies expressing KIS dsRNAs.

(A) Representative Western Blot measuring KIS-L protein levels in whole head extracts of control flies (*tim-GAL4/+* [*tg4/+*]) and flies expressing two different dsRNAs directed against KIS (NIG-Fly3696R-1 [NIG3696R-1] and VDRC46685) under the control of *tim-GAL4* (*tg4*). (B) Quantification of three independent Western Blots. KIS-L levels was normalized with the Tubulin loading control. Error bars correspond to standard deviations. KIS-L is reduced by about 30% in whole head extracts of flies expressing KIS dsRNAs, compared to control. (C) Images obtained by confocal microscopy showing the s-LNvs (shown in the insert on the upper panels and indicated by an arrowhead on the lower panels) and l-LNvs of *tim-GAL4 UAS-dcr2/+* controls (*tg4 dcr2/+*; upper panels) and of *tim-GAL4 UAS-dcr2/VDRC46685* (*tg4 dcr2/VDRC46685*) flies (lower panels). The brains were stained with an anti-PDF antiserum (B) and an anti-KIS-L antibody (A). KIS-L is almost undetectable in the nuclei of s- and l-LNvs of flies expressing the KIS dsRNAs, while it is strongly expressed in non-circadian neighbor neurons (lower panels), and in the s- and l-LNvs of control flies (upper panels).

groups of dorsal neurons (DN1s, 2s and 3s). We verified that KIS-L expression was indeed specifically down-regulated in circadian neurons by staining brains from flies expressing KIS dsRNAs in clock tissues and control flies with an antibody directed against KIS-L [43] along with an anti-PDF antibody. KIS-L was strongly expressed in the LNvs of wild-type flies, as well as in non-circadian neurons. KIS-L levels were unaffected in non-circadian neurons of flies expressing the dsRNAs with *TIM-GAL4*, but KIS-L expression was severely downregulated in the LNvs (Fig. 4C).

In summary, our results identify KIS as a crucial regulator of CRY-dependent circadian photoresponses. This validates our screen strategy.

KISMET Functions in Circadian Neurons Regulating Circadian Light Responses

Since KIS regulates constant light responses, it should be expressed in circadian neurons known to control these responses. To identify easily circadian neurons, we stained brains expressing a lacZ reporter gene in all clock neurons (line R32, [58]) with antibodies directed against β -GAL and KIS-L, because our results indicate that this isoform regulates light responses (see above). We found KIS-L to be expressed in l- and s-LN_vs, in the LN_ds, and in DN1s and 3s (Fig. 5A). Most of these neurons have been implicated in circadian behavioral photoresponses [26, 29, 33, 59-65]. In particular, the LN_ds and

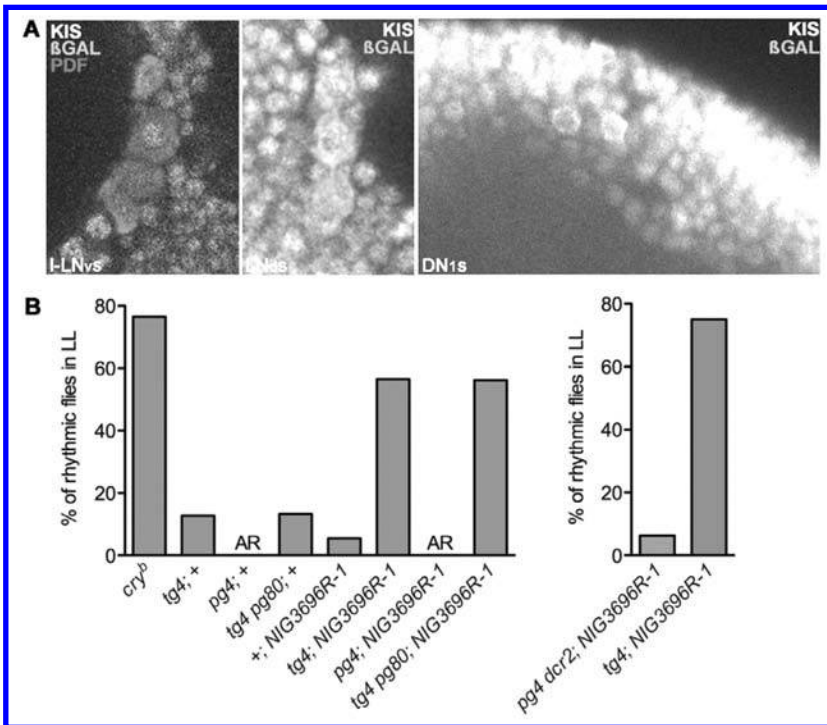


Figure 5. KIS is expressed and functions in PDF negative circadian neurons to control behavioral responses to constant light.

(A) Whole brains of flies expressing lacZ in all circadian neurons (line R32 [58]) were stained with anti-BGAL (B), anti-PDF (C) and anti-KIS-L (A) antibodies. The B color indicates the colocalization of BGAL and PDF. KIS is detected in the nuclei of the LN_vs, LN_ds and DN1s. (B) KIS was downregulated in different groups of circadian neurons using a combination of tissue-specific GAL4 and GAL80 drivers. Left panel: The expression of KIS dsRNAs (NIG-Fly3696R-1 [NIG3696R-1] carrying s-TIM) was driven by either TIM-GAL4 (*tg4*; carries *ls*-TIM) to down-regulate KIS in all circadian neurons, pdf-GAL4 (*pg4*; carries s-Tim) to restrict KIS RNA interference to the LN_vs, or with tim-GAL4 combined with pdf-GAL80 (*tg4 pg80*; *ls*-TIM) to downregulate KIS expression in PDF negative circadian neurons only. Right panel: Since pdf-GAL4 is inserted on a second chromosome containing s-TIM allele while tim-GAL4 is associated with *ls*-TIM allele, we also drove KIS dsRNAs expression with a pdf-GAL4 UAS-dcr2 (*pg4 dcr2*) recombinant 2nd chromosome bearing *ls*-TIM allele. This ensured that the absence of LL rhythms with pdf-GAL4 is not caused by the more sensitive s-TIM variant. The histograms show the percentage of rhythmic flies for each genotype in LL ($n = 14-16$). AR: complete arrhythmicity. Left and right histograms are independent experiments; this explains the small variation in rhythmicity with TIM-GAL4.

DN1s have been shown to be able to generate LL rhythms when the CRY input pathway is inhibited in these cells. That KIS is expressed in these cells, and that KIS down regulation results in LL rhythms clearly support the idea that KIS is a crucial regulator of the CRY input pathway.

We were therefore curious to verify that behavioral rhythms observed under constant illumination in KIS RNAi flies were due to KIS down regulation in dorsally located circadian neurons, and not in the PDF positive LN_vs. We thus used the pdf-GAL4 driver [66] to restrict KIS RNAi expression to the LN_vs, and a combination of TIM-GAL4 and pdf-GAL80 to express KIS dsRNAs in dorsal neurons only [67]. The KISMET down-regulation in the LN_vs alone did not affect the behavior in LL: all flies were arrhythmic. On the other hand, flies expressing KIS dsRNAs in PDF negative circadian neurons were rhythmic in LL (Fig. 5B). The absence of LL rhythms when driving KIS dsRNAs only in the LN_vs is not due to inefficient KIS down regulation: pdf-GAL4 and TIM-GAL4 are equally efficient at down regulating KIS expression. Together, these results demonstrate that KIS activity is required in PDF negative light-sensitive circadian neurons for normal CRY-dependent circadian photo responses.

KIS Genetically Interacts with CRY and Regulates TIM Degradation

The CRY targets TIM to proteasomal degradation [16, 20, 21]. The prediction would therefore be that if KIS regulates the CRY input pathway, light-dependent TIM degradation would be inhibited by KIS down regulation. Unexpectedly, we did not observe any defect in TIM light-dependent protein cycling in the head extracts of flies expressing KIS dsRNAs (data not shown). This is probably because RNA interference does not completely abolish KIS expression in the eyes, which are the main contributors of TIM protein in head extracts. Since CRY levels appear to vary significantly in different circadian tissues [68-70], we reasoned that CRY (or its signals to the pacemaker) might be limiting in the PDF negative neurons generating LL rhythms (LN_vs, DN1s), but not in the eyes. This would explain why LL behavior is particularly sensitive to KIS levels. We, therefore, over expressed CRY in all clock neurons of flies expressing KIS dsRNAs. As we anticipated, this genetic manipulation rescued the behavioral phenotype resulting from KIS knockdown: the double-manipulated flies behaved like wild-type flies as they became arrhythmic after their release in LL (Fig. 6A). Thus, when CRY is not limiting, circadian photo responses are much less sensitive to KIS levels.

We, therefore, decided to express KIS dsRNAs in cry^m mutant flies [18]. The cry^m allele encodes a truncated form of CRY lacking the last 19 amino acids of its C-terminal domain. This truncated CRY is very unstable but remains functional. In cry^m flies, TIM levels oscillate in LD but the amplitude of this molecular rhythm is significantly reduced relative to wild-type flies, because CRY levels are limiting [18] (Fig. 6B and 6C). Interestingly, when we expressed KIS dsRNAs in cry^m flies, TIM cycling amplitude was further reduced to about half of what it normally is in cry^m flies. This effect was highly reproducible and statistically significant ($p < 0.05$, t test). Notably, TIM levels remained higher during the day, even though they were reduced during the night. Note that TIM cycling is not sensitive to eye color: no difference was observed in amplitude between the white-eyed cry^m flies (y w; cry^m) and deep orange-eyed cry^m flies (y w; TIM-GAL4 UAS-dcr2/+; cry^m; Fig. 6B and 6C). Thus, we are confident that the addition of the KIS

dsRNA transgene (in *y w*; *tim-GAL4 UAS-dcr2/VDRC46685*; *cry^m*), which only very slightly darkens eye color compared to control flies (*y w*; *tim-GAL4 UAS-dcr2/+*; *cry^m*), does not contribute to the reduction in TIM cycling amplitude. Moreover, in *cry⁺* flies, CRY and TIM levels are unaffected by this slightly darker eye color (data not shown).

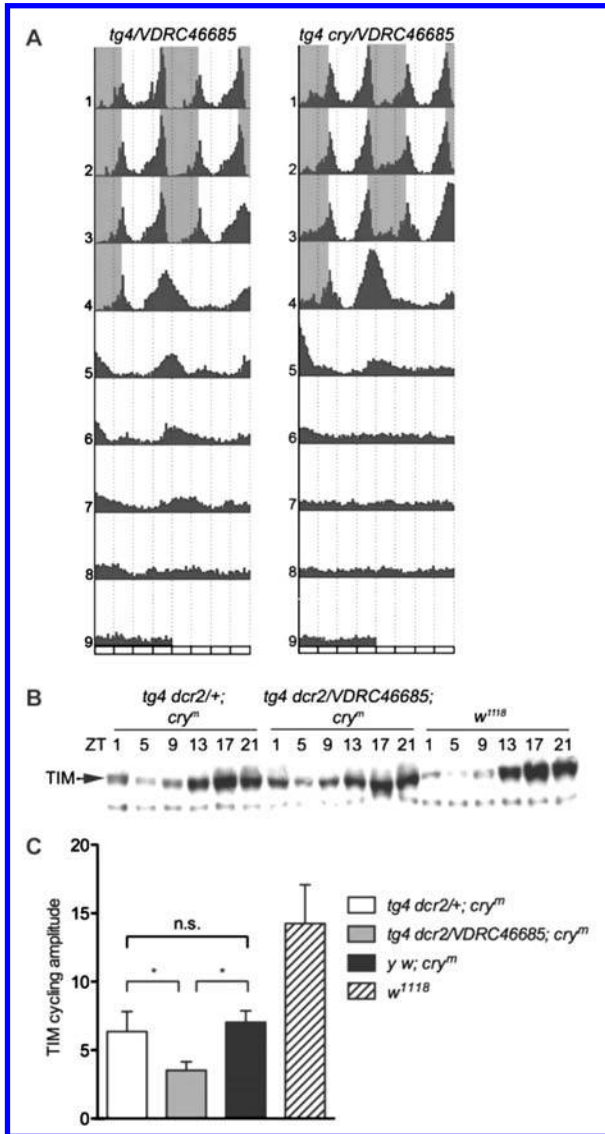


Figure 6. Kismet and *cry* genetically interact.

(A) Increasing CRY signaling in flies expressing KIS dsRNAs rescues the LL phenotype. Actograms show the locomotor activity of *TIM-GAL4/VDRC46685* (*tg4/VDRC46685*; homozygous for *ls-TIM*) and *TIM-GAL4 UAS-myccry/VDRC46685* flies (*tg4 cry/VDRC46685*; *s-tim/ls-tim* heterozygous). The presence of one *s-TIM* allele in flies overexpressing CRY potentially contributes to the rescue, because the *S-TIM* protein is more sensitive to CRY signaling [87]. This contribution is small however. Indeed,

Figure 6. (Caption Continued)

50 percent of TIM-GAL4/VDRC46685 flies carrying one s-TIM allele are rhythmic in constant light (see Table 3). In addition, CRY overexpression also rescues arrhythmicity in a *l*s-TIM homozygous background, although a slight increase in residual rhythms was detected during the first 3 days of LL. $n = 15\text{--}16$ flies/genotype. (B) Western blot showing TIM oscillations in whole head extracts of control (w^{1118}), TIMGAL4 UAS-*dcr2/+*; cry^m/cry^m (*tg4 dcr2/+*; cry^m) and TIM-GAL4 UAS-*dcr2/VDRC46685*; cry^m/cry^m (*tg4 dcr2/VDRC46685*; cry^m) flies entrained to an LD cycle. All genotypes are homozygous for *l*s-TIM. (C) The amplitude of TIM protein rhythms is reduced in cry^m flies expressing KIS dsRNAs. TIM protein levels were quantified by Western Blot at ZT17 (peak) and ZT5 (trough) and normalized with the Tubulin loading control. The histogram represents the ratio between the two values. Each bar represents the average of 4 independent experiments per genotypes, except $y w$; cry^m ($n = 3$). Error bars represent standard deviations (* $p < 0.05$; t-test).

In summary our results demonstrate that KIS interacts genetically with *cry* and regulates circadian photo responses not only in the brain pacemaker neurons, but also in peripheral oscillators such as the eyes.

CONCLUSION

In most organisms, intracellular molecular pacemakers called circadian clocks coordinate metabolic, physiological, and behavioral processes during the course of the day. For example, they determine when the animals are active or resting. Circadian clocks are self-sustained oscillators, but their free-running period does not exactly match the day length. Thus, they have to be re-set by environmental inputs to stay properly phased with the day:night cycle. The fruit fly *Drosophila melanogaster* relies primarily on Cryptochrome (CRY)—a cell-autonomous blue-light photoreceptor to synchronize its circadian clocks with the light:dark cycle. With a genetic screen, we identified over 20 candidate genes that might regulate CRY function, KISMET (KIS) is among them: it encodes a chromatin remodeling factor essential for the development of *Drosophila*. We show that, in adult flies, KIS is expressed and functions in the brain neurons that control daily behavioral rhythms. KIS determines how *Drosophila* circadian behavior responds to light, but not its free-running period. Moreover, manipulating KIS and CRY activity simultaneously demonstrates that these two genes interact to control molecular and behavioral circadian photo responses. Our work therefore reveals that KIS regulates CRY signaling and thus determines how circadian clocks respond to light input.

KEY WORDS

- **CHARGE syndrome**
- **Chromatin-remodeling enzyme KISMET (KIS)**
- **Circadian rhythmicity**
- **Constant darkness (DD)**
- **Cryptochrome (CRY)**
- **Day:night cycle**
- ***Drosophila***
- **Jetlag (JET)**
- **Light-dependent degradation**

- **Peakphaseplot function**
- **Period (PER)**
- **Timeless (TIM)**
- **Ubiquitination**
- **Western Blot**

ACKNOWLEDGMENTS

We are grateful to P. Rørth for the generous gift of the EP line collection, to J. Tamkun for the anti-KIS-L antibody, and to H. Benes and J. Nambu for sharing unpublished GstS1 and morgue mutants. We thank S. Jackson, M. Tanouye, O. Shafer, H. Steller, I. Edery, the Vienna *Drosophila* RNAi Center (VDRRC), the Japanese National Institute of Genetics (NIG-Fly), and the Bloomington *Drosophila* Stock Center for other flies' stocks and C. Helfrich-Förster for the anti-CRY antibody. We thank M. Emery-Le and C. Kotarski for technical assistance with the EP line screen and D. Wentworth and D. Szydlak for additional technical support. We are also grateful to F. Rouyer and M. Boudinot for the FaasX software, and to J. Levine for the Matlab analysis toolbox. We also thank members of the Emery, Reppert, and Weaver lab for helpful discussions and comments on this work.

AUTHORS' CONTRIBUTIONS

Conceived and designed the experiments: Raphaëlle Dubruille, Alejandro Murad, Michael Rosbash, and Patrick Emery. Performed the experiments: Raphaëlle Dubruille, Alejandro Murad, and Patrick Emery. Analyzed the data: Raphaëlle Dubruille, Alejandro Murad, and Patrick Emery. Wrote the paper: Raphaëlle Dubruille and Patrick Emery.

Chapter 2

Complications in High Caloric Diet-Fed Rats

Camila de Moraes, Ana Paula Couto Davel, Luciana Venturini Rossoni, Edson Antunes, and Angelina Zanesco

INTRODUCTION

Obesity has been associated with a variety of diseases such as type II diabetes mellitus, arterial hypertension, and atherosclerosis. Evidences have shown that exercise training promotes beneficial effects on these disorders, but the underlying mechanisms are not fully understood. The aim of this study was to investigate whether physical pre-conditioning prevents the deleterious effect of high caloric diet in vascular reactivity of rat aortic and mesenteric rings. High caloric diet increased triglycerides concentration (sedentary diet (SDD): 216 ± 25 mg/dl) and exercise training restored to the baseline value (trained diet (TRD): 89 ± 9 mg/dl). Physical pre-conditioning significantly reduced insulin levels in both groups (trained control (TR): 0.54 ± 0.1 and TRD: 1.24 ± 0.3 ng/ml) as compared to sedentary animals (sedentary control (SD): 0.87 ± 0.1 and SDD: 2.57 ± 0.3 ng/ml). On the other hand, glucose concentration was slightly increased by high caloric diet, and RT did not modify this parameter (SD: 126 ± 6 ; TR: 140 ± 8 ; SDD: 156 ± 8 and TRD 153 ± 9 mg/dl). Neither high caloric diet nor RT modified NOx- levels (SD: 27 ± 4 ; TR: 28 ± 6 ; SDD: 27 ± 3 and TRD: 30 ± 2 μ M).

Obesity is a public health problem and it is a major risk factor for a variety of diseases including arterial hypertension, diabetes mellitus, atherosclerosis, and dyslipidemia [1]. Particularly, atherosclerosis is a chronic inflammatory disease associated with endothelium dysfunction and vascular smooth muscle growth resulting in imbalance of vasodilator and vasoconstrictor production by endothelial cells and decrease in vessel lumen [2]. It has been pointed out that oxidative stress associated with alterations in plasma lipid concentration are the main causes of atherosclerosis and both factors play a key role in this cardio-inflammatory disease [3-5].

Evidences have shown that high fat diet provokes alterations in lipid profile and endothelium dysfunction leading to impairment of vascular relaxing responses in rats and pigs [6-9]. A number of studies have reported that the beneficial effect of physical training in lowering LDL-cholesterol and increasing HDL-cholesterol particles [10], as well as improving the endothelium-derived relaxing response, lead to a prevention of atherosclerosis due to increased nitric oxide (NO) production and/or its bioavailability [11-18]. However, no studies exist investigating the effect of run training associated with high caloric diet in the vascular responsiveness in rats.

Therefore, the aim of the present study was to test the hypothesis that prior physical training promotes beneficial effects in the relaxing response of aortic and mesenteric rings from animals fed with high caloric diet and the underlying

mechanism mediating this phenomenon. We also evaluated whether run training attenuates the endocrine-metabolic alterations produced by high caloric diet fed-rats.

MATERIALS AND METHODS

Animals and Experimental Protocol

The animal protocols were approved by the Ethics Committee for Experimental Research of the State University of Campinas (UNICAMP). Male Wistar rats (10-weeks-old) were obtained from the Animal Care Facility of UNICAMP. Animals were maintained on a 12 hr light/dark cycle, housed in groups of four animals and had free access to water and high caloric diet (56% of carbohydrate, 18% of protein and 26% fat) or standard rat chow (40% carbohydrate, 26.5% protein and 3.8% as fat; Purina Co., Campinas-São Paulo, Brazil). Animals were divided into four groups: SD, TR, SDD and TRD.

Experimental protocol consisted of 4 weeks of run training program prior to high caloric diet consumption, after which high caloric diet and exercise training were carried out simultaneously for further 8 weeks. Animals were trained in a treadmill with an intensity of 70–80 % of maximal oxygen consumption, in sessions of 60 min, 5 days a week. Only the animals adapted to the treadmill were used in trained groups. The scheme below illustrates the experimental protocol design.

Concentration-Response Curves

Aorta and superior mesenteric arteries were removed carefully and placed in freshly prepared Krebs solution containing (mM): NaCl, 118; NaHCO₃, 25; glucose, 5.6; KCl, 4.7; KH₂PO₄, 1.2; MgSO₄, 1.17 and CaCl₂, 2.5. The arteries were cleaned of all adherent tissue and cut into rings of approximately 2 mm. Each ring was suspended between two wire hooks and mounted in 10 ml organ chambers with Krebs solution at 37°C, pH 7.4, and continuously aerated with a mixture of 95% O₂ and 5% CO₂ under a resting tension of 10 mN. The tissues isometric tension was recorded by a force-displacement transducer (UgoBasile, Varese, Italy) connected to a Power Lab 400™ data acquisition system (AD Instruments Pty Ltd, Castle Hill, Australia).

After 1 hr of stabilization period, intact endothelium aortic and mesenteric rings were pre-contracted with phenylephrine (1 μM). Cumulative concentration-response curves to acetylcholine (ACh, 10 nM-100 μM) and sodium nitroprusside (SNP, 100 pM-100 nM) were obtained in aortic and mesenteric rings with intact endothelium. Concentration-response data were evaluated for a fit to a logistics function in the form:

$$E = E_{\max} / ((1 + (10^c / 10^x)^n) + \Phi)$$

where E is the response; E_{\max} is the maximum response that the agonist can produce; c is the logarithm of the EC50, the concentration of agonist that produces half-maximal response; x is the logarithm of the concentration of agonist; the exponential term, n , is a curve fitting parameter that defines the slope of the concentration-response line, and Φ is the response observed in the absence of added agonist. Nonlinear regression

analyses to determine the parameters E_{\max} , log EC50 and n were done using GraphPad Prism (GraphPad Software, San Diego-CA, USA) with the constraint that $\Phi = 0$.

Lipid Profile, Glucose and Insulin Concentration

After 12 weeks, animals were sacrificed after an overnight fasting. Blood samples were taken from descendent aorta under anesthesia with pentobarbital sodium (30 mg/kg, i.p.). Plasma and serum were immediately separated by centrifugation (8,000 g). Glucose levels and lipid profile were assessed by using specific commercial kits (colorimetric method, Labor lab, São Paulo, Brazil). Insulin concentration was determined by radioimmunoassay as described previously [19]. Homeostasis Model Assessment (HOMA), an index of insulin resistance was calculated according to a method previously described [20].

Determination of Plasma Nitrite/Nitrate (NO_x) Levels

In order to evaluate the NO production, the plasma levels of nitrite/nitrate (NO_x) were measured. Briefly, immediately after arterial blood collecting, the samples were centrifuged (8,000 g) for 10 min, and the resulting plasma supernatant was stored at 80°C. Plasma samples were ultra filtered through micro filter cups (Microcon Centrifugal Filter Units, 10 kDa; Millipore, Bedford, MA, USA). The NO_x concentration of the resulting filtrate solution was determined using a commercially available kit (Cayman Chemical, Ann Arbor, MI, USA) according to the manufacturer's instructions. This assay determines the total NO based on the enzymatic conversion of nitrate to nitrite by nitrate reductase. After the conversion, the spectrophotometric measurement of nitrite is accomplished by using the Griess Reaction. The resulting deep purple azo compound absorbs light at 540–550 nm.

Western Blotting Assay for Cu/Zn Superoxide Dismutase

In order to evaluate the contribution of Cu/Zn superoxide dismutase (SOD-1) in endothelial cells in response to exercise training, aortic, and mesenteric expression of SOD-1 was determined by Western blotting assays. Frozen segments of aorta and mesenteric arteries were homogenized and protein concentration was determined using Bradford method [21]. Samples containing 50 µg proteins were loaded into gels and electrophoresed, and proteins were subsequently electroblotted in polyvinylidene difluoride membranes. Primary antibody was mouse anti Cu/Zn SOD (1:1500, SIGMA, St. Louis, MO, USA). Chemiluminescent signals (ECL plus Amersham, Piscataway, NJ, USA) were captured on X-ray film (Hyperfilm Amersham, Piscataway, NJ, USA), and scanning densitometry was used to quantify the immunoblot signals.

Drugs and Solutions

Acetylcholine, sodium nitroprusside, and phenylephrine were purchased from SIGMA (St. Louis, MO, USA). All other reagents used were of analytical grade.

Statistical Analysis

Data are presented as means ± standard error mean (SEM) of n experiments. Comparison of studied parameters and agonist responses was performed by analysis of

variance (ANOVA two-way) to determine high caloric diet consumption and exercise training interference in results. Pearson correlation was used to determine association between triglycerides concentration and endothelium dependent relaxation evoked by acetylcholine. Statistical program SPSS 10.0 was used and the level of statistical significance employed was $p < 0.05$.

DISCUSSION

The present study is the first to show that physical pre-conditioning at moderate intensity restores the impairment of relaxing response in mesenteric rings from high caloric diet-fed rats, which was positively associated with reduction in triglycerides concentration and up-regulation in SOD-1 expression.

Although a variety of experimental models of obesity exist, such as genetic, drugs, and diet manipulations, dietary-induced obesity is the most relevant experimental model regarding to human obesity [22]. Our present findings show that run training was effective to reduce the body weight gain and the amount of food intake, indicating that aerobic physical exercise is an important approach in the management of both parameters in this particular experimental obesity model.

Impairment of endothelium-dependent relaxation of blood vessels has been consistently demonstrated in a number of studies as a consequence of obesity [6, 7, 23]. A variety of factors have been proposed to explain the obesity-related endothelial dysfunction including alteration in the adipocyte-derived hormones resistin, adiponectin, and leptin [24, 25], high plasma triglycerides concentration and increase of oxidative stress [6, 7, 23, 26]. In the present study, high caloric diet significantly produced an impairment of endothelium-dependent relaxation for ACh in mesenteric rings, confirming previous studies.

It is well documented that physical exercise promotes beneficial effects in lipid profile [10, 27, 28]. Particularly, plasma triglycerides concentration is reduced after exercise training by increasing lipoprotein lipase activity in plasma clearing triglycerides from its circulation and replenishing it to the skeletal muscle stores, to the process of excitation-contraction coupling (27). Our findings show that physical exercise was efficient to decrease triglycerides concentration after high caloric diet, which was positively correlated with the improvement of maximal relaxation responses to ACh in isolated mesenteric rings. These findings indicate that triglycerides concentration is an important marker for endothelial dysfunction.

High caloric diets are frequently associated with insulin resistance and consequently hyperinsulinemia [29, 30]. This condition is related to high level of free fatty acids that increases cellular diacylglycerol leading to activation of different protein kinase C isoforms that phosphorylates serine/threonine sites of insulin receptor (IR) and its substrates. The IR phosphorylation reduces its ability to activate PI3K leading to decrease of the glucose transporters GLUT-4 translocation to the cellular membrane resulting in the impairment of glucose uptake [31]. In our study, a marked increase in insulin concentration was found in SDD group that was attenuated after exercise training for 12 weeks, showing clearly the beneficial effects of physical exercise in the management of hyperinsulinemia. Similarly, high caloric diet consumption increased

blood glucose level, but exercise training failed to restore it to the baseline. The reasons for that could be the magnitude of the alterations in glycemia (approximately of 24 percent) as compared to insulinemia (approximately 194 percent) in SDD group. Previous studies have also showed that only a slight increase (or no change) in glucose concentration is seen in dietary-obese rats [30-33].

Either in human or laboratory animals, the cardiovascular benefits of exercise training have been associated with a variety of cellular and molecular alterations including up-regulation of endothelial NO synthase (eNOS), increase in expression and/or activity of antioxidant enzymes, as well as decrease in prooxidant enzyme systems [34, 35]. The antioxidant defense systems consist of enzymes such as SOD, catalase and glutathione peroxidase, and non-enzymes including vitamins and flavonoids [36]. The antioxidant enzymes are scavengers of reactive oxygen species (ROS) causing an increase of NO bioavailability to the vascular smooth muscle and enhancement of endothelium-dependent vasodilatation [37-39].

Considering the variety of the receptors and signaling pathways present in the vascular smooth muscle and endothelial cells to trigger the relaxing response, the evaluation of exercise training in the responsiveness of vascular blood vessel is a complex issue. Additionally, multiple interactions exist between the stimulus of an agonist and the vascular response including the affinity of receptor-agonist, metabolism of drugs, existence of antioxidant and prooxidant enzymes in the cell, and the contribution of several protein regulators in the phosphorylation process [35]. At least three isoforms of SOD exist in mammalian tissues, namely Cu/Zn SOD (SOD1), MnSOD (SOD2) and extracellular SOD (EcSOD or SOD3) that are located in cytosol, mitochondria, and vascular smooth muscle, respectively [40, 41]. Thus, to assess the underlying mechanisms by which exercise training ameliorates the vascular responsiveness in this particular model we have chosen to analyze SOD-1 expression in both arteries and plasma NO_x concentration for two reasons. First, SOD-1 represents a major cellular defense against superoxide anion and peroxynitrite formation in endothelial cells. Second, the primary focus of our study was to evaluate the effect of exercise training on endothelium function.

Interestingly, in both aortic and mesenteric rings, an increase in SOD-1 expression in trained groups was found. This up-regulation of SOD was accompanied by an increased in relaxing response for endothelium-dependent agonist. Therefore, our findings clearly show a strong relationship between the improvement in relaxing response seen in trained animals and up-regulation of SOD-1 expression. This is consistent with previous reports in porcine aorta showing that chronic exercise training increases SOD-1 expression associated with improvement in relaxing response [42, 43].

In the present study, either high caloric diet or exercise training did not modify the NO production, as estimated by plasma NO_x quantification. Previous studies also failed to show a direct correlation between increased NO production and improvement of endothelium-dependent dilation after exercise training [8, 42-47], which may be attributed to differences in duration, intensity, and frequency of the training program employed in each study. In fact, to evaluate the effect of exercise training on molecular mechanisms, it is important to consider the total volume of an exercise

training program, which is based upon the frequency, intensity, and duration. Accordingly, previous study found that 4 weeks of exercise training produced an increase of NO production that was positively associated with the improvement of relaxing response for endothelium-dependent agonist [48].

RESULTS

Body weight at initial time of the study was similar in all groups. High caloric diet consumption provoked an increase in body weight gain in SDD group, approximately 13 percent as compared with SD group. Exercised animals (TR and TRD) showed a smaller weight gain, approximately 16 percent, as compared with their sedentary groups (SD and SDD). The amount of food intake was also smaller in trained animals (TR and TRD groups) as compared with its matched-sedentary animals (SD and SDD groups). The data is summarized in Table 1 and illustrated in Fig. 1.

Table 1: Effect of Exercise Training on Body Weight, Triglycerides, Serum Glucose, Insulin and Nitrite/Nitrate Concentration from Animals Fed with Standard Chow or High Caloric Diet.

	SD	TR	SDD	TRD
Initial body weight (g)	306 ± 7	297 ± 6	306 ± 8	301 ± 8
Final body weight (g)	478 ± 9	401 ± 8 ^a	538 ± 11 ^c	452 ± 14 ^{bd}
Triglycerides (mg/dl)	91 ± 11	55 ± 8 ^a	216 ± 25 ^c	89 ± 9 ^{bd}
Glucose (mg/dl)	126 ± 6	140 ± 8	156 ± 8 ^c	153 ± 9
Insulin (ng/ml)	0.87 ± 0.10	0.54 ± 0.10 ^a	2.57 ± 0.32 ^c	1.24 ± 0.32 ^b
HOMA IR	0.61 ± 0.11	0.45 ± 0.09 ^a	2.42 ± 0.24 ^c	1.08 ± 0.32 ^{bd}
Nitrite/nitrate (μM)	27 ± 4	28 ± 6	27 ± 3	30 ± 2

Data are mean ± S.E.M. for $n = 8$ animals in each group. SD: sedentary, TR: trained, SDD: sedentary diet, TRD: trained diet. ^atrained vs sedentary; ^btrained diet vs sedentary diet; ^csedentary diet vs sedentary; ^dtrained diet vs trained.

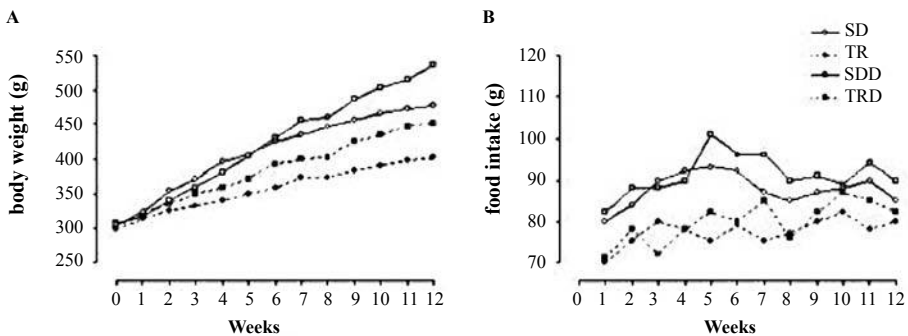


Figure 1: Body weight gain (A) and mean food intake (B) during experimental protocol.

High caloric diet consumption for 8 weeks provoked a marked increase in triglycerides concentration in SDD group, approximately 138 percent, which was almost restored to the basal values by exercise training. Furthermore, exercise training per se reduced triglycerides levels, approximately 40 percent (Table 1). Glucose concentration was significantly greater in SDD group, about 24 percent, as compared with SD

group, and run training did not modify this parameter. Similarly, high caloric diet markedly increased insulin concentration in SDD group, approximately 194 percent as compared to SD group. Exercise training for 12 weeks attenuated the increase of insulin concentration, approximately 52 percent in TRD group as compared with SDD animals. Additionally, exercise training per se produced a decrease in insulin concentration (38 percent) as compared to SD group (Table 1).

In order to verify the insulin resistance, HOMA index was calculated in all groups. High caloric diet produced an increase of HOMA index whereas exercise training alone or associated with high caloric diet consumption produced a significant reduction in this parameter, indicating improvement in insulin sensitivity. To evaluate the production of NO metabolites in response to exercise training, the plasma NOx concentration was measured. Our findings showed that NOx levels were not modified in all groups (Table 1).

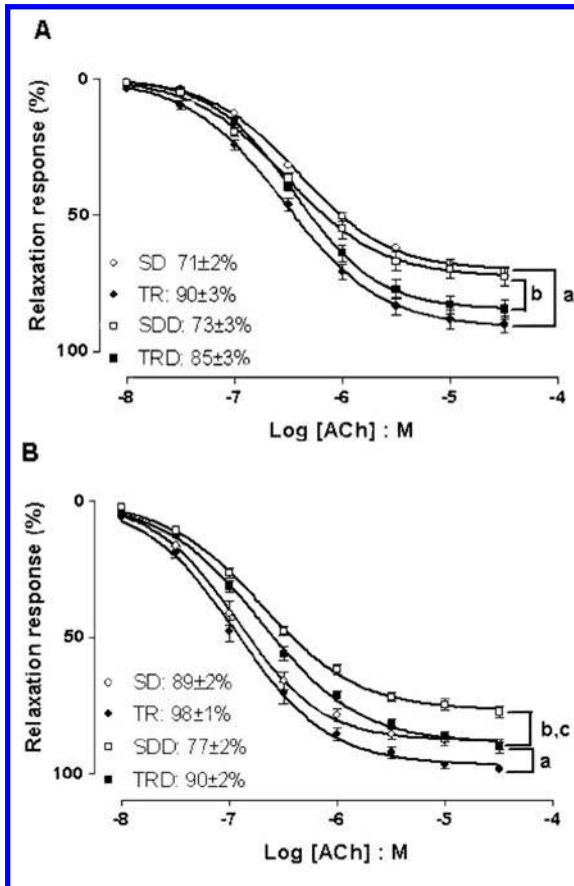


Figure 2: Concentration response curves to ACh in aortic (A) and mesenteric (B) rings. Data are means \pm SEM of $n = 5-6$ in each group. SD: sedentary, TR: trained, SDD: sedentary diet, TRD: trained diet. a) trained versus sedentary; b) trained diet versus sedentary diet; c) sedentary diet versus sedentary.

Endothelium-dependent relaxation responses were evaluated by construction of full concentration-response curves to ACh in aortic and mesenteric rings. In aortic rings, run training per se produced an increase of the maximal responses to ACh, compared with SD group. Similarly, an increase in the maximal responses to ACh in aortic ring from TRD group was observed. In mesenteric rings, the maximal responses to ACh was reduced in SDD animals while the run training for 12 weeks reversed the impairment of the relaxation responses produced by high caloric diet in TRD group (Fig. 2). Similarly, run training alone (TR group) provoked an increase of the maximal responses for ACh (10%). No changes were found in the potency values for this muscarinic agonist in all groups. The data is illustrated in Fig. 2. a strong correlation between triglycerides concentration and impairment of relaxing response for ACh was found in both preparations (Fig. 3).

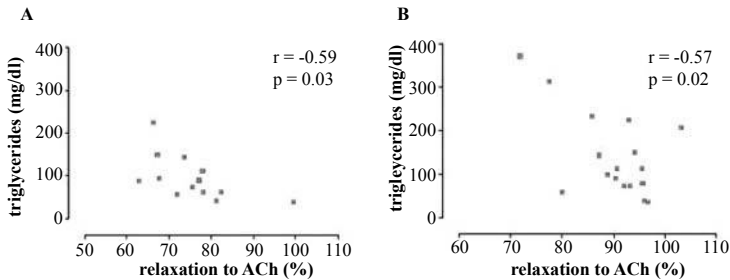


Figure 3: Correlation between triglycerides concentration and maximal relaxation responses to acetylcholine in aortic (A) and mesenteric (B) rings.

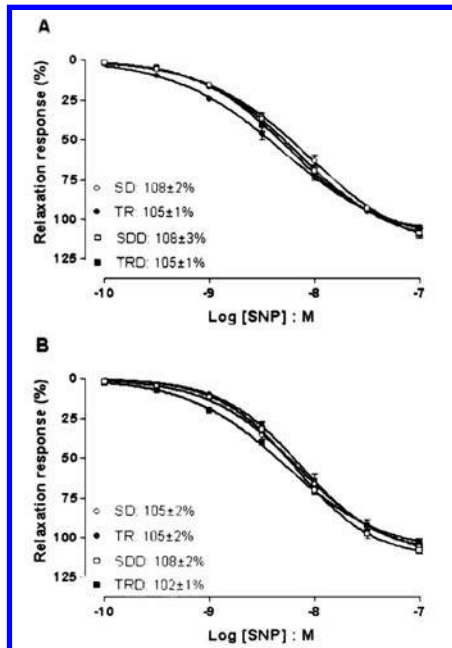


Figure 4: Concentration response curves to SNP in aortic (A) and mesenteric (B) rings. Data are means \pm SEM of $n = 5-6$ in each group. SD: sedentary, TR: trained, SDD: sedentary diet, TRD: trained diet.

Figure 4 illustrates the concentration-response curves to SNP in aortic and mesenteric rings. This NO donor produced concentration-dependent relaxing responses in both preparations in all groups. Neither maximal responses nor potency values were altered by exercise training (TR group) or high caloric diet consumption (SDD and TRD groups) in both preparations.

Data from Western blotting analysis in isolated aorta and mesenteric arteries from trained animals fed with standard chow or high caloric diet (TR and TRD groups) showed an increase in the expression of antioxidant enzyme SOD-1, approximately 30 percent. In mesenteric artery, SOD-1 expression was significantly reduced in SDD animals, but not in aortic rings (Fig. 5).

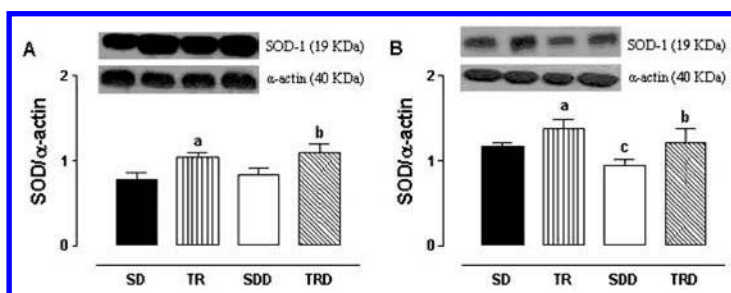


Figure 5: Effects of exercise training in the SOD-1 expression from isolated rat aorta (panel A) and mesenteric (panel B) arteries. Representative Western blot (top) and quantitative analysis (bottom) for SOD-1 protein expression. Data are means \pm SEM of $n = 7-8$ per group. SD: sedentary, TR: trained, SDD: sedentary diet, TRD: trained diet. a) trained versus sedentary; b) trained diet versus sedentary diet; c) sedentary diet versus sedentary.

CONCLUSION

In our study, the improvement in endothelial function found in both arteries from trained high caloric-fed rats, was directly related to an increase in NO bioavailability to the smooth muscle due to SOD-1 up regulation.

KEY WORDS

- Endothelial NO synthase (eNOS)
- Glucose transporters GLUT-4
- HDL-cholesterol
- Homeostasis model assessment (HOMA)
- LDL-cholesterol
- Insulin receptor (IR)
- Reactive oxygen species (ROS)
- Sedentary control (SD)
- Sedentary diet (SDD)
- Superoxide dismutase (SOD)
- Trained diet (TRD)
- Trained control (TR)

AUTHORS' CONTRIBUTIONS

Camila de Moraes conceived of the project, collected and analyzed the data and wrote the manuscript; Ana Paula Couto Davel and Luciana Venturini Rossoni participated in the Western blotting analyses; Edson Antunes provided laboratories conditions and participated in the project conception; Angelina Zanescó participated in the project conception, the study design, data analysis and writing the manuscript.

ACKNOWLEDGEMENTS

We are grateful for financial support from Coordenação de Aperfeiçoamento de Pessoal de Nível Superior (CAPES) and Fundação de Amparo à Pesquisa do Estado de São Paulo (FAPESP). L.V.R. is a research fellow from CNPq.

Chapter 3

Young Wild-Type Mice and Serotonin-Related Variables

Ricardo Albay III, Angela Chen, George M. Anderson, Maggie Tatevosyan, and Skirmantas Janušonis

INTRODUCTION

The blood hyperserotonemia of autism is one of the most consistent biological findings in autism research, but its causes remain unclear. A major difficulty in understanding this phenomenon is the lack of information on fundamental interactions among the developing brain, gut, and blood in the mammalian body. We therefore investigated relationships among the body mass, brain mass, the volume of the hippocampal complex, the gut length, and the whole-blood levels of tryptophan and 5-hydroxytryptamine (5-HT, serotonin) in young, sexually immature wild-type mice. The study provides information on the covariance structure of several central and peripheral variables related to the body serotonin systems. In particular, the results indicate that body mass should be included as a covariate in studies on platelet 5-HT levels and they also suggest a link between brain growth and gut length.

The present study was motivated by the platelet hyperserotonemia of autism, a long-standing problem in autism research. It is an extension of our previous experimental and theoretical investigations [1-3] that suggest that the platelet hyperserotonemia is inherently a systems problem in that it requires understanding relationships among various components of the peripheral serotonin (5-hydroxytryptamine, 5-HT) system, and the developing brain.

The platelet hyperserotonemia of autism is defined as elevated 5-HT levels in the blood platelets of individuals diagnosed with autism spectrum disorders (ASDs) [4-6]. To date, this finding has been replicated by many studies in ethnically diverse autistic groups [7-15]. While a number of genes may contribute to ASD risk [16-21], the replicability of the platelet hyperserotonemia suggests that these genes may affect a small set of biological networks [3, 22].

The 5-HT sequestered in platelets is synthesized from tryptophan by enterochromaffin cells in the gut wall [23], with negligible contribution from serotonergic neurons of the enteric nervous system [24]. Some of the gut 5-HT diffuses into the systemic blood circulation, where most of it is rapidly cleared by the liver and lungs [25, 26]. The remaining free 5-HT in the blood plasma can be taken up by platelets that express the serotonin transporter (SERT). Early studies have suggested that the platelet hyperserotonemia of autism may be caused by altered function of SERT in blood platelets [27]. More recent research has shown that SERT polymorphic variants do partially determine platelet 5-HT uptake rates [28], but that these polymorphisms, alone, do not cause the

platelet hyperserotonemia of autism [28, 29] or contribute to autism itself [10, 30-33]. Other studies have suggested that the platelet hyperserotonemia may be caused by altered 5-HT production in the gut [1, 34-37], but current experimental evidence remains inconclusive. Also, no link between platelet hyperserotonemia and increased intestinal permeability has been found in children with pervasive developmental disorders [38].

Several studies have recently proposed that the platelet hyperserotonemia of autism may be caused by interactions among several components of the peripheral 5-HT system [2, 14, 37, 39]. Specifically, the amount of 5-HT stored in blood platelets may depend on the dynamic interplay among the gastrointestinal system, blood circulation, vascular beds, and platelets themselves [2]. Understanding these interactions in the peripheral 5-HT system may lead to new insights into the normal function of the central nervous system. Tryptophan, the 5-HT precursor, is actively transported across the blood brain barrier (BBB) and, while 5-HT is generally thought not to cross the BBB, some transfer may occur at elevated 5-HT concentrations [40]. Brain neurons express the same SERT as platelets [41], and SERT is also expressed by brain endothelial cells [42, 43]. Also, brain and enteric neurons express many of the same serotonin receptors [44].

Our previous theoretical investigation has shown that platelet 5-HT levels may be a function of a number of parameters and their interactions, among them the volume of the circulating blood and the length of the gut [2]. Based on these previous findings, we investigated correlative relationships among several key components of the peripheral 5-HT system and the brain in young, sexually immature mice. Specifically, we measured the body mass, the brain mass, the volume of the hippocampal complex, the relaxed gut length, and the whole-blood 5-HT and tryptophan levels in the same individual wild-type mice at 2 weeks after birth. In this study, the hippocampal complex served as a convenient brain structure, the borders of which are clearly defined in Nissl-stained sections. The hippocampal complex may also play a role in ASDs [45-47].

The principal aim of the present study was to reveal the system's covariance structure [48] which can guide experimental design and can be used in advanced, causal modeling. Therefore, strong emphasis was placed on statistical power in an effort to obtain reasonably accurate correlation coefficients, rather than merely significant or non-significant results [49]. One of the advantages of this approach is that the obtained covariance matrix can be combined with the results of future studies and used in structural equation modeling, a powerful modeling technique for complex systems.

The focus of the present study was restricted to a postnatal developmental time that may offer insights into central and peripheral alterations in ASDs. We have previously shown that, by 2 weeks after birth, 5-HT_{1A} receptor-knockout mice develop platelet hyperserotonemia [1]. Studies in rats suggest that at this time the development of the hippocampus and the cerebellum are strongly controlled by the state of the brain serotonin system. In the first two postnatal weeks, the expression of 5-HT_{1A} receptors increases in the forebrain, but strongly decreases in the cerebellum [50]. Between postnatal days 10 and 21, the expression of 5-HT_{1A} receptors in the pyramidal cells of the hippocampus shifts from somatic to dendritic and, between postnatal days 10

and 16, the expression of 5-HT1A receptors in S100-positive hippocampal astrocytes declines from 90–20 % [51]. The binding of 5-HT4 receptors in the globus pallidus and the substantia nigra sharply increases between postnatal days 9 and 12 and then strongly decreases between postnatal days 12 and 21 [52]. Even though little is known about whether similar changes occur in the human brain, they appear likely since the 5-HT1A expression in the human cerebellum shifts from high in the neonatal stage to very low in adulthood [53] resembling the developmental pattern of 5-HT1A receptor expression in rats [50].

MATERIALS AND METHODS

Animals

Timed-pregnant, wild-type CD-1 mice were purchased from Charles River Laboratories, Inc. (Wilmington, MA). They arrived at 15–17 days of gestation and were housed in the UCSB animal facility in individual cages on a 12:12 light/dark cycle (lights on at 07:00, off at 19:00). Mice were checked every morning (before 12:00) and the delivery day was considered to be postnatal day (PD) zero. The pups were kept with the dam until used. Pups from 6 litters were analyzed. All litters were of normal size (12–14 pups). All experiments were approved by the UCSB Institutional Animal Care and Use Committee.

Tissue Harvesting

A total of 63 pups from 6 litters were used in the study. At postnatal day 14 (5 litters) or 15 (1 litter), individual pups were removed from the cage, weighed, and immediately decapitated. The trunk blood was collected into a 1.5 ml microcentrifuge tube containing 25 μ L of 5 percent Na₂EDTA dissolved in water, as previously described [1]. The tube was immediately pulse-vortexed at low speed and kept at room temperature until the dissections of the brain and gut were completed. Following the dissections, the blood sample was visually examined for blood clots, the volume of the collected blood was measured, and the sample was stored in 20 μ L aliquots at -75°C . The brain was dissected out of the skull with a fine rongeur, immediately weighed in phosphate-buffered saline (0.1 M PBS, pH 7.2) on a precision balance, immersion-fixed overnight in 4% paraformaldehyde in PBS at 4°C , allowed to sink in 30% sucrose in PBS at 4°C , and processed as described below. The gastrointestinal tract (the stomach through the rectum) was dissected out of the trunk and allowed to relax in PBS at 4°C for 10–13 days before photographed. The distal tail was stored at -75°C for sex-genotyping. All analyzes were done blindly with respect to the values of the other variables in the same individual mice.

Brain

Following cryoprotection, 17 brains (from 2 litters) were embedded in 20% gelatin (type A; 275 bloom), immersed in formalin with 20% sucrose for 3 hr. at room temperature, and sectioned coronally on a freezing microtome at 50 μ m thickness into PBS in 96-well trays. Every lost section was recorded and the percentage of missing sections was not allowed to exceed 9%. The sections were immediately mounted onto glass slides

coated with 0.5% gelatin and 0.05% chromium potassium sulfate, allowed to air-dry, Nissl-stained with 0.25% thionin, dehydrated in a graded series of ethanols, cleared in Xylenes, and coverslipped with Permount. Since fixation and embedding may alter tissue volume [54, 55], care was taken to ensure all brains and sections were exposed to the reagents for the same length of time.

Images of serial sections were captured with a Zeiss Axio Imager Z1 equipped with a color digital camera (AxioCam HRC Rev. 2) using a 1× objective (Fig. 1A), imported into the Reconstruct software (version 1.0.9.6; <http://synapses.clm.utexas.edu/tools/index.stm>), and the outline of the left hippocampal complex was traced from the most rostral section containing the pyramidal cells, to the most caudal section containing the dentate gyrus (Figs. 39-64 of reference [56]). In this rostro-caudal block, the traced regions included the hippocampus proper, the fimbria, the dentate gyrus, the presubiculum, and the subiculum. If a section was missing, the thickness of each of the two neighboring sections was digitally increased by 50 percent. The quality of tracing was assessed by rotating the 3D-reconstruction and visually inspecting it for discontinuities (Fig. 1B). No digital smoothing was used.

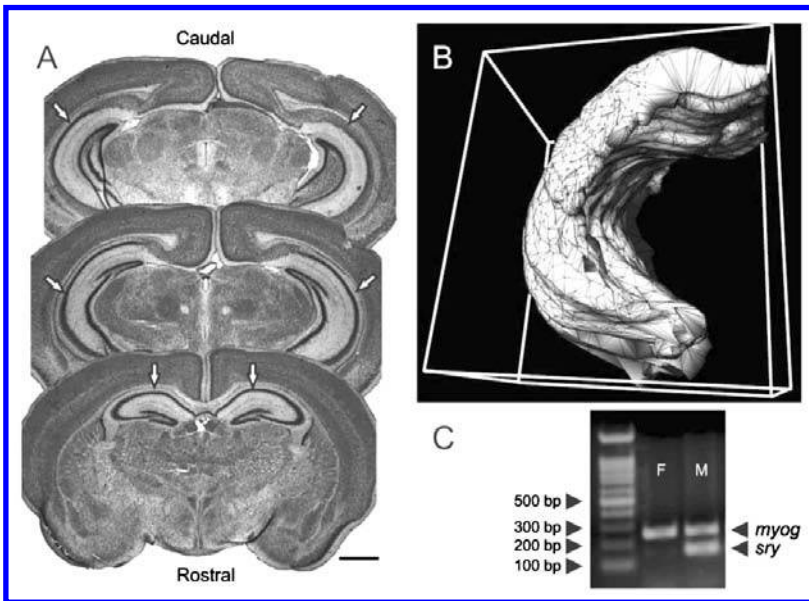


Figure 1: Three-dimensional reconstruction of the hippocampal complex and sex-genotyping. (A) Representative Nissl-stained sections through the mouse brain used in three-dimensional reconstructions of the hippocampal complex. Scale bar is 1 cm. (B) A three-dimensional reconstruction of the hippocampal complex. (C) The *sry* and *myog* (control) bands in female (F) and male (M) pups detected by sex-genotyping.

Guts

To our knowledge, there are no standard protocols for measuring gut length. Since the length of the gut increases considerably after dissection (probably due to muscle relaxation), we investigated this process experimentally (see Results; Fig. 2) and

developed a protocol that allowed measuring gut length with high reliability. Following 10–13 days of relaxation in 0.1 M PBS (pH 7.2) at 4°C, the gastrointestinal tracts were digitally macro-photographed (Fig. 2A) in 10 cm Petri dishes with shallow PBS (in order to avoid vertical loops). A millimeter-ruler was included in the images for scale. The images were imported into reconstruct, and the length of the gut was determined by tracing both sides of the gut from the pylorus of the stomach to the caecum and averaging the length of the two traces. The remaining part of the gut was not measured because it was difficult to control if the dissection included the most distal part of the gastrointestinal tract. This approach produced consistent measures over many days (Fig. 2B), and was superior to obtaining only one trace equidistant from the two sides of the gut.

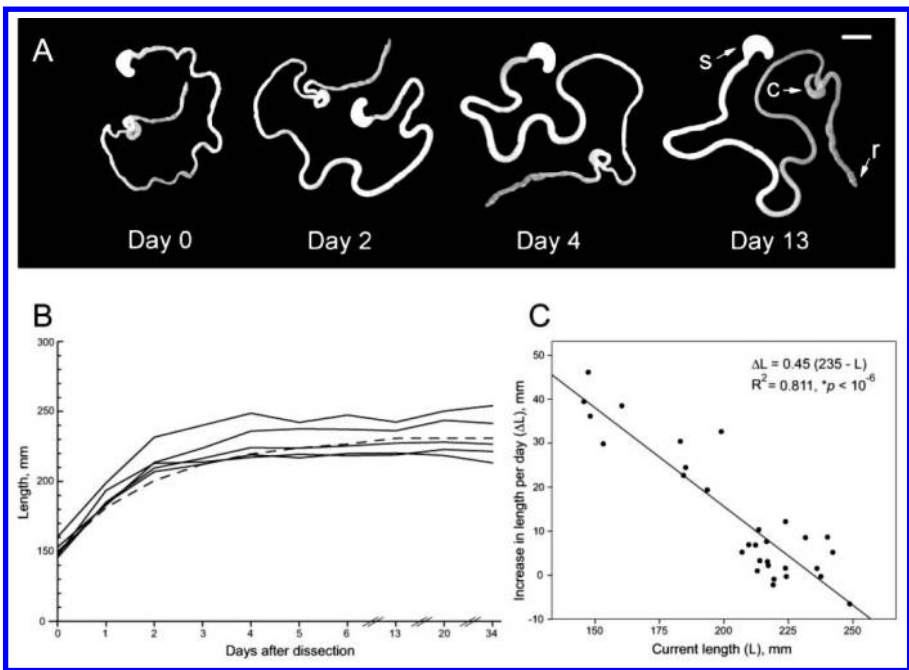


Figure 2: Gut relaxation. (A) The relaxation of the same representative gastrointestinal tract kept in PBS at 4°C and photographed at 0, 2, 4, and 13 days after dissection. Abbreviations: s, stomach; c, caecum; r, rectum; scale bar is 1 cm. (B) The relaxation of five guts (measured from the pylorus of the stomach to the caecum) is kept in PBS at 4°C and measured over the course of 34 days. The dashed line represents the theoretical relaxation (Eq. 2) of a gut with the initial length of 150 mm. (C) The relationship between the current gut length and the increase in gut length per day. The data points were obtained from the five guts used in (b); for better precision of the linear regression (line), only the initial 6 days were included in the analysis. The rate of relaxation was calculated as the absolute difference in length between the current day and the next day.

Whole-Blood Tryptophan and 5-HT

The concentration of tryptophan and 5-HT in the blood samples was measured by HPLC as previously described [1]. Blood samples were prepared by the addition of 100 μ L of 25% ascorbic acid, 100 μ L of 5% sodium metabisulfite, 10 μ L of 10 ng/

μL N-methylserotonin (NMS, internal standard) to frozen whole blood samples. After thawing and mixing, 75 μL of 3.4 M perchloric acid was added, the samples were kept on ice for 10 min, centrifuged, and the supernate was stored at -80°C until analyzed. The analysis was performed by HPLC with fluorometric detection: a 25×0.46 Altex Ultrasphere column heated to 40°C was eluted with a mobile phase consisting of 70% 0.1 M NaH_2PO_4 (pH 4.7) containing 150 mg/L octyl sulfate, 20% methanol. The compounds were detected with a Shimadzu RF 10-AXL fluorometer, with excitation and emission wavelengths of 285 and 345 nm, respectively, quantitated by comparing peak height ratios (analyte/NMS) to those observed for standards, and concentrations expressed as ng per ml. The neurochemicals were determined with typical intra- and inter-assay coefficients of variation of less than 5 and 10 percent, respectively. In the final calculations, the dilution of the collected blood in the Na_2EDTA solution was factored out; therefore, the reported values represent tryptophan and 5-HT concentrations in the undiluted whole blood.

Genotyping

Since sexing of young mice based on the appearance of their external genitalia is difficult, the anogenital distance can be used as a more reliable measure. In the present study, several organs had to be rapidly extracted destroying the body in the process. Therefore, in order to avoid ambiguity and human errors, mice were sexed by genotyping. This approach also allows permanent storage of the extracted DNA which can be used for future analyses. Genomic DNA was isolated with the DNA Isolation Kit (Lamda, St. Louis, MO). Briefly, 1 cm of the tail was digested in a lysis buffer at 56°C overnight, the DNA was precipitated with ethanol, dissolved in 150 μL of Tris-EDTA buffer (TE, pH 8.0), and stored at -20°C . The sry region located on the Y chromosome was amplified by polymerase chain reaction (PCR) using the HotStarTaq Master Mix Kit (Qiagen, Valencia, CA). The sry primers were 5'-AACAACTGGGCTTTGCACATTG-3' (forward) and 5'-GTTTATCAGGGTTTCTCTCTAGC-3' (reverse), and the control (myog) primers [57] were 5'-TTACGTCCATCGTGGACAGC-3' (forward), 5'-TGGGCTGGGTGTTAGTCTTA-3' (reverse). The PCR reaction mixture (50 μL) contained 25 μL of the Master Mix, 1 μL (0.5 μM) of each primer, 0.5 μL of the DNA sample, and 20.5 μL of water. The amplification was performed in a PxE thermal cycler (ThermoFisher Scientific) with the following conditions: initial activation at 95°C for 15 min, 33 cycles of amplification (94°C for 40 sec; 60°C for 40 sec; 72°C for 1 min), and final extension at 72°C for 9 min. The PCR products were run at 120 V on 1.5 percent agarose gel in Tris-acetate-EDTA buffer (TAE) containing 5 percent ethidium bromide and digitally imaged with a DigiDoc-It UV transillumination system (UVP, Upland, CA). The amplicon sizes were 146 bp/166 bp (sry, doublet) and 245 bp (myog) (Fig. 1C).

Statistical Analysis

Statistical analysis was carried out in SPSS 16.0.2 (SPSS Inc., Chicago, IL). Conceptually, the analysis was based on the general linear model (GLM) that considers correlation, ANOVA and ANCOVA to be special cases of linear regression [58]. Residuals were tested for normality with the ShapiroWilk test (with the level of significance of

$p < 0.05$) and for independence with the Durbin-Watson test (DW; independence was assumed if the DW value was in the 1–3 range).

Unless otherwise noted, the forced-entry method was used in linear regression. A non-linear relationship between two variables was considered to be linear “in the parameters” [58], which allowed using standard GLM methods. In backward (step-wise) regression, Fisher’s F critical value for variable removal was set at the standard significance level of 0.1. Pearson’s correlation between two variables was used if the residuals of the linear regression between these two variables were normally distributed (otherwise, the Mann-Whitney test was used). The emphasis on the normality of residuals rather than of variables themselves follows the standard approach in GLM models. Specifically, it allows treating Student’s independent t-test as a special case of Pearson’s correlation, between a continuous variable and a dichotomous variable (e.g., sex; Table 1).

Table 1: Differences Between the Sex Groups and the Cross-correlations Between the Variables.

	M (g)	BM (g)	BM/M	HC (mm ³)	Trp (ng/mL)	5-HT (ng/mL)	5-HT/ Trp	Gut (mm)
Sex	F < M .185 63	F < M .273 63	F < M .325 63	F < M .286 17	F < M .584 58	F > M .245 58	F > M* .040 58	F > M .861 33
M		.768** < 10 ⁻⁶ 63	-.825** < 10 ⁻⁶ 63	.662** .004 17	-.089 .507 58	-.594** 10 ⁻⁶ 58	-.304* .020 58	.688** 10 ⁻⁵ 33
BM			-.165 .196 63	.619** .008 17	.056 .676 58	-.433** .001 58	-.262* .047 58	.400* .021 33
BM/M				-.571* .017 17	.229 .084 58	.465** 2.10 ⁻⁴ 58	.315* .016 58	-.745** 10 ⁻⁶ 33
HC					-.368** .008 16	-.505* .046 16	-.124 .649 16	.427 .146 13
Trp						.116 .387 58	-.430** .001 58	-.293 .110 31
5-HT							.818** < 10 ⁻⁶ 58	-.264 .152 31
5-HT/Trp								-.004 .983 31
N	63	63	63	17	58	58	58	33
Mean	6.511	.387	.061	8.127	16424	2069	.128	221.30
STD	.954	.028	.008	1.054	2439	536	.037	11.25

Abbreviations: M, body mass; BM, brain mass; HC, volume of the hippocampal complex; Trp, blood tryptophan concentration; 5-HT, blood 5-HT concentration; Gut, length of the relaxed gut; N, total number of cases; STD, standard deviation. The two sex groups were compared using the exact Mann-Whitney test if the variable was BM/B or 5-HT/Trp; otherwise, Student’s independent t-test was used. Spearman’s correlation was used if either of the two non-dichotomous variables was BM/M or 5-HT/Trp; otherwise, Pearson’s correlation was used. In the sex row, the “greater than” (“less than”) sign indicates that the mean of the female group was greater (less) than the mean of the male group. In all other cells, the first number is the value of the correlation coefficient. In all cells, the second (bold) number is the significance of the corresponding test. In all cells, the third number is the total number of cases used in the test. The residuals of the linear regression with sex as the predictor variable and M or 5-HT as the dependent variable were not normally distributed ($p = 6.10^{-5}$ and 8.10^{-6} , respectively). Therefore, the differences between the mean M and 5-HT values in the two sex groups were retested with the exact Mann-Whitney test, which confirmed they were not significant ($p = 0.124$ and 0.168 , respectively).

DISCUSSION

To date, relationships among body mass, brain mass, gut length, and whole-blood tryptophan and 5-HT levels have not been systematically investigated in a genetically uniform population of any mammalian species. [Table 1](#) provides information for future top-down [2, 25] and bottom-up (e.g., structural equation modeling) studies and can also be used in the design of multidimensional experiments where prior considerations of statistical power are important.

We found a strong negative correlation between the body mass and whole-blood 5-HT levels. The strength of this relationship was influenced by the presence of several pups with low body mass but no gross anatomical abnormalities. The elevated blood 5-HT levels were unlikely to be caused by developmental delay, since blood 5-HT levels increase, not decrease, during postnatal development in mice [1]. It has been reported that extremely low levels of maternal peripheral 5-HT result in smaller mouse embryos that also exhibit abnormalities in many organ systems [60, 61]. It is intriguing to speculate that a less severe decrease in maternal peripheral 5-HT may also result in reduced body mass and compensatory overproduction of peripheral 5-HT in the offspring. However, peripheral administration of the immediate 5-HT precursor 5-hydroxytryptophan (5-HTP) to pregnant rats also leads to embryos with reduced body mass [62].

The observed relationship between body mass and blood 5-HT levels is predicted by our theoretical model of platelet 5-HT levels [2]. According to the model (equations (22) and (27) of [2]), platelet 5-HT levels (P) are given by the following equation:

$$P = [aQ(b + \Omega_g^{-1}) + c]^{-1},$$

where Q is the total cardiac output, Ω_g is the volume of the gut wall, and where the positive a , b , and c can be considered constant in this study. The cardiac output is likely to be directly proportional to body mass (i.e., $Q = kM$, where M is body mass and k is a positive constant). The gut length also scales with body mass ([Table 1](#)), but an increase in body mass is unlikely to increase gut length by the same factor. Therefore, the volume of the gut wall may scale as $\Omega_g = rM (1/\text{hr}) + s$, where $r > 0$, $s \geq 0$, and $\text{hr} \geq 1$ are constants. This allows expressing P as a function of M and, since the derivative of P with respect to M is always negative (i.e., $dP/dM < 0$), platelet 5-HT concentration should decrease as the body mass increases. Importantly, this relationship may not hold true for developmental processes [1] because other parameters, here considered constant (e.g., the levels of extracellular 5-HT in the gut wall, the platelet 5-HT uptake rate constant; see Janušonis (2008)), may undergo developmental changes.

Body mass is almost never controlled in experimental studies on the platelet hyperserotonemia of autism [9, 11, 12]. In the light of the present findings, including body mass as a covariate may reduce uncontrolled variability in platelet 5-HT levels. Recent findings show that low birth mass may carry an increased risk for ASDs [63] and that head circumference strongly correlates with body mass in ASD patients [64]. Intriguingly, the maturation of thalamocortical projections appears to be influenced by body mass in normal mice [65].

We found a non-linear relationship between the gut length and the brain/body mass ratio. While there appears to be little association between the brain/body mass ratio and the relaxed gut length if guts are of average length, short guts predict a higher brain/body mass ratio (Fig. 3C). The biological nature of this relationship is unclear. It is conceivable that the length of the gut modulates how much tryptophan reaches the systemic blood circulation and, since tryptophan can cross the BBB, its availability in the brain may affect brain growth through 5-HT synthesis [66]. Intriguingly, it has been recently hypothesized that a decrease in gut length has had a major impact on the evolution of the human brain [67, 68].

The analysis also suggested a tentative relationship between blood tryptophan levels and the volume of the developing hippocampal complex. Tryptophan depletion is known to affect the development and function of the hippocampus [69-71]. Our results suggest that even relatively small, natural fluctuations of blood tryptophan levels may modulate its size. Interestingly, at PD14, the mean blood tryptophan concentration in the CD-1 strain (16424 ng/ml) was considerably higher than that in the C57BL/6 strain (11563 ng/ml) [1]. Since the tryptophan levels were assessed by the same method in both the studies, a statistical comparison between them suggests that this difference between the two strains is significant ($t(66) = 6.17$, $p = 4.7 \cdot 10^{-8}$). It would be interesting to know if the mean volumes of the hippocampal complex also differ in these strains.

No sex differences were observed with regard to all variables. The marginally significant sex difference between the blood 5-HT/tryptophan ratios could be spurious considering the large number of tests. Also, the correlation between blood tryptophan and 5-HT was non-significant, consistent with previous reports in humans [34] and in C57BL/6 mice at postnatal day 14 [1].

The strong statistical relationships found in the present study should be cross-validated in other mouse strains and (when feasible) in humans. It should be noted that all of the reported relationships are empirical and do not imply direct causality; however, these findings may stimulate further experimental research where causality is addressed. For instance, mice lacking the serotonin 5-HT_{1A} receptor show elevated levels of anxiety [72] and develop an autistic-like blood hyperserotonemia [1]. While these two phenomena may appear unrelated, they may be explained by the expression of 5-HT_{1A} receptors both in the brain [51, 73, 74] and in the gut [75]. Serotonin 5-HT₄ receptors play important roles in the developing brain [76, 77] and the gut [44, 78], and recently 5-HT₄ mRNA has been reported in blood platelets [79]. Therefore, altered expression of 5-HT₄ receptors may simultaneously affect all of these sub-systems, even if they are separated by the BBB. Experimental methods, used in combination with modern statistical approaches, can provide important information about the interactions among components of the peripheral and central 5-HT systems, which are often studied in isolation.

RESULTS

Data Screening

The collected data for each of the variables was screened for quality blindly with respect to the values of the other variables. As described below, objective criteria were

used to eliminate some cases from further analysis. Since in all reconstructed cases the percentage of missing sections in the hippocampal complex did not exceed 9 percent, all of the reconstructions were used. Cases with guts clearly damaged during dissection (e.g., split into more than two pieces) were not used in further analyses that included gut length as a variable. We investigated whether the presence of blood clots in some blood samples affected their tryptophan or 5-HT concentration. The mean tryptophan concentrations were not significantly different in the samples with and without blood clots ($t(61) = 0.47, p = 0.644$), but the mean 5-HT concentration was significantly lower in the former group ($t(61) = 2.44, p = 0.018$). Therefore, cases with blood clots ($N = 5$) were disregarded in all further analyses that included tryptophan or 5-HT as variables.

The collected blood volume varies from case to case and is strongly affected by the constriction of major blood vessels, the angle between the trunk and the collecting tube, and other factors. We therefore asked whether the amount of the collected blood correlated with the measured tryptophan and 5-HT concentrations (if all the other parameters are equal and the measurements are accurate, no significant effect should be observed). The correlation between blood sample volume and blood 5-HT concentration was significant ($r = -0.385, p = 0.003$). However, the collected blood volume is also influenced by body size. Therefore, we calculated the partial correlation between blood sample volume and blood 5-HT concentration controlling for body mass, and found that this correlation became non-significant ($r = -0.085, p = 0.532$). In contrast, the partial correlation between body mass and blood 5-HT concentration controlling for blood sample volume was highly significant ($r = -0.495, p = 9 \cdot 10^{-5}$). Therefore, all of these cases ($N = 58$) were used in further analyses that included tryptophan or 5-HT as variables. The relationship between body mass and blood 5-HT concentration was investigated further.

ANOVA showed significant litter effects on body mass ($F_{5,57} = 40.3, p < 10^{-6}$), brain mass ($F_{5,57} = 15.5, p < 10^{-6}$), hippocampal volume ($F_{1,15} = 7.9, p = 0.013$), blood tryptophan levels ($F_{5,52} = 10.8, p < 10^{-6}$), blood 5-HT levels ($F_{5,52} = 16.0, p < 10^{-6}$), and a near-significant litter effect on gut length ($F_{5,27} = 2.54, p = 0.052$).

Gut Relaxation

After dissection, the length of the gut increases over the course of several days until it reaches a plateau (Fig. 2A, B). We followed the relaxation of five guts in PBS at 4°C and plotted the rate of their length increase as a function of their current length (Fig. 2C). Linear regression revealed a strong relationship between these variables ($R^2 = 0.811, F_{1,28} = 120.5, p < 10^{-6}$); the residuals were normally distributed ($p = 0.18$) and independent ($DW = 2.45$). This linear relationship suggests that gut relaxation can be modeled with the differential equation

$$dL / dt = k(\gamma L_0 - L), \quad (1)$$

where dL/dt is the current length increase rate as a function of the current gut length (L), L_0 is the initial gut length on the dissection day, γL_0 is the final gut length (where

$\gamma > 1$ is a constant independent of L_0), and k is the length increase rate constant. Based on Eq. (1), we reanalyzed the gut relaxation data with linear regression using dL/dt as the dependent variable and L_0 and L as the two predictor variables. Since according to Eq. (1) $dL/dt = 0$ when $L_0 = L = 0$, the intercept of the regression line was fixed at the axis origin. The regression revealed that Eq. (1) well describes the relaxation process, since L_0 and L explained virtually all variance in the length increase rate ($R^2 = 0.947$, $F_{2, 28} = 250.8$, $p < 106$). The residuals were normally distributed ($p = .993$) and independent ($DW = 1.72$). The regression yielded $k = 0.49$ day⁻¹ and $\gamma = 1.54$. Since the solution of Eq. (1) is

$$L(t) = \lambda L_0 + L_0 e^{-kt}(1 - \gamma), \quad (2)$$

plugging the obtained numerical k and γ values into Eq. (2) shows that, at 4°C, the gut reaches 95 percent of its final length ($1.54 L_0$) in 4 days and 99 percent in 7 days. In the present study, we allowed guts to relax for 10–13 days; however, shorter relaxation times (6–8 days) should be sufficient to obtain accurate measurements.

Cross-Correlations

In the initial analysis, the residuals of the linear regression between each of the variable pairs were tested for normality. Of the seven pairs that failed the normality test (irrespective of which of the two variables was the non-dichotomous dependent variable), five included at least one of the “ratio variables” (“brain mass/body mass” or “blood 5-HT concentration/blood tryptophan concentration”). This result is expected since the ratio of two normally distributed variables is not normally distributed, and can even be bimodal [59]. Based on these results, the Mann-Whitney test was used to compare the “ratio variables” in the two sex groups; for all the other variables, Student’s *t*-test was used. Likewise, Spearman’s correlation coefficient was used to correlate two variables when either of them was a “ratio variable”; otherwise, Pearson’s correlation was used. The results of these calculations are given in Table 1.

In the interpretation of the results, the Bonferroni correction for multiple tests was used. The type I error ($\alpha = 0.05$) was divided by the total number of tests (36; Table 1) to yield the significance level of $\alpha^* = 0.0013$. As expected, highly significant positive correlations were found between body mass and brain mass ($p < 106$) and between body mass and gut length ($p = 105$). Also, a highly significant negative correlation was found between body mass and the brain/body mass ratio ($p < 106$), possibly due to allometric scaling of brain size.

The cross-correlational analysis revealed a strong negative correlation between the body mass and blood 5-HT levels ($p = 106$). Also, significant correlations were found between brain mass and blood 5-HT levels, and between the brain/body mass ratio and blood 5-HT levels ($p = 0.001$ and 0.0002 , respectively). Since body mass, brain mass and the brain/body mass ratio cross-correlate, we next tested which of the three variables or their linear combinations could best predict blood 5-HT levels using stepwise (backward) linear regression. It revealed that body mass, alone, could best predict blood 5-HT levels (Fig. 3A) and that inclusion of the other two variables did not statistically improve this prediction. This model yielded $R^2 = 0.352$ ($F_{1, 56}$

= 30.5; $p = 10^{-6}$; adjusted $R^2 = 0.341$); the residuals were normally distributed ($p = 0.21$) and independent ($DW = 1.15$). Since two males had unusually high blood 5-HT concentration (over 3500 ng/mL), we next investigated the origin of these outliers and their influence on the regression model. No blood clots were observed in these samples (all cases with blood clots had been eliminated prior to the analysis) and the tryptophan concentration measured in these same samples was in the normal range (Fig. 3B). Since Cook's distances (Cook's D) can be used to estimate the influence of individual cases on a regression model, we calculated this statistics for all regression points and found the largest Cook's D to be 0.66, below the critical value of 1. While the two cases could not be eliminated based on any of these objective criteria, we next excluded these two cases and recalculated the regression model. After this adjustment, blood 5-HT concentration was still best predicted by body mass ($R^2 = 0.210$; $F_{1, 54} = 14.3$; $p = 0.00039$; adjusted $R^2 = 0.195$).

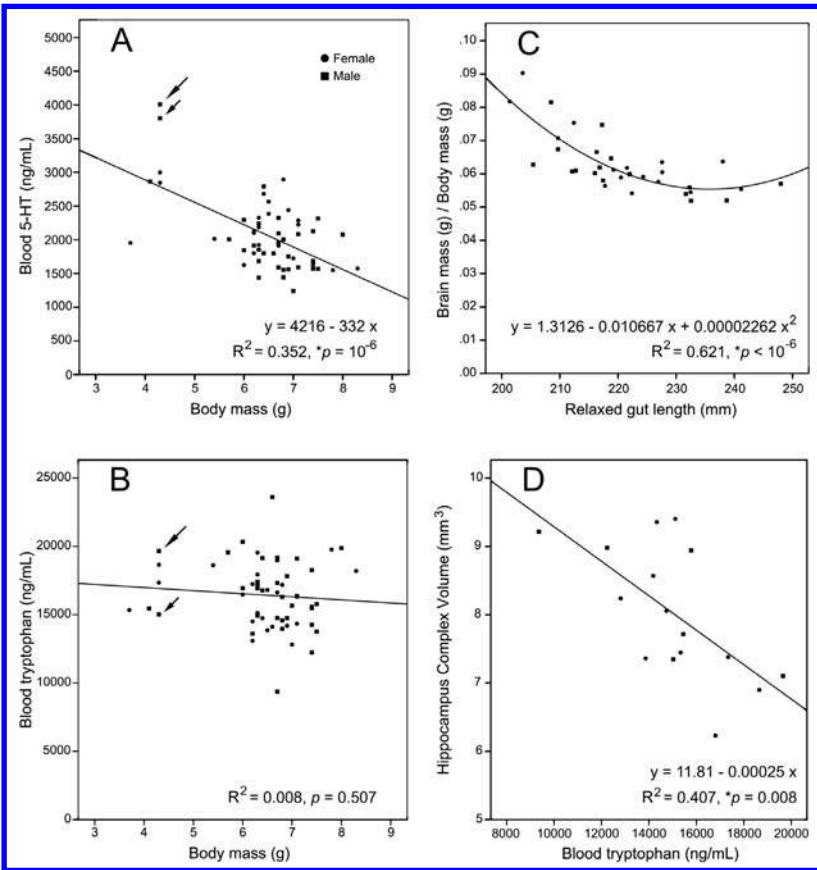


Figure 3: Relationships between highly correlated variables. (A) The relationship between body mass and blood 5-HT concentration. The long and short arrows indicate two potential outliers with high blood 5-HT concentration. (B) The blood tryptophan concentration of the two potential outliers in (A) appears to be normal (the corresponding arrows). (C) The relationship between gut length and the brain/body mass ratio. (D) The relationship between blood tryptophan concentration and the volume of the hippocampal complex.

All pups with body mass less than 5 g came from the same litter. Their tissues were collected at PD14, the same developmental time at which the other four litters were processed. The litter was of normal size (14 pups; another litter had the same number of pups), and the pups showed no gross anatomical abnormalities. These pups were used in all the other analyses (including the reconstruction of the hippocampal complex) and did not appear to be outliers there (Fig. 3C, D). The correlation between the body mass and blood 5-HT remained significant if only the litter means were considered (Fig. 4A).

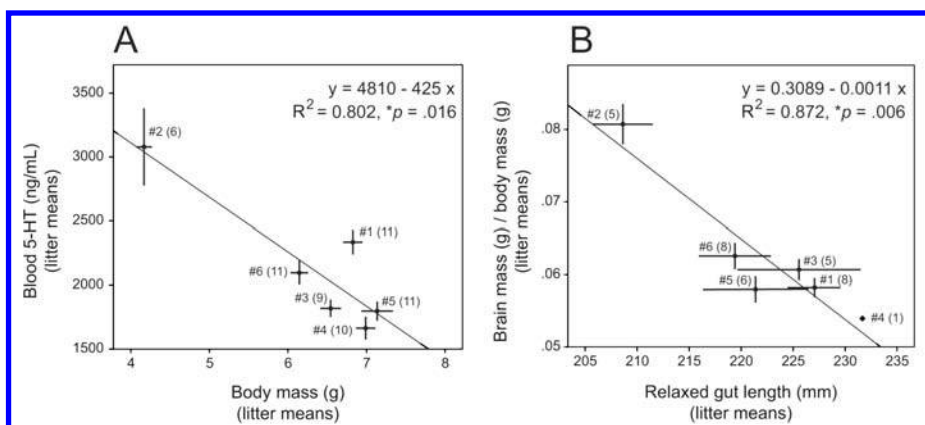


Figure 4: Relationships between the litter means of highly correlated variables. (A) The relationship between the litter means of body mass and blood 5-HT concentration. (B) The relationship between the litter means of gut length and the brain/body mass ratio. In (A) and (B), point #N (M) represents litter N with M cases analyzed; the horizontal and vertical bars represent the standard errors of the means.

Next, we analyzed the strong correlation between the gut length and the brain/body mass ratio ($p = 10^{-6}$). Since the residuals of the linear regression between these two variables were not distributed normally ($p = 0.03$), we modeled their relationship with a quadratic polynomial (Fig. 3C). The regression yielded $R^2 = 0.621$ ($F_2, 30 = 24.6, p < 10^{-6}$; adjusted $R^2 = 0.596$); the residuals were normally distributed ($p = 0.26$) and independent ($DW = 1.16$). The constant at the quadratic term was significantly different from zero ($t(30) = 3.36, p = 0.002$), further supporting the non-linearity of the relationship. The correlation between gut length and the brain/body mass ratio remained significant only if the litter means were considered (Fig. 4B).

The correlation between blood tryptophan concentration and hippocampal complex volume did not meet the significance criterion after the Bonferroni correction. However, it was highly significant considered separately (Fig. 3D). The linear regression yielded $R^2 = 0.407$ ($F_1, 14 = 9.63, p = 0.008$; adjusted $R^2 = 0.365$); the residuals were normally distributed ($p = 0.58$) and independent ($DW = 1.40$).

CONCLUSION

The study provides information on the covariance structure of several variables related to the central and peripheral serotonin systems. In particular, the results indicate that body mass should be included as a covariate in studies on platelet 5-HT levels and they also suggest a link between the brain growth and gut length.

KEY WORDS

- **Blood brain barrier (BBB)**
- **Genotyping**
- **High-performance liquid chromatography (HPLC)**
- **Hippocampal complex**
- **Organ harvesting**
- **Platelet hyperserotonemia of autism**
- **Serotonin syndrome**
- **Serotonin transporter (SERT)**
- **Tryptophan and 5-hydroxytryptamine**

AUTHORS' CONTRIBUTIONS

Ricardo Albay III, Angela Chen, and Maggie Tatevosyan performed the brain and gut analyses; Angela Chen genotyped the pups; George M. Anderson performed the blood HPLC analysis; Skirmantas Janušonis, Ricardo Albay III, and George M. Anderson analyzed the results; Skirmantas Janušonis conceived the project, supervised all of its stages, and wrote the manuscript.

ACKNOWLEDGEMENTS

We thank Rebecca M. Maichrowicz for her assistance with brain histology and Ilya Shifrovich for his assistance with HPLC. This research was supported by the UCSB-Santa Barbara Cottage Hospital Special Research Award (SJ) and UCSB URCA grants (RA and MT).

Chapter 4

Neurogenesis of Peripuberal and Adult Rabbits

Giovanna Ponti, Paolo Peretto, and Luca Bonfanti

INTRODUCTION

Adult neurogenesis in mammals is restricted to some brain regions, in contrast with other vertebrates in which the genesis of new neurons is more widespread in different areas of the nervous system. In the mammalian cerebellum, neurogenesis is thought to be limited to the early postnatal period, coinciding with the end of the granule cell genesis and disappearance of the external granule cell layer (EGL). We recently showed that in the rabbit cerebellum the EGL is replaced by a proliferative layer called “subpial layer” (SPL) which persists beyond puberty on the cerebellar surface. Here we investigated what happens in the cerebellar cortex of peripuberal rabbits by using endogenous and exogenously-administered cell proliferation antigens in association with a cohort of typical markers for neurogenesis. Surprisingly, this neurogenic process continues to a lesser extent in the adult, even in the absence of a proliferative SPL. The genesis of neuronal precursors is restricted to the molecular layer, giving rise to cells immunoreactive for GABA, and for the transcription factor Pax2, a marker for GABAergic cerebellar interneuronal precursors of neuroepithelial origin that ascend through the white matter during early postnatal development. The multipolar cells are Map5+, contain Olig2 and Sox2 transcription factors, and are detectable in all cerebellar layers. Some dividing Sox2+ cells are Bergmann glia cells.

The cerebellum of non-mammalian vertebrates, such as fish, is characterized by striking neurogenesis throughout life [1]. By contrast, the mammalian cerebellum after the early postnatal genesis of granule cells is known as one of the most static structures in the central nervous system (CNS) under the profile of cell renewal. Cerebellar neurons in mammals are generated both centrifugally and centripetally from different sources, at different developmental stages. Purkinje neurons and interneurons originate from the neuroepithelium of the fourth ventricle whereas granule cells come from actively proliferating cell precursors which accumulate in the EGL after tangential migration from the rhombic lip [2]. The EGL persists after birth on the cerebellar surface until it provides the granule cell population by radial migration during early postnatal periods whose duration is strictly dependent on the species [3-6]. On the other hand, the genesis of cerebellar cortex interneurons occurs by migration through the subjacent white matter and is completed in rodents before the end of granule cell genesis. All neuroepithelium-derived, GABAergic interneurons, including basket, stellate, and Golgi II cell precursors are produced by a common pool of progenitors [7] and express the paired box transcription factor Pax2 [8].

We have recently shown that in the rabbit cerebellum between the fourth and the fifth postnatal week the EGL is replaced by a proliferative layer which then persists

beyond puberty [9]. We called it the SPL [9] since it is structurally different from the EGL, being characterized by the occurrence of tangential chains of neuroblasts reminiscent of those described in the forebrain subventricular zone (SVZ) [10, 11]. The rabbit SPL is also transient since it is completely exhausted around the sixth month of postnatal life [9].

Here we analyzed the rabbit cerebellar cortex during the period of SPL occurrence and after its disappearance. We show that a remarkable genesis of cells, mostly neuronal precursors, is detectable within the cerebellar cortical layers at peri-puberal stages, in sharp contrast with the present knowledge in mammals. Besides a residual granule cell genesis which is exhausted very soon, most of these cells differentiate into a population of neuronal cells whose morphology does not fit with any of the known cerebellar cortex neuronal types, and to a lesser extent into a population of Map5+ synantocyte-like progenitors [12, 13]. Surprisingly, by extending our analysis to older animals we found that a remarkable number of cells belonging to both the interneuron and synantocyte types continue to be generated in fully adult animals, even in the absence of a proliferative SPL.

MATERIALS AND METHODS

BrdU Injections and Tissue Preparation

Experimentation was conducted in accordance with the current EU and Italian laws (Italian Ministry of Health, authorization n. 66/99-A). Three postnatal (P 10), 28 peripuberal (3-month-old: n = 22; 4-month-old: n = 2; 5-month-old: n = 2; 6-month-old: n = 2), and 6 adult (1-year-old: n = 3; 3-year-old: n = 3) New Zealand White rabbits (*Oryctolagus cuniculus*, Charles River, Milan, I) were used for light/confocal microscopy. Sixteen animals (3-month-old) received intraperitoneal injections of BrdU (Sigma; 40 mg/Kg). Three received a single injection and were killed after 2 hr. Thirteen rabbits received one daily injection for 5 days and were killed 2 hr, 5, 10, 30, 60 days (n = 3 each survival time, except for 5 days: n = 1) after the last injection. All adult rabbits received one daily injection for 5 days and were killed after 10 days after the last injection. In addition, four peripuberal (3-month-old) rabbits that received one daily injection of BrdU for 15 days, and were killed after 2 months since the first injection, were used for electron microscopy.

Animals were anaesthetized with a ketamine/xylazine solution (100 mg/Kg body weight: 33 mg/Kg body weight) and perfused as previously described [35, 9, 71]. Cerebella were extracted carefully to preserve the pia mater, post-fixed 6 hr (light microscopy), then the hemicerebella separated. All postnatal, all adult, and 26 peripuberal cerebella, were frozen at -80°C and cryostat (25 μm thick) sectioned in series, whereas three peri-puberal cerebella were sectioned with a vibratome (100 μm thick). According to the aims of different experiments, cerebella were cut along sagittal and coronal orientation.

Histological Procedures and Immunohistochemistry

Immunohistochemical reactions were carried out by using single peroxidase and double immunofluorescence methods on cryostat sections incubated overnight at room

temperature with primary antibodies (Table 3). All polyclonal antisera used did not give any problem or aspecificity on the rabbit cerebellar tissue.

Immunohistochemistry for singles stainings was revealed using indirect peroxidase techniques with biotinylated secondary antibodies (anti-goat IgG, anti-mouse IgM, anti-rabbit IgG, Vector Labs, Peterborough, UK; mouse IgG, Sigma, Saint Louis, USA), treated with an avidin-biotin complex (Vector Elite kit; Vector Labs; Peterborough, UK) and detected with 3,3'-diaminobenzidine (DAB) in TRIS-HCl 50 mM pH 7.6, containing 0.025% hydrogen peroxide for 3 min then washed in TRIS-HCl 50 mM pH 7.6.

For double staining indirect immunofluorescence procedures using FITC-avidin (Vector Labs)+Cy3 conjugated antibodies (anti-mouse IgG+IgM; anti-Rabbit IgG Jackson Immunoresearch Laboratories, West Grove, USA) were used. Antibodies were diluted in 0, 01 M PBS, pH 7.4, containing 0.5% Triton X-100. Fluorescent specimens mounted in Mowiol 4-88 (Calbiochem-EMD Chemicals, Darmstadt, and D) were observed with a laser scanning Olympus Fluoview confocal system.

Cells undergoing apoptotic cell death were detected by TUNEL analysis using the Apop-Tag Kit (Chemicon) according to the supplier's instructions. Microglial cells were detected with Fluorescein Griffonia (Bandeiraea) Simplicifolia lectin 1, Isolectin B4 1/200 (FL-1201 Vector Laboratories, Burlingame, USA).

Pre-Embedding Immunoelectron Microscopy

The ultrastructural localization of exogenously-administered BrdU was obtained employing a pre-embedding immunoperoxidase reaction [61]. Rabbits were perfused with 4% paraformaldehyde and picric acid 1% in 0,1 M sodium phosphate buffer (PBS), postfixed 6 hr at 4°C, washed overnight in cold PBS, and vibratome sectioned (70 µm thick). After aldehydes blocking in 100 mM NH₄Cl for 2 hr at room temperature (RT), slices were washed in PBS, pre-treated with 2 M HCl for 15 min at 37°C, neutralized for 10 min in buffer at pH 8, 4 and subsequently incubated in 1% NGS + 0.1% Triton X-100 in PBS for 1 hr at 4°C and then in anti-BrdU diluted 1:500 in PBS overnight at RT. After washing in PBS, slices were incubated in biotinylated anti-rat IgG (Vector labs) diluted 1:200 for 2 hr. Sections were subsequently washed and treated with an avidin-biotin complex (Vector Elite kit; Vector Labs) for 1 hr at RT. After washing, sections were processed for visualization with 0.2% diaminobenzidine (Sigma, Saint Louis, USA) in TRIS-HCl 50 mM pH 7.6, containing 0.025% hydrogen peroxide for approximately 3 min then washed in TRIS-HCl 50 mM pH 7.6. Small pieces of the molecular layer containing single BrdU+ nuclei not associated with blood vessels were dissected under a stereomicroscope, washed in PBS, postfixed in 2% Osmium Tetroxide and FeCN 3% for 1 hr at 4°C, washed overnight with maleate buffer, counterstained in uranyl acetate 1%, washed with maleate buffer, dehydrated and embedded in araldite as previously described [71]. Semi-thin sections (1 µm thick) stained with 1% toluidine blue and 0, 5% NaHCO₃, were cut sequentially and observed in light microscopy until identification of the BrdU-marked nuclei. Starting from this point, ultra-thin sections were harvested and examined with a Philips CM10 transmission electron microscope.

Quantitative Analyses

Countings of PSA-NCAM+ and Map5+ cells have been performed at different ages (3, 6, 12, and 36 months for PSA-NCAM; 3 and 36 months for Map5; n = 3, each age considered except for 6 months n = 2). The analysis has been conducted on six representative parasagittals cryostat sections (cut at different medial-lateral levels) from each animal. The cells present in each layer (molecular layer, granule cell layer, and white matter axis of the lamellae) were counted, and results were expressed as number of cells/10 mm of pial surface (in a total surface of 275 mm; see [Table 1](#)). The number of different PSA-NCAM+ morphological types was also evaluated and expressed as percentages in [Fig. 2R](#). Cells present in the SPL, due to the presence of chains, were extrapolated by considering 2 bipolar cells/chains as previously described [9]. The number of PSA-NCAM and Map 5 + cells, in each layer and at different post-natal ages (PSA-NCAM: 3-month-old versus 6-month-old and 3-month-old versus adult; MAP5: 3-month-old versus adult) has been analyzed with Student's Test- T (Primer statistical software for Windows). The number of PSA-NCAM and Map5+ cells, in different layers (ML versus GL) at the same post-natal age, has been analyzed with Student's Test- T.

Finally the total number of PSA-NCAM+ versus Map5+ cells has been analyzed in 3-month-old and adult animals with Student's Test- T. A value of $p \leq 0.05$ was accepted as statistically significant.

Quantitative analysis of BrdU+ cells was performed in nine 3-month-old rabbits that received 5 daily injections, and were subsequently killed after 2 hr (n = 3), 10 (n = 3) and 60 (n = 3) days after the last injection. These countings were carried out on cortical tissue corresponding to a total of 200 mm pial surface in three representative parasagittal cryostat sections (cut at different medial-lateral levels; based on the fact that the newly generated cells were distributed homogeneously in the entire cortical extension; see Results) taken from cerebella of each animal (see [9]). The BrdU-immunoreactive nuclei present on a single focal plane of the molecular and granule cell layer were counted. Nuclei in the SPL (5 μ m beneath the pial surface) have not been taken into account.

The number of BrdU+ cells has been analyzed by one-way ANOVA (Primer statistical software for Windows) with main factor time (post-injection survival times). Post-hoc comparisons were carried out with Tukey HSD test.

The number of BrdU+ cells in each cerebellar layer at the different survival time has been analyzed with Student's test T. A value of $p \leq 0.05$ was accepted as statistically significant.

The amount of apoptotic cell death was analyzed by counting TUNEL-labeled cells in the cerebellum of 3-, 4- and 36- months-old animals (n = 3). Immunoreactive nuclei present on a single focal plane of the SPL and cerebellar cortical layers were counted in three representative sections, and expressed as number of cells/10 mm of pial surface (in a total surface of 275 mm; see [Table 1](#)). The number of TUNEL+ cells at the different postnatal ages has been analyzed with Student's test T. A value of $p \leq 0.05$ was accepted as statistically significant.

The percentage of double labeled cells versus BrdU+ cells was evaluated for PSA-NCAM, Pax2, Map5, Sox2. These countings were carried out on three animals for each BrdU treatment (see above). Cortical tissue corresponding to a total of 200 mm pial surface in six representative parasagittal cryostat sections (cut at different medial-lateral levels) taken from cerebella of each animal.

The percentage of bipolar and intermediate or neuronal-like BrdU/PSA-NCAM double labeled cells was then compared between 5 and 15 days after BrdU injection. These countings were performed as the other double labeling countings. The data was analyzed with Student's Test T. A value of $p \leq 0.05$ was accepted as statistically significant.

DISCUSSION

Persistent neurogenesis is a phylogenetically highly conserved feature in the animal world [29]. A general rule views the genesis of new neurons to be rather widespread in invertebrates and in non-mammalian vertebrates such as fish, reptiles, and birds, but more restricted to specific brain areas in mammals [30]. In this animal class adult neurogenesis is consistently present only within two brain areas: the forebrain SVZ and the hippocampal dentate gyrus [30-33]. Yet, recent comparative studies have started showing that important differences also exist among mammals, concerning the topographical location of neurogenesis, the internal arrangement of adult neurogenic sites, and the mode/direction of cell migration (reviewed in [33, 34]). For instance, striking differences have been found to characterize the rabbit brain, in the form of parenchymal chains leaving the SVZ for the mature parenchyma in young animals [35], as well as remarkable genesis of interneurons within the adult caudate nucleus [36].

Unlike the brain, the mammalian cerebellum is considered completely incapable of cell renewal after the end of the postnatal granule cell genesis. Thus, plasticity in this CNS region is thought to be limited to synaptic rearrangement of pre-existing circuits [37]. In contrast, we recently demonstrated the existence of a proliferative SPL on the rabbit cerebellar surface, which persists beyond puberty (from the second to the fifth month of life) as an extension of the EGL, although with different structural features [9]. Since a great number of newly-born elements are also detectable within the cerebellar cortical layers of these rabbits, here, after investigating the nature, distribution, and fate of the newly generated elements in young animals we show that two populations of neuronal and glial progenitors continue to be generated during adulthood.

Protracted Genesis of Neuronal and Glial Progenitor Cells in the Peripuberal Rabbit Cerebellum

We started from previous cell countings of BrdU+ nuclei carried out in 3-month-old animals, indicating that a huge amount of cells are newly generated within the cortex, about 1/3 of them surviving during the first 2 weeks after the injection of the marker [9] (Fig. 6A). In order to reveal the nature of newly-born cortical elements, the cells containing BrdU+ nuclei were visualized in double stainings with the most typical developmental markers PSA-NCAM, DCX, CRMP-4, and

Map5. All these molecules are implicated in dynamic cellular events both during developmental and adult neurogenesis, and allow the visualization of the whole cell morphology, including cell body and processes [11, 16, 38, 39].

A great number of cells expressing and co-expressing such markers were detectable in the cerebellum of peripuberal and puberal rabbits, in overt contrast with their complete absence in the postnatal cerebellum of rodents [9, 40, 41]. Different molecules were associated with specific morphologies: PSA-NCAM and DCX, which are known to be strongly expressed in newly generated neuronal precursors [11, 16, 38], were found in bipolar and neuronal-shaped cells, whereas Map5 was found in multipolar cells reminiscent of an intermediate astrocytic/oligodendrocytic shape (Fig. 1A).

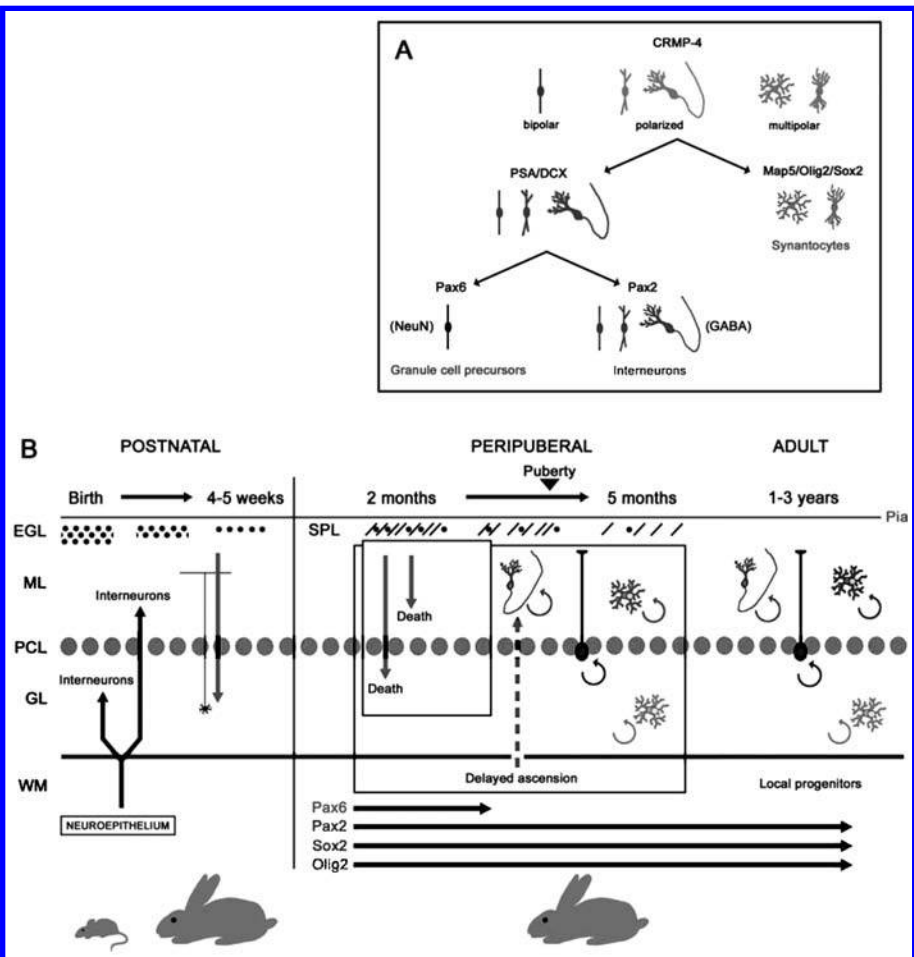


Figure 1: Model for protracted cell genesis in the cerebellum of the peripuberal and adult rabbit. A, Summary of antigen distribution and morphologies associated with different populations of newly-born cells in the rabbit cerebellar cortex B, Protracted neurogenesis in the postnatal/peripuberal cerebellum and persistent neurogenesis in the adult. All processes represented at the right of the vertical line are typical of rabbits.

The fact that polarized neuronal cells and multipolar cells actually belong to two distinct populations of newly-born cerebellar cortical cells was confirmed by their selective expression of distinct nuclear transcription factors: the PSA-NCAM+/DCX+ cells (Fig. 3G, H, K) were immunoreactive for Pax2 [8, 17], and were consistently negative for both Sox2 and Olig2 (Figs. 3 and 8A). By contrast, all MAP5+ cells were Olig2+, Sox2+, and Pax2-negative (Figs. 4 and 7A).

Interneurons and Synantocyte/Polydendrocyte-Like Cells are Generated in the Cerebellum of Peripuberal Rabbits

The neuronal cells displayed shapes reminiscent of the differentiative sequence previously described in brain neurogenic sites, involving bipolar cells that subsequently emit cell processes and give rise to ramified neurons [42]. These cells expressed the anti-adhesive, membrane-bound molecule PSA-NCAM [11], and the two cytosolic phosphoproteins CRMP-4 and DCX, both implicated in the regulation of the actin cytoskeleton in motile cells [39, 43]. All these molecules are strictly associated to adult-generated neuronal precursors in the hippocampus and SVZ, being required for their migration and structural plasticity [11, 16, 38]. In addition, the PSA-NCAM+/DCX+ neuronal cells expressed in their nuclei the marker for GABAergic cerebellar interneurons Pax2. This transcription factor specifically identifies the neuronal precursors of neuroepithelial origin ascending through the cerebellar white matter to colonize the cerebellar cortex during the early postnatal period [7, 8, 17]. The facts that these cells are restricted to the molecular layer and are immunoreactive for GABA confirms that they are independent from granule cell genesis (Fig. 6H). Indeed, the existence of a subpopulation of PSA-NCAM+/DCX+ newborn cells with bipolar morphology and antigenic features of granule cell precursors (NeuN and Pax6) was restricted to the third-fourth postnatal month (Fig. 1B). A substantial genesis of granule cells in peripuberal rabbit cerebella can also be excluded for several reasons: i) Most newly generated cells belonging to the neuronal population were found within the molecular layer, and those displaying a differentiated neuronal morphology and GABA-ergic expression were found exclusively in this layer; ii) The subpopulation of Pax6+ cells was no more detectable after the fourth postnatal month, in contrast with the other two cell populations that persisted up to adulthood (see below). In addition, even at earlier stages these cells did not give rise to ectopic granules which have been described in the molecular layer of the rabbit [44], since they were never seen to form clusters. Finally, the identity of newly generated cells with terminally differentiated granule cells of the granule cell layer seems to be excluded by the absence of labeling with the cerebellar granule cell marker GABAA receptor subunit $\alpha 6$ [45] in BrdU+ cells at different survival times, both in the molecular and the granular layers.

A second group of newly-born elements that were detectable beyond puberty involved multipolar cells immunoreactive for Map5, Sox2, and Olig2. In the 3-month-old rabbits these cells represented a small population (about 1/9 with respect to the newly generated neuronal cells), whereas their relative amount increased in the adult, reaching almost half of the total. The microtubule-associated protein Map5 (MAP1B) has been described in cells of both the neuronal and glial lineage. It is believed to play an important role in the outgrowth of neurites from neurons [46] and it is present in

proliferating neuroblasts of the embryonic mouse telencephalic ventricular zone [47]. In addition, although negligible in astrocytes, its expression precedes the development of the mature oligodendrocyte phenotype and interactions between microtubules and Map5 have been suggested to have a role in the formation and stabilization of myelin-forming processes [48]. In general, the expression of Map5 and its mRNA remains at relatively high level in neurogenic/structurally plastic regions of the adult brain [46, 49-51]. Rabbit Map5+ multipolar cells displayed morphological features of astrocytes, molecular profiles of oligodendrocyte precursors [13, 52], and nuclear transcription factors that are expressed by multipotent progenitor cells [53-56]. Taken together, such features suggest that these cells fall into the population previously described in rodents and referred to as synantocytes (since they form multiple contact with neurons, astrocytes, and oligodendrocytes; [13], or as polydendrocytes (being related to oligodendrocytes but with more processes and functions; [52]).

Due to the impossibility to localize in the rabbit tissue the Ng2 antigen, a general marker of synantocytes/polydendrocytes in rodents, - in spite of the different antibodies employed (see Methods and Table 3), we do not know if the rabbit Map5+ cells represent a sub-population of Ng2+ cells. Since the number of Map5+ cells in rabbit is lower compared to Ng2+ cells in rodents [13], they could be a newly generated sub-population of immature progenitors. It is worth noting that a similar population of Map5+ cells could not be detected in the cerebellum of humans [57]. In other words, in the rabbit nervous tissue Map5 seems to function as a marker for young, dividing synantocytes/polydendrocyte-like cells that, due to their spatial distribution and molecular profile, could be a reservoir of proliferating, multipotent progenitor cells within the cerebellum of lagomorphs.

Dynamics of Neurogenic Processes in the Rabbit Cerebellum and Persistence of Neurogenesis in the Adult Rabbit Cerebellum

The results of the present study show that the dynamics of neurogenic processes in the peripuberal and adult rabbit cerebellum is strikingly different from those described in rodents and presently known in mammals (summarized in Fig. 1B). In rabbits, the end of cell genesis and the neurochemical maturation of the cerebellum have been fixed around the second postnatal month [58, 59]. Yet, recent studies [9] and the results reported here show that the production of new cell progenitors in the rabbit cerebellum, including neuronal precursors, does not cease after the end of granule cell genesis, but continues at remarkable rates up to and beyond puberty, although progressively decreasing with age. During this period, which is paralleled by the occurrence of a persistent SPL on the cerebellar surface, both GABAergic interneuronal precursors and synantocyte-like cells are generated, whereas a residual genesis of granule cell precursors is restricted to the stage preceding the fourth postnatal month. This fact, in accordance with cell fate and positional information provided by transcription factors Pax2, Olig2, and Sox2, suggests that the persistence of both the neuronal and synantocyte/polydendrocytes-like cell populations is not related with the SPL. The transient existence of this layer could be linked to the protracted proliferation and tangential migration of cell precursors in subpial position, which is restricted to the EGL in rodents [60] but finds a permissive environment for a longer time in lagomorphs.

By extending the countings of BrdU+ nuclei up to 60 days after the last injection we show that most of the cells that remain in the cortex after the first wave of death actually survive for 2 months (Fig. 6). Although cytoplasmic and cytoskeletal markers used to visualize the neuronal cells during the first 34 weeks after their birth subsequently fade and disappear, thus hampering the identification of specific cell shapes, BrdU/PSA-NCAM double stainings confirm that a consistent population of newly-born cells maintains traces of PSA-NCAM up to 60 days post-injection survival. Yet, such type of staining does not provide information about the morphology of these cells, some of which could be dying. For this reason, some BrdU+ cells were detected at the same long term survival by electron microscopy using a pre-embedding technique [61]. Although cytology was hardly detectable, this approach confirmed that healthy cells showing the morphology of both neurons and synantocytes were still in place at that time. The occurrence of synaptic profiles onto the soma of these newly generated cells confirms that they are young neurons establishing contacts with the surrounding cerebellar tissue.

The gradual disappearance of early developmental markers such as PSA-NCAM and DCX can be interpreted as a normal process of cell differentiation in postnatal/adult neurogenic systems [9-11, 43]. On the other hand, the absence of general markers of neuronal differentiation and/or specific markers for cerebellar neurons in further steps of cell maturation (see Table 2) could be a peculiar feature of rabbit cerebellar neurogenesis. Also the expression of the molecule Map5 in newly-born synantocytes seems to be specific to rabbits, thus confirming that protracted cerebellar neurogenesis in this species can share common rules with other neurogenic systems yet displaying unexpected features. For these reasons, further studies are required to unravel the identity and fate of the newly generated cerebellar cells.

The surprising result of the present study consists of evidence that a numerically reduced but still active genesis of both interneuronal and synantocyte-like precursors was detectable in the cerebellar cortex of adult animals, up to 3 years of age, and even in the absence of a proliferative SPL (Fig. 1B). This process was qualitatively similar to that observed at peripuberal stages, involving PSA-NCAM+/DCX+/Pax2+ bipolar- and neuronal-shaped cells in the molecular layer, and Map5+/Olig2+/Sox2+ multipolar cells in all cerebellar layers. Although continuous genesis of glial progenitors and synantocyte-like cells has been described to occur in wide areas of the whole central nervous system (CNS) [12, 13], no genesis of neuronal precursors has ever been reported in the adult mammalian cerebellum. The occurrence of newly-born GABA+ neuronal precursors in the adult rabbit cerebellum suggests that a diluted but widespread genesis of interneurons does occur within the molecular layer of lagomorphs.

Another element of striking novelty in the context of mammalian neurogenesis consists of a protracted capability of rabbit Bergmann glial cells to undergo cell division. The occurrence of the transcription factor Sox2 in the Bergmann glia of rodents [28] has been viewed as a quiescent stem cell potential that cannot be extrinsecated in the highly static cerebellar tissue. On the other hand, such a possibility appears to be real in the environment of the peripuberal/adult rabbit cerebellar cortex.

The Rabbit Cerebellar Cortex: a Permissive Tissue for Widespread Neurogenesis?

Addition of cortical cells in the cerebellar cortex of adult rabbits, a long time after the complete disappearance of the proliferative SPL clearly rules out the possibility of a superficial source of cell progenitors in the adult. Accordingly, the absence of cell proliferation and markers of neurogenesis within the roof of the fourth ventricle also excludes a periventricular source, thus indicating that all cortical cells born in adult rabbits come from local progenitors. Other elements gathered in the present study converge to this assumption, such as the highly homogeneous distribution of newly generated cells in the whole cerebellar cortex, the persistence of Pax-2 transcription factor in newly-born cells, namely a landmark for neuronal precursors of neuroepithelial origin during development [8, 17], and the capability of Bergmann glial cells to undergo division.

Local, parenchymal cell progenitors capable of generating neurons have been described to occur within the rabbit caudate nucleus [36]. These cells are independent from the adjacent SVZ and give rise to migrating neuroblasts organized in chains exiting in striatal neurons during adulthood.

The presence of typical bipolar-shaped cells endowed with a cohort of molecules linked to structural plasticity and cell migration in the young, and to a lesser extent, adult rabbit cerebellum does suggest that some of the ex-novo generated cells can also change their position before final differentiation. This aspect appeared to concern mainly the neuronal population, in accordance with previous literature that referred to other neurogenic systems wherein PSA-NCAM+/DCX+ neuronal precursors are generated following a neurogenic sequence occurring within 2 week temporal window [42] (reviewed in [11, 30]). Thus, adult neurogenesis from local parenchymal progenitors could be a feature typical of lagomorphs, involving both brain and cerebellum (see also [42, 62]).

In the context of adult cerebellar neurogenesis, also the multipolar, Map5+ cells could be considered as a novel population of progenitor cells, peculiar to the rabbit cerebellum. Since most of these cells are newly generated and do not populate the CNS as densely as reported for Ng2+ cells in rodents (reviewed in [13]), it is likely that they represent immature cell progenitors trapped in the rabbit cerebellar cortex after pre/post-natal development, that continue to divide locally throughout life. In rabbit, the dividing Bergmann glia could represent the primary source of these progenitor cells, a hypothesis that is strengthened by the fact that all these cells express the transcription factor Sox2, and the multipolar cells also express Olig2. Sox2 is implicated in the proliferation/maintenance of neural stem cells and in adult neurogenesis [53-55]. In particular, it is important in maintaining embryonic stem cells in a pluripotent state that actively inhibits neuronal differentiation in neural precursor cells [63]. Also Olig2 is involved in the development of neuronal and glial precursors, and continues to be expressed in multipotent progenitor cells of the adult CNS [64], although its role remains obscure (reviewed in [65]). Thus, the presence of these transcription factors suggests that multi-polar Map5+ cells could be multipotent progenitors instead of simple glial progenitors.

Possible Functional Implications and Future Perspectives

An explanation for differences in neurogenic potential between rodents and lagomorphs could reside in the pronounced variation in life span among these animal species, influencing distinct patterns of growth, maturation, and senescence that may have an impact on the extent and plasticity of neurogenesis throughout life (see [30, 34]). In this context, tissue growth may be a critical feature for the regulation of adult neurogenesis, what could explain why teleost fish species that have indeterminate growth also have continual addition of new neurons throughout life and striking capacity for brain repair and regeneration [1].

This perspective leaves open the intriguing possibility that an undetected, delayed genesis of neuronal and glial progenitor cells could exist in other mammalian species characterized by slow growth and long lifespan, including primates and humans. It is known that brain neurogenic sites exist in these species [66, 67], but their activity declines with age [68] even more dramatically than in rodents [69]. Furthermore, it is believed that what really hampers the self-repair of adult mammalian brains might be linked to their failure in allowing the proliferation/migration/differentiation of parenchymal progenitor cells rather than a lack of progenitors [70]. Uncovering whether the potentialities proper of the rabbit CNS do exist in young humans could be of paramount importance in the perspective of modulating widespread adult neurogenesis, beyond the highly restricted periventricular and hippocampal neurogenic zones. In this context, the rabbit brain and cerebellum could be a suitable model for studying nervous tissue permissiveness in mammals.

RESULTS

Animals analyzed in the present study will be referred to as postnatal when a typical EGL is present in the cerebellum (from birth to 5 weeks of life), peripuberal when a SPL is detectable on the cerebellar surface (from 25 months), and adult (1–3 years old rabbits, devoid of cerebellar SPL). Although in rabbits puberty occurs around the fourth month of life, animals aged 2–5 months were considered to be part of a homogeneous group due to the occurrence of the SPL. Most of the qualitative and quantitative analyses performed on peripuberal rabbits are referred to the 3-month-old subjects, and differences are reported concerning older animals at specific stages.

Newly-Formed Cells with Specific Morphologies are Largely Present in the Cerebellar Cortex of Peripuberal Rabbits

We have previously shown that the cerebellum of peripuberal rabbits is characterized by a proliferative superficial layer (PSL) which contains chains of newly generated neuroblasts (Fig. 2A) [9]. In addition, by using markers of cell proliferation the occurrence of many newly generated cells is also visible within the cortical layers, a substantial amount of these cells being still detectable 2 weeks after their birth [9]. In order to visualize the morphology of these cells, we employed antibodies raised against markers of structural plasticity, namely the polysialylated form of the neural cell adhesion molecule (PSA-NCAM) and the collapsin response mediator protein-4 (CRMP-4) (Fig. 2). In spite of the progressive reduction of the SPL during the fourth and fifth month of the rabbit postnatal life, followed by its disappearance at the sixth

month, many cells expressing the above-mentioned markers were still detectable in the cortex, particularly in the molecular layer (Fig. 2B–D; Table 1). Staining with CRMP-4, although fainter than PSA-NCAM, revealed cells falling into three main morphological types: bipolar, polarized neuronal-like, and multipolar (Fig. 2). The PSA-NCAM was detectable in bipolar and polarized, but not in multipolar cells. On the other hand, multipolar cells showed a stellate, highly ramified morphology and were immunoreactive for the cytoskeletal protein Map5 (Map1B; Fig. 2I, J) [14, 15].

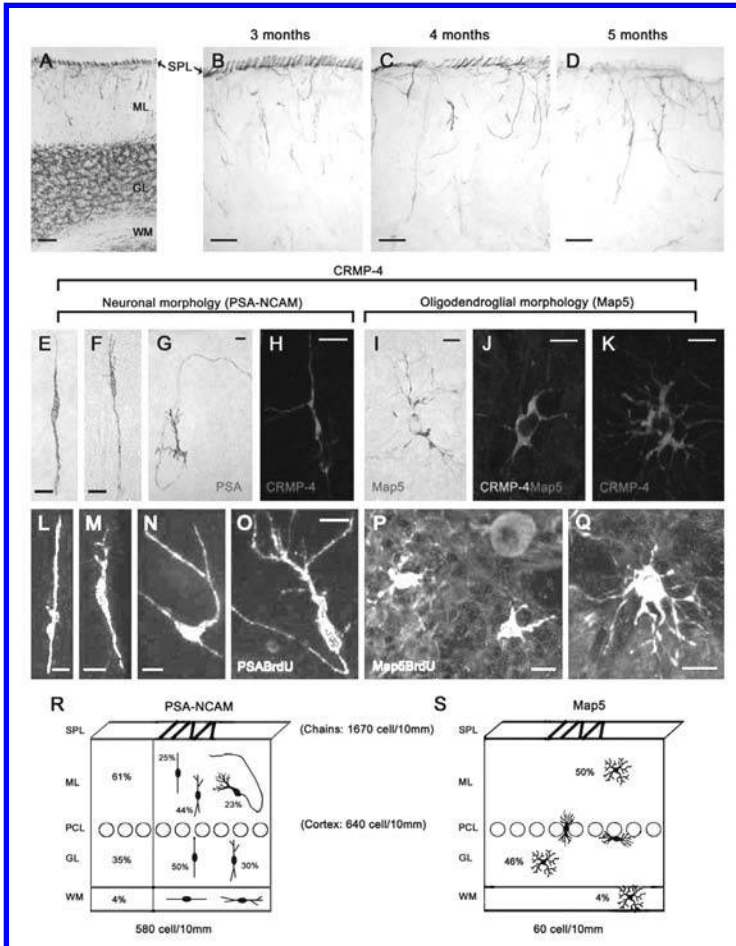


Figure 2: Newly generated cells in the cerebellar cortex of peripubertal rabbits. In addition to the chain of neuroblasts of the SPL; [9], the peripubertal rabbit cerebellar cortex contains PSA-NCAM+ cells in all layers (A). In parallel with the progressive dilution and disappearance of the SPL, numerous PSA-NCAM+ cells remain detectable in the molecular layer (B–D). PSA-NCAM (E–G) and Map5 (I, J) identify two morphologically-distinct cell populations, both immunoreactive for CRMP-4 (H, J, K). PSA-NCAM+ cells are bipolar- and neuronal-shaped (E–H), whereas Map5+ cells are multipolar (I–K). All these cell types are newly generated, as revealed by BrdU staining (L–Q) at different post-injection survival times (5 [L], 10 [M, N], 15 [O–Q]). On seeing the quantitative analysis of the two cell populations in different cerebellar layers (R, S) for PSA-NCAM+ cells in the molecular (ML) and granule layer (GL) different morphologies are also indicated. Bars: A–D, 50 µm; E–Q, 10 µm.

Table 1: Number of Cells (cells/10 mm) Immunoreactive for PSA-NCAM and Map5 in the Peripuberal and Adult Rabbit Cerebellar Cortex.

Age (months)	PSA-NCAM (neuronal-like)				Map5 (multipolar)	
	Peripuberal		Adult		Peripuberal	Adult
	3	6	12	36	3	36
SPL	1670+/-292.7	0	0	0	0	0
ML	360+/-38.9	42.80+/-8.30	12.01+/-5.0	2.44+/-0.7	29.9+/-11.9	2.95+/-1.45
GL	200+/-42.1	2.20+/-1.10	1.27+/-0.7	0.14+/-0.1	27.5+/-11.9	2.40+/-1.80
WM	20+/-2.9	0	0.07+/-0.1	0	2.3+/-1.4	0.15+/-0.15

T-test on PSA-NCAM+ and Map5+ cells, in each layer, and at different post natal age. PSA NCAM+: 3 month-old (ML $p=0.003$; GL $p=0.019$); 3 month-old vs adult (ML $p=0.003$; GL $p=0.018$); Map5+: 3 month-old vs adult (ML $p=0.790$; GL $p=0.431$); T-test on PSA-NCAM+ and Map5+ cells, in different layers (ML vs GL) at the same post-natal ages: PSA-NCAM+: 3 month-old ($p=0.033$); adult ($p=0.178$); Map5+: 3 month-old ($p=0.893$); adult ($p=0.835$).

Quantitative analyses showed that the bipolar/polarized PSA-NCAM+ cell population represents about 90% (580 cell/10 mm \pm 84) on 10% of multipolar, Map5+ cells (60 cell/10 mm \pm 25), with respect to all cortical cells identified by these markers (see Fig. 2R, S).

Bipolar cells were mainly radially-oriented, showing the typical morphology of migrating elements, with a leading and a trailing process (Fig. 2E). Polarized neuronal cells were observed in the molecular layer with no particular orientation (Fig. 2A–D, G, H). They showed a piriform cell body (15–20 μ m long), a long, thin axonal-like process with a U-shaped direction remaining within the molecular layer, and one to three thicker, dendritic-like processes on the opposite side of the cell (Fig. 2G, H). The quantitative analysis showed that most PSA-NCAM+ cells (61%; 360+/-38,9 cells/10 mm see Fig. 2R and Table 1) reside in the molecular layer, the remaining percentage being widespread in the granule cell layer (35%; 200+/-42,1 cell/10 mm) and, to a lesser extent, in the white matter (4%; 20+/-2,9 cells/10 mm) (Fig. 2R). In addition to the typical bipolar and neuronal-like morphologies, many intermediate forms characterized by an axonal-like process on one side and some dendritic branches on the opposite side (Fig. 2F, M, N), were frequently observed (the relative percentages with respect to the total are given in Fig. 2R). The complete set of morphologies, including the neuronal shape, was detectable exclusively within the molecular layer (Fig. 2R).

The Map5+ multipolar cells were characterized by a spheric cell body, about 8–10 μ m in diameter. These cells showed many, ramified processes reminiscent of the stellate-shaped elements known as synantocytes [12, 13]. Those located in the proximity of Purkinje neurons showed a flattened shape when cut transversely (Fig. 2S). In contrast to PSA-NCAM+ cells, they were more homogeneously distributed in both the molecular and granule cell layer (see Fig. 2S and Table 1; ML: 29, 9 \pm 11, 9 cell/10 mm; GL 27, 5 \pm 11, 9 cell/10 mm) and, to a lesser extent, in the white matter (2, 3 \pm 1, 4 cell/10 mm).

Morphological observations and countings carried out on both sagittal and coronal sections revealed that PSA-NCAM+ and Map5+ cell populations were homogeneously distributed in all dorsal/ventral and medial/lateral lamellae. To test which among these cells are newly generated we performed double labelings with systemically-administered

5-bromo-2'-deoxyuridine (BrdU) then revealed at different post-injection survival times. As previously described [9], after 2 hr (hr) most cell proliferation was observed to occur in the SPL, whereas at subsequent survival times (5–15 days) double stainings of 5-bromo-2'-deoxyuridine (BrdU) with PSA-NCAM and Map5 respectively, clearly revealed that a large population of cells expressing such markers in the peripuberal rabbit cerebellar cortex were newly generated (Fig. 2L–Q).

Newly-born Elements in the Cerebellar Cortex of Peripuberal Rabbits belong to Distinct Populations of Neuronal and Glial Cell Precursors

Neuroepithelial-Derived Interneuronal Precursors

The group of PSA-NCAM+ cells including the bipolar, intermediate, and polarized neuronal morphologies was also immunoreactive for the microtubule binding protein doublecortin (DCX) [16], thus confirming they actually represent a neuronal population (Fig. 3A–D). In the rabbit cerebellar cortex, PSA-NCAM, and DCX actually

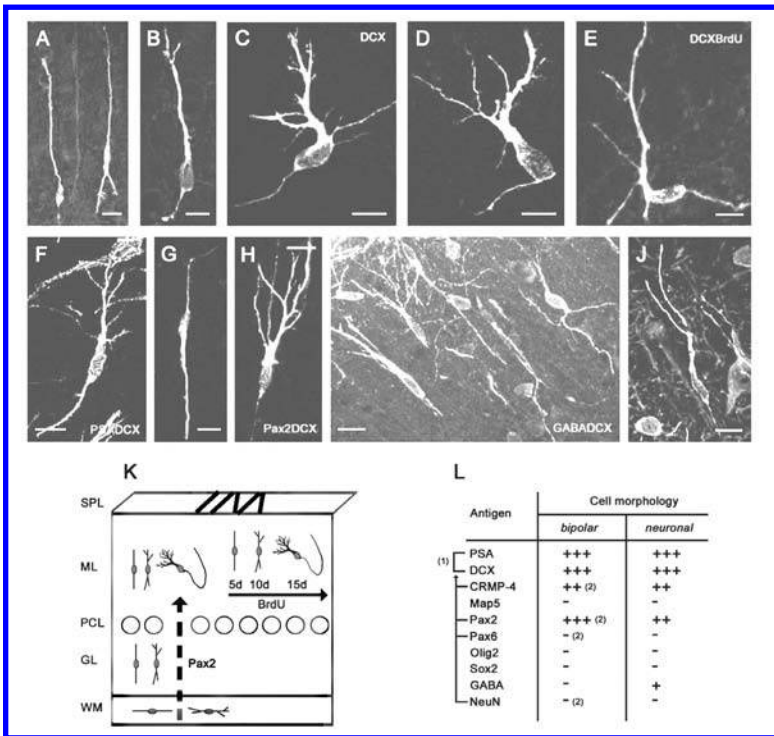


Figure 3: Newly generated, neuronal-shaped cells in the cerebellar cortex of peripuberal rabbits. Bipolar, intermediate, and neuronal-like shaped cells are immunoreactive for the neuronal marker DCX; A–D and double stained with BrdU (E; 15 days survival post-injection), PSA-NCAM (F), Pax2 (G,H), and GABA (I,J). See also Table in (L); (1), Overlapping populations; (2), Antigens whose immunoreactivity is present/absent in a subpopulation of bipolar cells (their counterpart being represented in Fig. 5L). (K) Model for the newly-born neuronal cell population: co-expression of PSA-NCAM, DCX, and BrdU (A) in different morphologies reveals a neurogenic sequence within 2 weeks, and co-expression with the transcription factor Pax2 (B) indicates that these cells are interneuronal progenitors of neuroepithelial origin ascended from the white matter (B arrow). Bars: 10 µm.

identify an almost overlapping cell population (Fig. 3F). Accordingly, in the BrdU/PSA-NCAM double stainings carried out at 5, 10, and 15 days post-injection survival times (Fig. 2L–O) the occurrence of bipolar double-labeled cells was more frequent at early survival times, whereas that of more differentiated morphologies (neuronal-like) was detectable at subsequent survival times. This indicates that a neurogenic sequence leading to a young neuronal cell type in the molecular layer does occur during a 2 week temporal window (Fig. 3E, K).

In order to further explore the nature and origin of this population of newly generated cells we combined the immunolocalization of the above described markers with different transcription factors involved in the specification of cell progenitors. The transcription factor Pax2, namely a marker for GABAergic cerebellar interneurons of neuroepithelial origin [8, 17], was detectable in PSA-NCAM+/DCX+ cells belonging to all morphological types (Fig. 3G, H, K). Pax2 staining was generally weaker in ramified cells compared with bipolar ones, thus being probably down-regulated as differentiation proceeds, as confirmed by the incidence of BrdU+/Pax2+ double stainings. The same cell population was consistently negative for both the transcription factors Sox2 and Olig2 (Fig. 3L). In addition, most polarized neuronal-like cells showed a remarkable staining for the GABA (Fig. 3I, J), another marker for cerebellar cortex inhibitory interneurons which is concentrated mainly in young neurons before they become terminally differentiated [18]. No GABA immunoreactivity was detectable in bipolar-shaped cells, or in the SPL.

By gathering data of co-expression of cell proliferation markers (at 2 hr–15 days survival) with markers for structural plasticity PSA-NCAM, CRMP-4, and DCX, the transcription factor Pax2, and the GABA in newly-born cerebellar cells (summarized in Fig. 3K, L), it can be concluded that a subset of GABAergic interneurons are generated within the molecular layer of the peripuberal rabbit cerebellum.

None of the newly generated cells were immunoreactive for specific markers of common cerebellar neuronal cell types, such as calbindin, calretinin, or parvalbumin (Table 2), during the first 2 weeks after their birth.

Table 2: Distribution of Other* Antigens in Newlyborn and Non-newlyborn Cell Populations in the Cerebellar Cortex of Peripuberal and Adult Rabbits.

Antigen	PSA-NCAM+ or Map5+ newborn cell morphologies			BrdU+nuclei at 30–60 days [§]	Non-newlyborn cells
	bipolar	neuronal-like	multipolar		
Parvalbumin	–	–	–	–	Purkinje, basket, stellate
Calbindin	–	–	–	–	Purkinje, Lugaro
Calretinin	–	–	–	–	Unipolar brush, Lugaro
Neurofilaments 20 KD	–	–	–	–	Neurons
Class III β -tubulin	–	–	–	–	Purkinje and Granule cells
MAP2	–	–	–	–	Purkinje and Granule cells
NeuN	–	–	–	–	Granule cells
$\alpha 6$	–	–	–	–	Granule cells
GFAP	–	–	–	–	Bergmann glia, astrocytes
Vimentin	–	–	–	a few astrocytes	Bergmann glia
S100 β	–	–	–	+(weak)	Bergmann glia, astrocytes
BLABP	–	–	–	+	Bergmann glia, glial progenitors
O4	–	–	–	–	–

* (antigens not displayed in Tables contained in the Figures).

§ (only in peripuberal animals).

Multipolar, Oligodendrocytic-Like Cell Precursors (Synantocytes)

The multipolar, Map5+ cells (Fig. 4A–C) were immunoreactive for CRMP-4 but not PSA-NCAM, DCX, or GFAP (Figs. 2I–K and 3D, M; Table 2). They were consistently double-stained for both the transcription factors Sox2 and Olig2 [19, 20] (Fig. 4H–K, L) but not for Pax2 (Fig. 4M). Thus, the distribution of a combination of cell markers and transcription factors suggests that the PSA-NCAM+/DCX+ cells and the Map5+ cells actually represent two distinct populations, the former being far more numerous than the latter, with a 9/1 ratio in the 3-month-old animals. Student's Test-T revealed that the number of PSA-NCAM+ cells in 3-month-old rabbits is significantly higher than the number of Map5+ cells (ML $p = 0,003$ GL $p = 0,019$; Fig. 2R, S and Table 1)

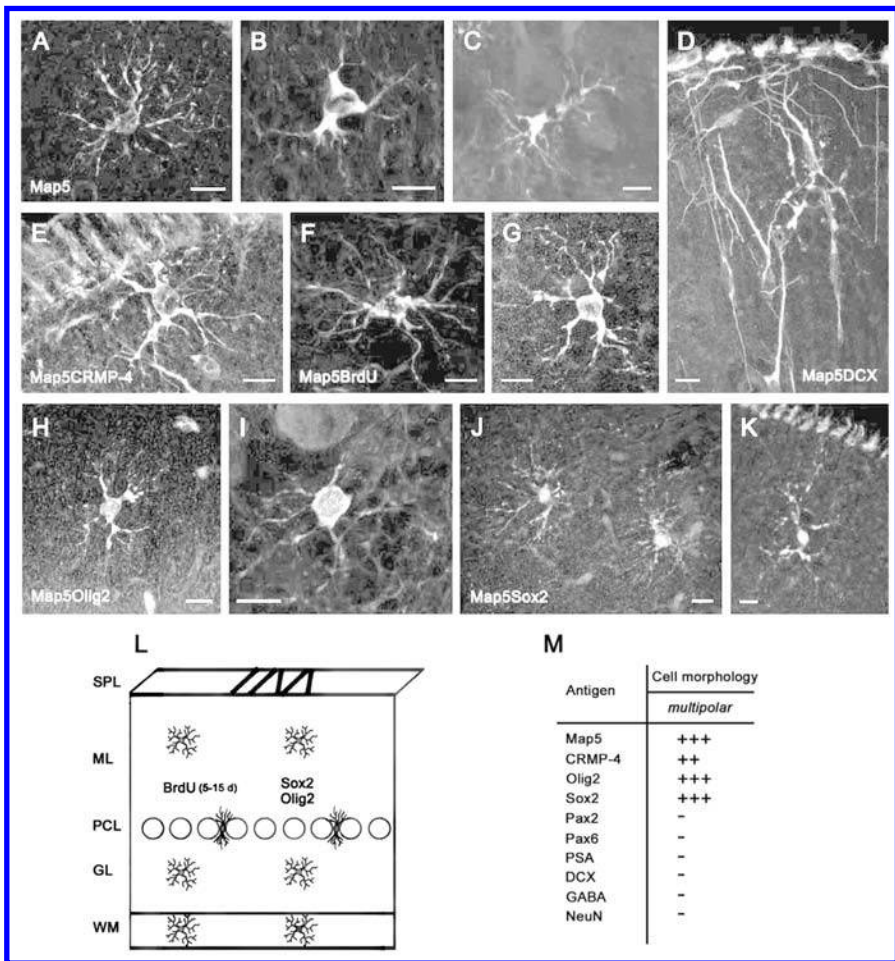


Figure 4: Newly generated, multipolar cells in the cerebellar cortex of peripuberal rabbits. Multipolar cells of different shape are immunoreactive for Map5 in different cerebellar layers (A, D–H, J, K, ML; B, C, I, GL) and CRMP-4 (E), but not DCX (D). These cells are newly generated, as they are marked with BrdU at 15 days survival post-injection (F, G). They also express the transcription factors Olig2 (H, I) and Sox2 (J, K). See also Table in (M). (L) Model for the newlyborn Map5+ cell population: the cells are homogeneously distributed in all cerebellar layers. Bars: 10 μ m.

Using BrdU/Map5 double stainings (Fig. 4F, G) many Map5+ multipolar cells were found to be generated, starting from the second week survival time after the injection of the DNA marker. No particular spatio-temporal pattern was detectable in these newly-born cells by considering different morphologies at different survival times and in different cerebellar layers (Fig. 4L). Unlike PSA-NCAM+/DCX+ cells, none of the Map5+ cells were found to be double-stained for BrdU at early (15 days) post-injection survival times, thus indicating that Map5 starts to be expressed later.

Table 3: Antibodies Used in this Study.

Antigen	Dilution	Antibody (clone)	Sp.	rb	Source	Cat. N
Proliferation markers						
Ki67	1:300	(mono) MIB-1	m	+	Dako	7240
BrdU	1:600	(mono) BU1/75	rat	+	Harlan	MAS250c
Markers of stem/progenitor cells						
Sox2	1:1500	(poly)	rb	+	Chemicon	AB5603
	1:500	(poly)	g	+	Chemicon	sc1739
BLBP	1:2000	(poly)	rb	+	Chemicon	AB9558
Neuronal markers						
Doublecortin (C18)	1:750	(poly)	g	+	Santa Cruz	sc8066
Class III β -tubulin (TUJ1)	1:1000	(poly)	rb	+	Covance	PRB435P
MAP5	1:5000	(mono)AA6	m	+	Chemicon	MAB366
MAP2	1:500	(mono)AP20	m	+	Chemicon	MAB3418
NeuN	1:400	(mono)A60	m	+	Chemicon	MAB377
Hu C/D	1:200	(mono)16A11	m	+	Molecular Probes	A21271
CRMP/Tuc-4	1:500	(poly)	rb	+	Chemicon	AB5454
GABA	1:5000	(poly)	rb	+	Sigma	A2052
Pax2	1:5000	(poly)	rb	+	Zymed	71-6000
Pax6	1:800	(poly)	rb	+	Covance	PRB278P
Calbindin	1:1500	(mono)	m	+	Swant	300
Parvalbumin	1:7000	(mono) PARV19	m	+	Sigma	P3088
Calretinin	1:2500	(poly)	rb	+	Swant	7699/4
α 6 GABA _A R	1:100	(poly)	rb	+	Chemicon	AB5453
Neurofilament 200 kD	1:400	(mono) NE14	m	+	Sigma	N5489
Glial markers						
Vimentin	1:800	(mono) V9	m	+	Dako	M0725
GFAP	1:1000	(poly)	rb	+	Dako	Z0334
Ng2	1:250	(poly)	rb	-	Chemicon	AB5320
	1:300	(mono)	m	-	Chemicon	MAB5384
	1:100	(mono) 132.38	m	-	sigma	N8912
O4	1:10000	(mono) 132.38	m	-	Upstate	05-710
	1:200	(mono) 81	m	+	Chemicon	MAB345
S100 β	1:10000	(poly)	rb	+	Swant	37
Olig2	1:1500	(poly)	rb	+	Chemicon	AB9610
	1:400	(poly)	g	+	R&D Systems	AF2418
Migration markers						
PSA-NCAM	1:3500	(mono)2-2B	m	+	AbCys	Abc0019
TAG-1	1:800	(mono)4D7	m	+	DSHB	TAG-1

Sp., species; m, mouse; rb, rabbit; g, goat; + works on rabbit tissue; ... does not work on rabbit tissue.

The immunocytochemical characterization of multipolar cells with transcription factors, markers of cell proliferation and neurogenesis, indicated that in the peripuberal rabbit cerebellar cortex, in addition to molecular layer interneurons another population of newly generated cells involves glial-like cell progenitors. These cells are reminiscent of synantocytes [13], a recently described cell type sharing morphology of protoplasmic astrocytes *in vivo* and antigenic features of oligodendrocyte precursor cells *in vitro*. This cell category could not be further identified by expression of Ng2 antigen [12], since none of the antibodies tested were working on the rabbit tissue (see Table 3). The absence of Map5, Olig2, and Sox2 immunoreactivity in bipolar-shaped cells does suggest that the newly-born multipolar cells come from local progenitors in each cerebellar layer.

None of the newly generated cells were clearly double-stained for the glial markers GFAP or O4 (Table 2). Also double stainings between BrdU and vimentin or S100 β , did not yield clear co-expression in identifiable glial cell types, due to the faint expression (S100 β) or prevalent localization of these markers in cell processes (vimentin) rather than in the cell body (not shown).

Residual Granule Cell Precursors

Bipolar-shaped cells in the cerebellar cortex of peripuberal rabbits represent about 30% of all cells detectable with the above-mentioned markers (Fig. 2R). As described above, a consistent part of these cells are Pax2+/PSA-NCAM+/DCX+ and belong to the population of newly generated neuronal progenitors (Fig. 3K). A subpopulation of the PSA-NCAM+/DCX+, but Pax2-negative bipolar cells were immunoreactive for NeuN [21] (Fig. 5F, G) and Pax6 [22, 23] (Fig. 5J, K), two markers for cerebellar granule cell precursors (Fig. 5H). The detection of Pax6+ and NeuN+ bipolar cells was restricted to the second and third postnatal months, being absent starting from the fourth month and so forth at all later stages (Fig. 5N). In addition, Pax6 immunoreactivity was never observed in neuronal-shaped cells (Fig. 5J). This indicates that some granule cell precursors continue to migrate from the SPL to the cortical layers during the early phases after the shift from EGL to SPL. Then, this protracted descent of granule cell precursors is exhausted before puberty. The late granule cell precursors seem not to differentiate into mature granule cells, since no immunoreactivity for the GABAA receptor subunit $\alpha 6$ [24] was detectable in newly-born cells (not shown). In addition, consistent apoptotic cell death was present in both layers of the cerebellar cortex in 3-month-old animals (Fig. 5M), whereas it is significantly reduced in the 4-month-old rabbits, particularly in the granule cell layer (Fig. 5M; summarized in Fig. 5N).

The occurrence of a residual descent of granule cell precursors raises questions about the persistence of SPL chains of tangentially-oriented cells. These chains are progressively reduced in number from the second to the fifth month, then disappearing from the cerebellar surface during the sixth month. The early neuronal markers DCX (Fig. 5A, B), NeuN (Fig. 5F), class III β -tubulin [25], and HuC/D protein (not shown) were detected in SP chains, thus confirming they are formed by neuroblasts (see also [9]). Yet, not all antigens detectable in the SPL were co-expressed in cortical cells (see Fig. 5). For instance, CRMP-4 although present in newlyborn neurons of the molecular layer was absent in SPL chains (Fig. 5C, D). By contrast, the neuronal cell adhesion

molecule TAG-1 [26] was detectable in a subset of these chains (Fig. 5B) but not in cortical cells (Fig. 5C). Similarly, Map5 (Map1B) which is involved in the control of microtubule organization in both neuronal and glial progenitors [14, 15], was present in all SPL chains but absent in DCX+ newly-born neurons (Fig. 5E). These data, in parallel with the neuroepithelial origin of the Pax2+ interneuronal population, suggest that the transient SPL does contain the last granule cell precursors which mostly fail to reach their final destination in the granule cell layer.

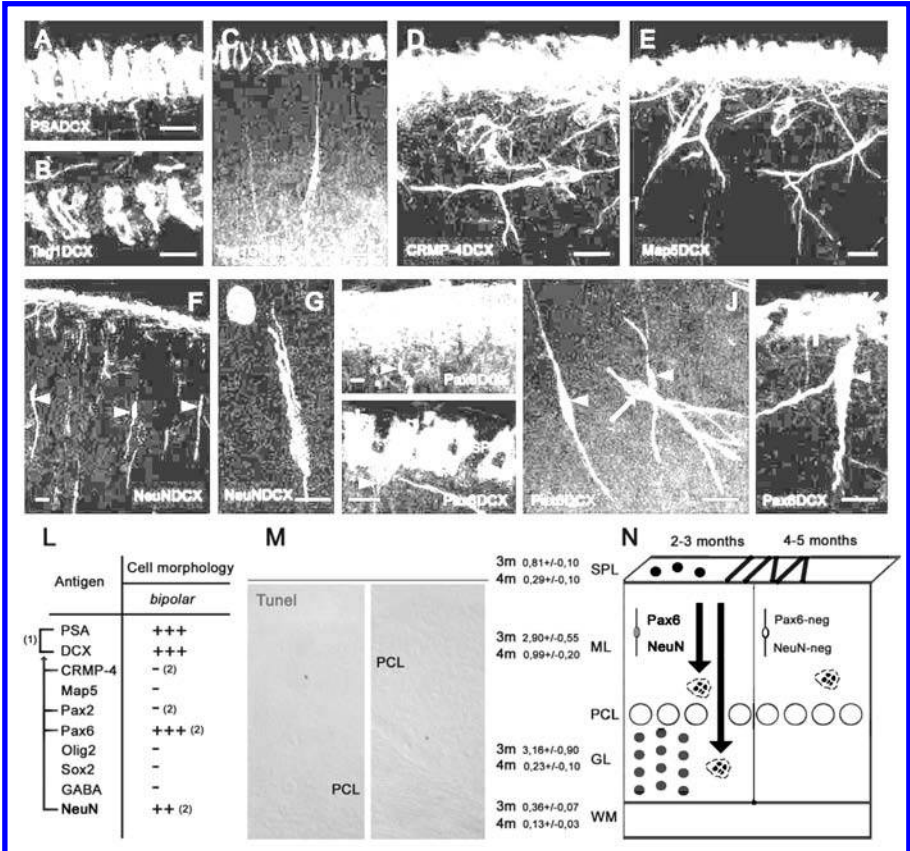


Figure 5: Residual granule cell precursors in the cerebellar cortex of peripuberal rabbits. Neuroblasts forming chains in the SPL are immunoreactive for PSA-NCAM (A), DCX (A, B, E), and Map5 (E), partially for Tag1 (B, C) and NeuN (F), but not for CRMP-4 (D). NeuN (F, G) and Pax6 (H–K) reveal residual granule cell precursors both in the SPL and in the ML, but they are not present in all DCX+ cells (J). See also Table in (L); (1), Overlapping populations; B lines, antigens revealing subpopulations of (1). (2), Antigens whose immunoreactivity is present/ absent in a subpopulation of bipolar cells (their counterpart being represented in Fig. 3L). (M), Cell death revealed with TUNEL technique is reduced in the shift from the third to the fourth month of age (3 m, 4 m), suggesting that granule cell genesis is coming to an end. Student’s T-test revealed a significant decrease of the number of TUNEL labeled cells in each layer (SPL $p = 0,010$; ML $p = 0,005$; GL $p = 0,004$ WM $p = 0,013$). This is confirmed by the fact that Pax6 and NeuN are no more detectable after the fourth postnatal month (N). Bars: 10 μ m.

Newly Generated Cells Followed for Survival Times Longer than 2 Weeks

Cell countings of BrdU+ cells extended up to 2 months survival indicated that most of the cells still alive in the cortex 2 weeks after their birth, actually survive for at least 2 months, in contrast with a remarkable drop occurring during the first 2 weeks [9] (Fig. 6A, B).

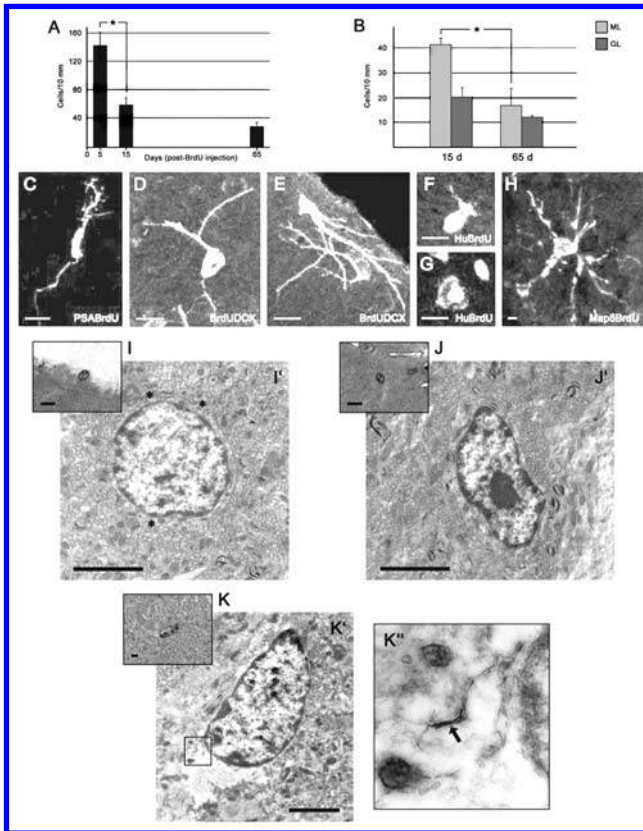


Figure 6: Newly generated cells 1–2 months after their genesis in the cerebellar cortex of peripuberal rabbits. Countings of BrdU+ cells in the cerebellar cortex at 5, 15, and 65 days after injection (A) reveal a marked drop during the first 2 weeks followed by a relative stabilization during the subsequent months ($F = 19,01$, $p = 0,001$). Post-hoc comparison revealed a decrease in the number of BrdU+ cells between 515 days. (B) The slight decrease observed at long term survival mainly affects cells in the molecular layer (ML). Student's T-test revealed that the decrease in the number of cells between 1565 days of survival in the ML shows a trend ($p = 0,09$) while in the GL it is not significant ($p = 0,45$). C–H, BrdU-stained cells visualized 1 month (C–G) and 2 months (H) after the last of 5 injections in association with different neuronal (D–G) and structural plasticity (A, H) markers, (GL) granule cell layer, I–K, Ultrastructural analysis of BrdU+ cells 2 months after systemic injection of the DNA marker. After the identification of the marked nuclei in semithin sections of the molecular layer (I, J, K, color insets), the same cells localized at the electron microscope in ultrathin sections (I', J', K'), showing a round cell soma and three initial, multipolar processes (asterisks), and two polarized neurons with an oval cell soma (J', K'). K', inset showing a higher magnification of an axo-somatic synapse (arrow). Bars: A–F, 10 μm ; I, I', J, J', K, K', 3 μm ; (the cells in ultrastructural photographs seem smaller than in confocal images since the sections are not cut through their main diameter).

Although some newly-born cells were still detectable in association with PSA-NCAM (Fig. 6C), DCX (Fig. 6D, E), and Hu protein (Fig. 6F, G) up to 30 days since their birth, after this period most of the BrdU+ nuclei were not identifiable through double stainings with cytoplasmic or membrane-bound markers that could reveal a specific cell morphology. Unlike neuronal precursor cells, the Map5+ cells started to express the cytoplasmic marker 2 weeks after their genesis. Then, the Map5 staining was still detectable until 65 days indicating that these cells maintain their multipolar morphology for months (Fig. 6H). Accordingly, also the number of BrdU+/Sox2+ double labeled cells was very high between 2 weeks and 2 months after their genesis.

No more GABA staining was detectable in newly-born cells at long survival times, this neurotransmitter being downregulated as cell differentiation occurs [18]. In addition, none of the newly generated cells aged more than 1 month were immunoreactive for the interneuronal markers calbindin, parvalbumin, calretinin (see Table 2).

Some BrdU/vimentin and BrdU/S100 β double stainings (not shown) were observed within the granule cell layer and Bergmann glial cell layer (Table 2). Most of these cells were not clearly identifiable as to their morphology. This indicates that also astrocytes could be generated at least within the granule cell layer, and suggests that some Bergmann glial cells might proliferate (see below).

Finally, rare Isolectin B4+ (IIB4) microglial cells (3, 16 +/- 1, 84%) that had incorporated BrdU were detectable at 65 days post-injection survival.

Thus, it appears that a large amount of newly generated neuronal precursors cannot be visualized beyond the first month after their birth, due to a lack of specific cytoplasmic/membrane-bound markers. For these reasons, in order to visualize the newly-born cells at longer survival times, we carried out an ultrastructural study on BrdU-treated rabbits that were left to survive 60 days after the first and 45 days after the last injection of the marker. After visualization of the BrdU+ nuclei by peroxidase staining, small pieces of the cerebellar molecular layer containing these cells were resin-embedded and processed for electron microscopy. The marked nuclei were easily identified in semithin sections (Fig. 6I–K) and subsequently photographed in the ultrastructure. Cell types corresponding to the size and shape of synantocytes (Fig. 6I') and neurons (Fig. 6J', K') were found, thus showing that elements belonging to both cell populations are still in place after 2 months. In two cells out of 8 cells analyzed, the occurrence of rare axo-somatic synaptic contacts was observed (Fig. 6K'').

Newly Generated Neuronal and Glial Cell Progenitors in the Cerebellum of Adult Rabbits

The cerebellum of adult rabbits was completely devoid of SPL. By contrast, some Ki67+ nuclei were still detectable in the cortex (Fig. 7H–J). The Ki67+ nuclei were frequently detected as “doublets” (Fig. 7H–J), indicating their feature of daughter cell progeny of a recent mitotic event [27]. The occurrence of newly generated cortical cells in these animals was confirmed by the detection of BrdU after 15 day survival (Fig. 7K, L, S). The newly-born cells were present in both cortical layers, more frequently located close to the Purkinje cell layer, on both sides.

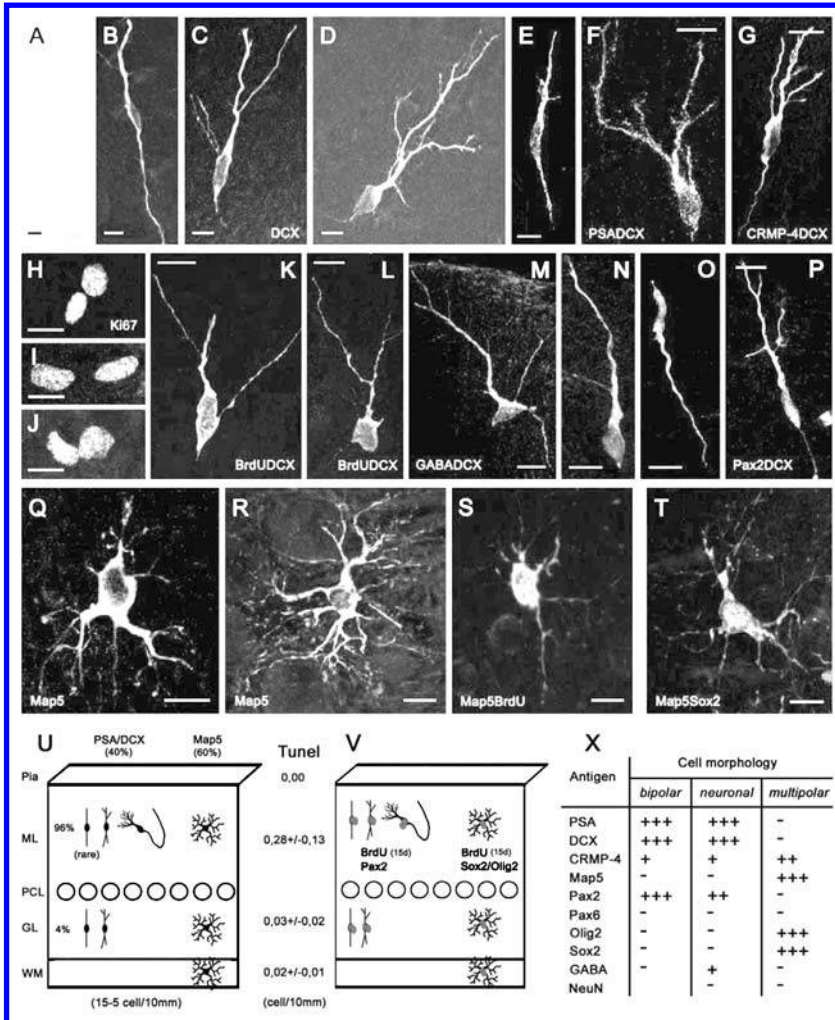


Figure 7: Newly generated cells in the cerebellar cortex of the adult rabbit. All morphological cell types, expressing and co-expressing the same markers as in the peripuberal rabbit cerebellum are detectable in the adult (1 and 3 years; A–G,Q,R). Cell proliferation is detectable in both cortical layers, as shown by Ki67 staining (H–J), and newly generated neuronal (K, L) and multipolar, glial-like cells (S) are visible after BrdU staining at 15 days survival. Also in the adult, the newly-born neuronal cells do contain GABA (M, N) and Pax2 (O, P), as well as the multipolar cells are immunoreactive for Sox2 (T). See also Table in (X). U, Absolute and relative amounts of PSA-NCAM+ and Map5+ cells in the adult cerebellum. V, Model for the newly-born PSA-NCAM+ and Map5+ cell populations in the adult. Bars: 10 µm.

By performing the same immunocytochemical analyses carried out in the peripuberal animals, similar PSA-NCAM+/DCX+ neuronal-shaped cells and Map5+ synantocyte-like cells were detected in the adult cerebellum (Fig. 7). Both cell types showed the same morphology, antigenic features, and layer distribution described in the 3-month-old cerebellar cortex. Nevertheless statistical analysis revealed that in the

adult the PSA-NCAM+/DCX+ and Map5+ cells are equilibrated (ML $p = 0,790$; GL $p = 0,431$) Accordingly the PSA-NCAM+/DCX+ neuronal cells were immunoreactive for GABA (Fig. 7M, N). By contrast, some differences concerned the absence of PSA-NCAM+/DCX+ cells within the white matter of adult cerebella, and the very rare occurrence of bipolar-shaped cells in the cortex (summarized in Figs. 7U and 7B).

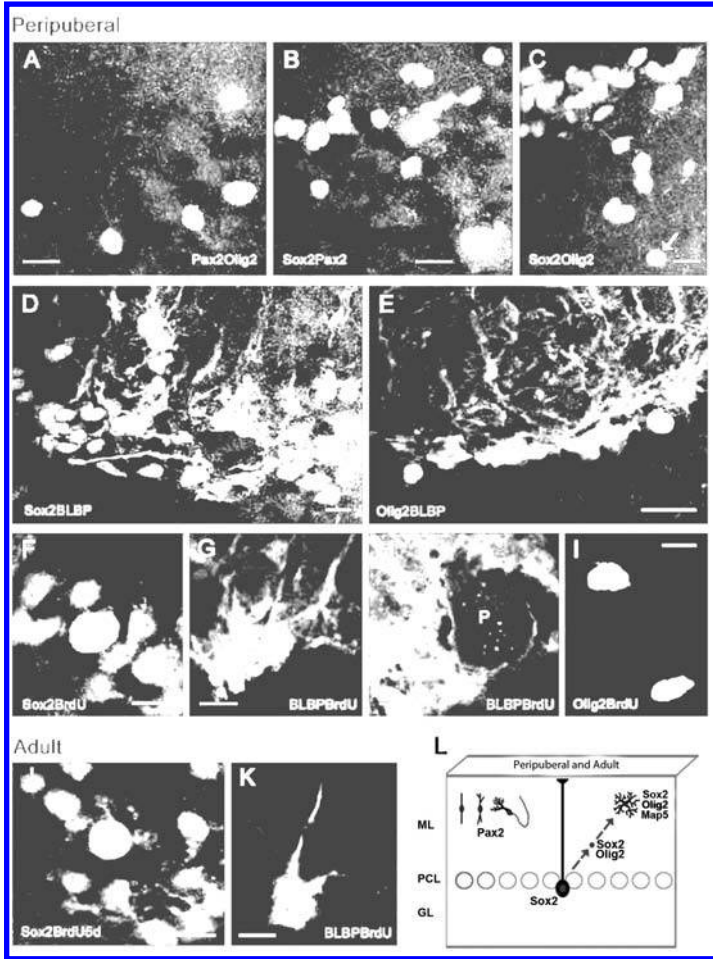


Figure 8: Relationships among transcription factors in newly generated neuronal and glial-like cell populations. Both Olig2 and Sox2 are never co-expressed with Pax2 (A, B), whereas some Sox2+ nuclei also contain Olig2 (C, arrow). Virtually all BLBP+ Bergmann glia cells contain Sox2 (D) but not Olig2 (E). Some large Sox2+ nuclei in the Purkinje cell layer do incorporate BrdU at 1–5 days postinjection survival (F). Incorporation of BrdU is also detectable in some Bergmann glia cells (G; two immuno-negative Bergmann glial cells are indicated by arrows), that retain the marker for at least 2 months (H) P, Purkinje neuron (immuno-negative). Also Olig2+ cells can incorporate BrdU at 1–5 days postinjection survival (I) (J, K), Proliferating Sox2+ nuclei and BLBP+ Bergmann glia cells in the Purkinje cell layer of the adult rabbit. (L). Schematic summary: Pax2+ neuronal precursors and multipolar glial-like cell precursors generated in the peripuberal and adult rabbit cerebellar cortex belong to two distinct populations. Sox2+, dividing Bergmann glia could generate Sox2+/Olig2+ precursors that then express Map5 in multipolar cells. Bars: 10 μ m.

Double stainings with DCX or Map5 and BrdU at 15 day survival after the injection revealed that both cell populations in the adult cerebellar cortex were newly generated (Fig. 7L, M, S). Similarly to what observed in peripuberal rabbits, the PSA-NCAM+ and DCX+ bipolar and neuronal cells co-expressed the two markers (Fig. 7E, F), and most of them were also immunoreactive for CRMP4 (Fig. 7G) and the transcription factor Pax2 (Fig. 7O, P). Accordingly, the Map5+ stellate-shaped cells co-expressed Sox2 (Fig. 7T) and Olig2 (not shown). On the other hand, no Pax6+ cell could be detected in the adult cerebellar cortex.

Countings carried out on adult animals (see Table 1) indicated that a further reduction in the number of newly generated cerebellar progenitor cells does occur with respect to the 6-month-old rabbit, with a ratio of 10/1 at the age of 3 years (Fig. 7U). About one half of these cells are neuronal progenitors, mostly localized in the molecular layer (see percentages in Fig. 7U).

Relationships among Cell Proliferation Markers, Transcription Factors, and Blbp in Newly Generated Cells of the Postnatal and Adult Rabbit Cerebellum

In order to get more insights about the origin of the two populations of newly generated cortical cells, cross double stainings among different transcription factors were carried out (Fig. 8). These experiments clearly showed that both Olig2 and Sox2 were never co-expressed with Pax2 (Fig. 8A, B), whereas some Sox2+ nuclei also contained Olig2 (Fig. 8C). These results support the hypothesis that the Pax2+ neuronal cell precursors belong to a distinct lineage with respect to the multipolar, glia-like cells.

Since it is known in mice that Sox2 is expressed in the nuclei of Bergmann glia [28] we used the marker Brain Lipid Binding Protein (BLBP) to visualize cell bodies of Bergmann glia, in order to further investigate this radial glia-derived cerebellar cell type in rabbits. Double labelings showed that virtually all Bergmann glia cells contain Sox2 (Fig. 8D) but not Olig2 (Fig. 8E). In addition, some large Sox2+ nuclei in the Purkinje cell layer did incorporate BrdU at 1–5 days postinjection survival (Fig. 8F), and incorporation of BrdU was also detectable in some Bergmann glia cells (Fig. 8G). These latter cells were able to retain the proliferation marker for at least 2 months (Fig. 8H). Also Olig2+ cells can incorporate BrdU at 1–5 days postinjection survival (Fig. 8I).

Proliferating Sox2+ nuclei and BLBP + Bergmann glia cells were also detectable in the Purkinje cell layer of adult rabbits (Fig. 8J, K).

On the whole, these results indicate that Sox2+ dividing Bergmann glia could generate cell precursors that in the following days will express both Sox2 and Olig2, and then Map5, thus becoming visible as multipolar cells (summarized in Fig. 8L). Furthermore, they confirm that Pax2+ neuronal precursors and multipolar glial-like cell precursors generated in the peripuberal and adult rabbit cerebellar cortex belong to two distinct populations.

KEY WORDS

- **Central nervous system (CNS)**
- **Collapsin response mediator protein-4 (CRMP-4)**
- **External Granular Layer (EGL)**
- **γ -Aminobutyric acid**
- **Golgi II cell**
- **GABA Subventricular Zone (SVZ)**
- **Polysialylated form of the neural cell adhesion molecule (PSA-NCAM)**
- **Proliferative superficial layer (PSL)**
- **Subpial layer (SPL)**

AUTHORS' CONTRIBUTIONS

Conceived and designed the experiments: Luca Bonfanti and Giovanna Ponti. Performed the experiments: Giovanna Ponti. Analyzed the data: Giovanna Ponti and Paolo Peretto. Contributed reagents/materials/analysis tools: Paolo Peretto. Wrote the paper: Luca Bonfanti. Other: Provided logistic support for the housing and treatment of animals: Paolo Peretto.

Chapter 5

Monkeys and Taste Development

Yiwen Wang, Vicktoria Danilova, Tiffany Cragin, Thomas W. Roberts, Alexey Kuposov, and Göran Hellekant

INTRODUCTION

Psychophysically, sweet and bitter tastes have long been considered separate taste qualities, already evident to the newborn human. The identification of different receptors for sweet and bitter taste located on separate cells of the taste buds substantiated this separation. Previous studies in non-human primates, *P. troglodytes*, *C. aethiops*, *M. mulatta*, *M. fascicularis* and *C. jacchus*, suggest that the sweet and bitter taste qualities are linked to specific groups of fibers called S and Q fibers. In this study we apply a new sweet taste modifier, lactisole, commercially available as a suppressor of the sweetness of sugars on the human tongue, to test our hypothesis that sweet taste is conveyed in S fibers. In *M. fascicularis*, lactisole diminishes the attractiveness of compounds, which taste sweet to humans. This behavior is linked to the activity of fibers in the S-cluster. Assuming that lactisole blocks the T1R3 monomer of the sweet taste receptor T1R2/R3, these results present further support for the hypothesis that S fibers convey taste from T1R2/R3 receptors, while the impulse activity in non-S fibers originates from other kinds of receptors. The absence of the effect of lactisole on the faint responses in some S fibers to other stimuli, as well as the responses to sweet and non-sweet stimuli in non-S fibers suggest that these responses originate from other taste receptors.

A series of elegant studies in genetically modified mice show that sweet and umami tastes are dependent on T1R-receptors, that bitter taste is caused by stimulation of T2R receptors, that these two receptors never are found in the same taste receptor cell (TRC) and that the TRC determines the behavioral response [1-7]. One study, for example, showed “that mice engineered to express a bitter taste receptor in “sweet cells” become strongly attracted to its cognate bitter tastants, whereas expression of the same receptor (or even a novel GPCR) in T2R-expressing cells resulted in mice that are averse to the respective compounds” [5]. The authors concluded that the taste receptor cells trigger intake behavior [5].

The above-mentioned discovery of a unique set of taste receptors for the sweet and bitter taste qualities has provided one answer to the long lasting question on how the sweet or bitter taste is created on the tongue. However, it has not solved the problem on how the information from the sweet and bitter receptor bearing taste cells is coded in the taste nerves.

The first suggestion that each of the human taste quality is related to a particular type of taste fiber was based on the recordings of the chorda tympani (CT) and

glossopharyngeal (GN) nerves of cat [8]. It was in many ways a seminal study and presented several observations that later studies confirmed. For example, it identified that different taste fibers respond to different taste qualities and noted that the NG nerve contains a larger proportion of mechanosensitive fibers than the CT. It also correctly connected a lack of response to sucrose with the inability of cats to appreciate sucrose. The reason for this was recently elucidated [9]. The sweet sensitive taste fibers were later discovered in dog [10].

Although the relationship between animal taste fibers and human taste qualities was strengthened by recordings of rhesus monkeys [11, 12], investigators recording from non-primates found a weak relationship between the human taste qualities and types of taste fibers. It is likely that the less than perfect parallel between rodent data and human taste qualities is the reason why the idea that each taste quality is conveyed in a unique group of taste fibers is not universally accepted and was probably one of the reasons why the across-fiber pattern was presented as an explanation of how tastes are coded [13]. According to this theory, every taste fiber contributes to every taste sensation [14-16]. One important consequence of this is that, whereas textbooks of Physiology detail the different TRCs and their specific receptors, there is little or nothing mentioned on the relationship between the responses from the taste receptor specific TRCs and the taste fibers, that is, how taste is coded in peripheral nerves.

One way to demonstrate if there is a connection between a taste quality and a specific group of taste fibers (that does not include any other fiber groups), is to apply a compound that changes or abolishes one of the taste qualities, and then study the accompanying changes in taste fibers. Lactisole is such a compound, because in humans it suppresses the sweet taste of sugars and artificial sweeteners [17], but has no effect on the perception of bitterness, sourness and saltiness [18, 19].

Here we report that lactisole, at concentration used in humans in *M. fascicularis* diminished its preference for sweet and decreased the response of sweeteners in its S fibers without affecting its behavioral response to non-sweet compounds, or the response in any other taste fiber type. These data present further support for our hypothesis that the taste of sweeteners is conveyed by S fibers and that the sweet taste quality is linked to this particular group of taste fibers.

MATERIALS AND METHODS

Animals and Stimuli

Behavioral and electrophysiological data were obtained from five female *M. fascicularis*, weighing 2.1–2.4 kg. Table 1 presents the compounds and concentrations used in the electrophysiological and behavioral experiments. We also used a second set of the same compounds mixed with 1.25 mM lactisole.

Behavioral Experiments

The animals were individually housed and had access to water throughout the behavioral tests. We utilized the two-bottle method (TBP). First, the animals went through a training period during which a graded cylinder with sucrose was left on each cage. When the animals consistently drank from the bottle, we switched to two graded cylinders

on the cage, one cylinder contained 50 ml water, the other 50 ml of sucrose. During this training period the animals learnt to sample the cylinders, whose left or right position was shifted at each occasion. In the next phase the sucrose was replaced with one of the sweeteners shown in Table 1. Since macaques like sweet, the animals rapidly learnt to sample the cylinders and consumed the sweeteners avidly. The training period was followed by tests of the effect of lactisole on the intake of these compounds. Then one cylinder contained the sweetener, while the other contained the same sweetener with 1.25 mM lactisole added. The tests were conducted in duplicate to verify results. We also compared the intake between water and 1.25 mM lactisole. These tests were conducted once a day for 15 min.

Table 1: Stimuli Used in Experiments.

Compound	Electrophysiological	Behavioral
Ace-K	3.5 mM	1.5 mM
Alitame	0.3 mM	-
Ascorbic acid	40 mM	40 mM
Aspartame	5 mM	0.5 mM
Aspartic Acid	50 mM	-
Caffeine	100 mM	-
Citric Acid	50 mM	50 mM
Ethanol	3000 mM	-
Lactisole	1.25 mM	1.25 mM
MSG	70 mM	-
NaCl	100 mM	500 mM
Saccharin	1.6 mM	0.1 mM
SC45647	0.1 mM	0.04 mM
SOA	1 mM	-
Stevioside	0.9 mM	-
Sucrose	300 mM	50 mM
WT Brazzein	0.015 mM	-
Xylitol	800 mM	120 mM
QHCl	5 mM	20 mM

The data on the effect of lactisole on the intake of non-sweet compounds was also obtained by comparing the intake of the same compound with and without lactisole. During the tests with the non-sweet compounds the bottles were left on the cage for 1–2 hr, as otherwise no solution would be consumed. The significance of the difference between the behavioral data obtained with and without lactisole was determined with t-tests: paired two samples for means with 90 percent confidence.

Surgery

The electrophysiological data was obtained from the right chorda tympani proper (CT) of the same animals as in the behavioral experiments. The anesthesia was initiated

with i.m. ketamine, 50 mg/animal. The monkey was then intubated and the anesthesia maintained with halothane (0.7–1.0 percent). Fluid losses were replaced with 5 percent dextrose and lactated Ringer's solution through an i.v. cannula. Body temperature, heart, and respiratory rates, CO₂ in expired air, and O₂ in blood were continuously monitored and recorded. The method to dissect the right CT has been described several times e.g., [20]. In short, an incision was made along the mandibular angle between the rostral lobes of the parotid gland and the mandibular bone. Then the tissue attached to the mandibular angle was dissected through and the caudo-medial side of the pterygoid muscle followed down to its origin at the pterygoid plate of the skull to the CT. The nerve was freed from its junction with the lingual nerve to a point close to the bulla tympani where it is covered by venous sinuses in most cases cf. [21].

Stimulation

The tastants were delivered to the tongue with an open flow system (Taste-O-Matic), controlled by a computer and custom made software. It delivered the solutions at given intervals, over a pre-set time, under conditions of constant flow and temperature (33°C) [20]. The stimulation time was chosen to be long enough to elicit a clear taste response, but as short as possible to obtain as much data as possible, since one never knows when a single fiber may fade. Usually 5 sec stimulation was applied. Between stimulations, the tongue was rinsed for 552 sec with artificial saliva described in [23]. The rinsing time was chosen to minimize cross-adaptation between stimuli. We also never applied two stimuli representing the same taste quality after each other. It should also be noted that the switch from rinse to stimulus and back to rinse was accomplished without any mechanical or temperature artifacts. As a control we repeated stimulation with NaCl, sucrose, QHCl and acid more than once during a cycle.

Electrophysiology; Recording Impulses from More than One Single Fiber in the Same Filament

The nerve impulses were recorded with an isolated differential amplifier and fed into an electrostatic recorder, displayed on an oscilloscope and the computer via a data acquisition card, which digitized the signal at a rate of 50 kHz with a 12 bit analog-to-digital converter. We used Recorder software (Plexon, Inc.) to set up the data acquisition channels, monitor the signals, control the data recording process, and save the whole raw neural signal and binary coded stimuli parameters with time marks. The data was then imported into Offline Sorter (OFS, Plexon, Inc) and NeuroExplorer (Plexon, Inc) for spike sorting and further analysis. The sorting method is based on the feature analysis method, which, using a sophisticated cluster analysis algorithm, separated waveforms according to their shapes and firing patterns. Our approach allowed us to obtain responses of 40 CT fibers in five monkeys.

Analysis of the spike trains included building of time histograms, numerical analysis and scoring of the spontaneous activity and responses to different compounds. As an extra control, we built histograms of the neuronal activity throughout the recording to estimate consistency of the spike trains and fiber responsiveness. The response measure usually used in single fiber recordings is the number of spikes per second over the

stimulation period. The spontaneous activity before a stimulation was deducted from the activity during stimulation.

To detect if there is an organization of the taste fibers, we used hierarchical cluster analysis (SYSTAT). It is a multivariate procedure for detecting natural groupings in the data. The responses to all stimuli were taken into consideration and the analysis considered each stimulus as an independent variable and calculated Pearson correlation coefficients between response profiles. We used correlation measures, because they are not influenced by differences in the absolute values of the responses. The whole matrix of the correlation coefficients was subjected to the analysis and we looked for similarities between whole patterns of response profiles. We used an average linkage method. The result was presented as a dendrogram.

Responses of fibers belonging to the same cluster were first evaluated by two-way ANOVA on ranked data. Differences between cluster's responses with and without lactisole were assessed using t-test. For all tests $P < 0.05$ were considered significant.

The four basic stimuli, NaCl, citric acid, QHCl, and sucrose, were also used to categorize each fiber by its best stimulus. The breadth of tuning (H) was calculated according to the formula [22].

DISCUSSION

The results of Fig. 1 demonstrated that lactisole suppressed the intake of sweeteners but had no effect on the intake of non-sweet tastants or water. The hierarchical cluster analysis used objective statistical methods to classify the taste fibers according to their responses in five clusters shown in Fig. 3. One cluster consisted of S fibers, which responded to sweet compounds. Comparison in S-fibers between the responses of sweet stimuli with and without lactisole showed that lactisole suppressed the response to sweeteners but had no effect on other stimuli or responses in other types of taste fibers (Fig. 2 and 4).

In the following, these results and conclusions will be discussed within the context of data from more than 20 earlier studies. We will discuss:

- a. Possible influence of diet on proportions of taste fiber types in two macaques.
- b. Comparison with earlier data obtained with the sweet taste modifiers miraculin and gymnemic acid (GA).
- c. The parallel between lactisole effects in homo and *M. fascicularis*.
- d. The relationship between the T1 receptors, lactisole and S fibers.
- e. Nerve impulses in S fibers elicited by non-sweet stimuli.
- f. Relationship between S fibers and cell types in the taste buds.

Possible Influence of Diet on Proportions of Taste Fiber Types in Two Macaques

A comparison between the taste fibers of the related, *M. mulatta*, suggests that diet differences are most likely reflected in their gustatory systems. *M. mulatta* is largely a vegetarian, while *M. fascicularis*, the crab eating monkey, also feeds on littoral species cf. [24]. One prediction, based on diet differences, is that, while it is important for

M. mulatta to be able to monitor sodium content in its diet, this may be less important for the *M. fascicularis*, because lack of sodium is not a problem for a species living along the sea. This suggestion is supported by the small proportion of N fibers in *M. fascicularis*, (15 percent), as compared to the 40 percent in *M. mulatta*. The 15 percent Na fibers in *M. fascicularis* parallels the 20 percent, based on the analysis of 14 stimuli in 25 fibers, presented by Sato in the same species [25]. Otherwise there were no major differences in fiber proportions, specificity or maximum response (measured as nerve impulse frequency) between the two macaques.

Comparison with Earlier Data Obtained with the Sweet Taste Modifiers Miraculin and GA

In humans miraculin adds sweetness to all acids and GA blocks all kind of sweetness. We have used miraculin and GA to resolve how taste is coded in peripheral nerves, because, if these compounds exert the same taste effects in our animal models, i.e., add sweet taste to acids after miraculin or block sweetness after GA, these effects must be reflected in taste nerve responses to sweet. In the following we summarize briefly the results of several primate studies.

The first study with miraculin was done in *Cercopithecus aethiops*, an Old-World monkey [26]. The study showed that miraculin almost doubled the response to 0.03 M citric acid in recordings from the whole CT. The effects on the nerve paralleled the effects recorded from the whole human CT nerve [26]. Similar results, together with more than doubled intake of acids, were obtained in later studies of other primates: *M. fascicularis*, *C. aethiops* [27], *Saguinus m. tamarin* [28], a New-World monkey, as well as in *M. mulatta* [29]. This suggested that single fiber recordings from non-human primates could shed light on how sweetness is coded in human taste nerves.

The first single fiber study of rhesus monkey, *M. mulatta*, using miraculin showed that fibers responding to sweet, responded also to acids after miraculin [30]. Otherwise there was no difference in the nerve responses recorded before and after miraculin. After miraculin the monkeys more than doubled their intake of acids, which paralleled the results of adding sucrose to the acids. The study concluded that the increased liking of sour was caused by a response in S fibers, not by a suppression of the response to sour compounds in H fibers [30]. This finding corroborates human sensory data which show that there is no change of intensity of sourness of acids, only an increase of sweetness [31].

Corroborative data was obtained in another primate, the marmoset, *Callithrix j. jacchus*. Thus, following miraculin application to the tongue, the marmosets consumed acids more readily than before and S fibers responded to acids, although they showed no response to acids before. Once again, miraculin exerted no effects on the responses in non-sweet fibers.

As mentioned above, GA blocks sweet taste on the human tongue [32-34]. In human CT nerves GA abolished or diminished the response to sweeteners but not the response to non-sweet compounds [35, 36]. Unfortunately, GA does not suppress sweet taste in monkeys as well as in all non-primates tested, although a number of earlier studies have suggested this [27]. On the other hand, in the phylogenetically to humans

closely related to chimpanzee, CT nerve recordings showed that GA abolished the response to sweet in S fibers, while it had no effect on the responses to any stimulus in non-S fibers. Behavioral data paralleled and supported the electrophysiology [37-39]. When the effect of miraculin in combination with GA was tested on a few chimpanzees' S fibers, the miraculin-induced S fiber response to acids was abolished. This parallels the observation in humans that GA removes the sweetness induced by miraculin on sour compounds.

Finally, S fiber responses have and can be used to assess sweetness of new compounds, as for example, Brazzein, a sweet fruit protein, in which we substituted one or more of its amino acids. Thus, we have used monkey S fiber recordings to determine changes of sweetness of 25 mutants of Brazzein. The results showed a high positive correlation ($r = 0.78$) with the results of assessment of sweetness of the same Brazzein mutants by a human sensory panel [40, 41].

In summary, the results with taste modifiers and sweeteners link the sweet taste quality to fibers of the S-cluster in all non-human primates tested. All these results support the hypothesis that activity in S fibers translates into hedonic positive responses and creates a taste, that with human terminology is best described as sweet [42-46].

Parallel between Lactisole Results in *Homo* and *M. fascicularis*

Here we used the same lactisole concentration as the one that suppressed sweet taste in humans [17, 19]. This shows that lactisole acts within the same concentration range in *M. fascicularis* as in *homo*.

Furthermore, the amount of suppression of each sweetener paralleled in human and in the behavior of *M. fascicularis*. The behavioral data in Fig. 1 showed most suppression of saccharin and sucrose, while aspartame and acesulfame-K occupied the middle ground followed by SC 45647. In our taste panel the intensity of saccharin and sucrose was also most suppressed. Aspartame and Brazzein lost about 50 percent of their sweetness and SC45647 was the least suppressed among the sweeteners we tested (data not shown). This order is the same as reported by Schiffman [17].

Finally, in *M. fascicularis* and humans lactisole does not significantly affect the intensity of salty, sour, and bitter compounds [19]. The responses in the N, H, and Q clusters of Fig. 2 and Fig. 4 support this conclusion. This suggests that lactisole affects the sense of taste of *M. fascicularis* and human in a similar way.

The Relationship between the T1 Receptors, Lactisole and S Fibers

Figures 2 and 4 show that lactisole decreased the responses to sweeteners in S fibers. The literature suggests that lactisole docks to a binding pocket within the trans-membrane domain (TMD) in the human T1R3 receptor [47-50]. The docking interferes with the response to sweeteners. According to Li, this TMD region, consisting of 10 residues, is the same in homo and apes, but A733 is replaced with V733 in rhesus monkey and baboon [51]. The change is probably the same in *M. fascicularis* and is apparently not preventing the effect of lactisole.

At this point it is not known if and how lactisole affects sweet taste in New-World monkeys, but the difference between human and New-World monkeys' TMDs is larger

than between Old-World monkeys and humans, as suggested by data from the squirrel monkey in which T735 and I739 replace A735 and T739 [51]. It is presently not known how far into the evolutionary tree the effects of lactisole reach, but it does not affect the sweet taste of rats [52, 53]. The elucidation of this might give further information on the nature of the T1R receptors.

The continuous trace of impulses in Fig. 5 demonstrates that there was no delay of the suppression by lactisole on the S fiber response to sweet. This suggests that the inhibition of a lactisole on the TMD region occurs basically at the same time as the binding of the ligand to its site on the extra cellular part of the receptor. In some experiments we used Brazzein and recorded a strong suppression of S fiber responses. However, we also noticed that after the lactisole mixture was rinsed away, a response was recorded. We interpret this as the result of a stronger binding to the receptor by Brazzein than by lactisole. This interpretation is supported by the psychophysical observation that the sweetness of Brazzein also lingers when the tongue is rinsed with water.

To summarize, our data suggest that the suppression of sweetness is the result of lactisole interfering with the TMD of the *M. fascicularis* T1R3 and that the sensory effect is conveyed in S fibers.

Nerve Impulses in S Fibers elicited by Non-Sweet Stimuli

Some S fibers respond to non-sweet compounds, although the response is less than to sweet compounds. Figures 2 and 4 show this. If these responses originated from non-sweet receptors, there should be no suppression by lactisole, because lactisole blocks only the sweet receptor T1R3. Figure 4 confirms this conclusion. Consequently, these impulses are not caused by stimulation of sweet receptors. On the other hand, these responses occurred in S fibers. If the impulse frequency is below sensory threshold it will give no taste, if above, it should. Then they should, according to our theory, give rise to a sweet taste. This presents an apparent contradiction. In the following we present possible explanations.

It is well known that the cells of the taste buds are rapidly turned-over, e.g., [54]. One consequence of the continuous turnover is a need to reestablish connections between S fibers and T1R bearing TRCs. Thus, it is not improbable that an S fiber in search for the appropriate cells to synapse with forms temporary connections with non-sweet TRCs, because initial hyperinnervation, followed by degeneration until normal connections are established, is a general feature in generation and regeneration. In the TB, mismatching connections degenerate, while the “right” ones remain, but before this happens, an S fiber could respond to non-sweet stimuli.

It is also possible that the compounds that elicited these responses have a sweet side taste to monkeys that is absent to humans. This is supported by the finding that the taste fibers of chimpanzee are significantly more narrowly tuned to human taste qualities than those of monkey. The fact is that there are almost no S fibers responses to non-sweet stimuli in chimpanzee CT fibers and therefore most likely also in human taste nerves [38, 39, 55, 56]. Thus these non-sweet compounds may have a hedonically positive side taste to *M. fascicularis* that it does not share with chimpanzee or human.

Relationship between S Fibers and Cell Types in the Taste Buds

Besides undifferentiated peripheral cells and basal cells, it is generally thought that the mammalian taste bud contains three major types of cells [57-59]. The largest group consists of glia cells, labeled type I cells by most investigators. They show no synaptic structures. The second type, labeled type II cells, is the TRCs. Some of these bear either T1R or T2R receptors and contain many of the constituents of the intracellular transduction components, such as gustducin and could be expected to synapse with nerves. However, they show no or few synapses with nerve endings in monkey [60] as well as in mouse and rat [57, 58, 61-70].

It seems that the “missing” presynaptic-like structures instead are present on a third cell type, type III. Some investigators claim that type III cells serve as the intermediate cells and receive input from more than one type II cell [71]. Thus, based on recordings from tongue slices with taste buds or patch clamp recordings of individual taste bud cells, they report that type III cells responded to many taste qualities [72, 73]. If this is the only manner that taste fibers are activated, the results should be that S fibers respond to several taste qualities,

However, we and other investigators have recent data that suggests that TRCs can directly activate taste fibers, by-passing the type III link [74, 75]. We found in mice with a combination of genetic, morphological, behavioral and *in vivo* and *in vitro* electrophysiological techniques, that adenosine 5'-triphosphate (ATP) released from the TBs could serve as a transmitter in the TB and that knocking out the receptors for ATP, the ionotropic purinergic receptors, (P2X2 and P2X3), eliminated the taste nerve response and strongly decreased the behavioral response to sweet and bitter [74].

Later Yoshida *et al.* added more support to this mechanism, when they identified gustducin in the TRCs containing ATP [75]. (Gustducin is not present in type III cells). Further, they showed that the amount of ATP increased in a firing rate-dependent manner to stimulation with saccharin, quinine, or glutamate. These findings suggest that the TRCs can directly activate taste nerves without involving any type III cells. This would allow a direct coupling between the T1R receptor bearing type II cells and S fibers.

Furthermore, a recent study in mice shows that the breadth of tuning between CT fibers and fungiform TRCs was not significantly different [76]. This would not have been the case if information from several types of taste receptors converged on the same CT fiber, because then the breadth of tuning for fibers would differ from that of taste cells. The only way to explain this is a more or less a one-to-one connection in regard to taste quality between TRCs and taste fibers.

Further support that taste qualities are conveyed separately, is offered by a recent study, which showed that neurons in the solitary tracts (NTS) respond selectively to bitter taste [77]. Even more interesting is that some of these NTS cells responded, not only uniquely to the bitter taste quality but also, within the bitter taste quality, to only one of the bitter stimuli used [77].

The above, does not refute an important role of the type III cells, because there are other neuropeptides and transmitters within the taste buds and the mechanisms observed by them [72, 73] may play a modulatory role or may be crucial for intragemmal

communication among the different types of cells in the TB as suggested by, for example, [78-81].

In summary, the data presented here suggests that the S and Q fiber clusters give rise to the sweet and bitter taste qualities respectively. Our data in regard to sweet is particularly strong and has withstood repeated tests in many species.

RESULTS

Behavior

Figure 1 shows the result of the two-bottle preference (TBP) tests. The left staple in each pair display the average consumption of the compound without lactisole, and the right ones with lactisole. Asterisks denote significant difference of the intake at 90 percent confidence limits.

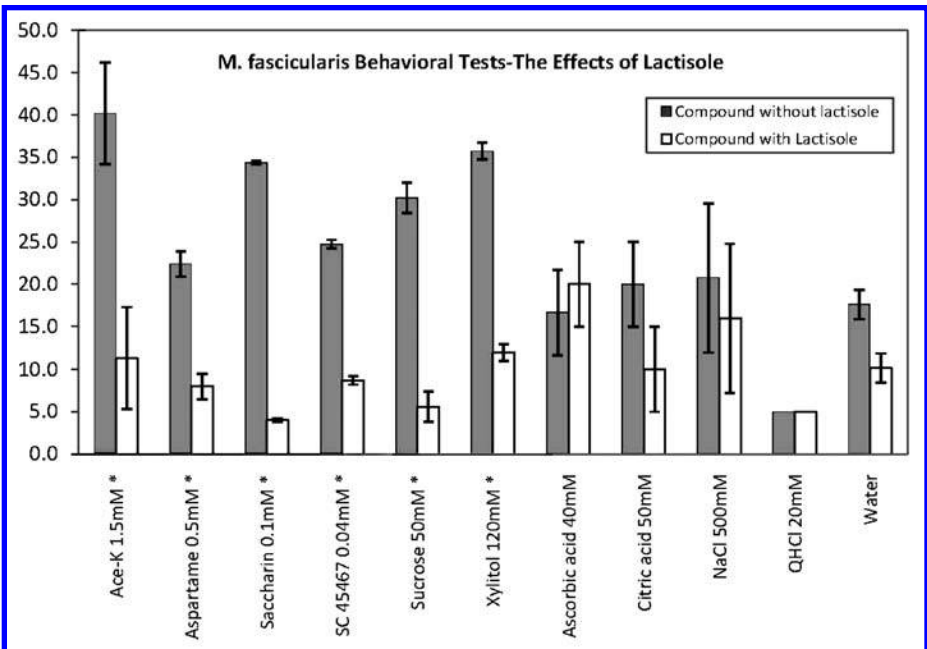


Figure 1: Results of two-bottle preference tests with one bottle with the tastant and the other with 1.25 mM lactisole added to the tastant. Each bottle contained 50 ml. It is evident that presence of lactisole made the sweetener less attractive, but had no significant effect on the intake of the non-sweet compounds. Error bars SE. The asterisk* signifies a significant difference in intake.

It is evident that lactisole in the sweeteners significantly lowered the intake, while it had no effect on the non-sweet compounds. Its largest effect was on the intake of saccharin and sucrose, followed by about equal effect on acesulfame-K, xylitol, aspartame, and SC 45467. There was no significant difference in the intake between water and 1.25 mM lactisole in water, or any of the non-sweet compounds with and without lactisole. Thus the difference in intake was only significant for the sweeteners.

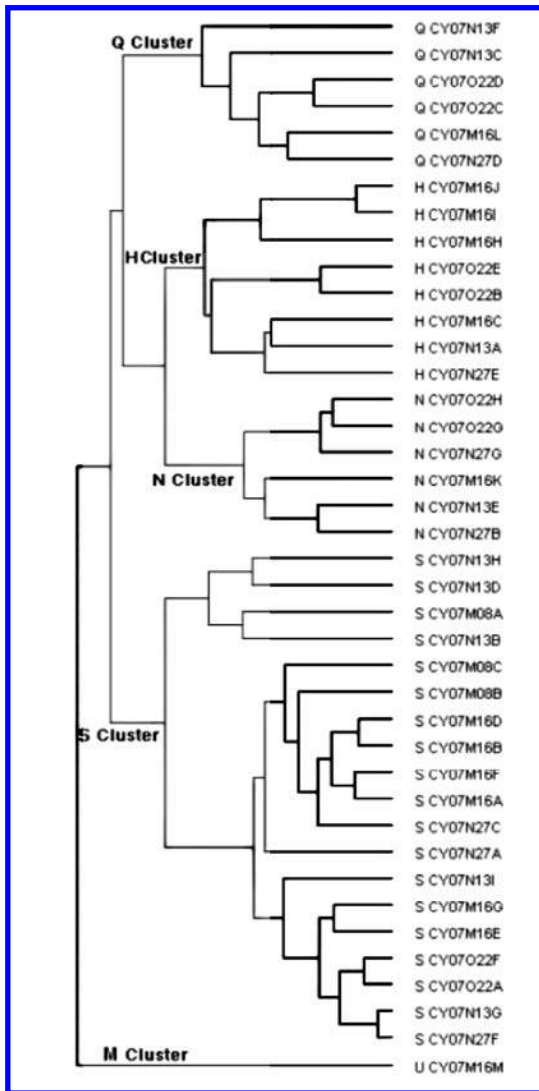


Figure 3: Results of hierarchical cluster analyses of the response profile of 40 CT taste fibers. Intercluster similarity was measured with the Pearson correlation coefficient, and the cluster analysis proceeded according to the average linkage method. Number of response categories of the fibers on the basis of their responses to the basic solutions is listed on the right. Q, H, N, S and M stand for QHCl, citric acid-, NaCl, sucrose, and MSG-best fibers.

The N cluster consisted of fibers that responded best to NaCl. Three of the fibers showed also a response to the acids and two of these fibers were clearly also stimulated by lactisole and to some extent by the sweeteners. It is likely that their response to sweetener/lactisole originates mostly from the effect of lactisole. Their breath of tuning (H), which gives a numerical value on how specific a group of fibers is, was 0.64, SD 0.05.

The H cluster consisted of acid-best fibers but five fibers responded also to the MSG stimuli. The breath of tuning was 0.63, SD 0.1, which indicates that they were about as specific as the fibers in the previous cluster.

The Q cluster fibers were predominantly responding to QHCl and to SOA, although acids and three sweeteners, saccharin, stevioside, and acesulfame-K, gave a response in two fibers. This may be explained by the observation that the taste of both saccharin and acesulfame-K includes a bitter component and stevioside has an additional licorice taste. As a group, the Q fibers were slightly more specific than the previous fibers ($H = 0.55$, SD 0.05).

The S fibers were more specific than any other ($H = 0.4$, SD 0.06) although the dendrogram suggests that these fibers could be composed of three subgroups of which the upper one consisting of 4 fibers was less specific than the other two. Although it may not be visible from Fig 2, in all 19 S fibers, the response to sucrose with lactisole was smaller than to sucrose alone. This is further shown in Fig. 4.

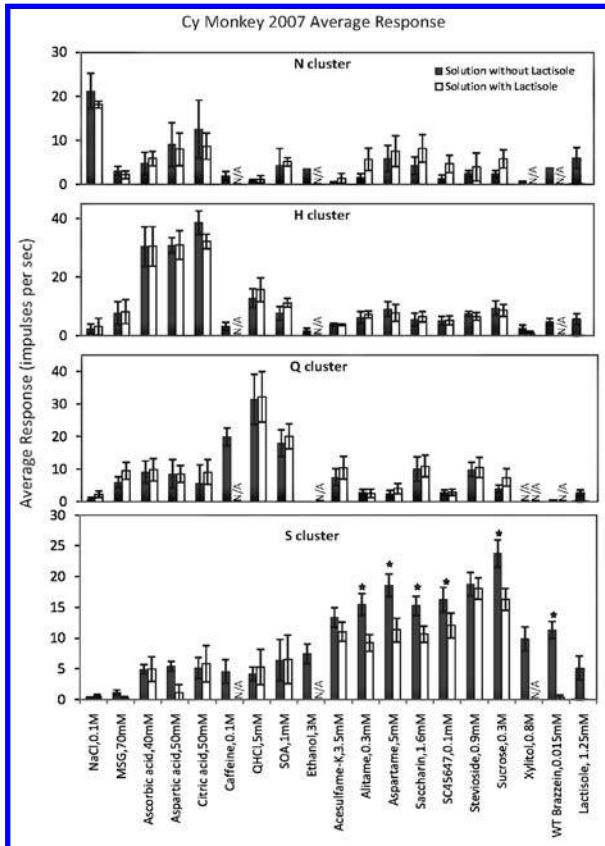


Figure 4: The average response profiles from the top the N cluster, H cluster, Q cluster, and S cluster. Error bars are SE. Dark columns, the tastants without lactisole, open columns, tastants with 1.25 mM lactisole added. Asterisks denote a difference between the two columns at a significance level of > 90%. Only the responses to sweeteners in the S fiber cluster were significantly suppressed by the addition of lactisole.

Dendrogram

Figure 3 presents the results of hierarchical cluster analysis of the 40 single taste fibers. We used the responses to all stimuli without lactisole. Listed on the left of the dendrogram is each fiber's response category and on the right its identity number. The cluster analysis clearly separated N, H, S, and Q clusters. The analysis identified 6 fibers in the N fiber cluster, 8 H fibers, 6 Q fibers, and 19 S fibers.

As shown in Fig. 2, fiber CY07N13E responded better to citric acid than NaCl. Therefore one might suspect that it is falsely classified into the N cluster. However, the cluster analysis only calculates the Euclidean distance between the fibers and because the result is not normalized, this fiber is closer to the N fibers than to any other group. In addition, the analysis placed another fiber (U CY07M16M) in an additional fifth cluster, which we labeled M based on its response to MSG alone or mixed with GMP. It was unique in its singular response to the stimuli representing the umami taste quality, MSG and MSG with GMP.

Effects of Lactisole

Figure 4 shows the effect of addition of lactisole on the responses of each of the above clusters. Only the data of fibers tested with the same stimulus with and without lactisole are included. Thus, the left column in each pair shows the response to the tastant alone, while the right column displays the response when lactisole had been added to the stimulus.

Error Bars are SE

The plot shows that the addition of lactisole did not significantly suppress the response to any stimulus in the N cluster. Lactisole in itself gave a response in the N fibers that may explain the increase of the response to some of the tastants with lactisole. In the H and Q cluster lactisole did not change the responses to any stimuli.

The data from the S cluster shows three features, relevant to the hypothesis that S fibers convey sweet taste. First, all S fibers responded to all the sweeteners tested. This indicates that they received input from the same receptor type. Second, lactisole suppressed the response of all sweeteners, although the effect was not significant in acesulfame-K and stevioside. On the average the responses of the lactisole containing sweeteners was 70%, SD 6, of the responses of stimulation with the sweetener alone. Third, lactisole did not suppress the responses of the non-sweet compounds. Thus, its effect was limited to the responses of sweeteners in S fibers.

Effect of Lactisole on Temporal Pattern or Temporal Intensity

Figure 5 presents two examples of the effect of lactisole on the temporal pattern or time intensity (TI) of a non-S fiber (Q fiber CY07N13F) and an S fiber (CY07M08A). The impulse activity of each fiber is displayed during 5 sec of rinsing with artificial saliva, followed by 5 sec of stimulation, and then by 10 sec of renewed rinsing with the artificial saliva. The upper trace in each pair shows the response without lactisole and the lower trace the response with lactisole added to the stimulus.

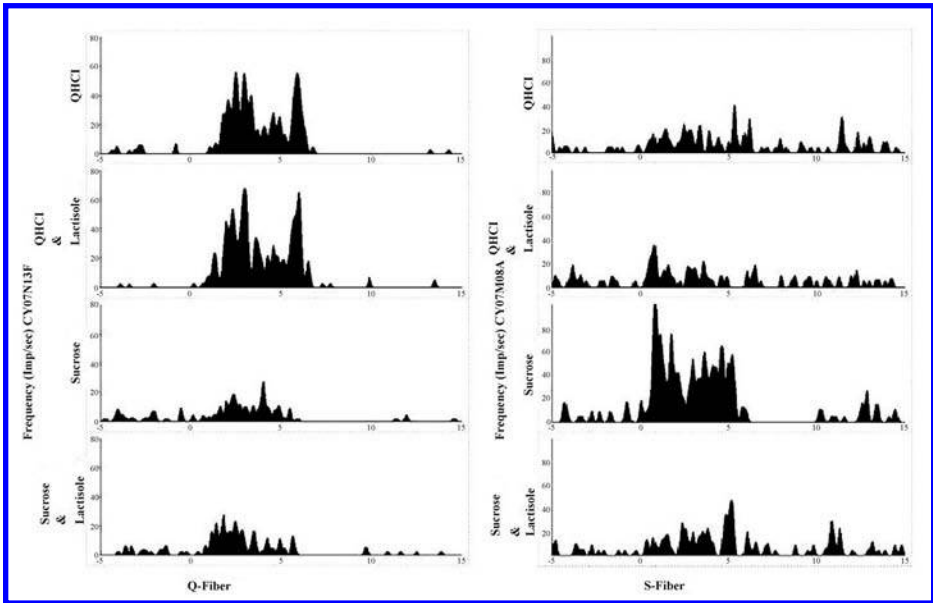


Figure 5: It presents two examples of the effect of lactisole on the temporal pattern also called time intensity (TI) of the responses of a non-S fiber (Q fiber CY07N13F) and an S fiber (CY07M08A). The impulse activity of each fiber is displayed during 5 sec of rinsing with artificial saliva, followed by 5 sec of stimulation and then by 10 sec of renewed rinsing with the artificial saliva. The upper trace in each pair shows the response without lactisole and the lower trace the response with lactisole added to the stimulus. Only in the S fiber the response to sucrose was suppressed by lactisole.

Several features should be noted. First, while sucrose gave a large response in the S fiber and Q HCl in the Q fiber, Q HCl also elicited a faint response in the S fiber and sucrose in the Q fiber. Second, only the response to sweet in the S fiber was diminished by lactisole addition; there was no effect by lactisole on the response to Q HCl or sucrose in the Q fiber or by lactisole on the response to QHCl in the S fiber. Third, the suppression of the sucrose response of the S fiber was visible in the nerve activity during the whole stimulation period and not only in part of it, for example, in the phasic or the tonic part.

Multidimensional Scaling

Based on a correlation matrix of the stimuli, we performed multi-dimensional scaling for compounds with and without lactisole. The spatial representation of the similarities among 16 stimuli without lactisole is shown in the upper diagram of Fig. 6. The stress value is 0.047. The top plot shows that the sweeteners before lactisole formed a tight group. The lower plot in Fig. 6 shows that adding lactisole to the compounds shrunk the distance between the sweet group and the non-sweet group. This suggests that the nerve response to sweet was less different from that of non-sweet compounds when the sweeteners contained lactisole. The interpretation could be that lactisole diminished the taste difference between sweet and non-sweet tastants.

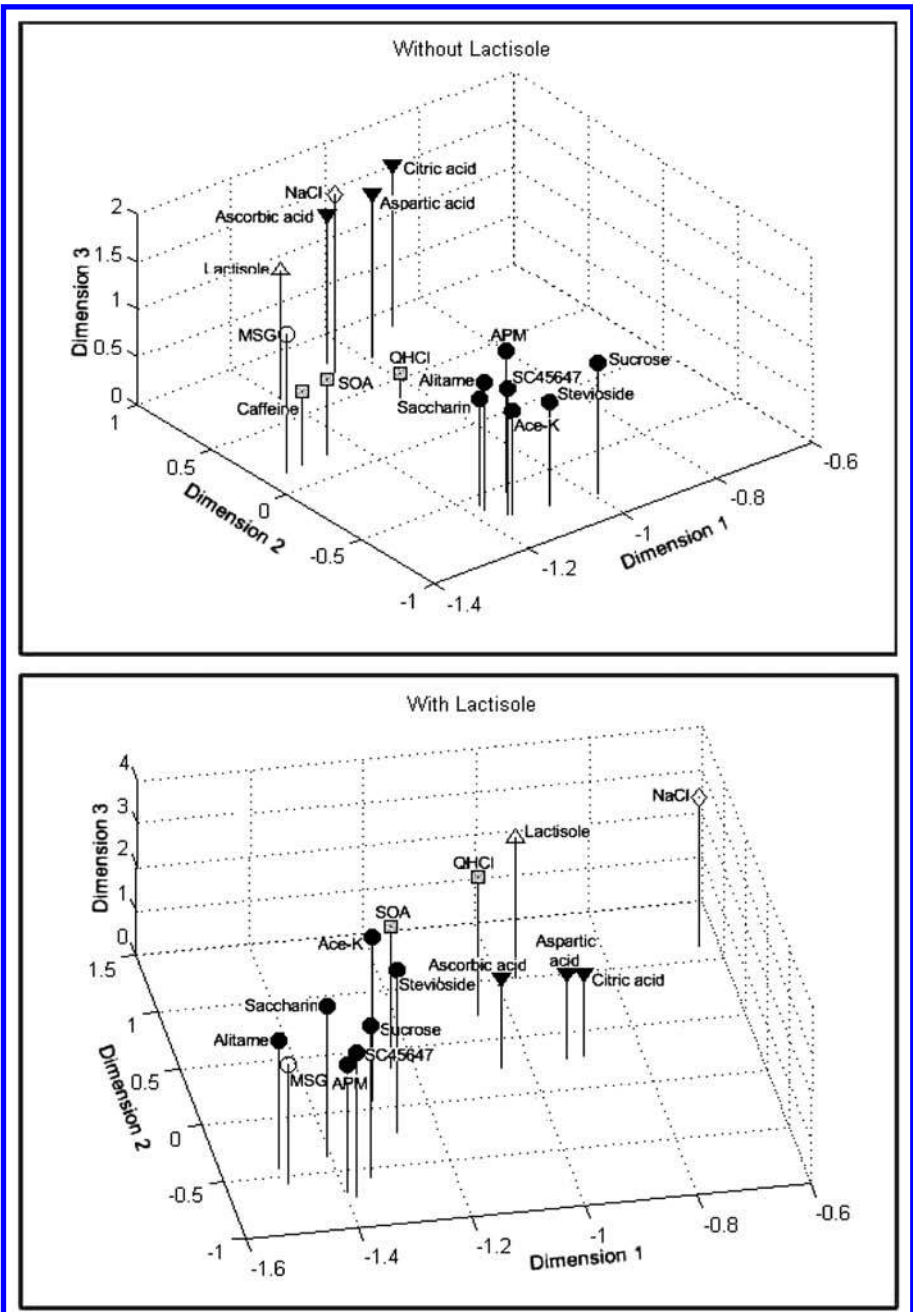


Figure 6: Distribution of 16 tastants in a 3-D space resulting from multi-dimensional scaling. The distribution was calculated with Pearson correlation coefficient between stimuli across 40 CT fibers. The stress value is 0.047. The top plot shows that the sweeteners before lactisole formed a tight group further away from the non-sweet stimuli than after lactisole. The results suggest that lactisole diminishes the taste difference between the sweeteners and other tastants.

CONCLUSION

In summary, the data presented here suggest that the S and Q fiber clusters give rise to the sweet and bitter taste qualities respectively. Our data in regard to sweet is particularly strong and has withstood repeated tests in many species

KEY WORDS

- **Chorda tympani (CT) nerves**
- **Glossopharyngeal (NG) nerves**
- **Gymnemic acid (GA)**
- **Miraculin (MA)**
- **NTS cells**
- **Open flow system (Taste-O-Matic)**
- **S and Q fibers**
- **Sweet cells**
- **T1R3 monomer**
- **T1R2/R3 receptors**
- **Two-bottle method (TBP)**
- **Taste receptor cell (TRC)**
- **Trans-membrane domain (TMD)**

AUTHORS' CONTRIBUTIONS

Tiffany Cragin collected the behavioral data, conducted the human taste experiments and participated together with Yiwen Wang in the statistical analyses and production of illustrations. Yiwen Wang was responsible for the software development and data recording during electrophysiological experiments and participated together with Tiffany Cragin in the statistical analyses and the production of illustrations. Vicktoria Danilova shared with Göran Hellekant the surgery and single fiber dissections. Göran Hellekant planned the project, did surgery, oversaw the data collection and processing, planned the illustrations and wrote the manuscript. Alexey Kuposov served during the acute experiments with producing stimuli and other necessities. Thomas W. Roberts constructed the hardware for recordings, built the stimulation equipment and maintained and renewed it. Göran Hellekant planned the project, did surgery, oversaw the data collection and processing, planned the illustrations and wrote the manuscript.

ACKNOWLEDGEMENTS

This research was supported by NIH grant R01 DC006016 to G. Hellekant. The study had been approved by the university of Minnesota Animal Care committee IACUC Code Number: 0712A23801.

Chapter 6

Intermittent Claudication in Canines

Alan MacInnes and James A. Timmons

INTRODUCTION

Patients suffering from Intermittent Claudication (IC) experience repeated periods of muscle contraction with low blood flow, throughout the day and this may contribute to the hypothesized skeletal muscle abnormalities. Our aim was to generate this basic physiological data, determining the “normal” response of healthy skeletal muscle tissue utilizing a canine gracilis model ($n = 9$), the muscle was stimulated to contract (5 Hz) for the 10 min periods (separated by 10 min rest) under low blood flow conditions (80 percent reduced), followed by 1 hr recovery and then a fourth period of 10 min stimulation. During the first period of contraction, adenosine triphosphate (ATP) was reduced by ~30 percent. During this period there was also a 10 fold increase in muscle lactate concentration and a substantial increase in muscle lactate and ammonia efflux. Subsequently, lactate efflux was similar during the first three periods, while ammonia efflux was reduced by the third period. Following the 1 hr recovery, muscle lactate and phosphocreatine concentrations had returned to resting values, while muscle ATP remained 20 percent lower. During the fourth contraction period, no ammonia efflux or change in muscle ATP content occurred. Despite such contrasting metabolic responses, muscle tension and oxygen consumption were identical during all contraction periods from 310 min.

The IC is the symptomatic manifestation of peripheral vascular disease, suffered by millions of patients worldwide. The IC is thought to occur when skeletal muscle blood flow fails to increase adequately during walking [1, 2] severely limiting the quality of life of the patient [3]. The effectiveness of current treatment strategies for IC is dismal [4-6]. Arguably, this reflects both the current inadequacies of the available pharmaceutical medications [4] and the lack of exercise rehabilitation programs [6]. In order to select potential therapeutic targets, we must establish a greater understanding of the physiological responses to repeated periods of skeletal muscle contraction under low blood flow conditions in both health and disease. In both preclinical models and in humans, accelerated muscle fatigue and increased “anaerobic” ATP regeneration is a feature of limb ischemia [7-11]. This, in turn, temporally relates to muscle pain and fatigue experienced by patients [2, 12-14]. Evidence for underlying muscle damage and degeneration in ambulatory IC patients has been presented [15, 16] but such observations may reflect co-morbidities and have not been directly linked to IC symptoms. In the studies by Holm *et al.* [13] muscle tissue from IC patients demonstrated an increased mitochondrial enzyme capacity. In patients with resting ischemia (and loss of mobility) this increased enzymatic activity was no longer observed [13]. To date Type I muscle fiber content has ranged from 35-70% and markers of mitochondrial

capacity have been elevated, unchanged or reduced; when compared to age matched controls. Overall, the characteristics of muscle tissue obtained from the IC patient gives little clue to the underlying pathophysiology of IC.

When studying muscle metabolism in IC patients, the impact of repeated period of contraction on muscle metabolism has never been considered. Furthermore, no study has examined healthy skeletal muscle during repeated periods of contraction with low blood flow and hence the “normal” physiological responses of healthy muscle tissue, under such conditions, have not been defined. Short cycles of complete ischemia are known to induce a protective response to subsequent prolonged ischemia (preconditioning) [1, 17]. There is little evidence that ischemia-reperfusion injury contributes to the symptoms of IC. It is, however, plausible that the metabolic response to contraction adapts during periods of intermittent walking and that this alters the metabolism and function of the muscle. In the present study we characterize for the first time, the metabolic responses of skeletal muscle, exposed to repeated periods of contraction with low blood flow, using the canine gracilis model [18] which reflects the metabolic responses observed in human skeletal muscle under similar circumstances [9]. We were particularly interested in characterizing muscle ATP catabolism and ammonia production. In humans, a 1 hr recovery period between 2–3 min maximum knee extension exercise bouts (with normal blood flow) was sufficient to attenuate muscle ammonia production [19]. This observation suggested to us that a 1 hr recovery period may be sufficient to observe an altered regulation of ATP homeostasis. Our investigation revealed that skeletal muscle protects the ATP pool 1 hr following three periods of “low flow” contraction, and this is associated with a complete lack of ammonia efflux from the muscle tissue.

MATERIALS AND METHODS

Surgical Procedures

After an overnight fast, each female dog (Animal Breeding Unit, PGRD UK, $n = 9$) was anaesthetized with sodium pentobarbitone (45 ± 1 mg/kg body mass (bm) followed by continuous infusion at 0.10 ± 0.01 mg/kg/min i.v. (Sagatal, Rhône Merieux, Harlow, UK). The trachea was intubated and the dogs were artificially ventilated (24 cycles/min, tidal volume = 13–15 ml/kg). The right brachial artery was cannulated, and systemic blood pressure was recorded using a pressure transducer and chart recorder. The left brachial artery and vein were cannulated for collection of arterial blood samples for monitoring of blood parameters (e.g. pH, hemoglobin (Hb), PCO_2 , and PO_2) using the Radiometer ABL 625GL (Copenhagen) and venous infusion of heparin, bicarbonate, or saline. A gracilis muscle was vascularly isolated, leaving only the main arterial and venous blood flows intact. The distal tendon of the muscle was attached to an isometric force transducer (Grass FTC 10, Quincy, Medfield MA, USA). The popliteal artery was catheterized for recording gracilis muscle perfusion pressure. Heparin was infused following surgery, (Multiparin, 1 U/kg/bm/min) for the duration of the experiment. The femoral artery supplying each gracilis muscle was cannulated proximally and distally and attached sequentially to a perfusion pump (Minipuls 3, Gilson, Villiers le bel, France). The muscle blood flow was fixed by setting the perfusion pump at 6.1 ± 0.1 ml/min. We have previously established this as being similar to the resting flow

rate in the gracilis muscle [18]. This flow rate was maintained for the duration of the experiment and equates to ~20 percent of the normal flow observed when this muscle was stimulated to contract with the blood supply intact at 3 Hz twitch. All experiments were carried out in full accordance with the United Kingdom Home Office Animals (Scientific Procedures) Act of 1986, and approved by the local ethics committee.

Muscle Stimulation Parameters and Blood Sampling

The resting length of the muscle was altered to obtain a standard tension of ~400 g/100 g muscle. After a 20 min equilibrium period, baseline values were collected (blood samples and muscle biopsies) and then muscle contraction was induced via electrical stimulation of the obturator nerve (Grass S88 stimulator, Quincy, Medfield, MA, USA). Square-wave impulses of 0.1 msec duration, 5 Hz frequency and a supramaximal voltage (10 V), resulting in complete muscle fiber recruitment and peak twitch tension, were applied for three periods of 10 min (with 10 min recovery) followed by 1 hr recovery and then a fourth 10 min period of contraction (as shown in Fig. 4). Arterial blood samples were taken throughout the experimental period (for monitoring the stability of the animal) and did not demonstrate any significant variation over time. Venous blood samples were obtained to calculate oxygen uptake and ammonia and lactate efflux. The difference between arterial concentration and venous concentration was used, along with the blood flow parameter, to make such calculations. Venous samples were obtained at rest, just prior to the onset of contraction, and at 3 min after the onset of contraction and 6 min after the cessation of contraction. In each case, venous sampling took appropriately 30 sec.

Metabolite Analysis

Blood gases, whole blood lactate and glucose were measured using the Radiometer ABL 625GL (Copenhagen). The analyzer was calibrated on a daily basis according to the manufacturer's instructions. Plasma ammonia was determined in 1 ml blood samples treated according to the standard instructions (Ammonia-Test Wako, Wako Chemicals, Osaka, Japan), and indophenol was measured using a spectrophotometer at a wavelength of 630 nm (UV-2400PC, Shimadzu, Tokyo, Japan). All biopsy samples were stored in liquid nitrogen. Subsequently, a portion was freeze dried, dissected free from visible connective tissue and blood, powdered and extracted in 0.5 M perchloric acid containing 1 mM EDTA. Following centrifugation, the supernatant was neutralized with 2.2 M KHCO_3 and used for determination of ATP, Phosphocreatine (PCr), creatine, and lactate as previously described [18] with the exception that a 96-well plate format was utilized using a Spectromax Plus (Molecular Devices). All data were reported as mean \pm SE. The analysis of variance was utilized to determine significant changes with respect to time, followed by post-hoc significance testing. A paired t-test was used to compare the intramuscular metabolic differences. Significance was accepted at the 5 percent level.

DISCUSSION

There is extensive information on the functional and biochemical characteristics of skeletal muscle in response to a single period of contraction under conditions of

low blood flow [10, 20, 21]. Responses to intermittent “cycles” of skeletal muscle contraction under conditions of low blood flow have not previously been reported. Our first new observation is that muscle ATP concentration was protected during the fourth period of contraction while the lack of ammonia release indicates that flux through Adenosine monophosphate (AMP) deaminase was dramatically attenuated. This altered biochemical response is particularly apparent if the second and fourth periods are contrasted. In both the cases presented contractile parameters were identical yet ammonia efflux was highest during the second period and completely attenuated during the fourth period of contraction.

During intense muscle contraction reamination of inosine monophosphate (IMP) to AMP is thought to be slow [22] and recovery of the adenine nucleotides is thought to be constrained to the post exercise period. During moderate intensity contraction, reduced blood flow to the muscle accelerates ATP degradation [18] to levels observed during supra-maximal exercise [23]. This results in otherwise “low intensity exercise” having an increased metabolic cost of recovery. The determinants of recovery following ischemia reflect the oxidative capacity of the muscle tissue, including oxygen delivery, but may also include muscle ribose-5-phosphate availability [24]. In the present study we directly assessed ATP degradation during the first and fourth periods of contraction and assessed flux through AMP deaminase indirectly, during each bout, by measuring ammonia efflux. Graham *et al.* [25] demonstrated that muscle ammonia efflux reached a maximum of ~300 μmol per min during intense one legged cycling, reflecting the net adenine nucleotide catabolism in the muscle. In the present study a much higher peak ammonia efflux was observed (1500 $\mu\text{mol min}^{-1} 100 \text{ g}^{-1}$ versus 314 $\mu\text{mol per min per leg}$), indicating that a relative lack of blood flow may be a more potent stimulus to adenine nucleotide loss than the intensity of muscle contraction (absolute ATP turn-over).

Mechanisms Explaining a Reduced Ammonia Production

Given the short recovery period between the first two periods of contraction, pre-contraction ATP is likely to have been lowered prior to contraction second period yet ammonia efflux was extremely high. This indicates that the 20 percent reduction in resting ATP, prior to the fourth period of contraction, cannot explain the complete lack of ammonia production. The PCr utilization was modestly reduced during the fourth period of contraction, when compared with the first period ($p = 0.051$). Although not substantial, it is suggestive of a more rapid increase in ATP derived from oxidative phosphorylation [8-11, 26]. A more rapid increase in the rate of oxidative ATP regeneration ensures that ATP homeostasis is better maintained [10]. Given that there was a 1 hr recovery period, prior to the fourth period of contraction, our data also provides an indication that muscle metabolism is altered for a substantially longer period of time following prior exercise than presently assumed.

Alterations in substrate utilization can influence muscle pH during contraction, and hence the activation of AMP deaminase, see [27]. There was a substantial reduction in muscle lactate accumulation and a measurable reduction in muscle lactate efflux. The reduced lactate production indicates that glycolytic flux was attenuated and hence (Table 2 and Fig. 3) it is reasonable to suggest that muscle pH did not decline

as much during the fourth period of contraction when compared with any of the first three periods of contraction. Given that flux through AMP deaminase, as assessed by muscle ammonia efflux and the change in muscle ATP, was essentially zero during the fourth period of contraction, it is unlikely that the attenuation of muscle acidosis fully explains the altered regulation of ATP catabolism but clearly it could have contributed. Less accumulation of substrate for AMP deaminase or specific inactivation of AMP deaminase, both could explain stabilization of the adenine nucleotide pool and reduced ammonia production [27].

Although there are no previous studies addressing the metabolic response of skeletal muscle to repeated contractions with low blood flow, there are a limited number of intermittent exercise studies (with high blood flow) which can be compared with the present data [19, 28]. During four bouts of ~3 min of isotonic contraction with 3 min of rest between each successive bout, there was a successive reduction in muscle pH and PCr utilization [28]. In this case, it is plausible that the reduced PCr utilization reflected greater resting muscle acetyl group availability [29]. Graham *et al.* [19, 25] provide insight into the impact of prior exercise on ammonia production. They demonstrated that a period of exhaustive exercise carried out 24 hr prior to 3 min intense contraction attenuated muscle ammonia production by ~50 percent while the total work done was similar [19]. This effect was independent of muscle glycogen status, which remained above 200 mmol kg⁻¹ dry muscle tissue, under all conditions. It is therefore conceivable that the metabolic response to walking, in IC patients, could be greatly altered by earlier walking activity, impacting on the outcome of any clinical assessment and almost certainly complicating the “disease” phenotype when studied in a laboratory setting.

The ATP loss can exceed 40 percent even during a single period of contraction with low blood flow [20] and thus the cessation of ammonia efflux during fourth period is highly unlikely to be a consequence of the 20 percent lower baseline ATP. Under the present experimental conditions amino acid deamination would represent only a small percentage of the observed muscle ammonia efflux [30, 31]. It could also be suggested that glutamine synthetase (GS) may have consumed ammonia, for example, during the fourth period of contraction. Again, given that the rate of ammonia production was observed, we feel that it is highly unlikely that GS activity is relevant for our observations. Finally, reduced ammonia production by AMP deaminase may have also reflected the activation of alternative routes of AMP metabolism, including 5' nucleotidase. The maximal capacity of 5' nucleotidase is much lower than AMP deaminase, and since ATP did not significantly decline during the fourth period of contraction we also feel that this is not a likely explanation for the attenuation of ammonia production and stabilization of muscle ATP.

RESULTS

General Model Characteristics

Blood flow was fixed at 15.7 ± 0.6 ml min⁻¹ 100 g⁻¹ muscle tissue throughout the study, reflecting a normal resting value but an 80 percent reduction in the value observed during contraction. Resting muscle tension averaged 444 ± 33 g 100 g⁻¹ muscle and was fixed prior to each contraction period. Resting muscle perfusion pressure ranged from 95/11 mmHg (pre-isolation perfusion pressure was ~125

mmHg). During contraction, muscle perfusion pressure ranged from 5559 mmHg. Arterial hemoglobin concentration was 13.8 ± 0.2 g dl and remained stable during the entire period of study (typically 8–10 hr). Control of ventilation, using a respiratory pump and room air, ensured that arterial saturation (SO_2 percent) was maintained at $\sim 100\%$, while arterial PCO_2 was stable at 45 ± 1 mmHg for the duration of the study. Arterial ammonia concentration varied between 16 and 24 μM and arterial glucose concentration averaged 6.5 ± 0.1 mM, both remaining stable throughout the study. Arterial lactate concentration was 1.2 ± 0.1 mM and was also stable for the duration of the experiment. Arterial creatine kinase activity (SI unit/L) varied from $40 \pm 559 \pm 19$ during the course of the study with no clear pattern with respect to time. There was no evidence of any muscle damage at any stage of these experiments. Additional experiments revealed that during 12 hr of pump mediated perfusion, peak muscle force development, checked utilizing a short burst of 5 Hz stimulation, was consistent over time, further demonstrating the stability of the model (data not shown).

Muscle Contractile Function and Oxygen Consumption

During the first period of contraction, peak tension was 3.38 ± 0.2 kg 100 g^{-1} muscle tissue. During the second and third periods of contraction, peak tension was reduced to 1.75 ± 0.1 and 1.64 ± 0.1 kg 100 g^{-1} muscle tissue, respectively. During the fourth period, peak tension recovered to 1.89 ± 0.2 kg 100 g^{-1} muscle tissue. Time to achieve peak tension was 27.0 ± 1.1 sec during first period 73.9 ± 3.1 sec, 87.0 ± 2.0 sec and 75.1 ± 4.9 sec during each successive contraction period. The force rapidly declined during the first minute of contraction during the contraction first period (1.34 ± 0.08 and 0.84 ± 0.08 kg 100 g^{-1} muscle tissue at 3 min and 10 min of contraction respectively). During contraction in the second, third, and fourth periods, muscle tension production did not differ from contraction in the first period at the 3 min time point (Table 1) or at the end of the 10 min stimulation period (0.84 ± 0.08 , 0.81 ± 0.06 and 0.83 ± 0.07 kg 100 g^{-1} muscle tissue respectively). The lack of difference in muscle tension production at 3 min, across stimulation periods, is consistent with the muscle oxygen consumption data from this time point which indicates a similar metabolic rate (Table 1 and Fig. 1).

Table 1: Represents metabolic and function data during the third and fourth minute of contraction.

	Peroid 1	Peroid 2	Peroid 3	Peroid 4
VO_2	2.3 ± 0.17	2.3 ± 0.16	2.3 ± 0.18	2.4 ± 0.18
Art $[\text{O}_2]$	17.9 ± 0.28	17.9 ± 0.3	17.9 ± 0.3	17.6 ± 0.4
Art $[\text{CO}_2]$	48.5 ± 0.6	48.5 ± 0.4	48.4 ± 0.5	47.8 ± 0.7
Ven $[\text{O}_2]$	3.69 ± 1.02	3.29 ± 0.86	3.19 ± 0.92	2.65 ± 0.73
Ven $[\text{CO}_2]$	64.9 ± 1.4	59.0 ± 0.76	58.6 ± 1.16	58.9 ± 1.37
Ven Sat %	18.8 ± 5.3	16.8 ± 4.5	16.3 ± 4.8	14.2 ± 4.1
Tension	1.34 ± 0.08	1.28 ± 0.09	1.20 ± 0.11	1.33 ± 0.12
Ammonia efflux	843 ± 237	1413 ± 217	646 ± 135	-175 ± 76
Lactate efflux	38.9 ± 4.6	46.2 ± 4.9	41.4 ± 4.3	22.0 ± 4.3

Muscle oxygen consumption (VO_2) units are $\text{ml O}_2 \text{ min}^{-1} 100 \text{ g}^{-1}$ wet tissue and value represents the arterial-venous oxygen content difference multiplied by blood flow. Oxygen (O_2) and Carbon dioxide (CO_2) units are ml/DL where 'art' = arterial and 'Ven' equal venous. Sat = Saturation. Tension produced is kg 100 g^{-1} wet tissue at 3 min into the stimulation protocol. Muscle lactate efflux value represents the venous-arterial [lactate] difference multiplied by blood flow. Venous blood sampling was initiated at the 3rd minute and took appropriately 30 sec to obtain.

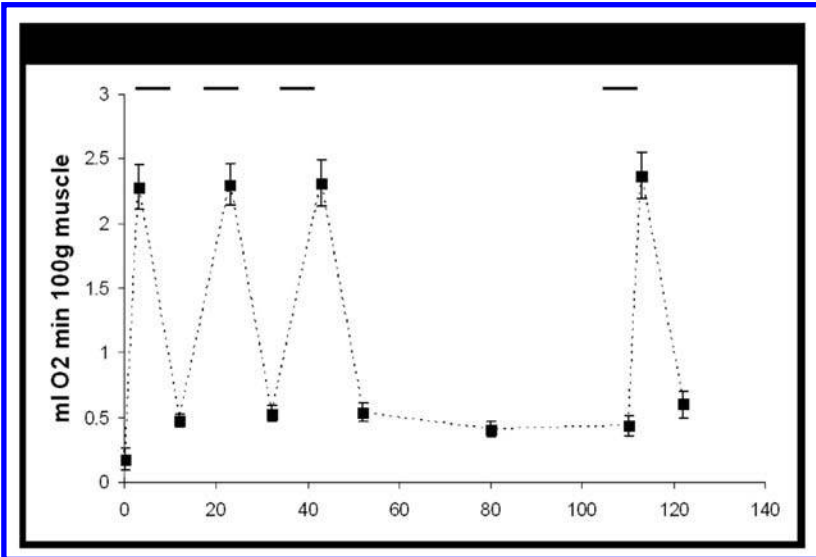


Figure 1: Skeletal muscle oxygen consumption measured at rest and during the third to fourth minute of contraction (this is when a venous blood sample was obtained). Oxygen consumption was calculated from the arterial-venous difference (oxygen content) and muscle blood flow. Oxygen consumption during contraction did not differ across the four stimulation periods. The G bars at the top of the graph represent the period of muscle stimulation.

Intramuscular Metabolites

During the first 10 min period of contraction, muscle ATP concentration fell by ~30 percent (Table 2). This was accompanied by a 10 fold increase in muscle lactate concentration. Net PCr degradation was substantial, indicating that the majority of muscle fibers were actively contracting at the time of obtaining the 10 min muscle biopsy sample. Following two additional periods of muscle contraction, separated by 10 min recovery; with 60 min of recovery following the third period of contraction muscle (See Fig. 4), ATP concentration failed to recover to initial levels (~20 percent lower than the initial concentration). However, during the subsequent contraction period (fourth period) ATP levels were maintained during contraction. Furthermore, the extent of the decline in PCr concentration was somewhat reduced (~15 percent, $p = 0.051$), while muscle lactate accumulation was ~50 percent lower than that observed during contraction first period (Table 2).

Table 2: Intramuscular metabolites prior to and at the end of the first and fourth period of muscle contraction.

	Period 1		Period 4	
	Rest	Contraction	Rest	Contraction
ATP	24.7 ± 1.5	17.4 ± 1.6*	19.7 ± 1.1*†	18.7 ± 1.2
PCr	86.1 ± 3.4	13.9 ± 4.0*	95.7 ± 6.0	35.1 ± 7.3*
Cr	55.3 ± 3.4	127.5 ± 3.4*	44.7 ± 4.5	105.3 ± 4.7*
Lactate	9.7 ± 1.6	105.3 ± 9.0*	9.4 ± 2.6	47.9 ± 8.9*†

All metabolites are mmol kg⁻¹ dry muscle. *indicates significant change from rest, $P < 0.05$. †indicates significant difference between period 1 and period 4, $P < 0.05$. For phosphocreatine, the difference between period 1 and period 4 resulted in a p value of 0.051.

Muscle Ammonia Efflux

Ammonia efflux from the contracting muscle was substantial during contraction in the first and second periods (Fig. 2) and somewhat reduced during contraction third period. The substantial ammonia efflux during second and third periods of contraction indicates that muscle adenine nucleotide catabolism continued during both these contraction periods. It is also interesting to note that muscle ammonia efflux remained elevated during 6 min following the completion of the contraction periods. This is consistent with the idea that temporal efflux reflects ~30 percent of the total ammonia production and therefore there is a delay in the efflux process. During the 1 hr recovery period ammonia efflux returned to the baseline value. During the fourth period of contraction there was a complete lack of ammonia efflux from the muscle. Despite this, peak tension was the second highest out of the fourth periods of stimulation, and the “steady state” tension and oxygen consumption was identical to the other three contraction periods (Table 1). It is therefore clear that the reduction in ammonia efflux is not a consequence of the lower ATP turnover.

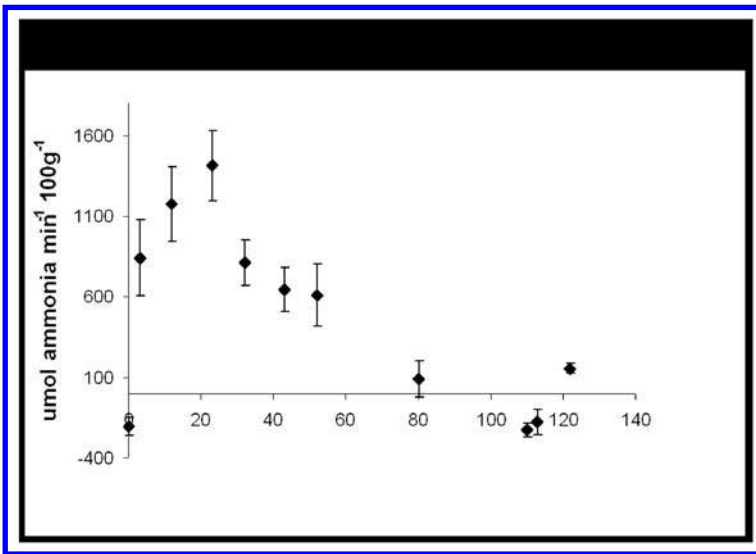


Figure 2: Represents muscle ammonia efflux measured during rest, during the third to fourth minute of contraction (this is when a venous blood sample was obtained), and during the first 2 minutes of recovery. Peak ammonia efflux from the muscle occurred during the second period of muscle contraction. During the fourth period of contraction there was no measurable release of ammonia from the muscle tissue. The G bars at the top of the graph represent the period of muscle stimulation.

Muscle Lactate Efflux

During the first period of muscle contraction there was a 10 fold increase in muscle lactate efflux (Fig. 3). Muscle lactate efflux remained elevated during the recovery period and during contraction second and third periods. This indicates a sustained and relatively high glycolytic flux. Muscle lactate efflux during fourth period mirrored the reduction in intramuscular lactate accumulation, being reduced by ~50 percent

(Fig. 3). The lactate efflux from the muscle over the first 60 min of contraction/recovery intervals would account for ~33 percent of total muscle glycogen stores (assuming glycogen as the only source of carbohydrate). As resting canine muscle glycogen concentration is ~250 mmol kg⁻¹ dry muscle [18], (and ignoring glycogen resynthesis during the 60 min recovery period) then muscle glycogen availability would most likely be in excess of 160 mmol kg⁻¹ dry muscle, prior to contraction in the fourth period and hence can not be considered to be depleted. The significant lactate accumulation and efflux during fourth period supports this interpretation.

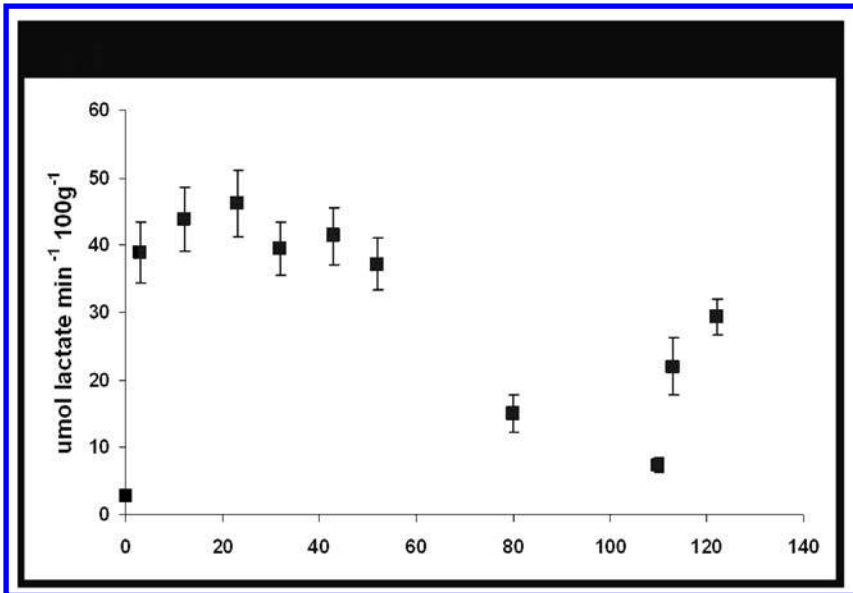


Figure 3: Represents muscle lactate efflux measured during rest and during the third to fourth minute of contraction (this is when a venous blood sample was obtained) and during the first 2 minutes of recovery. Peak lactate efflux muscle was similar during the first three periods of muscle contraction. Following 60 min recovery lactate efflux had returned to baseline. The G bars at the top of the graph represent the period of muscle stimulation.

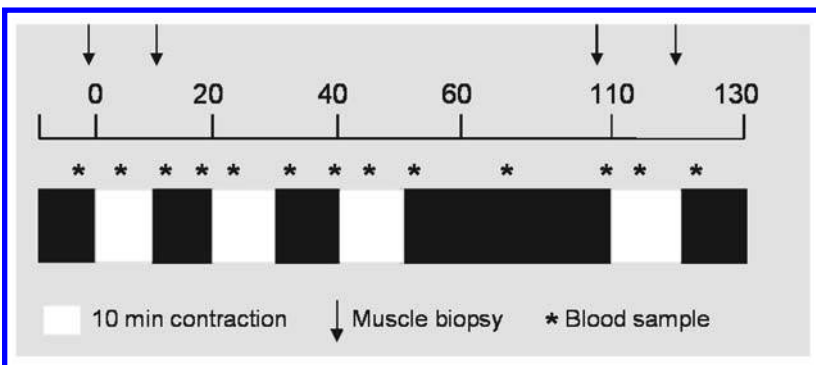


Figure 4: Overview of experimental design.

CONCLUSION

We can hypothesize that following three periods of contractions with low blood flow, adenine nucleotides loss is prevented by an endogenous mechanism, involving modification of AMP deaminase activity. The present study also provides support for the idea that flux through AMP deaminase is not essential for continued muscle contraction while inhibition of AMP deaminase may represent a potential strategy for protecting muscle metabolism in peripheral vascular disease patients [32-35].

KEY WORDS

- **Adenosine monophosphate (AMP)**
- **Adenosine triphosphate (ATP)**
- **Anaerobic ATP regeneration**
- **Canine gracilis model**
- **Glutamine synthetase (GS)**
- **Intermittent claudication (IC)**
- **Inosine monophosphate (IMP)**
- **Low intensity exercise**
- **Normal physiological responses**
- **Phosphocreatine (PCr)**

AUTHORS' CONTRIBUTIONS

James A. Timmons originated the study idea and James A. Timmons and Alan MacInnes designed and carried out the study. The article was written by Alan MacInnes and James A. Timmons.

Chapter 7

Body Mechanics of Moving Cats

Kristin L. Bishop, Anita K. Pai, and Daniel Schmitt

INTRODUCTION

The metabolic cost associated with locomotion represents a significant part of an animal's metabolic energy budget. Therefore, understanding the ways in which animals manage the energy required for locomotion by controlling muscular effort is critical to understanding limb design and the evolution of locomotor behavior. Many quadrupedal animals, particularly those that specialize in long distance steady locomotion, do, in fact, reduce the muscular contribution required for walking by adopting pendulum-like center of mass movements that facilitate exchange between kinetic energy (KE) and potential energy (PE) [1-4]. However, animals that are not specialized for long distance steady locomotion may face a more complex set of requirements, some of which may conflict with the efficient exchange of mechanical energy. For example, the “stealthy” walking style of cats may demand slow movements performed with the center of mass close to the ground. Force plate and video data show that domestic cats (*Felis catus*, Linnaeus, 1758) have lower mechanical energy recovery than mammals specialized for distance. A strong negative correlation was found between mechanical energy recovery and diagonality in the footfalls and there was also a negative correlation between limb compression and diagonality of footfalls, so that more crouched postures tended to have greater diagonality. These data show a previously unrecognized mechanical relationship in which crouched postures are associated with changes in the footfall pattern which is in turn related to reduced mechanical energy recovery.

It has long been known that animals that walk and run use energy-saving mechanisms that reduce the amount of muscular contribution required to accelerate and decelerate the center of mass during locomotion [1], [reviewed in 2]. Although widely accepted, most of the data supporting these models among vertebrates have been derived mainly from species that are specialized for steady locomotion over long distances, including humans, large birds, dogs, and horses [1-4]. It is often assumed that minimizing energy costs during steady locomotion represents the most important selection pressure on the organ systems that support locomotion. This appears to be the case for long-distance specialists [1-4]. However, the extent to which mammals with other locomotor priorities use these energy saving mechanisms, remains less well explored. Studies of monkeys [1], frogs [5], lizards [6], and tortoises [7] have shown greater variability in walking mechanics with respect to walking speed and lower mechanical energy recovery than is seen in distance specialists, yet little attention has been devoted to the reasons for these differences. Without such data, it is difficult to evaluate the critical variables that influence gait and postural choices in animals.

One way to explore this problem is to consider the compromises that animals may have to make when balancing the value of locomotor behaviors that reduce muscular effort and those that promote other important performance targets. Cats represent an ideal model animal to explore the balance of different locomotor goals such as energetic efficiency and stealth because cats consistently walk with their limbs more flexed than distance specialists, and because they often adopt a stealthy hunting style that requires approaching the prey without being detected.

The ways in which the stealthy gait used by cats may reduce locomotor efficiency are clear from the consideration of current models for locomotor mechanics. The energy saving mechanism that is thought to be used during walking is a pendulum-like mechanical energy exchange in which KE is stored temporarily as gravitational PE as the center of mass rises and vaults over the relatively stiff stance leg, and is then returned as KE as the animal falls under gravity [1-5]. If PE and KE fluctuations are precisely out of phase and of the same magnitude, then the total external mechanical energy of the system remains constant and no energetic input is required to sustain motion.

The exchange of PE and KE reduces the muscular contribution needed to accelerate and decelerate the center of mass, although there is currently little data showing a direct relationship between the mechanical energy exchange and metabolic costs. In some animals, especially small ones, the savings may be relatively low. However, the amount of muscular effort needed to control movements of the center of the mass is reduced as exchange increases. As a result, the costs of locomotion are reduced by some percentage as energetic exchange increases. This mechanism has been well-documented in animals that habitually use steady, relatively long-distance locomotor strategies; for example, dogs can recover up to 70 percent of the mechanical energy used while walking [3, 8]. Tortoises and frogs, in contrast, have low levels of energetic exchange [5, 7]. There is only one previous study [9] that explored center of mass movements in cats, and that study included only one step in the analysis. Cats, which use a broad range from more to less crouched postures, provide an ideal opportunity to parse the specific relationships between footfall patterns and limb posture and energetic exchange in mammals.

MATERIALS AND METHODS

Animals and Equipment

Methods followed Duke University IACUC guidelines (IACUC # A365-04-12). Six adult cats were used in this study. Animals were studied in two phases separated by 1 year. Three cats were studied in each phase. In both the phases the cats were allowed to walk freely along a 6-meter runway. A 1.75-meter section of the runway was instrumented with a force plate, which measured ground reaction forces in three dimensions. For the first three cats a single multi-component Kistler (9281B) force platform (Kistler Corporation, Amherst, New York) was placed below the central section. For the remaining three cats, four Kistler force sensors were built directly into the central section of the runway. Both plates were calibrated with the same weights. All force plate data were collected with and processed by Kistler Bioware software.

Full strides for all cats were video recorded, using a camera placed perpendicular to the animal's path of motion. The first three cats were video recorded at 60 Hz using a Panasonic WVD5000 (Panasonic, Secaucus, NJ). Force plate and video records were coordinated using an Event Video Control Unit (Peak Performance, Englewood Colorado).

The remaining three cats were partially shaved and marked with contrasting, non-toxic paint to aid in kinematic analysis. These cats were video recorded at 125 Hz using a Photron Fastcam Super10K (San Diego, CA) digital video camera. Force plate and video signals were coordinated using an electronic trigger to initiate simultaneous video and force plate data collection. The marked cats had markers placed as close to the centers of rotation of the joints as possible at the shoulder, elbow, wrist, hip, knee, ankle, and metatarsal-phalangeal joint.

After data collection, the synchronized video and force data were cropped to a single stride. Force data were cropped within Bioware and video was cropped using Virtual dub video software. The markers and the footfalls were digitized using DLT Data viewer [16] within Matlab (MathWorks, Natick, MA). The resulting x, y coordinate data were used to compute joint angles, limb duty factor (the proportion of the stride during which each limb is in contact with the ground), and diagonality. The hip marker was used to compute average forward velocity. A line was fit through the x coordinates of the hip position through the stride and the slope of the line was used as the average forward velocity. Only steady velocity strides were used in the analysis. To assess this we computed the residuals from the linear fit of the position data. This gives an estimate of how well the raw data is characterized by a steady velocity; any acceleration will result in high residuals. We excluded strides with maximum residuals greater than 5 percent. This estimate is conservative because it incorporates both digitizing error and deviations from steady velocity.

Energy Calculations

The force data were processed using Matlab. The accuracy of the force measurements was verified both by calibrating the plate before and after each day of data collection, and by comparing the vertical component of the ground reaction force over the entire stride to the body weight of the animal, taken just after data collection. Only trials in which the vertical force fell within 20 percent of the body weight were used for further analysis. The methods for calculating center of mass movements and mechanical energy exchange followed those described elsewhere [1, 3, 5]. Measured forces were divided by the cat's body mass to compute accelerations, and the accelerations were integrated twice to calculate the velocity and displacement of the center of mass. The average forward velocity measured from the video was used as the integration constant for the forward component of the instantaneous velocity calculations. The calculated velocities were de-trended prior to the second integration to compute position. The displacement values were normalized around zero by subtracting the mean from each data point.

Potential energy was calculated from the vertical component of the displacement of the center of mass as

$$PE = mgh \quad (1) \text{ Eq.}$$

where m is body mass, g is gravitational acceleration (9.8 ms^{-2}), and h is the vertical position of the center of mass relative to its starting position. The KE was calculated from the instantaneous velocity as

$$KE = \frac{1}{2}mv^2 \quad (2) \text{ Eq.}$$

where m is body mass and v is the magnitude of the resultant velocity vector. For each time step, total mechanical energy (TME) was calculated as the sum of PE and KE. Percent recovery was then computed as

$$\% \text{Recovery} = \frac{\sum PE + \sum KE - \sum TME}{\sum PE + \sum KE} \times 100 \quad (3) \text{ Eq.}$$

where the sums refer to the sum of all positive energy changes over the course of the stride.

Several factors can influence the degree of mechanical energy recovery during a stride. The phase relationship between PE and KE peaks is a very important determinant of the amount of energy that can be exchanged. However, it is often the case, particularly in slow walks, that clear peaks in the energy profiles cannot be distinguished objectively [2, 5]. Following Ahn *et al.* [5], we avoid this problem by using a quantity called congruity. Congruity is computed as

$$\text{Congruity} = \frac{d}{dt} PE \times \frac{d}{dt} KE. \quad (4) \text{ Eq.}$$

Congruity is therefore positive when PE and KE change in the same direction (in phase) and negative when they change in opposite directions (out of phase). As a summary value, we use percent congruity, defined as the percentage of the stride in which congruity is positive. A high percent congruity means that PE and KE fluctuate largely in phase and we expect low mechanical energy recovery, whereas a low percent congruity means that PE and KE fluctuate largely out of phase and we expect high energy recovery.

We quantified the extent to which cats adopted a crouched posture as a normalized hip height. This was calculated as the vertical component of the distance from the hip to the floor divided by the sum of the lengths of all of the leg segments, such that a normalized hip height of one means that the limb is fully extended and values below one approaching zero indicate greater limb flexion.

Statistics

All correlations were computed using linear and quadratic least squares regression models with a significance level of $p = 0.05$. Results from regressions performed on the individuals separately, did not conflict with those for the total data set. Only whole data set results were reported. Means are reported plus or minus one standard deviation.

DISCUSSION

The degree to which PE and KE can be effectively exchanged in an inverted pendulum model depends on both the relative magnitudes of PE and KE fluctuations and their phase relationship. PE fluctuations can be influenced by the amount of vertical displacement of the center of mass, which in turn can be influenced by the amount of limb flexion during stance phase. Increased limb flexion decreases the effective limb length and may reduce the vertical oscillation of the center of mass if other variables such as limb protraction and angular excursion remain equal. Therefore, we hypothesized that because cats walk with greater limb flexion than distance specialists, they may have lower mechanical energy recovery compared to long distance specialists because of reduced oscillations in the vertical position of their center of mass if the other variables that affect recovery such as amplitude of KE fluctuations and phase relationship between PE and KE remain unchanged. Accounting for limb compression is important, for a full understanding of walking mechanics in animals. A recent study modeling human walking found that a pendulum model with completely stiff limbs that produced reasonable predictions of percent recovery did a poor job of predicting the force profile of actual human walking, and that incorporating spring elements due to limb compression (flexion) produced a much closer match with empirical data [10].

RESULTS

Our data support the hypothesis that cats have a less effective pendular mechanical energy-saving mechanism than distance specialists. The average energy recovery ($17.6 \pm 11.3\%$ (s.d.), $n = 6$) achieved by the cats was very low and their maximum energy recovery (37.9%) was substantially lower than the maximum energy recovery reported for distance specialists [1, 3]. Energy recovery values for trots were all relatively low suggesting a clear walk-trot transition (Fig. 1). Considering only walks, there was a statistically significant regression slope, but very poor predictive power in the relationship between velocity and recovery (linear fit: $r^2 = 0.1779$, $p = 0.002$; quadratic fit: $r^2 = 0.1830$, $p = 0.002$, $n = 6$). Although previous studies on walking mechanics [1, 3] found a hyperbolic, curvilinear relationship between velocity and percent recovery with optimal mechanical energy recovery at a moderate speed in a small number of distance specialists, the cats in this study showed no evidence of such a relationship (Fig. 1). This suggests that velocity is not as good a predictor of mechanical energy recovery in cats as it has been found to be in distance specialists, and other explanations must be sought for variation in recovery. Similar variability in energy recovery with respect to velocity has been documented in reptiles and amphibians [5-7, 11], and uniformly low energy recovery across a range of speeds was found in small mammals [12, 13]. It appears, therefore, that animals that do not specialize in long distance travel show a much less stereotyped pattern than that of distance specialists. However, previous studies did not explore the source of this variation.

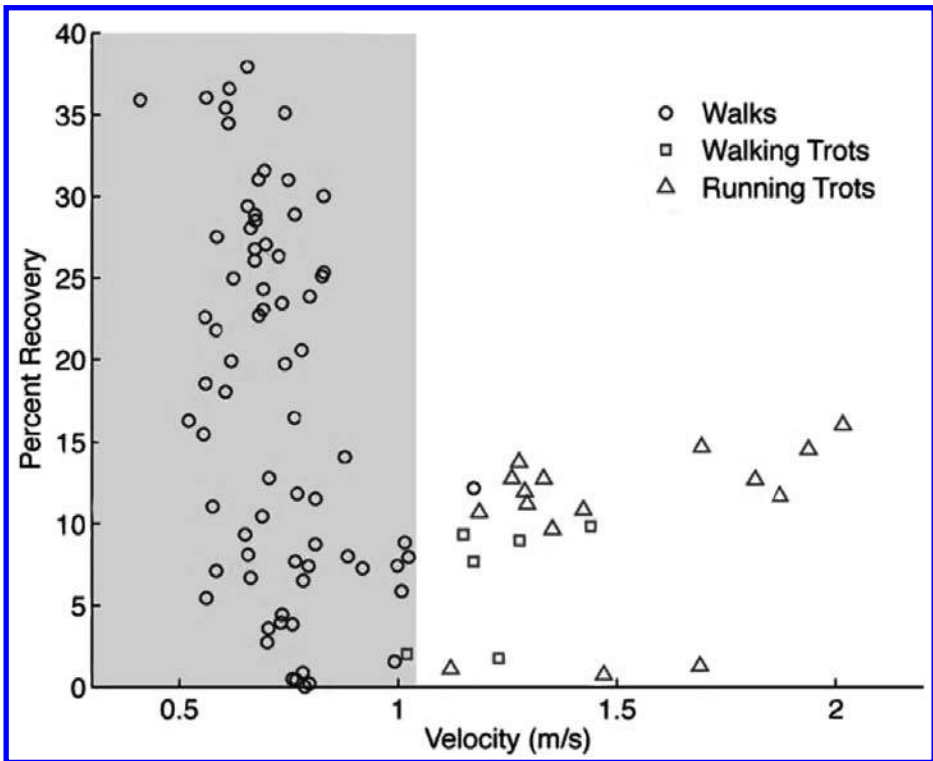


Figure 1: Percent recovery of mechanical energy due to exchange of PE and KE versus velocity for walking and trotting strides. Shaded area de-lineates the range of typical walking speeds. The walk/trot transition occurs around 1 m/s, which corresponds to a Froude number of 0.5 for these cats. Recovery values all fall below 40 percent and there is a low correlation between energy recovery and velocity for walking strides (linear fit: $r^2 = 0.1779$, $p = 0.002$; quadratic fit: $r^2 = 0.1830$, $p = 0.002$).

The timing of footfalls can also affect the magnitude of PE fluctuations. Diagonality is defined as the percentage of a stride by which ipsilateral (same side) feet follow one another. In a pacing gait, the ipsilateral front and hind feet strike the ground at the same time and the diagonality is 0 percent. In a trot, the ipsilateral front and hind feet strike the ground half the stride time apart, and the diagonality is 50 percent. For a stride with a diagonality of 25 percent, the contacts of the four feet are evenly spaced in time. It has been argued on theoretical ground that if mass is evenly distributed between the forelimbs and hind limbs and an animal walks with a diagonality of 25 percent, the vertical position of its center of mass will move so little as to allow almost no energy exchange [3]. This is because at the point in the stride when the front end is at its highest point, the hind end is at its lowest point and vice versa, so the front and back ends oscillate around the center of the mass, resulting in zero PE fluctuation [3]. It has been shown [3] that dogs avoid this problem both by having more of their mass concentrated anteriorly and by consistently using diagonality around 15 percent when walking.

Griffin *et al.* [3] argue that dogs maintained high levels of recovery because of the mass distribution bias toward the forelimbs and because dogs chose diagonalities close to 15 percent, and that lower or higher diagonalities would lower mechanical energy recovery, is a logical conclusion but has not been fully tested because the dogs in this study used a narrow range of diagonalities. Cats are an ideal model, in which to study the effect of diagonality on recovery. Like dogs, cats have a weight distribution pattern biased toward the forelimb [14]. However, cats naturally use a wide range of diagonalities while walking (Fig. 2). Therefore the data presented here can be used to directly test Griffin *et al.* [3] theoretically predicted relationship between footfall pattern and pendular energy recovery.

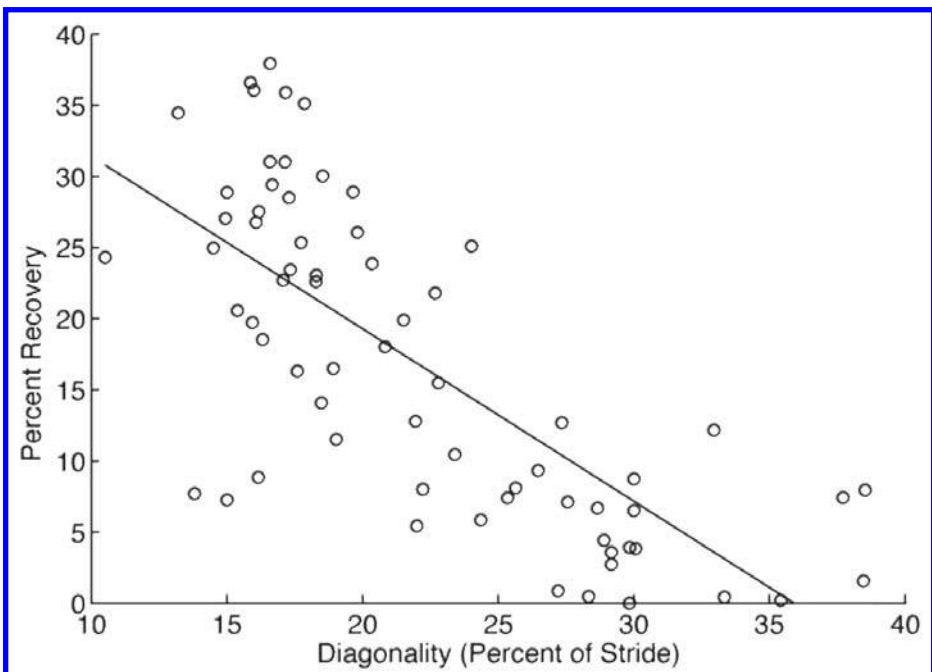


Figure 2: Percent recovery of mechanical energy due to exchange of PE and KE versus diagonality for walking strides. Diagonality is defined as the percentage of a stride by which ipsilateral (same side) feet follow one another. There is a strong negative correlation between recovery and diagonality, such that energy recovery decreases as the footfalls become more evenly spaced in time (linear fit: $r^2 = 0.5417$, $p < 0.001$; quadratic fit: $r^2 = 0.5567$, $p < 0.001$).

The prediction that diagonality influences mechanical energy recovery is supported by our results. Cats in this study often used footfall patterns with diagonality close to 25 percent and had low energy recovery when they did. In walking gaits, energy recovery was significantly, inversely correlated with diagonality (linear fit: $r^2 = 0.5417$, $p < 0.001$, $n = 5$) (Fig. 2). This supports Griffin's [3] model and is consistent with other studies that found recoveries that were low and/or highly variable in animals, that also used gaits with a high diagonality [5-7, 11, 12].

A second important factor that can influence mechanical energy recovery is the phase relationship between PE and KE fluctuations. Phase relationships are typically computed by identifying peaks in the energy fluctuations, but clear energy peaks are often not readily apparent. In these cases the phase relationship can be characterized by calculating congruity, the product of the derivatives of PE and KE with respect to time [5]. Congruity is positive when PE and KE change in the same direction and negative when they change in opposite directions. This can be expressed as a percentage of the stride during which congruity is positive. A high percent congruity indicates that PE and KE fluctuate largely in phase allowing little mechanical energy recovery, whereas a low percent congruity is associated with out of phase PE and KE fluctuations and high energy recovery.

The cats in this study had a strong, significant relationship ($r^2 = 0.7351$, $p \ll 0.001$, $n = 6$) between recovery and congruity, thus changes in phase of PE and KE fluctuations explain the vast majority of the variation in recovery (Fig. 3). This contrasts with our prediction that the magnitude of vertical oscillations of the center of mass would be the primary influence on mechanical energy recovery; our data rejects this hypothesis. No relationship was found between energy recovery and the maximum vertical displacement of the center of mass during a stride (linear fit $r^2 = 0.0480$, $p = 0.0607$, $n = 6$). Therefore, diagonality appears to influence energy recovery not through its effect on vertical oscillations of the center of mass as theoretically predicted, but through an effect on the phase relationship between PE and KE fluctuations.

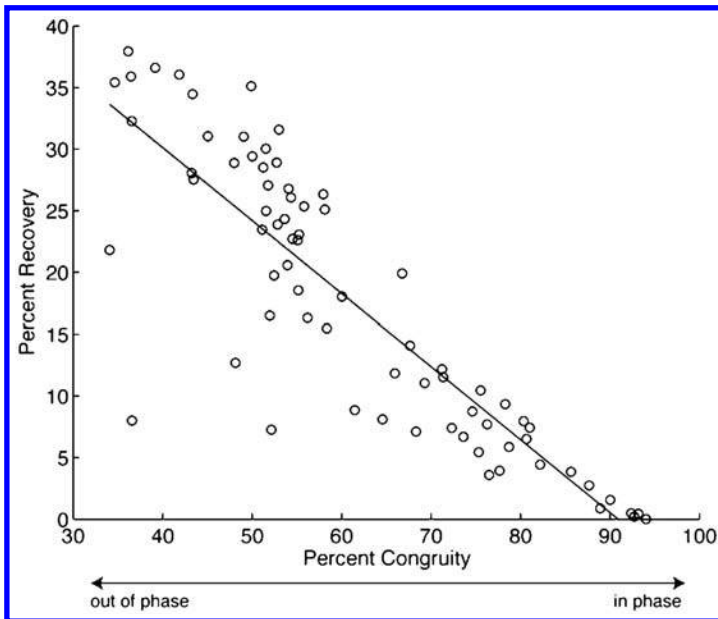


Figure 3: Percent recovery of mechanical energy due to exchange of PE and KE versus percent congruity for walking strides. The majority of the variation in recovery is explained by variation in congruity, indicating that the phase relationship between changes in PE and KE is the primary determinant of mechanical energy recovery (linear fit: $r^2 = 0.7351$, $p \ll 0.001$; quadratic fit: $r^2 = 0.7352$, $p \ll 0.001$).

In this study, there was also a clear association between crouched posture and diagonality. The cats in our study used a wide range of postures from very crouched to relatively extended, and the adoption of these different postures was not associated with walking speed. We found a significant curvilinear relationship between diagonality and normalized hip height (quadratic fit: $r^2 = 0.5455$, $p < 0.001$, $n = 3$) (Fig. 4). During crouched strides in which the hip was held relatively close to the substrate, cats used higher diagonality. It is likely that evenly spaced footfalls increase stability [15] and are thus helpful during stealthy approach to prey. However, by choosing such diagonality during crouched gaits, cats sacrifice energetic efficiency. The reduced mechanical energy recovery that results from this footfall pattern may be compensated somewhat by decreased collisional energy losses. In a numerical simulation of stiff-legged walking [8], it was found that collisional energy loss due to the change in direction of the center of mass was lowest when limb phase (diagonality) was 25 percent.

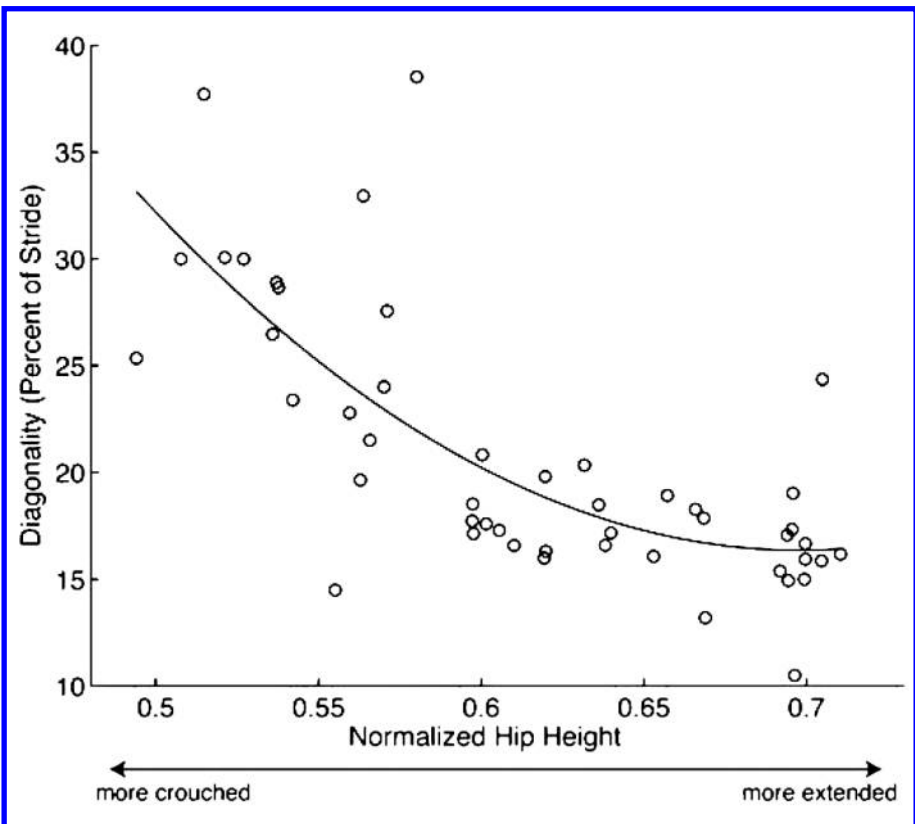


Figure 4: Diagonality versus mean normalized hip height during stance phase for walking strides. The height of the hip was normalized by total leg length. There is a strong negative correlation between diagonality and hip height, such that footfall pattern becomes more evenly spaced when limbs are more compressed (linear fit: $r^2 = 0.4959$, $p < 0.001$; quadratic fit: $r^2 = 0.5455$, $p < 0.001$).

The data presented here suggests ways in which animals can balance complex and sometimes conflicting performance criteria when walking. Some animals may gain the greatest selective advantage by reducing metabolic energy costs by reducing muscular contribution whereas others gain the greatest advantage by avoiding detection while avoiding predators or stalking prey. Those animals may be unable to achieve high levels of mechanical energy recovery as a result of choosing more diagonal footfall patterns and more crouched postures which tend to increase the congruity of PE and KE fluctuations, but may gain stability during stealthy walking by choosing this kind of gait and posture. This novel study of cats highlights these compromises very clearly. The strong associations found between posture and diagonality, and between diagonality and mechanical energy recovery within this single species demonstrates that cats tune their behavior to different critical demands depending on the locomotor context. Cats provide a good comparison with distance specialists such as canids because they consistently walk with their limbs in a more flexed posture, which, as we have seen here within cats, is associated with poorer mechanical energy exchange through its effect on footfall pattern. Dogs tend to use lower diagonality and have higher energy recovery [3] than cats, and it seems likely that this is due at least in part to their more extended posture. Little is yet known about the relationship between pendular energy recovery and the metabolic costs associated with walking, particularly in the more poorly studied non-distance specialists. If fluctuations in PE and KE are small to begin with, the cost of supplying this energy through muscular work may be small. Although further study is needed regarding the metabolic costs of reduced pendular exchange during walking, the consistent differences between the results found here and those reported for distance specialists suggest the possibility of an evolutionary tradeoff between energetic efficiency and stealthy locomotion, highlighting the importance of the interplay of conflicting performance goals to evolutionary outcomes.

CONCLUSION

Low energy recovery was not associated with decreased vertical oscillations of the center of mass as theoretically predicted, but rather with posture and footfall pattern on the phase relationship between potential and kinetic energy. An important implication of these results is the possibility of a tradeoff between stealthy walking and economy of locomotion. This potential tradeoff highlights the complex and conflicting pressures that may govern the locomotor choices that animals make.

KEY WORDS

- **Kinetic energy (KE)**
- **Potential energy (PE)**
- **Total mechanical energy (TME)**
- **Quadrupedal animals**

ACKNOWLEDGMENTS

We thank T. Mitchell for assistance with data collection and E. von Wettberg for help with statistics. Thanks also to T. Roberts, T. Griffin, M. O'Neill, and C. Wall and two anonymous reviewers for helpful discussion.

AUTHORS' CONTRIBUTIONS

Conceived and designed the experiments: Kristin L. Bishop and Daniel Schmitt. Performed the experiments: Kristin L. Bishop, Anita K. Pai, and Daniel Schmitt. Analyzed the data: Kristin L. Bishop, Anita K. Pai, and Daniel Schmitt. Contributed reagents/materials/analysis tools: Daniel Schmitt. Wrote the paper: Kristin L. Bishop and Daniel Schmitt. Text editing: Anita K. Pai.

Chapter 8

Wound Repair on Horses with Equine CTNNB1 and PECAM1

Zoë Ipiña, Vincenzo Miragliotta, Josiane Lefebvre-Lavoie, Jacques G. Lussier, and Christine L. Theoret

INTRODUCTION

Wound healing in horses is fraught with complications. Specifically, wounds on horse limbs often develop exuberant granulation tissue (EGT) which behaves clinically like a benign tumor and resembles the human keloid, in that the evolving scar is trapped in the proliferative phase of repair, leading to fibrosis. Clues gained from the study of over-scarring in horses should eventually lead to new insights into how to prevent unwanted scar formation in humans. cDNA fragments corresponding to CTNNB1 (coding for β -catenin) and PECAM1 (equine platelet endothelial adhesion molecule-1) genes, potentially contributing to the proliferative phase of repair, were previously identified in a mRNA expression study as being up-regulated in 7 day wound biopsies from horses. This study is the first to characterize equine cDNA for CTNNB1 and PECAM1 and to document that these genes are expressed during wound repair in horses. It appears that β -catenin may be regulated in a post-transcriptional manner while PECAM1 might help thoracic wounds mount an efficient inflammatory response in contrast to what is observed in limb wounds.

Repair of wounds located on the limbs, but not the body, of horses is often accompanied by the formation of EGT which behaves clinically like a benign tumor and resembles the human keloid [1, 2], in that the evolving scar is trapped in the proliferative phase of repair, leading to fibrosis. This condition ultimately generates extensive scarring, detrimental to function. Indeed, a recent study reported that approximately 7 percent of injuries leading to the retirement of racehorses are the result of a wound [3]. Efforts to enhance wound repair and to prevent unwanted scar formation in both humans and horses have been disappointing, possibly owing to insufficient knowledge of the underlying mechanisms.

We recently identified genes expressed in wound margin biopsies of horses, using suppression subtractive hybridization (SSH) [4]. Two hundred and twenty six cDNAs were found to be differentially expressed during the proliferative phase of repair of normal body wounds, 129 of which matched against GenBank databases. In the study described herein, we targeted a previously identified SSH-derived cDNA fragment corresponding to (CTNNB1) and a second corresponding to (PECAM1) for their potential contribution to the proliferative phase of repair, which is aberrant following wounding on the limbs of horses. CTNNB1 had already been demonstrated to play a role in fibroproliferative disorders [5, 6] and PECAM1 was chosen because of its known interaction with β -catenin [7].

Beta-catenin is an 88-kDa highly conserved protein that is a structural component of the adherens junction (AJ), a cadherin-dependent adhesive structure intricately linked to the actin microfilament network and located between adjacent epithelial cells. Beta-catenin is a central mediator in the canonical wingless (Wnt) signaling pathway, which exerts remarkable control over cellular phenotype and behavior [8]. When the Wnt pathway is quiescent, β -catenin participates in AJs which must disassemble to allow for cell migration, a process critical to epithelialization following wounding. When freed from intercellular contacts, β -catenin is phosphorylated and targeted for degradation [6]. Activation of the Wnt pathway inhibits phosphorylation, leading to cytosolic stabilization of β -catenin. This stabilized form subsequently translocates to the nucleus where it functions as a transcriptional co-activator of T cell factor/lymphoid enhancer factor (Tcf/Lef) target genes [9].

Beta-catenin plays a cell-specific role during wound repair. Protein levels are transiently elevated in mesenchymal cells during the proliferative phase of repair [5], which is thought to regulate the growth of dermal fibroblasts [10, 11]. Moreover, β -catenin stimulates the growth of microvascular endothelial cells [12]. In contrast, β -catenin inhibits migration of human epithelial cells *in vitro*, which may impair wound closure *in vivo* [13]. Hyperplastic wounds in man exhibit a prolonged phase of elevated β -catenin protein levels and concurrent tcf-dependent transcriptional activation of target genes involved in fibroproliferative processes, such as α -smooth muscle actin (α -SMA), fibronectin (FN) and collagen type III (COLIII) [5]. A transgenic mouse model, in which stabilized β -catenin is expressed in mesenchymal cells, develops aggressive fibromatosis (desmoid tumors) and hyperplastic cutaneous wounds [11].

The PECAM1 (CD31) is a 130-kDa transmembrane glycoprotein member of the immunoglobulin super family that is constitutively expressed on platelets, specific cells of the immune system, as well as on endothelial cells, particularly at the intercellular junctions [14]. Its ectodomain mediates adhesion [15] while its cytoplasmic portion that serves as a scaffold for cytoskeletal proteins [16] and for signaling [17]. PECAM1 has been implicated in a number of important biological processes including modulation of adhesion [18], cell migration [19], inflammatory cell infiltration [20, 21], phagocytosis by macrophages [22], endothelial permeability [23] and angiogenesis [24, 25].

The PECAM1 binds tyrosine-phosphorylated β -catenin having left AJs and become localized to the cytosol [16]. Precisely, PECAM1 functions as a reservoir for tyrosine-phosphorylated β -catenin, maintaining localization at the plasma membrane. This dynamic interaction is involved in the proliferation phase of angiogenesis [16]. Biswas *et al.* [7] identified PECAM1 as a modulator of microvascular endothelial cell proliferation via its participation in the Wnt signaling pathway, thereby stabilizing and promoting the accumulation of transcriptionally active β -catenin.

In the present study we hypothesized that the temporal expression pattern of these two genes with potential roles in angiogenesis and cell proliferation would differ between body wounds which heal normally and limb wounds which are predisposed to the formation of EGT in horses. The specific objectives of this study were to characterize the full-length equine CTNNB1 and PECAM1 cDNAs, and to

study the spatio-temporal expression profile of their mRNAs and proteins during the repair of body and limb wounds. The ultimate objective of our research program is to contribute to a better understanding of the dermal repair process, and permit the development of novel diagnostic and therapeutic strategies to resolve wound healing complications in the horse, which could ultimately be extrapolated to man.

MATERIALS AND METHODS

Cloning of Equine CTNNB1 and PECAM1

Isolation of the full-length equine cDNAs was undertaken by screening size-selected cDNA libraries. The sizes of the full-length equine PECAM1 and CTNNB1 cDNA were estimated by virtual Northern blot analysis. Briefly, total RNA was isolated from a wound edge biopsy obtained 7 days following creation of a square 6.25 cm² full-thickness wound on the lateral thoracic wall [4] and transformed into cDNA by the SMART cDNA synthesis method (BD Biosciences Clontech, Mississauga ON) as described [41]. The cDNA was separated by gel electrophoresis, transferred onto a nylon membrane and hybridized with an equine radioactive probe (CTNNB1 = 535 bp: [GenBank: DN625863]; PECAM1 = 492 bp: [GenBank:DN625893]) generated from a previous gene expression profiling experiment [4]. On the basis of the hybridized size, a specific library was established via the pDrive plasmid cloning technique (Qiagen PCR cloning kit; Qiagen, Mississauga ON) and screened by radioactive hybridization as described [41]. Positive hybridizing bacterial colonies were grown, their plasmid contents were isolated (QIA-prep, Qiagen) and the size of the cloned cDNA was analyzed via gel electrophoresis analysis, following EcoR1 digestion.

Since only a 3'-truncated cDNA fragment was obtained for CTNNB1 following the library screening, a PCR reaction was performed to characterize 5' upstream sequences. Oligos were designed based on conserved regions of human [GenBank: NM_001904], swine [GenBank: NM_214367] and murine [GenBank:NM_007614] sequences. PCR reactions were performed using SMART cDNAs from a 7 day wound edge biopsy, Advantage 2 DNA polymerase (BD Biosciences Clontech) and PCR primers (sense: 5'-GCGTGGACAATGGCTACYCAAGC-3'; anti-sense: 5'-CCAGGCCAGCTGATTACTGTAC-3'). The PCR product was cloned in the pDrive plasmid and produced as described above.

The cDNAs were sequenced via the dideoxy sequencing method (Big Dye Terminator 3.0; ABI Prism, Applied BioSystem, Branchburg NJ) and analyzed on an ABI Prism 310 sequencer (Applied BioSystem). Nucleic acid sequences were analyzed by BLAST and protein sequences deduced from cDNAs were analyzed by PSI- and PHI-BLAST [42] against GenBank data banks.

Equine Tissues and RNA Extraction

Thoracic and limb normal skin, as well as wound edge biopsies were taken at specific times during the repair process from four normal, 2–3 year old Standardbred mares, as described [33]. Briefly, five square 6.25 cm² areas were excised on the dorso-lateral aspect of one randomly assigned metacarpus beginning just above the fetlock, and on the lateral thoracic wall, 1.5 cm apart in a staggered vertical column, then left to

heal by second intention. Excised skin from the lowermost wound was kept as time 0 sample. One wound per site (thorax; limb) was sampled at the following times in each horse: 1, 2, 3, 4, and 6 weeks. To avoid repeated trauma, each wound, beginning with the most distal one, was designated for a single biopsy. Full-thickness specimens were taken with an 8 mm diameter biopsy punch to include a 3–4 mm strip of peripheral skin, the migrating epithelium and a 3–4 mm strip of granulation tissue from the wound center, when present. Biopsy samples were divided in half; one half was formalin-fixed and paraffin-embedded (FFPE) for immunohistochemical studies while the other was snap-frozen in liquid nitrogen and stored at 80°C, until further processing. Total RNA from all samples was extracted and analyzed as previously described [43]. Samples of 3 and 6 month old EGT were obtained from two clinical cases presented to the Centre Hospitalier Universitaire Vétérinaire of the Université de Montréal and FFPE for immunohistochemistry. These experiments were approved by the Animal Ethics Committee of the Faculté de Médecine Vétérinaire of the Université de Montréal and were sanctioned by the Canadian Council on Animal Care.

Semi-Quantitative RT-PCR Analyses of Temporal Expression of mRNA

Total RNA was first transformed into cDNA. One µg of total RNA from samples of healing thoracic wounds (n = 4 mares) was pooled for each biopsy time; the same was done for limb wound samples. From each of these pools, RNA was reverse-transcribed with an oligo-dT30 primer and PowerScript (BD Biosciences Clontech) to generate the first strand cDNA using the SMART PCR cDNA synthesis kit (User manual: PT3041-1; BD Biosciences Clontech) [44]. Second cDNA strands were produced and PCR-amplified using Advantage 2 DNA polymerase (BD Biosciences Clontech). To perform semi-quantitative RT-PCR, SMART cDNA pools were used in a 25 µl PCR reaction with the Advantage 2 DNA polymerase kit (BD Biosciences Clontech). Gene-specific PCR primers were designed in the open reading frame (ORF) of the equine cDNA sequence for: CTNNB1 (sense: 5'-GGACCACAAGCAGAGTATTGAAGG-3'; anti-sense: 5'-AATTCGGTTGTGAACATCCCGAGC-3'; [GenBank:DQ267491]), PECAM1 (sense: 5'-GGGACATATACCTGCACCGCA-3'; anti-sense: 5'-TTACTCGCCTGCGACTCATGC-3'; [GenBank:DQ310372]) and glyceraldehyde-3-phosphate dehydrogenase (GAPDH; sense: 5'-CAAGTTCCATGGCAGTCACGG-3'; anti-sense: 5'-AAAGTGGTCGTTGAGGGCAATGC-3'; [GenBank:AF157626]) [4]. For all samples, PCR was performed in triplicate by Mastercycler® ep. The number of cycles used was optimized for each gene to fall within the linear range of PCR amplification: GAPDH = 18 cycles; CTNNB1 = 23 cycles; PECAM1 = 22 cycles. The PCR reactions (20 µl/reaction) were resolved on a 2% TAE-agarose gel (40 mM Tris acetate; pH 8; 1 mM EDTA) with ethidium bromide (0.5 µg/ml); PCR products were visualized by UV and the images were digitized. The digitized signals for each gene were analyzed by densitometry using the NIH Image program [45].

Immunoblot Analyses

Specimens of equine skin and platelets were homogenized in M-PER buffer (Pierce, Rockford, IL) that was supplemented with a mix of protease inhibitors (Complete; Roche Applied Science, Laval, QC) as recommended by the manufacturer. Samples

were homogenized at 7,000 rpm with a polytron PT1300D (Kinematica AG, Littau-Lucerne, Switzerland). The protein extracts were centrifuged at $10,000 \times g$ for 5 min at 4°C, and the recovered supernatant (whole cell extract) was stored at 80°C until electrophoretic analyses were performed. Protein concentration was determined by the Bradford method [46] (Bio-Rad Protein assay, Bio-Rad Laboratories Inc., Hercules, CA). Protein extracts (100 µg proteins/sample) were heat-treated (5 min, 100°C) and size-fractionated via a one-dimensional SDS-PAGE, then electrophoretically transferred onto polyvinylidene difluoride membranes (PVDF; Hybond-P, Amersham Pharmacia Biotech). Immunoblots were performed as described [47]. The membranes were incubated either with the mouse anti-human β -catenin monoclonal antibody (dilution 1:1,000; sc-7963; Santa Cruz Biotechnology, Inc.) or with the goat anti-mouse PECAM-1 polyclonal antibody (dilution 1:200; sc-1506; Santa Cruz Biotechnology, Inc. Santa Cruz, CA). As secondary antibodies, a sheep anti-mouse IgG-HRP (dilution 1:10,000; NA931; Amersham Pharmacia Biotech) and a donkey anti-goat IgG-HRP (dilution 1:5,000; sc-2020; Santa Cruz Biotechnology, Inc.) were used. Detection of immunoreactive proteins was performed by the enhanced chemiluminescence system (ECL Plus, Amersham Pharmacia Biotech) following the manufacturer's protocol, and exposed to Hyperfilm (Amersham Pharmacia Biotech). Autoradiographic images were digitized using a ScanMaker 9800XL flatbed scanner (Microtek lab, Inc., Redondo Beach CA).

Immunohistochemical Localization of β -Catenin and PECAM1

PBS-buffered formalin-fixed tissues from both locations (thorax and limb) in all four horses were prepared as described [47]. Paraffin-embedded tissues were cut to 3 µm thickness, mounted on SuperfrostPlus slides (Fisher Scientific, Pittsburgh PA), deparaffinized and then rehydrated. Antigenicity lost during the fixation process was retrieved by the pressure cooker heat treatment for 15 min [47]. Non-specific binding sites were saturated by 30 min incubation in blocking buffer: TBS (100 mM Tris; pH 7.5; 150 mM NaCl), 1 percent bovine serum albumin and 1 percent fat-free skim milk. For the antibody raised in goat, the fat-free skim milk was omitted; the saturation step was substituted by 30 min incubation in TBS-Tween (100 mM Tris; pH 7.5; Tween 0.2 percent). Tissue sections were incubated overnight at 4°C with the primary antibodies (β -catenin 1:25; PECAM1 1:50) diluted in blocking buffer. Negative control tissue sections were incubated similarly. After three 10 min washes in TBS, complexes were detected by incubation for 2 hr at room temperature with an anti-goat/mouse IgG alkaline phosphatase conjugated (Sigma-Aldrich) diluted to 1:100 in blocking buffer. Tissue sections were washed twice in TBS and once in TBS-MgCl₂ (100 mM Tris pH 9.5, 50 mM MgCl₂) and incubated with the NBT/BCIP alkaline phosphatase substrate (Roche Applied Science). Sections were mounted in Vectamount® Permanent Mounting Medium (Vector Laboratories, Burlingame CA). Photographs were taken under bright field illumination using a Nikon Eclipse E400 microscope equipped with a digital camera (Nikon Coolpix 4500). Digital images were processed and assembled by Photoshop software (Adobe Systems Inc., San Jose CA).

Statistical Analysis

Gene-specific signals (CTNNB1; PECAM1) were normalized with corresponding GAPDH signals for each sample. A repeated-measures (RM) linear model, with site (thorax versus limb) and biopsy time as within-subject factors, was used to determine the effects of site and time on gene expression. When the RM linear model indicated significant differences ($P < 0.05$), priori contrasts were used to compare pre-selected individual means. All analyses were carried out with a P value < 0.05 , using SAS v. 9.1. (Cary, N.C.).

DISCUSSION

The purpose of this study was to determine the temporal expression of CTNNB1/ β -catenin and of PECAM1 during the repair of body and limb wounds in horses, in an effort to define some of the molecular mechanisms leading to undue scarring. At the time of the study, the cDNAs were not characterized for the horse, therefore both were cloned and sequenced. Hybridization of the size-selected libraries revealed the clones containing the full-length sequence of PECAM1 but only a truncated fragment of CTNNB1. Fortunately, the latter allowed the design of a homologous oligonucleotide that was used, along with a heterologous one, to amplify the full-length equine CTNNB1 cDNA sequence.

Results show equine CTNNB1 to be a highly conserved gene and to contain all 16 exons reported in humans. The excellent identity of the sequences for CTNNB1 in mammals (close to 100 percent) validates the quality of the equine sequence we obtained, despite the required amplification by PCR. A high rate of degradation may have contributed to our inefficiency in obtaining the correct hybridization size for the full-length CTNNB1 gene in horse; indeed, in man there exists in the 3'-UTR one copy of AU-rich element (ATTTA), a motif known to contribute to short lived mRNAs.

CTNNB1, first cloned by McCrea *et al.* [27] in *Xenopus laevis*, shows no similarity in sequence to the genes for the α -catenins reported in other species while the β -catenin protein shares 70% amino acid identity with both plakoglobin, found in desmosomes, and the product of the *Drosophila* segment polarity gene "armadillo". Analysis of equine predicted β -catenin, against a protein conserved domains database (PROSITE), showed the presence of nine Armadillo/plakoglobin repeat profiles, an approximately 40 amino acid long repeated sequence motif. Proteins that contain this type of domain combine structural roles and signaling functions, by generating and transducing signals affecting gene expression [28]. The calculated expected molecular weight (85, 5 kDa) concurs with that previously reported for the other species.

A preliminary mRNA gene expression profiling study identified a cDNA fragment that corresponded to PECAM1, suggesting its up-regulation in response to dermal wounding [4]. The equine sequence determined herein contained the 16 exons present in the full-length human PECAM1, the predominant isoform detected in human tissue and endothelial cells [26]. This contrasts with the main isoform found in murine endothelium which lacks exons 14 and 15 [29]. While it is possible that other isoforms also exist in horses, our data suggest that, at least in skin, the full-length form predominates.

Processes occurring during the proliferative phase of wound repair ensure restoration of the structural and functional characteristics of skin which depend on both the epithelial and the mesenchymal components of the wound. The severity of scarring of horse limb wounds is related to an excessive proliferative phase where angiogenesis and fibroplasia are exacerbated [30-33]. This may result from dysregulation of the molecular components governing the growth of mesenchymal cells. In the study reported herein, we have focused on two molecules, CTNNB1 and PECAM1, for their proposed role in endothelial cells and fibroblast proliferation.

The temporal patterns we report for mRNA expression of CTNNB1 and PECAM1 resemble one another. Both the genes were constitutively expressed in normal intact skin, but while dermal trauma induced the expression of both mRNAs, the response was more acute for PECAM1 whose levels were significantly increased over 1 week baseline following wounding compared to 2 weeks for CTNNB1. This significant up-regulation of mRNA was maintained for the duration of the study for PECAM1 at both anatomic locations and for CTNNB1 in thoracic wounds; conversely, the expression of CTNNB1 in limb wounds was not significantly elevated following wounding. Finally, mRNA expression in thoracic wounds significantly surpassed that of limb wounds for PECAM1, 1 week post-wounding, and for CTNNB1, 3, 4, and 6 weeks post-wounding.

While it was possible that the temporal pattern of mRNA expression might reflect the different levels at the various sampling sites, the wounds were very close together such that we think it unlikely that anatomic or metabolic differences (blood supply, muscle coverage, etc.) are important. Previous studies using a similar model [30-33] have not reported an influence of the exact location on the body or the lower limb. Likewise a current study has shown no difference in the rate of closure between wounds located distally or more proximally on the lower limb (Monteiro *et al.*, unpublished data).

The correspondence in the patterns of mRNA expression following wounding is consistent with the PECAM1/ β -catenin protein partnership proposed by Biswas *et al.* [7, 34, 35]. Indeed, the cytoplasmic portion of PECAM1 binds cytosolic β -catenin and this dynamic interaction is involved in angiogenesis [16]. More specifically, by enhancing the accumulation of stabilized β -catenin, PECAM1 modulates microvascular endothelial cell proliferation via transcriptional activation of growth promoting genes. Furthermore, a significant increase in PECAM1 mRNA levels preceded that of CTNNB1 following wounding in our study, consistent with the fact that upon cytokine stimulation, the endothelial cells initially induce PECAM1, followed by an increased expression of β -catenin [7].

While one might have anticipated higher levels of equine CTNNB1 mRNA in limb wounds pre-disposed to the development of EGT, a form of fibroproliferative disease, our opposite findings may reflect the mechanism of post-transcriptional regulation of β -catenin during wound repair, which controls how mRNA is translated into protein. Indeed, Cheon *et al.* documented that in the absence of any change in mRNA level, β -catenin protein, expressed primarily in dermal mesenchymal cells, was nonetheless transiently increased during the proliferative phase of normal wound healing in humans

while exhibiting a sustained elevation in hyperplastic wounds [5]. Thus, a lack of correlation between mRNA and protein levels might underlie our unexpected findings; specifically, why CTNNB1 mRNA levels remained elevated when immunostaining for β -catenin waned, and why CTNNB1 mRNA levels in thoracic wounds surpassed those of limb wounds at weeks 3, 4, and 6 of healing.

In horse, epithelial cells migrate slowly on limb wounds which are concurrently afflicted by over-abundant fibroblast proliferation; both are influences attributed to β -catenin protein [10, 13]. Although immunohistochemical studies did not suggest quantitative differences in β -catenin expression between body and limb wounds, our investigations did reveal that while the protein remains transcriptionally active (nuclear stain) in dermal mesenchymal cells for the duration of the study, the intensity of the stain diminishes between the fourth and sixth weeks of healing. This pattern suggests that the signal would have disappeared entirely from normally healed wounds had the study been extended a few weeks. Conversely, strong immunostaining for β -catenin was detected in the biopsies of 3 and 6 month old EGT, a condition characterized by exaggerated angiogenesis and fibroplasia and which resembles hyperplastic scarring in man, in whom a prolonged duration of β -catenin protein elevation has been reported [5]. Our findings may indicate that mesenchymal cells in EGT are behaving as though in a prolonged active proliferative phase of wound healing. In other words, the high levels of β -catenin would encourage proliferation and motility of the dermal cells, generating a larger dermal component to the wounds and hampering remodeling which requires reduced β -catenin levels [5].

While the design of our study cannot establish a cause-and-effect relationship between the prolonged elevation of β -catenin and the development of equine EGT, transgenic mouse models expressing a stabilized form of β -catenin in mesenchymal cells develop hyperplastic cutaneous wounds [11]. Fibroblasts derived from these mice display increased proliferation, motility and invasiveness when grafted into nude mice. Moreover, primary cell cultures demonstrate Tcf-dependent transcriptional activation [11], consistent with the hypothesis that nuclear β -catenin transactivation of target genes is a primary component of fibrosis.

In contrast to the membrane staining of epithelial cells reported by Cheon *et al.* [5], we identified nuclear β -catenin within epithelial cells of intact skin. Our finding is similar to that of Tsuji *et al.* [36] who reports nuclear immunostaining for β -catenin from the upper spinous to the granular cells in normal, intact human epidermis. The presence of stabilized, transcriptionally active β -catenin no doubt reflects keratinocyte proliferation and differentiation in response to continued renewal of the epithelial component of equine skin [37, 38].

While PECAM1 is best known as a promoter of angiogenesis, its ability to facilitate neutrophil transendothelial migration [20, 21] and thus boost the acute inflammatory response [39] is particularly intriguing in view of the data obtained herein. Indeed, it is tempting to draw a parallel between the inefficient and prolonged inflammatory response to wounding in the horse limb [33] and the significantly inferior expression of PECAM1 mRNA in wounds at this site compared to those of the thorax, first week following injury. Conversely, while differences in expression

between the two sites disappear from the second week on, one might have expected an increase in the limb wounds where new blood vessels are particularly abundant within the granulation tissue [33], in relation to PECAM1's role in angiogenesis. Interestingly, the expression pattern of PECAM1 isoforms has been shown to change during tube formation *in vitro*, indicating specialized roles for specific isoforms of PECAM1 during angiogenesis [26]. While our data suggest that we have cloned the predominant isoform of equine PECAM1, it is possible that another isoform is responsible for modulating endothelial cell adhesive properties during the angiogenesis in the horse. Finally, the PECAM1 mRNA expression pattern found in our study corroborates previous assertions concerning the sluggishness hindering the repair of equine wounds, particularly those located on the extremities [1, 30, 33]. To this effect, a recent study in mice showed that both mRNA and protein expression of PECAM1 were induced 3 days following dermal wounding but mRNA expression returned to baseline by day 12 [40]. In contrast, expression of equine PECAM1 mRNA was significantly up-regulated in both thoracic and limb wounds for the 6 week duration of the study.

Immunohistochemistry revealed that, as expected of an endothelial cell marker, PECAM1 is principally present in blood vessels. As such, our data reflects that previously reported by Lepault *et al.* [33] who documented, histologically, more pronounced angiogenesis in healing limb than body wounds of horses. The concomitant presence of PECAM1 and β -catenin on endothelial cells of wound granulation tissue further supports the dynamic interaction between these two molecules, which may modulate the proliferation phase of angiogenesis [7, 16].

RESULTS

Cloning and Characterization of Equine cDNA for CTNNB1 and PECAM1

The cDNA fragments used for the virtual Northern analyses came from sequences previously obtained from a gene expression profiling experiment using SSH screening aimed at identifying mRNAs that were increased or induced during the proliferative phase of wound repair in the horse [4].

Screening of the size-selected library from equine thoracic wound margin biopsies collected 7d post-operatively for CTNNB1 cDNA resulted in the cloning of a truncated cDNA fragment. Thus, a PCR reaction was performed to characterize 5' upstream sequences of the ORF. The equine CTNNB1 cDNA characterized consisted of 2382 bp [GenBank:DQ267491] that included a partial 5'-untranslated region (UTR) of 9 bp, an ORF of 2346 bp encoding a 781-amino acid protein with a theoretical molecular weight of 85.5-kDa, an isoelectric point of 5.5, and a partial 3'-UTR of 27 bp. Amino acid homology search in GenBank by PsiBlast revealed orthologous proteins with an overall identity level of 100% for porcine [GenBank:NM_214367], and 99% to human [GenBank:NM_001904] and canine [GenBank:XM_856013] CTNNB1 proteins. The analysis against a protein conserved domains database (PROSITE) showed the presence of 9 Armadillo/plakoglobin ARM repeat profiles (R151-S191, Q193-G236,

G235-G277, G277-G319, G319-G362, G400-G442, G442-A484, Y489-A532, N594-A636).

The virtual Northern analyses allowed determination of the approximate molecular weight of the full-length PECAM1 cDNA, which corresponded to 3.1–3.7 kb. The SSH cDNA fragment was thus used as probe to screen, by hybridization, the appropriate size-selected cDNA library generated from equine thoracic wound margin biopsies collected 7d post-operatively. The full-length equine PECAM1 cDNA was cloned and consisted of 3381 bp [GenBank:DQ310372] that included a 5'-untranslated region (UTR) of 156 bp, an ORF of 2217 bp encoding a 738-amino acid protein with a theoretical molecular weight of 82.3-kDa, an iso-electric point of 8.2, and a 3'-UTR of 1008 bp containing one polyadenylation signal. Amino acid homology search in GenBank by PsiBlast revealed orthologous proteins, with an overall identity level of 76% to canine [GenBank:XM_848326], 75% to porcine [GenBank:NM_213907], and 72% to human [GenBank:NM_000442] and bovine [GenBank:NM_174571] proteins. The equine sequence determined herein contains the 16 exons present in the predominant form of full-length human PECAM1 [26]. While our study does not exclude the possibility of PECAM1 isoforms in the horse, in normal skin and wound edge biopsies, we detected only the full-length isoform for PECAM1.

Temporal Expression of CTNNB1 and PECAM1 mRNAs in Body and Limb Wounds

Semi-quantitative RT-PCR showed an induction of CTNNB1 mRNA expression in response to wounding though up-regulation was less acute than for PECAM1. The repeated measures linear model revealed a non-significant effect of site, across time ($P = 0.49$), when used to analyze the temporal expression of CTNNB1 mRNA during wound repair in the horse, though constitutive expression of CTNNB1 in unwounded skin at time 0 was significantly greater in the limb, than in the thorax ($P = 0.0014$; Fig. 1). Statistical analysis of the results obtained for CTNNB1 mRNA expression revealed a significant effect of time across groups ($P = 0.0002$). Expression was induced in thoracic skin in response to wounding, with significantly elevated levels attained from 1 week. The level of expression of CTNNB1 mRNA was significantly greater in thoracic than limb wounds from 3 weeks on; after 6 weeks of repair, RT-PCR showed a persistent induction of CTNNB1 in thoracic wounds.

The repeated measures linear model revealed a non-significant effect of site, across time ($P = 0.93$), when used to analyze the temporal expression of PECAM1 mRNA during wound repair in the horse, though constitutive expression of PECAM1 in unwounded skin was significantly greater in the limb than in the thorax ($P < 0.03$; Fig. 2). Thereafter, the effect of site varied from one time to another. Semi-quantitative RT-PCR showed an induction of mRNA expression in response to wounding, with a significantly higher level reached in thoracic than in limb wounds after only 1 week of repair ($P = 0.0174$). PECAM1 mRNA expression did not return to baseline levels by the end of the 6-week study at either location. Indeed, the effect of time, across sites, was significant ($P < 0.0001$).

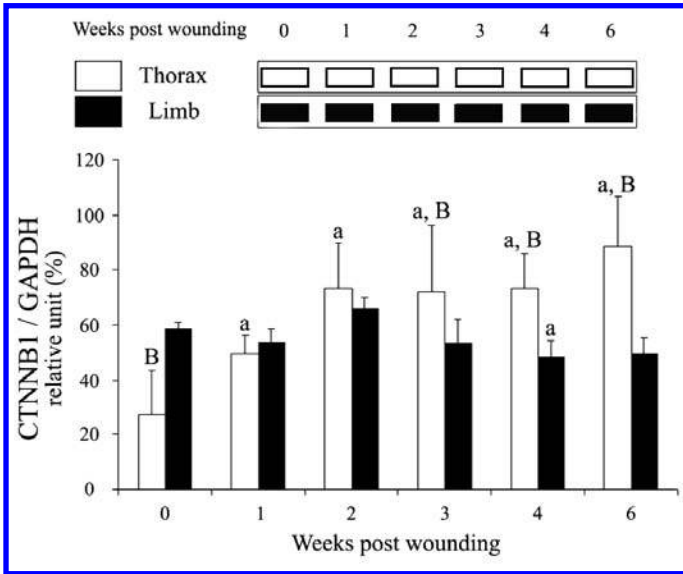


Figure 1: Regulation of equine CTNNB1 mRNA by wounding of thorax and limb skin. Total RNA was extracted from wound margin biopsies isolated 1, 2, 3, 4, and 6 weeks post-wounding, then used in mRNA expression analyses by semi-quantitative RT-PCR as described in Methodology. Bar graphs represent the average of measures, performed in triplicate, on the mRNA of the four horses included in the study. Top: Regulation of CTNNB1 mRNA (AF 752 bp) in wound biopsies from the thorax and the limb. Bottom: Relative changes in CTNNB1 mRNA in biopsies of thorax and limb wounds. The intensity of CTNNB1 signals was normalized with the control gene GAPDH. Different letters denote samples that differed significantly ($P < 0.05$) from time 0 of the same site (a); between anatomic sites at the same time (B). Data are presented as means \pm SEM.

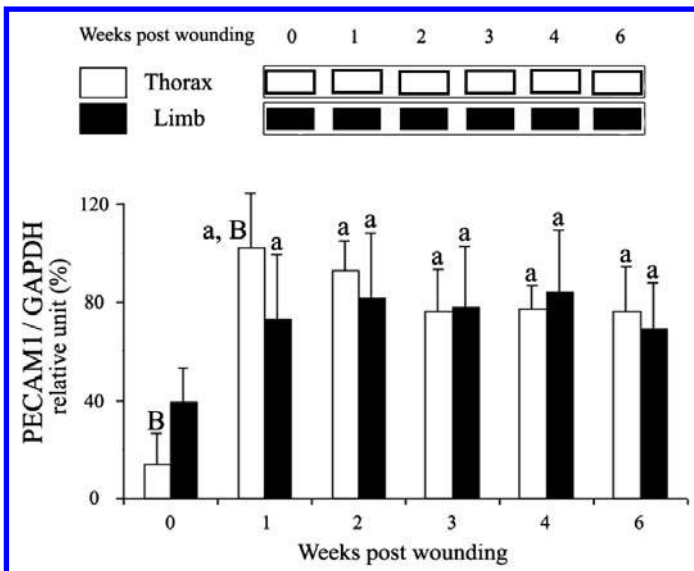


Figure 2: Regulation of equine PECAM1 mRNA by wounding of thorax and limb skin. Total RNA was extracted from wound margin biopsies isolated 1, 2, 3, 4, and 6 weeks post-wounding, then used in mRNA expression analyses by semi-quantitative RT-PCR as described in Methodology. Bar graphs

Figure 2: *(Caption Continued)*

represent the average of measures, performed in triplicate, on the mRNA of the four horses included in the study. Top: Regulation of PECAM1 mRNA [amplified fragment (AF) 548 bp] in wound biopsies from the thorax and the limb. Bottom: Relative changes in PECAM1 mRNA in biopsies of thorax and limb wounds. The intensity of PECAM1 signals was normalized with the control gene GAPDH. Different letters denote samples that differed significantly ($P < 0.05$) from time 0 of the same site (a); between anatomic sites at the same time (B). Data are presented as means \pm SEM.

Protein Localization in Healing Body and Limb Wounds

Immunoblotting showed a specific band of the expected molecular weight in equine skin protein extract for β -catenin determining that the commercial mouse monoclonal antibody raised against amino acids 680–781 mapping at the C-terminus of β -catenin of human origin (sc-7963; Santa Cruz Biotechnology) was specific for equine tissues (data not shown). Cellular localization of β -catenin in normal skin and wound tissues was determined by immunohistochemistry. In normal unwounded skin, the epidermis showed nuclear reactivity, which was also present in the sheaths of the hair follicles and some sebaceous glands (Fig. 3a). No immunoreactive signal was noted in the extracellular matrix (ECM), or the fibroblasts populating the dermis, but endothelial cells were positively stained on their luminal side (Fig. 3b). No qualitative or quantitative differences in staining were detected between thoracic and limb skin samples, nor later on between thoracic and limb wound samples. While epithelialization was incomplete within 2 weeks following wounding, the intact epidermis adjacent to the wound continued not only to show nuclear reactivity, but also new membrane reactivity at the wound edge (Fig. 3c). The dermis contiguous to the wound showed the same pattern as pre-operatively while the granulation tissue filling the wound bed showed nuclear and cytoplasmic staining of both the fibroblasts and the microvascular endothelial cells. In the fourth week of repair the epidermis and the dermis showed the same staining pattern as described for the second week samples. The granulation tissue fibroblasts were strongly stained in a nuclear fashion while the endothelial cells were also labeled with the anti- β -catenin antibody. Six weeks following wounding, immunostaining for β -catenin protein had started to wane. The epidermis, which covered the wound bed in most cases, showed the nuclear staining pattern observed pre-operatively in intact skin. The granulation tissue, which had become less cellular, was weakly stained compared to that of 4 week biopsies and exhibited a staining pattern more nuclear than cytoplasmic. In 3 month and 6 month old EGT, fibroblasts as well as endothelial cells appeared strongly stained in a nuclear/cytoplasmic fashion (Fig. 3d).

The commercially available PECAM1 antibody (sc-1506; Santa Cruz Biotechnology) stained very specifically endothelial cell membranes, as expected. The PECAM1 antibody stained the luminal membrane of endothelial cells lining dermal blood vessels in normal, unwounded skin (Fig. 4a) and in wound biopsies. Consequently, the staining pattern paralleled that of angiogenesis following wounding. At weeks 1 and 4 the presence of more blood vessels within the granulation tissue filling the wound bed translated into more PECAM1 immunostaining, particularly in limb wounds (Figs. 4c and 4d). In 3 month old EGT, there were large and strongly PECAM1-positive vessels while in 6 month old EGT the vessels were smaller and more organized such that the PECAM1 staining was slightly weaker (Fig. 4b).

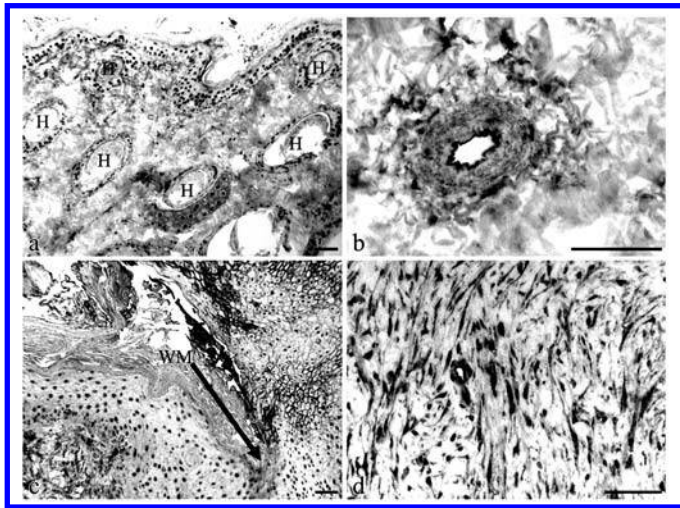


Figure 3: Immunohistochemical localization of β -catenin in the epidermal compartment of equine skin or wounds. Immunohistochemistry was performed on formalin-fixed, paraffin embedded tissues incubated with anti- β -catenin antibody as described in Methodology. Staining was absent when the primary antibody was omitted or substituted with normal serum (data not shown). The scale bar is equal to 0.1 mm. a) Unwounded limb skin. H = hair follicle. b) Unwounded limb skin. Endothelial cells stained with β -catenin antibody. c) Wound margin biopsy taken from 2 week old limb wound. WM = wound margin. d) Three month old exuberant granulation tissue.

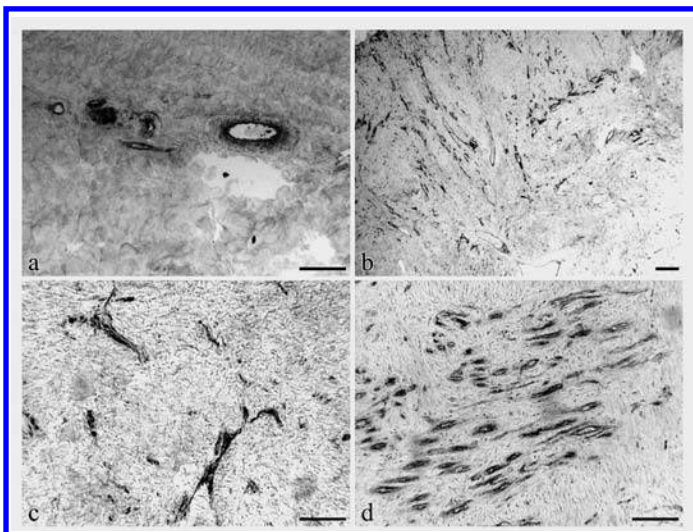


Figure 4: Immunohistochemical localization of PECAM1 in the dermal compartment of equine skin or wounds tissues. Immunohistochemistry was performed on formalin-fixed, paraffin embedded tissues incubated with anti-PECAM1 antibody as described in Methodology. The blood vessel endothelial cells are stained. Staining was absent when the primary antibody was omitted or substituted with normal rabbit serum (data not shown). The scale bar is equal to 0.2 mm. a) Unwounded thoracic skin. b) Six month old exuberant granulation tissue. c) Wound margin biopsy (focusing on granulation tissue) taken from 4 week old healing thoracic wound. d) Wound margin biopsy (focusing on granulation tissue) taken from 4 week old healing limb wound.

CONCLUSION

This study is the first to characterize equine cDNA for CTNNB1 and PECAM1 and to document that the genes are expressed over the different phases of wound repair in horses. Our findings suggest that β -catenin and PECAM1 might interact to modulate endothelial cells and fibroblast proliferation during wound repair in the horse.

Most previous studies investigating the roles of β -catenin and PECAM1 in wound healing have used *in vitro* techniques. Since wound repair is a complex process involving the interplay of several cell types, signaling pathways, extracellular matrix components and soluble factors, the role of various factors and their interactions may best be evaluated using an *in vivo* approach. Thus, while data interpretation can be challenging, the value of our study lies in the fact that the findings are more representative of what truly occurs in the patient.

In an effort to develop targeted therapies to prevent the formation of EGT leading to excessive scarring of equine limb wounds, future studies should quantitatively verify the temporal protein expression of β -catenin and PECAM1 and attempt to elucidate how the two molecules interact. The clues gained from studying the equine model may eventually lead to new insights, into how to prevent unwanted scar formation in humans.

KEY WORDS

- Adherens junction (AJ)
- α -Smooth muscle actin (α -SMA)
- β -Catenin
- CTNNB
- Equine tissues
- Exuberant granulation tissue (EGT)
- Fibronectin (FN)
- PECAM
- Subtractive hybridization (SSH)
- T cell factor/lymphoid enhancer factor (Tcf/Lef)

AUTHORS' CONTRIBUTIONS

Vincenzo Miragliotta, Zoë Ipiña, and Josiane Lefebvre-Lavoie were responsible for generating the majority of the data, including analysis of the wound healing experiments: Zoë Ipiña was responsible for cloning; Vincenzo Miragliotta and Josiane Lefebvre-Lavoie contributed to the cloning and carried out the immunoblotting and the immunohistochemistry; Vincenzo Miragliotta helped to draft the manuscript.

Jacques G. Lussier and Christine L. Theoret were the senior investigators who conceived the study and participated in its design and coordination; Christine L. Theoret drafted the manuscript and Jacques G. Lussier helped in the drafting.

ACKNOWLEDGEMENTS

This work was funded by a discovery grant (Christine L. Theoret) from the Natural Sciences and Engineering Research Council (NSERC) of Canada. Vincenzo Miragliotta was the recipient of a PhD scholarship from the Italian Education, University and Scientific Research Ministry. Neither the funding body played a role in study design; in the collection, analysis, and interpretation of data; in the writing of the manuscript; nor in the decision to submit the manuscript for publication.

The authors thank Guy Beauchamp for help with statistical analysis.

Chapter 9

Genetic Factors of Scrotal Hernia in Commercial Pigs

Zhi-Qiang Du, Xia Zhao, Natascha Vukasinovic, Fernanda Rodriguez, Archie C. Clutter, and Max F. Rothschild

INTRODUCTION

Scrotal hernia in pigs is a complex trait likely to be affected by genetic and environmental factors. A large-scale association analysis of positional and functional candidate genes was conducted in four previously identified genomic regions linked to hernia susceptibility on *Sus scrofa* chromosomes 2 and 12, as well as the fifth region around 67 cM on chromosome 2, respectively. In total, 151 out of 416 single nucleotide polymorphism (SNPs) discovered were genotyped successfully. Using a family-based analysis we found that four regions surrounding *ELF5*, *KIF18A*, *COL23A1* on chromosome 2, and *NPTX1* on chromosome 12, respectively, may contain the genetic variants important for the development of the scrotal hernia in pigs. These findings were replicated in another case-control dataset. The SNPs around the *ELF5* region were in high linkage disequilibrium with each other, and a haplotype containing SNPs from *ELF5* and *CAT* were highly significantly associated with hernia development. Extensive re-sequencing work focused on the *KIF18A* gene did not detect any further SNPs with extensive association signals. These genes may be involved in the estrogen receptor signaling pathway (*KIF18A* and *NPTX1*), the epithelial-mesenchymal transition (*ELF5*) and the collagen metabolism pathway (*COL23A1*), which is associated with the important molecular characteristics of hernia pathophysiology. Further investigation on the molecular mechanisms of these genes may provide more molecular clues on hernia development in pigs.

Most of the inguinal and scrotal hernias (hernia inguinalis and scrotalis) are birth defects in humans, under the control of genetic and environmental factors. However, the molecular mechanism of etiology remains elusive [1-5]. In the pig breeding industry, infrequent incidence of inguinal and scrotal hernias can happen for certain pig breeds and lines and genetic factors are believed to drive the hernia development [6-8]. Without clinical examination, these two defects cannot be easily distinguished, and most of the time, this is the case.

Genome-wide association analyses (GWA) have now been frequently applied in the search for human disease susceptibility loci [9]. This approach could not be realized without the advancement of next-generation sequencing and genotyping technologies, as well as the massive efforts spent in the annotation of the structural and functional properties of the human genome (HapMap and ENCODE projects) [10, 11]. Moreover, attempts to identify the causal genes or gene sub-networks for a disease-linked genomic region have employed large-scale candidate gene association analyses

[12-15], linkage disequilibrium (LD) fine mapping [16], and more recently, reversely engineered molecular network methods [17].

Our previous genome-wide linkage studies have identified several genomic regions related to the hernia incidence in Pietrain-based lines [18, 19]. The quantitative trait loci (QTL) regions on *Sus scrofa* chromosomes (SSC) 2 and 12 have been replicated in seven other independent paternal families derived from three commercial Pietrain-based pig lines [19]. Moreover, in the same genomic regions on SSC2 and SSC12, QTL have been identified in another pig breed, Landrace, using affected sib pairs, which suggest that common genetic origins may be involved even for different pig populations [20]. We continued to refine the interesting regions by LD analysis, and found three independent regions, at approximately 3, 42 and 65 cM on SSC2, and the first 20 cM region on SSC12, with genes segregating for the risk to develop inguinal and scrotal hernias [19].

Since the pig whole genome sequencing project is not yet completed, we had to use all available sequence information in pigs, as well as the comparative information from the human genome. Taking into consideration the practical concerns of experimental power in the design of GWA and candidate gene association analyses in human disease studies [9, 21, 22] and the genomic distribution of LD status in pigs [23], we selected 99 positional candidate genes located in the afore-mentioned interesting regions on SSC2 and SSC12 to conduct a regional large-scale re-sequencing and association study for the genetic causes of scrotal/inguinal hernia. The possible dysfunction of these genes can result in the aberrant collagen metabolism (the most probable reason considered for hernia development) [24-27], the smooth muscle breakdown [28, 29], an altered apoptosis pathway [30], the sex hormone de-regulation [31-33], and the de-differentiation of fibroblasts derived from the stem cells during epithelial-mesenchymal transition (EMT) [34].

MATERIALS AND METHODS

Animals

We collected 1,467 pigs born between 1991 and 2002, from six commercial pig breeding lines (Pietrain, Duroc, etc.) and pigs from crossbred herds, which were classified as affected or unaffected for scrotal hernias. These pigs were divided into two different datasets with regard to with or without family information. The family-based Pietrain lines had 946 individuals from 298 pig nuclear families, including unaffected sires, dams, and male offspring (90 percent affected). The case-control dataset was composed of 100 unaffected and 421 affected males, which included animals derived from two Duroc lines, two Landrace lines, one Large White line, and crossbred animals (Pietrain boars crossed to commercial females). We extracted the genomic DNA of all animals, and adjusted the DNA concentration to 12.5 ng/ μ l.

Discovery of Polymorphisms and Genotyping

We selected the positional and biological candidate genes after text mining the published data resources and literature. These genes were extensively examined for their comparative locations on pig chromosomes 2 and 12. In addition, according to the

comparative gene position on SSC2 to *Homo sapiens* (HSA) chromosomes 5, 11, and 19, and SSC12 to HSA17, gene information (positions and functions) on four human chromosomes (5, 11, 17, and 19) were downloaded and curated. We further constructed the gene networks by putting them into PubGene (www.pubgene.org), not only to examine their relationships, but also to select more relevant candidate genes.

The latest information from the pig genome sequencing project from the Sanger Center (www.sanger.ac.uk/cgi-bin/humace/clone_status?speciesPig) was also checked and the sequences of whole BAC clones in the interesting regions were downloaded, and annotated by blasting against human genome sequence. Furthermore, human mRNA transcript sequences of selected genes in the Ensembl database were used as templates to retrieve homologous pig sequences by a cross-species blast using the NCBI pig sequence database with HTGS or Trace-WGS options. Polymerase chain reaction (PCR) primers were then designed accordingly to amplify the available pig genomic sequences using Primer3 (<http://frodo.wi.mit.edu/>).

We optimized all the primers using a gradient PCR approach in a 10 μ l system, and five individuals from each pig line (five in total) were used for SNP discovery. After sequencing the PCR products, the sequences were aligned and compared using Sequencher software version 3.0 (Gene Codes, Ann Arbor, MI, USA). Some of the potential SNPs were confirmed by restriction fragment length polymorphism (PCR-RFLP) tests using suitable restriction endonucleases (New England Biolabs, Beverly, MA, USA).

The SNP genotyping was carried out commercially on the Sequenom MassARRAY® system. Two positive controls, two negative controls and one blank were put on the same plate for the purpose of quality control. Multiplex primers were designed using AssayDesign 3.1. After PCR amplification, samples were then spotted onto a 384 well SpectroChip® by a robot dispenser, which enabled an automated readout by laser excitation in a compact MALDI-TOF mass spectrometer. SNP genotypes were collected by the Typer 3.4 Software. Each SNP was checked to estimate the Hardy-Weinberg equilibrium status and the minor allele frequency (MAF).

Statistical Analysis

All SNPs were analyzed individually by the transmission disequilibrium tests (TDT) on the family-trios and the case-control data. Three software packages widely used in human disease studies, FBAT (v2.0.2c), Haploview (v4.0), and PLINK (v1.02), were employed in this study [48-50]. Haploview was also used to examine the linkage disequilibrium status amongst all SNPs, by the two pairwise LD statistics, D' and the correlation coefficient (r^2), as well as the haplotype association analyses.

Given that a large number of SNPs were genotyped, we evaluated the robustness of our results using the FDR. FDR values ($p < 20$) were calculated using package “multtest” in R (<http://www.r-project.org>) to evaluate the expected ratio of erroneous rejections of the null hypothesis to the total number of rejected hypotheses among all the genes or SNPs analyzed [51].

DISCUSSION

After comprehensive SNP discovery and genotyping by using first a family-based analysis, which was replicated in another case-control dataset, we found that four regions surrounding *ELF5*, *KIF18A*, *COL23A1* on *SSC2* and *NPTX1* on *SSC12*, respectively, may contain the genetic variants, important for the development of the scrotal hernia in pigs.

The mapping of causal variants for complex disease traits requires the correctly assigned physical order and orientation of genomic sequences, and genetic relationship among genetic markers in specific genomic regions (LD status and functional annotation), which is still under development for pig genomics researchers now [23, 36].

Here, family based analysis was first used to identify the four interesting regions, and then a case-control analysis similar to an admixture mapping method was used to replicate the results. Admixture mapping, or mapping by admixture linkage disequilibrium, is widely used in human disease studies now, to track the common underlying genetic factor(s) for different populations. It needs fewer markers, is more robust to allelic heterogeneity, and can achieve higher mapping resolution than traditional linkage studies [37]. We successfully replicated the results that revealed four genomic regions on *SSC2* and *SSC12* may underlie the development of porcine scrotal hernia. We observed some discrepancy of the significance level of the association analyses between the family-based and case-control datasets. The main reason for the discrepancy could be the experimental power, affected by the population structure, cryptic relatedness, sample size and so on [9, 21, 22]. The case-control design has more power to detect underlying factors than family-based design. However, it could also lead to more false positive results due to hidden population structures, unless the optimal selection of case and control samples took into consideration the genetic background, geographical distribution, age, sex, etc. The family-based studies were more robust to population stratification, though with reduced power. Thus, many studies used several populations, family-based and/or case-controlled, to replicate and confirm the results.

Interestingly enough, genes fine mapped to be associated with scrotal hernia are implied in the pathway regulated by the estrogen receptors (*KIF18A* and *NPTX1*), collagen metabolism (*COL23A1*), and the epithelial-mesenchymal transition (EMT) (*ELF5*). These were three of the original five pathways that had been previously suggested. When treated with ICI 182,780 (the anti-estrogen fulvestrant), *KIF18A*, as a motor protein, was found to be able to bind to $ER\alpha$, elicit the estrogen non-genomic response and activate the ERK-pathway as well [38], and during mitosis it can control the chromosome compression and movement [39]. The down-regulation of *NPTX1* was observed after ICI 182,780 treatment on rat efferent ductules, along with the altered expression of genes related to extracellular matrix organization, such as matrix metalloproteinase 7 (*MMP7*) [40]. These data suggest that estrogen can be related to the normal function of both *KIF18A* and *NPTX1*. Sex hormone de-regulation has been considered as one of the reasons for hernia development [31-33], but significant association of genetic variants in *ESR1* and *ESR2* with scrotal hernia was found not using the same datasets [41]. We suspect that genetic polymorphisms in both *KIF18A* and *NPTX1*, as they could

possibly be linked to estrogen, could also affect the function of estrogen, or be affected, and thus involved in the abnormal development of scrotal hernia, though the exact molecular mechanism is still unclear.

Aberrant collagen metabolism has been considered to be the main reason considered for hernia development [24-27], and COL23A1 was identified to be associated with hernia development in our study. One of the major expression sites of COL23A1 is skin [42], and its increased expression relates to the recurrence and metastasis of prostate cancer, which implies to the existence of extracellular matrix turnover [43]. This could also suggest the involvement of COL23A1 in hernia development. The ELF5 gene, the exclusively epithelium-specific Ets transcription factor, can respond to hormonal cues, and determine the mammary gland development [44-46]. Its mis-expression can also disrupt the specification and differentiation of epithelial cells [47], thus it is possibly involved in the process of the epithelial-mesenchymal transition [34], which is a remarkable characteristic of the etiology of scrotal hernia [1, 2, 4].

All these genes can potentially function in the development of hernia, but the exact molecular mechanism still needs further investigation. One common observation is that rates of hernias are less in purebred lines than in crossbreds, suggesting that the frequency of unfavorable alleles for one or more loci may be high in some lines and the opposite ones exist in the other lines. When crossed, the frequency of undesirable alleles at many loci can come together. Given that this complex disease trait is under the influence of possibly many genetic and environmental factors, and the interaction between them, a specific molecular sub-network associated with the disease trait will need to be defined [17]. This, in turn, requires more time and energy to be put in the search for causal variants for scrotal hernia in pigs.

RESULTS

Based on the nucleotide sequence information provided by the markers in the three regions associated with scrotal hernia on SSC2 at approximately 3, 42, and 65 cM, which existed in genomic DNA sequences (NCBI accession numbers: BH021488, DQ648562 and CL352219), we blasted them against the NCBI nucleotide database, and selected a first set of four important candidate genes distributed in the three specific sub-regions, i.e. the homeodomain interacting protein kinase 3 (HIPK3) and the complement regulatory protein CD59 molecule (CD59) in region II, the cathepsin F (CTSF) in region I, and the mitochondrial LON peptidase 1 (LONP1). Then new candidate genes were selected on both ends of the first set of genes, combining the comparative genomic information between human and pig, and the information from the constructed gene networks, too. This further enabled us to select additional positional candidate genes from HSA5q35 potentially involved in human inguinal hernia [35], e.g. the collagen type XXIII, alpha 1 (COL23A1) and the ADAM metallopeptidase with thrombospondin type 1 motif, 2 (ADAMTS2), which are likely to map the region surrounding 67 cM on SSC2 potentially linked to hernia susceptibility (Fig. 1).

Figure 1: (Caption Continued)

linked to the risk of hernia development. Three regions (I, at 3 cM; II at 42 cM; III, at 66 cM) and a fourth region (IV at 70 cM) could be potentially linked to scrotal hernia. These regions were indicated by the C frames. B, The gene map was built based on the latest porcine physical fingerprint contigs (FPC) map (Sanger Porcine Genome Sequencing Project). Genes in contigs 1, 3, 5, and 8 on SSC2 were selected to cover the four regions, respectively. Contigs 6 and 7 were also used to search for candidate genes. C, Single marker association analyses. SNPs of genes located in region II were significantly associated with pig hernia in Pietrain-based line. The small B box includes SNPs in ELF5 significantly associated with scrotal hernia. D, LD heatmap was constructed by Haploview. Genes in region II were found to be in high LD with each other. The B box indicates the common haplotype formed by ELF5-1, ELF5-3, ELF5-5, ELF5-8, and EHF1 was significantly associated with scrotal hernia. E, 26 new SNP markers were added into the region II region (C arrowhead), with focus on the 1 MB region including EHF-ELF5-CAT, and the 6 MB region covering KIF18A. Re-sequencing work on KIF18A did not detect any further association signal. The B box defines the haplotype composed of ELF5-1, ELF5-3, ELF5-5, ELF5-8, CAT-E11-1, CAT-5U-5, and CAT-5U-1 to be highly significantly associated with scrotal hernia.

In order to give a better coverage over the interesting regions, we have chosen 99 genes in total, both functionally and positionally, from the five interesting regions linked with scrotal hernia in pigs on SSC2 and SSC12. For these 99 genes, we discovered 451 SNPs (dbSNP accession numbers: 107794144–107794595) (average: 4.21 SNPs per gene, range: 1–27) (278 SNPs in 64 genes on SSC2, 138 SNPs in 35 genes on SSC12, respectively). Due to the cost and development of multiplexes, we have assayed 181 SNPs from 89 genes in six iPLEXes by the Sequenom platform (average: 30 SNPs per iPLEX, range: 28–37). After quality evaluation of the genotype data, 151 SNPs (dbSNP accession numbers: 107794444–107794595) are in Hardy-Weinberg equilibrium ($p > 0.01$), with acceptable genotyping success rates (> 85 percent), and no deviation of Mendelian inheritance existed in our pig families for these SNPs. We adopted the iterative strategy for the practical genotyping procedure. The genotype data was analyzed after one round of genotyping, and then based on the results we got, we chose new SNPs for new assays, according to their positions and functional importance, as well as the requirement of maximizing the number of genes included in the iPLEXes to be studied to increase the marker coverage density.

In the family-based Pietrain lines, we found several SNPs in the four regions on SSC2 were significantly associated with scrotal hernia incidence, respectively, after single marker association analysis (Fig. 1, Table 1). One SNP in the epidermal growth factor-containing fibulin-like extracellular matrix protein 2 (EFEMP2) located in region I (Fig. 1C), one SNP in LONP1 in region III, and one SNP in COL23A1 around 67 cM were found to be significantly associated with scrotal hernia, respectively (Table 1, Fig. 1C). Interestingly, four SNPs, ELF5-1, ELF5-8, HIPK3-1, and KIF18A-E3-3, in three genes located in or close to region II, the E74-like factor 5 (ELF5), HIPK3 and the kinesin family member 18A (KIF18A), were significantly highly associated with scrotal hernia ($p < 0.01$) (Table 1). Even after FDR correction, they were still significant at $p < 0.05$. The localization of the four SNPs was right under the hernia QTL region around 42 cM on SSC2 (Fig. 1A), and they were in high LD with each other (Fig. 1D). Furthermore, a common haplotype formed by five SNPs, ELF5-1, ELF5-3,

ELF5-5, ELF5-8, and EHF1, from ELF5 and a neighboring gene EHF, but not HIPK3 and KIF18A, was significantly associated with scrotal hernia ($p < 0.001$).

In order to further dissect the association from region II on SSC2, we added 26 markers surrounding the interesting genes, ELF5 (1 MB region) and KIF18A (6 MB region) (Fig. 1E). At this stage of the genotyping and analyses, the SNP in intron 3 of KIF18A gave the highest association signal. Furthermore, we sequenced 15 exons (exons 2–16), except exon 1 of KIF18A, which were found in an unordered sequenced BAC clone CH242-13K2 on chromosome 2 (NCBI accession number: CU633215), and genotyped 14 SNPs from this gene. However, the newly genotyped SNPs from KIF18A were not significantly associated with scrotal hernia ($p > 0.05$). In the catalase gene (CAT), which is very close to ELF5 physically and oriented differently in humans, three new SNPs, two in the 5'-untranslated region (UTR), CAT-5U-5 and CAT-5U-1, and one in intron 11, CAT-E11-1, were found to be associated significantly with scrotal hernia. The SNP CAT-E11-1 was still significant after multiple testing procedure ($p < 0.05$). It seems that the closer the SNP to ELF5, the stronger the association (Table 1). In addition, a haplotype (AAAAGCA), now composed of seven SNPs from ELF5 and CAT, ELF5-1, ELF5-3, ELF5-5, ELF5-8, CAT-E11-1, CAT-5U-5, and CAT-5U-1, is significantly highly associated with scrotal hernia ($p = 9.0E-04$) (Fig. 1E), which emphasizes that further sequencing could be directed upon this region.

Table 1: Association Analysis Results on Two Datasets: the Family Based Data and the Case-control Data.

Chr.	Gene	SNP	Family based analysis			Case- control		OR
			Flat	Haploview	PLINK	Haploview	PLINK	
			P-value	P-value	P-value	P-value	P-value	
2	<i>APIP</i>	APIP-1-13	0.023	0.023	0.146	0.003	0.002	0.70
	<i>ELFS</i>	ELF5-1	0.005	0.004	0.005	3.27E-05	5.93E-05	0.54
		ELF5-3	0.018	0.016	0.0937	0.325	0.241	0.63
		ELF5-5	0.002	0.002	9.23E-04	4.20E-07	1.44E-04	0.46
		ELF5-8	0.025	0.020	0.047	0.488	0.268	0.64
	<i>CAT</i>	CAT-E11-1	0.004	0.004	0.029	0.005	0.006	0.62
		CAT-5U-5	0.045	0.046	0.078	0.032	0.050	0.52
		CAT-5U-1	0.032	0.034	0.052	0.001	0.002	0.42
	<i>HIPK3</i>	HIPK3-1	0.008	0.006	0.008	0.478	0.752	0.55
	<i>KIF18A</i>	KIF18A-E3-3	0.001	0.001	0.004	0.006	1.47E-03	0.58
<i>LONP1</i>	LONP1-2	0.020	0.031	0.094	0.060	0.043	0.67	
<i>ADAMTS2</i>	ADAMTS2-E2021-1	0.034	0.034	0.019	4.00E-04	3.77E-05	1.38	
<i>COL23A1</i>	COL23A1-E2	0.008	0.008	0.003	3.22E-07	4.76E-10	1.60	
12	<i>RAC3</i>	RAC3-12-4	0.020	0.020	0.108	0.951	0.381	0.71
	<i>PYCR1</i>	PYCR1-1	5.40E-05	8.18E-05	1.74E-04	0.181	0.186	0.30
		PYCR1-E4-E5	8.80E-05	8.77E-05	7.96E-04	0.588	0.581	0.45
	<i>NPTX</i>	NPTX1-4-2	9.99E-06	1.49E-05	2.23E-05	0.053	0.021	0.94
		NPTX1-3	4.03E-04	8.00E-04	5.17E-05	1.90E-08	2.95E-09	1.52
	<i>CARD14</i>	CARD-1-1	0.059	0.035	0.015	0.394	0.419	1.34
		CARD-4-3	0.031	0.025	0.072	0.156	0.275	1.31
	<i>PRPSAPI</i>	PRP-110	0.031	0.028	0.080	9.52E-04	8.91E-04	0.63
	<i>MIF4GD</i>	MIF-17	0.014	0.014	0.008	0.490	0.304	3.00
	<i>ICT1</i>	ICT-16-1	0.051	0.045	0.056	0.163	0.691	0.32

Note: SNPs in bold were in haplotypes significantly associated with scrotal hernia. Four SNPs in *ELFS* were found to constitute a haplotype together with the SNP EHF1 in EHF. Then after fine mapping, these four SNPs, together with three SNPs in *CAT*, formed another haplotype, more significantly associated with scrotal hernia (Figure 1E).

On SSC12, we focused on the first 20 cM region which supports a hernia QTL, and several genes in this region were found to be significantly associated with scrotal hernia (Fig. 2, Table 1). Four SNPs in the pyrroline-5-carboxylate reductase 1 (PYCR1) and the neuronal pentraxin I (NPTX1), PYCR1-1, PYCR1-E4-E5, NPTX1-3, and NPTX1-4-2, were significantly highly associated with scrotal hernia ($p < 0.0001$), respectively. The significance of the association signal is higher for these SNPs than those on SSC2. We observed low LD between them, as well for the remaining SNPs genotyped in this region.

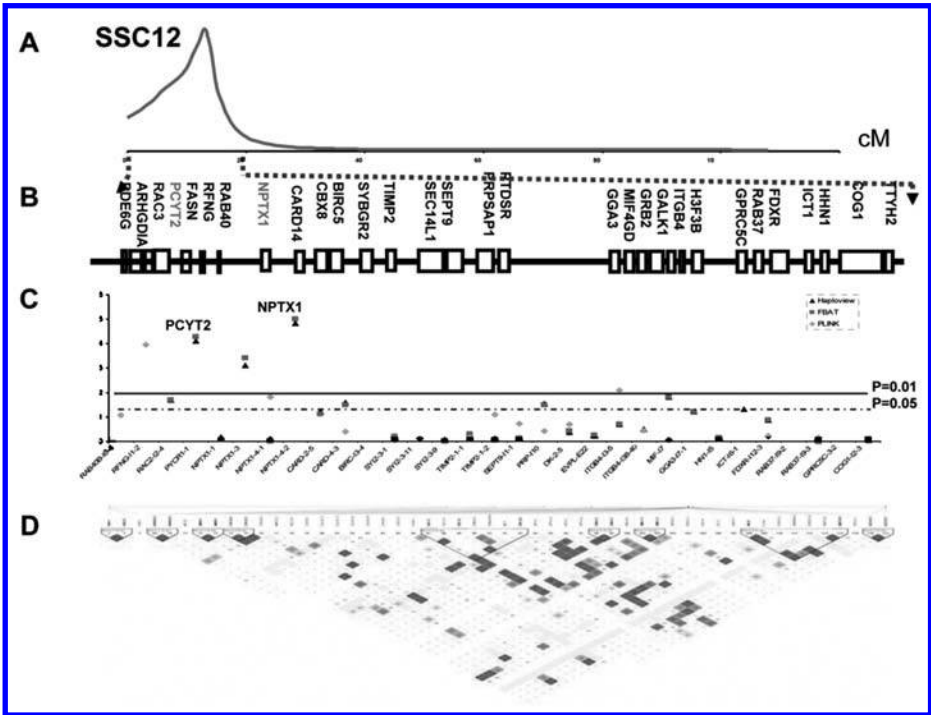


Figure 2: Extensive positional candidate gene analyses of the first 20 cM genomic region for hernia development on SSC12. A, The first 20 cM region was implied in hernia development on SSC12. B, Gene map was built based on the latest porcine physical FPC map (Sanger Porcine Genome Sequencing Project). C, Single marker association analyses. SNPs in PYCR1 and NPTX1 are highly significantly associated with scrotal hernia (global $p < 0.0001$). D, LD heatmap constructed by Haploview shows that no extensive high LD block exists between these SNPs.

We further analyzed the case-control dataset, composed of an admixture of several pig lines, two Duroc lines, two Landrace lines, one Large White line, and crossbred animals (Pietrain boars crossed to commercial females). This dataset gave the replication of the same significant association results as that in the family-based dataset, and seemed to demarcate the region associated with scrotal hernia (Table 1). On SSC2, two SNPs in ELF5 (ELF5-1 and ELF5-5) were significantly highly associated with scrotal hernia ($p < 0.001$). Two SNPs in CAT (CAT-E11-1 and CAT-5U-1) were significantly

associated ($p < 0.01$), and another SNP, CAT-5U-5, at $p < 0.05$ level. The SNP in HIPK3 was not associated any more. The same SNP in intron 3 of KIF18A (KIF18A-E3-3) was associated with scrotal hernia, like in the family-based analysis ($p < 0.01$). The SNP in COL23A1 (COL23A1-E2) was significantly highly associated with hernias ($p < 0.001$). On SSC12, the SNP NPTX1-4-2 in NPTX1 was found to be significantly associated with scrotal hernia in pigs ($p < 0.05$), and another one, NPTX1-3, also highly significant ($p < 0.001$). However, SNPs from PYCR1 were not significant in case control samples.

CONCLUSION

Extensive re-sequencing work focused on the KIF18A gene did not detect any further SNPs with extensive association signals. These genes may be involved in the estrogen receptor signaling pathway (KIF18A and NPTX1), the epithelial-mesenchymal transition (ELF5) and the collagen metabolism pathway (COL23A1), which is associated with the important molecular characteristics of hernia pathophysiology. Further investigation on the molecular mechanisms of these genes may provide more molecular clues on hernia development in pigs.

KEY WORDS

- Collagen metabolism pathway (COL23A1)
- Epithelial-mesenchymal transition (EMT)
- Fingerprint contigs (FPC)
- Genome-wide association analyses (GWA)
- Homeodomain interacting protein kinase 3 (HIPK3)
- Linkage disequilibrium (LD)
- Minor allele frequency (MAF)
- Polymerase chain reaction (PCR)
- Quantitative trait loci (QTL)
- Single nucleotide polymorphism (SNPs)
- Sus scrofa chromosomes (SSC)

AUTHORS' CONTRIBUTIONS

Conceived and designed the experiments: Max F. Rothschild. Performed the experiments: Zhi-Qiang Du and Xia Zhao. Analyzed the data: Zhi-Qiang Du and Max F. Rothschild. Contributed reagents/materials/analysis tools: Natascha Vukasinovic, Fernanda Rodriguez and Archie C. Clutter. Wrote the paper: Zhi-Qiang Du and Max F. Rothschild.

Chapter 10

Acute Heat Stress Effect on Milk Serotonin of Cows

Nissim Silanikove, Fira Shapiro, and Dima Shinder

INTRODUCTION

Exposure to heat stress (HS) induced a rapid and acute (within 24 hr) reduction in the milk yield (MY) in proportion to the heat load. This decrease was moderated by cooler night-time ambient temperature. The reduction in MY was associated with corresponding responses in plasminogen activator/plasminogen-plasmin activities, and with increased activity (concentration) of the (1–28) N-terminal fragment peptide that is released by plasmin from β -casein (β -CN (1–28)). These metabolites constitute the regulatory negative feedback system. Previously, it has been shown that β -CN (1–28) down-regulated milk secretion by blocking potassium channels on the apical aspects of the mammary epithelial cells. So we can calculate that the potassium channels in mammary tissue became more susceptible to β -CN (1–28) activity under HS. Thus, the present study highlighted two previously unreported features of this regulatory system: (i) That it modulates rapidly in response to stressor impact variations; and (ii) That the regulations of the mammary epithelial potassium channel sensitivity to the inhibitory effect of β -CN (1–28) is a part of the regulatory system.

In hot climates, high ambient temperatures, high direct and indirect solar radiation, wind speed and humidity, are the main environmental stressing factors that impose stress on animals [1, 2]. Cattle have a higher metabolic rate than most of the other domestic ruminants, and a poorly developed water retention mechanism in the kidney and gut [1, 3]. Furthermore, as a consequence of aggressive selection for milk production over the last 5 decades, modern cows in Israel and the USA produce 40–70 l of milk per day, compared to 10 l day⁻¹ or less in their ancestors. Each 10 l day⁻¹ of MY roughly doubles the metabolizable energy requirement of cows, and 35 percent of this energy is dissipated as heat [2]. High-yielding cows are affected more than low-yielding ones [4, 5] because the upper critical temperature shifts downward as milk production, feed intake, and heat production increase [1].

Acclimation involves phenotypic responses to environmental changes, which are reflected in hormonal signals, and also in alterations in target tissue responsiveness to hormonal stimuli [6, 7]. The time required for acclimation varies according to the tissue types, and ranges from a few days to several weeks; for example, changes in metabolism in response to HS occur over a few days [8, 9].

However, this picture does not cover all situations; some external environmental stresses, such as dehydration [10, 11] and acute HS [1, 12, 13], may very quickly (within 24–48 hr and take the animals beyond their current acclimatized-adaptive range, which necessitates the induction of emergency physiological responses in order

to avoid sudden death. Such immediate measures include an acute reduction in milk yield, because milk production, particularly in high-yielding dairy cows, intensifies the effects of these external stresses [1, 10].

Milk secretion and mammary function are regulated acutely by local autocrine feedback mechanisms that involve milk-borne factors which are sensitive to the frequency and efficiency of milking [14, 15]. Sustained changes in the frequency of milking and milk secretion are associated metabolic adaptations [16], and with longer-term adaptations in the degree of differentiation and, ultimately, the number of mammary epithelial cells [17, 18]. Consequently, such changes may affect the above-described homeostatic processes. It has been hypothesized that the fast modulation of milk secretion in response to external factors, such as emotional stress, harsh physical conditions such as HS, and water deprivation also depends on such a negative-feedback regulatory system, which increases the potential for survival in response to stress [19, 20]. This negative feedback system was shown to comprise of an endogenous milk enzymatic system, the plasminogen activator (PA)-plasminogen (PG)-plasmin (PL), that specifically forms a β -casein (CN) fragment (f) (1–28) from β -CN, which acts as the negative control signal by closing potassium channels on the apical membrane of the epithelial cells of the mammary gland [19, 20]. Down-regulation of these channels induces undefined inwardly directed cellular signals that inhibit milk secretion. Interestingly, a further activation of the PA-PG-PL system, which was coupled with more extensive degradation of casein induced involution of the mammary gland in lactating goats and cows and forcefully activated the innate immune system [20–23]. Based on these findings, a casein hydrolyzed preparation was developed to reduce the suffering from mammary gland engorgement associated with abrupt cessation of milking (the conventional procedure to induce involution in modern dairy cows), [24] and to treat and prevent common clinical and subclinical infections of the udder in dairy cows [25, 26].

The concept that PA-PG-PL- β -CN f(1–28) is involved in milk-born negative feedback regulation of milk secretion was supported experimentally under conditions that simulated stress (intramammary treatment with dexamethasone) [19, 27], and by exposure of cows to dehydration [19].

The aims of the present study were:

1. To examine the hypothesis that the PA-PG-PL- β -CN f(1–28) system is involved in regulation of milk secretion under acute HS.
2. To assess whether this system is sufficiently sensitive to react to diurnal changes in environmental HS.
3. To examine whether the potassium channels that act in response to β -CN f(1–28) are also regulated.

MATERIALS AND METHODS

Study Layout

The experiment was carried out at the height of summer (late July) in the experimental dairy herd of the Agricultural Research Organization, at the Volcani Center at Bet Dagan.

Eighteen Israeli Holstein cows, between their second and fourth lactations, with MYs of 48–52 l day⁻¹ were subjected to the study. The cows were allocated to three treatments, each of the six cows, according to the lactation number and MY. The treatments were: treatment C—the cows had access to shade and benefited from the conventional cooling procedures in the herd; treatment D—the cows were denied access to shade, but benefited from the cooling procedures; and treatment E—the cows were denied access to both shade and cooling procedures. The cows were held in small yards; those in treatment C had 10 m² of a shaded slatted floor and 10 m² of an unshaded concrete—surfaced yard per animal, whereas those in treatments D and E had 20 m² of an unshaded concrete—surfaced yard per animal. The cows were fed before and during the experiment with a typical Israeli total mixed ration (17% protein) containing 65% concentrate and 35% forage, which was offered ad lib in mangers; water was available at all times. At noon, milking was done before the start of the experiment, milk samples were taken from all cows, and then the cows were allocated to treatments. Milk samples were taken during the morning and noon milking of the subsequent two days; after the last measurement of rectal temperature at 1400 on the second day the cows were returned to their original group.

The cows were milked three times daily (0530, 1230, and 2130), and the exact milking times were individually recorded automatically [13]. The cooling system has been described previously [28]. Briefly, an array of fans produced air velocities of 2 m/sec or more from 0600–2400. In addition, fans and sprinklers were sequentially activated to repeat cycles of wetting (0.5 min) and ventilation (4.5 min) for seven 0.5 hr periods every 1.5–2 hr, between 0730 and 1830.

Ambient Conditions

Air temperature and relative humidity were recorded at a meteorological station located 1.5 km from the farm. The average maximal (noon) temperature during the three days of the experiments were 31, 35, and 37°C, minimal (night) temperatures were 18, 20, and 22°C, relative humidity was 81, 85, and 88%; the temperature humidity index (THI, see reference [1] for definition) values at mid-day were 80, 82, and 88.

Rectal Temperature and Respiration Rate

Respiration rates were determined at 1300 by visually measuring the breathing rates with the aid of a stopwatch. Rectal temperature was measured at 1400 to nearest 0.1°C, with an interchangeable thermistor probe system (model 46TUC Tele-thermometer, Yellow Springs Instruments, Yellow Springs, OH).

Gross Composition, Plasmin Activity, Na⁺ and K⁺ Concentrations

Gross composition, the activities of PA, PG, and PL and the concentrations of Na⁺ and K⁺ in the milk were determined essentially as described previously [22, 27, 29].

K⁺ Uptake into Skim Milk Vesicles

Milk was fractionated into clear infranatant (Inf; i.e., milk serum devoid of vesicles and casein), skim-milk-derived vesicles (SMV), and casein by a combination of centrifugation and ultracentrifugation [30]. The Inf and SMV were stored at –80°C prior to

analysis. The clear Inf was used to measure K⁺ channel blocker activity by comparing 86Rb uptake into SMV, with those obtained after incubation of the SMV in sucrose solution. Protein concentrations in Inf and SMV preparations were assayed by the Bradford method.

The procedure for assaying K⁺ uptake into the SMV was originally described by Shennan [31] and applied for assessing the activity of the milk-borne potassium channel inhibitor, as described previously [19]. Briefly, the uptake at 23°C, was initiated by adding 10 µl of 86RbCl to a reaction medium consisting of 25 µl of SMV, 325 µl of the working solution (control) or 300 µl of working solution, and 25 µl of test samples. Disposable Pasteur pipettes, plugged with polymer filter wool and filled with a cation exchange resin (Dowex, hydrogen form, 50–100 dry mesh, 8 percent cross-linked), were used to separate intravesicular from extravesicular isotopes. Four min after the addition of 86RbCl, a 200-µl sample of the reaction mixture was applied to the Dowex column, which was then washed with 2 ml of an ice-cold solution that was collected in scintillation vials. The radioactivity of the samples was counted in a Liquid Scintillation Counter (Tri Carb, Hewlett-Packard).

Preparation of B-Cn F (1–28) and Measurement of its K⁺ Channel Blocking Activity

The β-CNf (1–28) was selectively precipitated from a plasmin digest of β-CN by using acidified calcium chloride and ethanol [19, 32]. The peptide was further purified by anion exchange fast protein liquid chromatography and the preparative mode of reversed-phase HPLC, which was also used to collect the peptide [19]. The identity of the major peak collected, which amounted to 95 percent of the total peptides, was verified by matrix-assisted laser desorption ionization time-of flight mass spectrometry at the Technion, Haifa, Israel. The K⁺ uptake into SMV was done by comparing SMV derived from the morning milking of control cows and the noon milking of experimental cows, that contained β-CN f (1–28) added at 5 µg ml⁻¹ (~1.5 µM), with a mixture that contained only the incubation solution.

Statistical Analysis

The data was statistically analyzed with the Fit Model procedure for repeated measurements, within the JMP software, Version 5 (SAS Institute, Cary, NC, USA), the between-subject factor was the treatment, and the within-subject factor was time. Differences were considered significant at $P < 0.05$. The model was:

$$Y_{ijklm} = \mu + \rho_i + \alpha_j + C_{(ij)k} + \gamma_l + \alpha\gamma_{il} + \varepsilon_{ijklm}$$

where Y_{ijklm} = the dependent variable, μ = overall mean, ρ_i = fixed effect of period (pre- or post-treatment; $i = 1$ or 2), α_j = fixed treatment effect j ($j = 1$ or 2), $C_{(ij)k}$ = random effect of cow k ($k = 1-18$) within period i and treatment j ; γ_l = effect of day l ($l = 1-3$ or $1-9$ for MY); $\alpha\gamma_{il}$ = effect of interaction of treatment j and day l ; and ε_{ijklm} = random error associated with cow k in period i and treatment j on day l .

Differences between treatments for period, or for specific days following the treatment were subjected to Student's t-test by means of the Tukey-Kramer Highest Significant Difference (HSD) test.

DISCUSSION

Our search for the involvement of apically located K^+ - channel in the mechanism of feedback regulation of milk secretion was inspired by the need for extensive apical K^+ conductance, since K^+ concentration of milk is considerably higher than that of plasma [19]. Indeed, K^+ channels have been localized in the apical aspect of mammary secretory epithelia [19, 31] and the present study, and have been shown to be associated in milk-borne negative feedback regulation of milk secretion [19, present study]. The voltage-dependent nature of the apical K^+ - channel [31], suggests that it belongs to the family of the voltage-gated potassium channels. Indeed, a KCNQ1 (a member of the voltage-gated K^+ - channels) and a number of its accessory subunits were recently localized in the human mammary epithelial cell line, MCF-7 (33). The assembly of KCNQ1 with the accessory units may shift the K^+ channel to an open state, associated with hyperpolarization of the membrane potential, which in general facilitates the secretory phenomena [33]. Thus, the milk-borne regulatory element (i.e., β -CN f (1–28)), which blocks apically located K^+ - channel [[19], present study] should cause depolarization of the membrane potential, and in-turn to down regulates cell metabolism and secretory activity. As discussed below, the present results further support the concept that apically located K^+ - channel and its natural milk-borne regulator are involved in negative feedback mechanism that controls milk secretion.

The involvement of PA-PG-PL system in regulation of milk secretion [19, 22] and the induction of mammary gland involution [23–26] are well established. The effect of the PA-PG-PL system was related to its contribution to enhanced degradation of the extracellular matrix [20, 34]. However, this alternative explanation fell to explain its effect on milk secretion and its sharp increase immediately after the start of active involution [20] (i.e., involution stage I) because in both the cases there is no increase in extracellular matrix degradation. The present results as discussed below in line with previous results [22–24], strongly suggest that the PA-PG-PL system works in mammary secretion by increasing casein degradation and liberation of active components, and that β -CN f (1–28) is a principal case in degradation product that involves the negative control of milk secretion.

Animals can adapt to hot environmental conditions by gradual acclimation [8]. As the present experiment was carried out in at mid-summer, it appears logical to assume that the cows were already acclimated to heat stress. Therefore, we first examined whether the treatments induced acute HS responses in the participating cows, and whether the effects of between-treatment differences in the imposed heat loads were significant?

The THI is a parameter that is widely used to describe the thermal stress imposed by climatic conditions on humans and farm animals. The THI is calculated from a combination of wet- and dry-bulb air temperatures for a particular day: THI values of 70 or less are considered comfortable, 75–78 stressful, and values greater than 78 cause extreme

distress [2, 6]. According to these criteria, cows in the three treatments were under extreme HS during all the days of the experiment, though the HS condition worsened quite dramatically on the second day. Nevertheless, the THI in this case obviously could not account for the differences between treatments in MY, in light of previous experimental findings that the THI accounted for only small proportion of the variance of HS related MY in dairy cows [1, 35]. This, is in part, because of wide variations between individuals, in part because the animal is related to its environment in a much more complex manner than is represented by this index, and in part because of the cooling measures applied, that help to relieve some of the heat stress. A major factor that is not taken into account in the THI is solar radiation [1]. Multiple regression analysis that used respiration rate and body temperature as the dependent response variables to derive an index of effective temperature load has shown that the constant associated with radiation (black globe temperature) was three times as great as that associated with ambient temperature (dry-bulb temperature) [36].

In order to solve the above problems, thermal physiologists adopted the stress-strain relationship from physical sciences as an applicable concept, with strain referring to an internal displacement from the resting or basal state brought about by external stress [1, 37]. Based on the differences in respiration rate and rectal temperature, the heat-load-related strain response diminished in the order, treatment E>treatment D>treatment C. A more detailed description than that provided by the classical thermoneutral zone concept of the relation between an animal and its environment was proposed [1], according to which, treatment E brought the cows deep into the noxious stage, in which coping attempts to maintain the correct body temperature are markedly unsuccessful, and drove them too close to the extreme stage, which is defined as that in which a vicious cycle of rising body temperature starts, that eventually may become lethal. Therefore, the experiment was terminated at this stage, and the cows were returned to their normal, most optimal conditions (with access to shade and cooling). This situation is consistent with previous reports that if hot conditions were sudden and prolonged, as is often the case in the Mediterranean areas and in some regions of the United States, cows cannot be regarded as acclimatized, as such heat-stress conditions are marked by falls in milk production and feed intake, and increased body temperature [1, 38].

Lactation is a physiological process that presents a substantial challenge to the homeostasis of the cardiovascular and fluid secretory system [1, 10, 12, and 13]. The acute and large decrease in milk secretion, particularly in treatment E, may, therefore, be considered as having vital importance that makes it necessary to enable the cows to survive the HS. Thus, our present results conflict with the concept that the initial reactions of the animal to acute HS represent merely an emotional rather than a thermoregulatory response (see discussion in reference [1]).

During the summer months, in Israel and hotter parts of the USA, MYs, as well as milk protein fat content, were found to be reduced, even in dairy herds in which the cows were cooled, which indicates that these reductions form part of their adaptive response [2, 6, 38]. On the other hand, acute stress in response to intramammary treatment with dexamethasone or to dehydration resulted in more intense inhibition of lactose and fluid secretion than of fat and protein secretion, which was reflected

in increased fat and protein concentrations in milk, though these increases did not compensate for the overall reduction in their yields [19, 30]. Thus, the present results regarding the effect of HS on fat and protein concentrations are consistent with the above-noted response to acute stress. In keeping with the previous findings [19, 20], in this chapter we present evidence that the acute reduction in milk secretion under HS is associated with the activation of the PA-PG-PL-release of β -CN (1–28) system. It has been shown that a decrease in Na concentration, increase in K concentration and the consequent decrease in the Na/K ratio is a sensitive indication of the disruption of the tight junction of the mammary gland epithelial cells, which relates to differing ion contents in milk and blood plasma [22, 39]. In previous studies stress-induced changes in milk secretion and composition were detected without evidence for disruption of the tight junction of mammary gland epithelial cells [19, 22, 27], which is also consistent with the present findings.

Isolation and regrouping has been shown to impose an emotional stress that is associated with reduced MY and activation of the systemic stress response [39, 40]. Thus, the significant reduction in MY in treatment C, may also relate to activation of a local negative-feedback control, in response to emotional stress. However, we could not test this hypothesis because of the confounding effect of the increase in HS between the start and second day of the experiment, which independently could have activated the negative-feedback regulatory system.

The present study highlighted two previously unreported features of this local negative-feedback regulatory system.

First, that is a very fast-responding and flexible system, which can respond to diurnal (night versus day) changes in the ambient conditions. Such a precise level of response to fluctuating conditions may be made possible, if the mammary gland cells themselves serve as a regulatory afferent component in the regulatory system. In keeping with such a hypothesis, there is evidence that local heat shock induces endogenous hyperfibrinolysis, which is equivalent to enhanced caseinolysis in the present case, by the upregulation of plasminogen activators [41].

The hypothesis that HS induces a short-term rapid regulatory response is consistent with evidence that in lactating cows under commercial production conditions, the effects of HS that may be experienced under exposure to high ambient temperatures during the day appears to be ameliorated when temperatures fall at night, and that lack of a cool night-time ambient temperature intensifies the reduction in MY [1, 38].

Secondly, we demonstrated that expression of potassium channels on the apical membrane serves as a regulatory component in the negative-feedback system, by increasing the apical-membrane K channel sensitivity to β -CN f (1–28) levels, and this, most likely, further contributes to the accuracy and efficacy of the system. A turnover with biological half-life of 7.3 hr was demonstrated for a KATP channel [42]; thus, the rapid night to day shift in the sensitivity to K^+ uptake through apical-membrane-derived vesicles is theoretically possible.

RESULTS

Respiration rate per minute measured on the second day of the experiment at 1300 varied significantly among the treatments being 68 ± 7 in treatment C, 102 ± 8 in treatment

D and 152 ± 10 in treatment E ($P < 0.01$). Similar ranking (39.1 ± 1 , 39.5 ± 1 , 41.6 ± 1 , respectively, $P < 0.01$) was recorded with respect to rectal temperatures measured at 1400 on the second day.

The MYs of all cows were in the range 48–49 l/d before the start of the experiment, and did not differ between the treatments at that time (Table 1). All treatments induced a significant drop in MY, starting at first day, which maximized at second day of the experiment (Fig. 1, Table 1). However, the treatments differed in the extent of the responses: treatment E (a maximal drop of 55.1% in comparison to the pre-treatment yield) > treatment D (-18.2%) > treatment C (-7.9%). After returning the cows to their original group in the afternoon of second day, the treatment's effects on MY faded within the next 4 days, and the recovery appeared to be slower (within 7–10 days) in treatment E (Fig. 1).

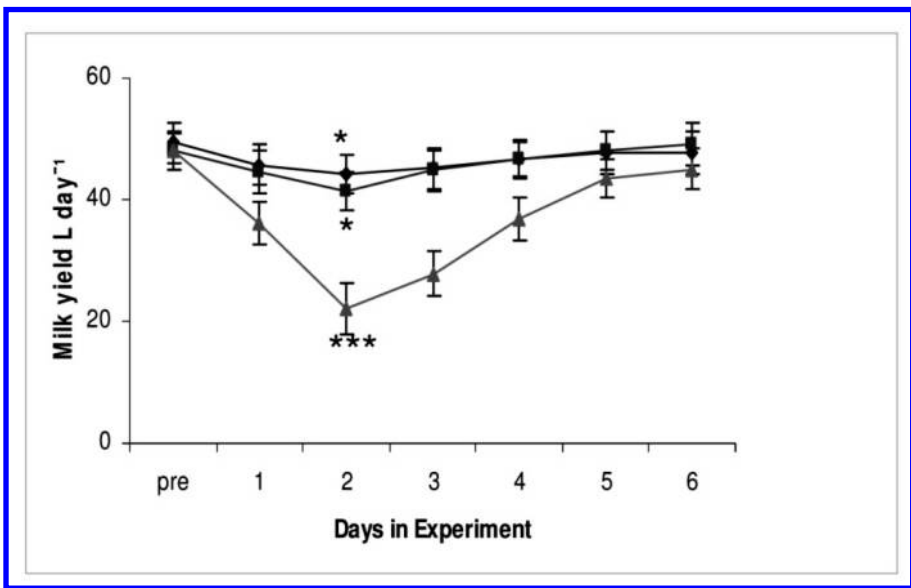


Figure 1: Effect of treatments on MY and its post-treatment recovery. (diamonds, treatment C; squares, treatment D; triangles, treatment E; * $P < 0.05$ in comparison with pre-treatment values; *** $P < 0.001$ in comparison with pre-treatment values and treatments C and D).

Table 1: Effect of Treatments on MY and on the Diurnal (day versus Night) Variations in Milk Secretion.

Treatment	Control (C)	SD	Cooling (D)	SD	Sun (E)	SD
Initial milk yield, Ld ⁻¹	47.9	3.1	49.3	3.5	48.1	3.6
Night, Lh ⁻¹	1.80 ¹	0.2	1.61 ¹	0.2	1.40 ¹	0.2
Day, Lh ⁻¹	1.45 ²	0.3	1.40 ²	0.2	0.65 ²	0.3
Day/Night yield ratio	0.81 ^a	0.09	0.88 ^a	0.1	0.46 ^b	0.07
Total yield, Ld ⁻¹	44.1	2.5	40.3	2.5	21.1 ^c	3.1
Decrease in milk yield, %	7.9 ^a	1.5	18.2 ^b	3.6	55.1 ^c	5.5

Value marked by different superscript numbers are significantly different within columns; value marked with different superscript letters are significantly different within rows.

Hourly milk secretion rates were determined by dividing the milk recorded at milking by the time interval (~8 hr) since the previous milking. Though, within each group, the yield tended to be higher between 0600 and 1400 than between 1400 and 2200, the figures did not differ statistically. Therefore, we pooled the MYs into night-time yield (2130–0530 the next morning) and daytime yield (0530–2130 on the same day). Within each group, the milk secretion rate was higher during the night than during the day according to treatments, E difference > treatment D difference = treatment C difference; the daytime yields being lower than the night-time ones by 48, 20, and 19 percent respectively. Consequently, the difference in MY between treatment E and treatments D and C was smaller during the night than during the day (Table 1).

The treatments did not induce changes in concentrations of lactose, Na (~16 mM), and K (~43 mM), nor, in the Na/K ratio (~2.7), but elicited increases in total fat and protein concentrations (Table 2). The increase in fat and protein concentration was more apparent in the samples taken at 1400 than in those taken at 0600 am, and the treatments differed in the magnitude of this response, in the order, treatment E > treatment D > treatment C. The increase in fat and protein concentrations elicited by the treatments did not compensate for the drops in their yields caused by the fall in MY; however, the differences between night and day secretions of fat and protein were not observed in treatment D (Table 2).

Table 2: Effect of Treatments on Milk Composition and on the Diurnal (Day versus Night) Variations in Milk Composition.

Treatment	Control (C)	SD	Cooling (D)	SD	Sun (E)	SD
Average	<u>Lactose Concentration (%)</u>					
Night	5.10 ^a	0.11	5.05 ^b	0.10	5.04 ^b	0.13
Day	5.10 ^a	0.09	5.05 ^b	0.11	5.05 ^b	0.12
	5.09 ^a	0.11	5.04 ^b	0.09	5.04 ^b	0.12
	<u>Lactose Yield</u>					
Night, g h ⁻¹	91.8 ^{1a}	5.5	81.3 ^{1b}	5.4	70.6 ^{1c}	5.6
Day, g h ⁻¹	73.8 ^{2a}	4.9	70.6 ^{2a}	5.3	35.1 ^{2b}	5.9
Day/Night yield ratio	0.80 ^a	0.09	0.87 ^b	0.10	0.46 ^c	0.08
Decrease in lactose yield, %	7.9 ^a	1.5	18.1 ^b	3.8	55.0 ^c	5.5
	<u>Fat Concentration</u>					
Average	3.17 ^a	0.08	3.25 ^b	0.05	3.31 ^c	0.09
Night	3.13 ^a	0.07	3.05 ^b	0.06	3.13 ^c	0.07
Day	3.19 ^a	0.05	3.35 ^b	0.05	3.40 ^c	0.09
	<u>Fat Yield</u>					
Night, g h ⁻¹	56.3 ^{1a}	3.8	49.1 ^{1b}	3.5	43.8 ^{1c}	3.6
Day, g h ⁻¹	46.3 ^{2a}	3.7	48.6 ^{2b}	3.7	22.1 ^{2c}	5.1
Day/Night yield ratio	0.82 ^a	0.07	0.99 ^b	0.15	0.50 ^c	0.12
Decrease in fat yield, %	7.8 ^a	1.4	15.9 ^b	1.1	49.5 ^c	1.2
	<u>Protien Concentration (%)</u>					
Night, g h ⁻¹	57.4 ^{1a}	3.9	51.0 ^{1b}	3.1	44.9 ^{1c}	4.5
Day, g h ⁻¹	46.7 ^{2a}	4.1	47.3 ^{2b}	3.5	22.9 ^{2c}	4.7
Day/Night yield ratio	0.81 ^a	0.08	0.93 ^b	0.15	51.0 ^c	1.0
Decrease in protien yield, %	7.9 ^a	1.5	15.8 ^b	1.2	49.4 ^c	1.8

Value marked with different superscript numbers are significantly different within columns; value marked with different superscript letters are significantly different within rows.

Table 3 shows that acute HS led to increased PA and PL activities, and reduction in the PG/PL ratio in the milk; the magnitude of this response diminished in the order

treatment E > treatment D > treatment C. As noted above with regard to MY and milk composition, there were marked differences between day and night values, and the between-treatments differences in this effect were greater in samples taken at the mid-day milking, and less in those taken at the morning milking (Table 3).

Table 3: Effect of Treatments on Plasminogen Activator-Plasminogen-Plasmin System in Milk and on the Diurnal (Day versus Night) Variations in their Activity.

Treatment	Control (C)	SD	Cooling (D)	SD	Sun (E)	SD
	<u>Average</u>					
Plasminogen activator (PA), unit ml ⁻¹	11.50 ^{1a}	0.11	15.06 ^{1b}	0.11	17.62 ^{1c}	0.21
Plasminoge (PG), unit ml ⁻¹	27.51 ^{1c}	0.90	25.60 ^{1b}	0.82	23.91 ^{1c}	0.70
Plasmin (PL), unit ml ⁻¹	5.11 ^{1a}	0.11	5.04 ^{1b}	0.09	9.12 ^{1c}	0.21
Plasminogen/plasmin, ratio	5.38 ^{1a}	0.12	5.08 ^{1b}	0.15	2.62 ^{1c}	0.25
	<u>Night</u>					
Plasminogen activator (PA), unit ml ⁻¹	10.80 ^{2a}	0.30	15.20 ^{2b}	0.15	15.42 ^{2c}	0.19
Plasminoge (PG), unit ml ⁻¹	30.43 ^{2a}	0.90	23.58 ^{2b}	1.30	29.11 ^{2c}	1.50
Plasmin (PL), unit ml ⁻¹	5.43 ^{2a}	0.09	4.90 ^{2b}	0.10	6.56 ^{2c}	0.11
Plasminogen/plasmin, ratio	5.60 ^{2a}	0.21	4.81 ^{2b}	0.30	4.44 ^{2c}	0.25
	<u>Day</u>					
Plasminogen activator (PA), unit ml ⁻¹	11.58 ^{3a}	0.17	15.80 ^{3b}	0.15	18.72 ^{3c}	0.29
Plasminoge (PG), unit ml ⁻¹	26.05 ^{3a}	0.17	26.61 ^{3b}	0.16	21.31 ^{2c}	0.15
Plasmin (PL), unit ml ⁻¹	4.95 ^{3a}	0.15	5.11 ^{3b}	0.15	10.40 ^{2c}	0.14
Plasminogen/plasmin, ratio	5.26 ^{3a}	0.16	5.21 ^{3b}	0.17	2.05 ^{2c}	0.25

Value marked with different superscript numbers are significantly different within columns; value marked with different superscript letters are significantly different within rows.

The data in Fig. 2 clearly show that acute HS increased the concentration of K⁺ channel blocker in the milk serum (whey devoid of SMV; Inf) as reflected in the inhibition of K⁺ uptake into SMV. The magnitude of this response diminished in the order treatment E > treatment D > treatment C.

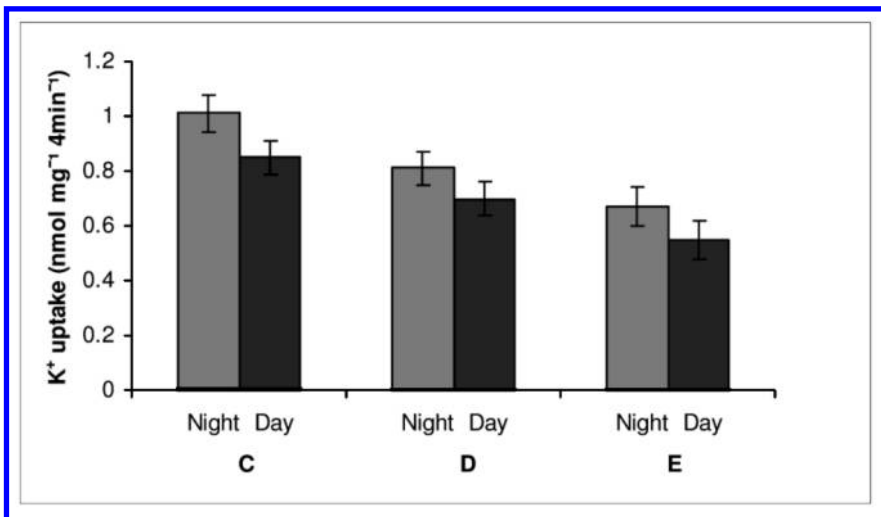


Figure 2: Effect of treatments and time of sampling on K⁺ uptake, into vesicles derived from milk serum and incubated with the respective infranatant (milk serum devoid of vesicles and casein micelles). All the treatments (C, Control, D, treatment D, E, treatment E) and sampling time within treatment (night versus day) effects were significant at P < 0.05).

Figure 3 depicts the results of K⁺ uptake determinations; it presents comparisons of all possible combinations of Inf and SMV sampled from the control cows in the morning milking with those sampled from the experimental cows at midday. The combination of Inf and SMV sampled from the morning milking of the control cows (Cinf-CSMV) served as the reference value. Inhibition of K⁺ uptake into the vesicles diminished in the order: Einf-ESMV>Einf-CSMV>Cinf - ESMV, with values of 52, 68, and 77% of Cinf-CSMV, respectively. The data in Fig. 3 is consistent with that in Fig. 2, which shows that acute HS increased the concentration of K⁺ channel blocker in the milk serum, in proportion to the HS level. However, the data also indicates that vesicles SMV coming from heat-stressed cows were more responsive to the activity of the K⁺ channel blocker.

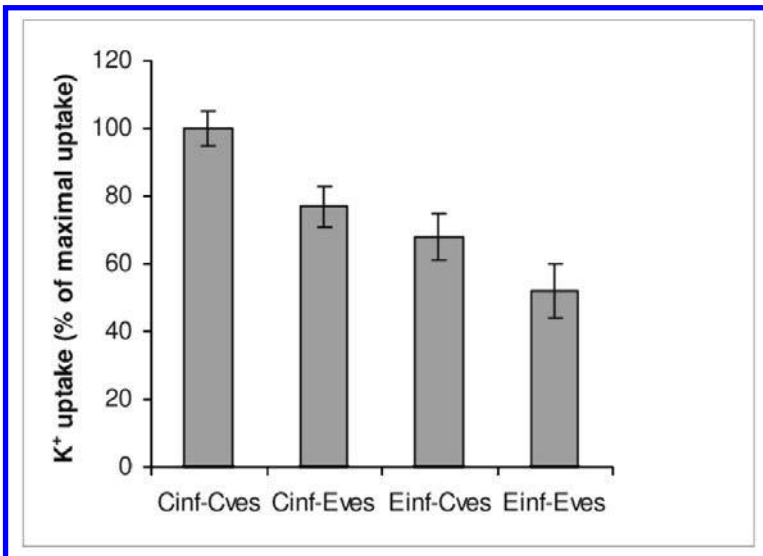


Figure 3: Effects on K⁺ uptake into the vesicles, of all combinations of incubating infranatant (milk serum devoid of vesicles and casein micelles) with milk serum-derived vesicles sampled from the control cows at the morning milking and experimental cows at the noon milking. All combinations differed significantly at P < 0.01.

Previously, we identified β -CN f(1–28), as the blocker of the putative K⁺ channel in milk serum-derived vesicles, which serve as a model of the K⁺ channel located on the apical aspect of mammary gland epithelial cells [19]. In order to refine the finding that vesicles derived from heat-stressed cows were more susceptible to the K⁺ channel blocker than those from unstressed cows, we incubated the vesicles derived from the morning milking of control cows and the noon milking of experimental cows, with a fixed amount (~1.5 μ M) of β CN f(1–28), and measured their K⁺ uptakes. The data in Fig. 4 clearly show that vesicles derived from the experimental cows were more susceptible to the channel blocking activity of β -CN f(1–28), than those derived from the control cows. In general, the level of inhibition obtained in this experiment was consistent with previous dose-response test results [19].

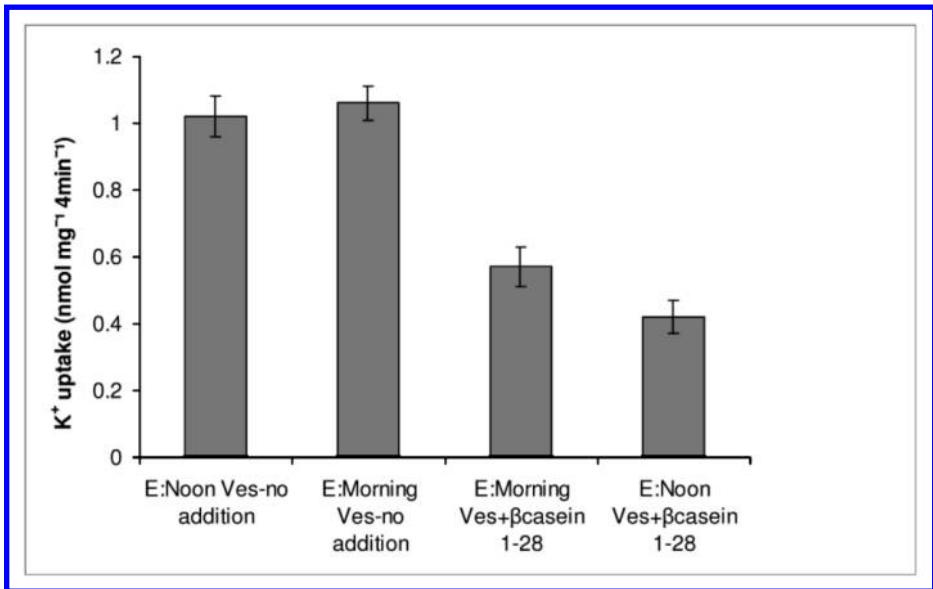


Figure 4: K⁺ uptake in milk serum-derived vesicles sampled from morning milking of control cows and noon milking of the experimental cows, with and without the presence 10 μM of β-CN f (1–28) in the incubation medium. The effect of the presence of β-CN f (1–28) was significant at P<0.001, whereas the effect of the source of the vesicles was significant at P<0.01).

CONCLUSION

We presented evidence that the acute phase in the regulatory inhibition of milk secretion in cows subjected to HS is related to the upregulation of the local PA-PG-PL-β-CN f (1–28) peptide in milk and that this peptide in turn down regulates the activity of K⁺ channels on apical-membranes derived vesicles. Further research is needed, to determine the nature of the interaction of β-CN f (1–28) with regulatory elements in the apical membrane of mammary gland epithelial cells, and to identify these channels and the components of the inward signal transduction. We are currently pursuing to hypothesize that the putative apical K⁺ channels belong to the family of voltage-gated channels and that β-CN f (1–28) causes membrane depolarization, explaining its milk down-regulatory effect.

KEY WORDS

- β-Casein (CN)
- Heat Stress
- Phenotypic plasticity
- Plasminogen activator (pa)
- Plasminogen (PG)-plasmin (PL)
- Skim-milk-derived vesicles (SMV)

AUTHORS' CONTRIBUTIONS

Nissim Silanikove conceived the project, supervised all of its stages, and wrote the manuscript; Fira Shapiro carried out the biochemical analysis; Dima Shinder carried out the potassium uptake measurements. All authors read and approved the final manuscript.

ACKNOWLEDGEMENTS

The authors would like to thank Dr. U. Mualem, the manager of the ARO Experimental Dairy Farm, at the time the experiment was carried out, for his valuable help in organizing the experiment.

Chapter 11

Insect Physiology and Detection of Moving Targets

Steven D. Wiederman, Patrick A. Shoemaker, and David C. O'Carroll

INTRODUCTION

We present a computational model for target discrimination based on intracellular recordings from neurons in the fly visual system. Determining how insects detect and track small moving features, often against cluttered moving backgrounds, is an intriguing challenge, both from a physiological and a computational perspective. Previous research has characterized higher-order neurons within the fly brain, known as “small target motion detectors” (STMD), that respond robustly to moving features, even when the velocity of the target is matched to the background (i.e. with no relative motion cues). We recorded from intermediate-order neurons in the fly visual system that is well suited as a component along the target detection pathway. This full wave rectifying transient cell (RTC) reveals independent adaptation to luminance changes of opposite signs (suggesting separate ON and OFF channels) and fast adaptive temporal mechanisms, similar to other cell types previously described. From this physiological data we have created a numerical model for target discrimination. This model includes non-linear filtering based on the fly optics, the photoreceptors, the first order inter-neurons (Large Monopolar Cells), and the newly derived parameters for the RTC. We show that our RTC-based target detection model is well matched to properties described for the STMDs, such as contrast sensitivity, height tuning and velocity tuning.

Certain flies (as well as other kinds of insects) detect and track small moving objects as they engage in rapid pursuits, demonstrating the capability to discriminate between targets (e.g. other flies) and an often cluttered, moving background [1, 2]. This is an especially challenging task considering that the fly compound eye limits visual resolution to one degrees [3].

Neurons sensitive to (and in some cases selective for) small moving targets have been described in a variety of insect species [4-7]. Recent intracellular investigations have more carefully characterized a number of target-selective neurons in the optic ganglia of the hoverfly [8-10]. These STMDs were found to be exquisitely selective for small targets subtending no more than a few degrees of the visual field, equivalent to just one or two “pixels” of the compound eye. The receptive fields of STMDs vary in size, with some extending just a few degrees, to those that encompass the whole eye hemifield. The target response may vary in magnitude across this region; however the size selectivity is independent of the target location [8] or the size and shape of the receptive field [9].

The STMDs respond to targets moving relative to a background, in many cases when the background itself is moving [9]. Conceptually, it would seem likely that

neural mechanisms required for such a task involve segregation of the motion of the target from the motion of the background. Surprisingly, while some of the STMDs exhibit a suppressed response in the presence of background motion, a sub-set responds robustly even when the targets move at the same velocity as the background, i.e. with no relative motion cues [9]. However, the response to wide-field background motion alone elicits no response. This implies that the spatial statistics of small targets, with respect to the background, form an important cue for discrimination, regardless of any additional role that may be played by other motion cues [9].

Computational Models for Target Discrimination

Understanding the computation that underlies small target selectivity and rejection of background motion presents a daunting challenge. Some models for target discrimination rely on inhibitory feedback of wide-field motion signals to localized motion detectors [11, 12], which may provide an explanation for small target selectivity, but would lead to inhibition by background motion. Another model, for what some thought at the time was the target selectivity of a higher order locust neuron [13], has lateral inhibitory interactions around a central unit. This model was based on cells responding transiently to both contrast increments (ON channel) and contrast decrements (OFF channel) in a full-wave rectified manner. A lateral unit, derived from the local signal spread of these channels, was hypothesized to mediate the inhibitory interactions on these centre units [14]. Here we examine and model a similar neuron type we refer to as the RTC. We show that fast temporal adaptation and lateral inhibitory connections, characteristic properties of RTCs, could provide the basis for an alternative model for small target selectivity, robust against wide-field background motion.

Full-wave Rectifying Transient Neurons

Extracellular recordings in the first optic chiasm between second and third order interneurons of the fly brain (between the lamina and medulla), first showed the presence of “on-off” cells (Arnett fibers) with full-wave rectification [15, 16]. Surprisingly, these cells were later re-examined and shown to adapt independently to luminance changes, depending on the polarity (increment or decrement) of the change [17]. This independent adaptation was also observed in medullary neurons in the locust [18]. These locust neurons had a “breakthrough response” when stimulated with a pulse of the same polarity but greater contrast than the prior adaptor. The authors hypothesized that this non-linear adaptation might enhance responses to the contrasting edges of visual features, while rejecting lower contrast “textual detail” [14, 19].

Spatial antagonism observed in the Large Monopolar Cells (LMC), an earlier first order interneuron in the lamina, appears to utilize inhibitory interactions between the nearest neighbor receptors [20]. However, in the “on-off” cell experiments [21], separated pulses (5°) revealed antagonism on a larger spatial scale, equivalent to several facets of the compound eye. The authors proposed a model where rectification occurs after lateral inhibition of the sub-units (Fig. 1A), however, unless the inhibitory influence of neighbors is excessively strong, it is difficult to explain why the summing of spatially separated rectified signals, responding to pulses of “like” sign, should produce an inhibition of the overall response as was observed [21]. These results lead us to propose the

possibility of a second-order of local inhibitory interactions between “like” ON channels and OFF channels, before they are re-combined via spatial pooling (Fig. 1B).

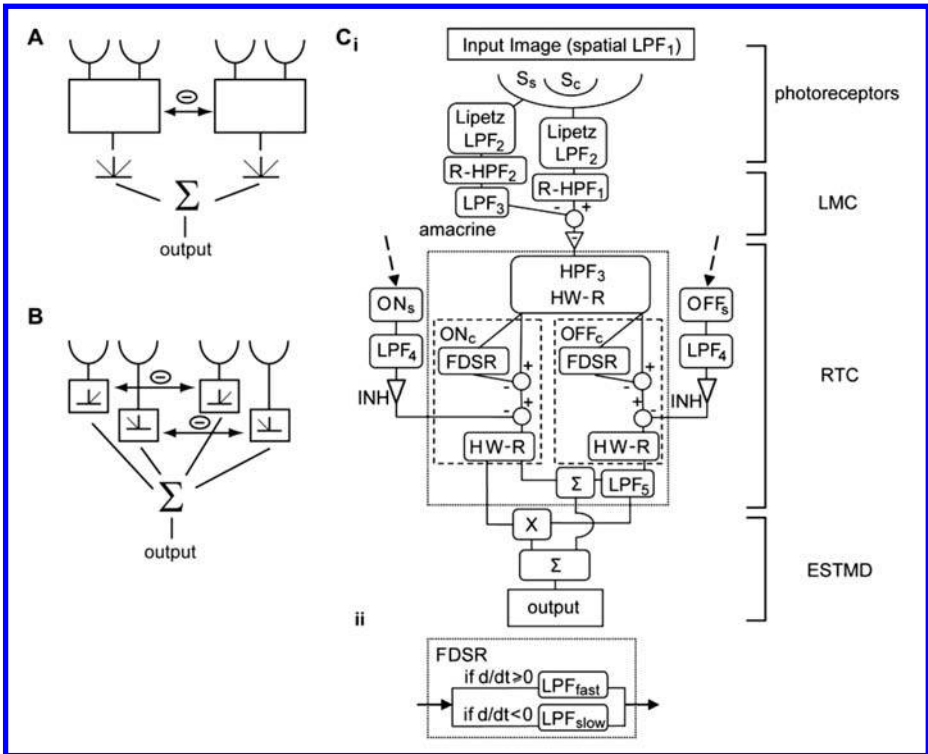


Figure 1: Model overviews. (A) Model of the “on-off” unit as described by Jansonius and van Hateren [21]. The transient sub-units exhibit fast adaptation and lateral inhibition before full-wave rectification and spatial pooling. (B) Our proposed version of rectifying transient cells where fast adaptive units are segregated into ON and OFF channels via half-wave rectification. Each polarity channel laterally inhibits one another before spatial pooling. (Ci) The detailed block diagram of the elementary small target motion detector (ESTMD) model. Early visual processing (photoreceptors, LMC and amacrine cells) is modeled with optical blurring (LPF1), a nonlinear compressive transform (Lipetz function) with an adaptive mid-point parameter, and spatiotemporal band-pass filtering (LPF2 and 3, R-HPF1 and 2). The signal is separated into independent channels (responding to contrast increments and decrements respectively) via further high-pass filtering (HPF3) and half wave rectification (HW-R). Each channel exhibits fast adaptation, implemented via the FDSR inhibition (see Cii). The channels are separately inhibited by a delayed (LPF4) signal derived from surrounding channels of the same type. The strength of this surround inhibition is determined by the free gain parameter INH. To implement sensitivity to the dark targets, the OFF channel is delayed (LPF5) and then recombined with an undelayed ON channel in either a linear (Σ) or quadratic (X) manner. (Cii) Fast depolarization, slow repolarization (FDSR). If the input signal is “depolarizing” (positive temporal gradient), a first-order low pass filter with a small time constant (LPF_{fast}) is used, otherwise for a “re-polarizing” signal (negative gradient) a larger time constant is applied (LPF_{slow}). The resulting processed signal represents an “adaptation state” which then subtractively inhibits the unaltered pass-through signal. [LPF1 Gaussian blur (half-width 1.4°); LPF2 $\tau = 2.5$ ms; R-HPF1 and 2 and 3 $\tau = 40$ ms, 30% DC; LPF3 and 4 $\tau = 2$ ms; LPF5 $\tau = 25$ ms; LPF_{fast} $\tau = 1$ ms; LPF_{slow} $\tau = 100$ ms; INH = 3 (free parameter)].

Rectifying Transient Cells in the Target Detection Pathway

We have developed a model for small target motion detection inspired by the properties of the higher order STMDs, and including a RTC-type component. We validate key stages of the model with intra-cellular recordings of the RTC in the fly (*Calliphora stygia*) medulla and with published physiological data. We investigate the temporal responsiveness of the RTC and obtain filtering parameters for the STMD model. We show that the properties of independent adaptation and lateral inhibitory interactions, as observed in “on-off” cells and the RTC, are well suited for a role in target detection. We show that the spatiotemporal signature associated with the motion of a small feature is the passing of two contrast boundaries of opposite polarities (i.e. due to the leading and trailing edges), with limited spatial extent which induces an excitatory response little affected by centre-surround inhibition or adaptation of the presumed ON and OFF channels. We include a stage for the re-combination of ON and OFF channel signals, as yet untested by electrophysiological experiments, which enhances small target sensitivity. Finally, we show that this model leads to enhanced target discrimination, even when there are no relative motion cues between the target and the background.

MATERIALS AND METHODS

Modeling

A model for an elementary small target motion detector (ESTMD) was created in Simulink (Mathworks), with image preparation and analysis tools programmed in Matlab (Mathworks). The term “elementary” refers to a single unit that would be pooled to emulate the “position invariant” nature of an STMD neuron [8]. Each major component in the model (Fig. 1C) is inspired by key stages in visual processing and will be discussed in detail later.

We neither attempt to emulate biophysical properties of cellular dynamics, e.g. compartmental modeling, nor are we developing a neural network representation. Rather we are building a numerical model based on linear and non-linear spatial and temporal filtering and typical feed-forward signal processing methods. This approach allows for the model to be implemented in engineering applications.

The ESTMD model was tested using a series of panoramic images (Fig. 2) (see Input Imagery) animated at a high temporal sample rate (5 kHz) to simulate continuous time. A 5×5 array of local “photoreceptor” inputs was used to evaluate the response of the central ESTMD (Fig. 3). Because the input imagery is a circular panorama, continuous motion allows estimation of the output of this ESTMD for all horizontal locations on the image. The region of interaction was shifted vertically in 1° increments to build up a two dimensional representation of the ESTMD outputs in a raster fashion (Fig. 3). The stimulus was rotated at 90°/s (within the optimal range for STMD neurons [8]) for two complete revolutions, with the first discarded, to avoid start-up transients.

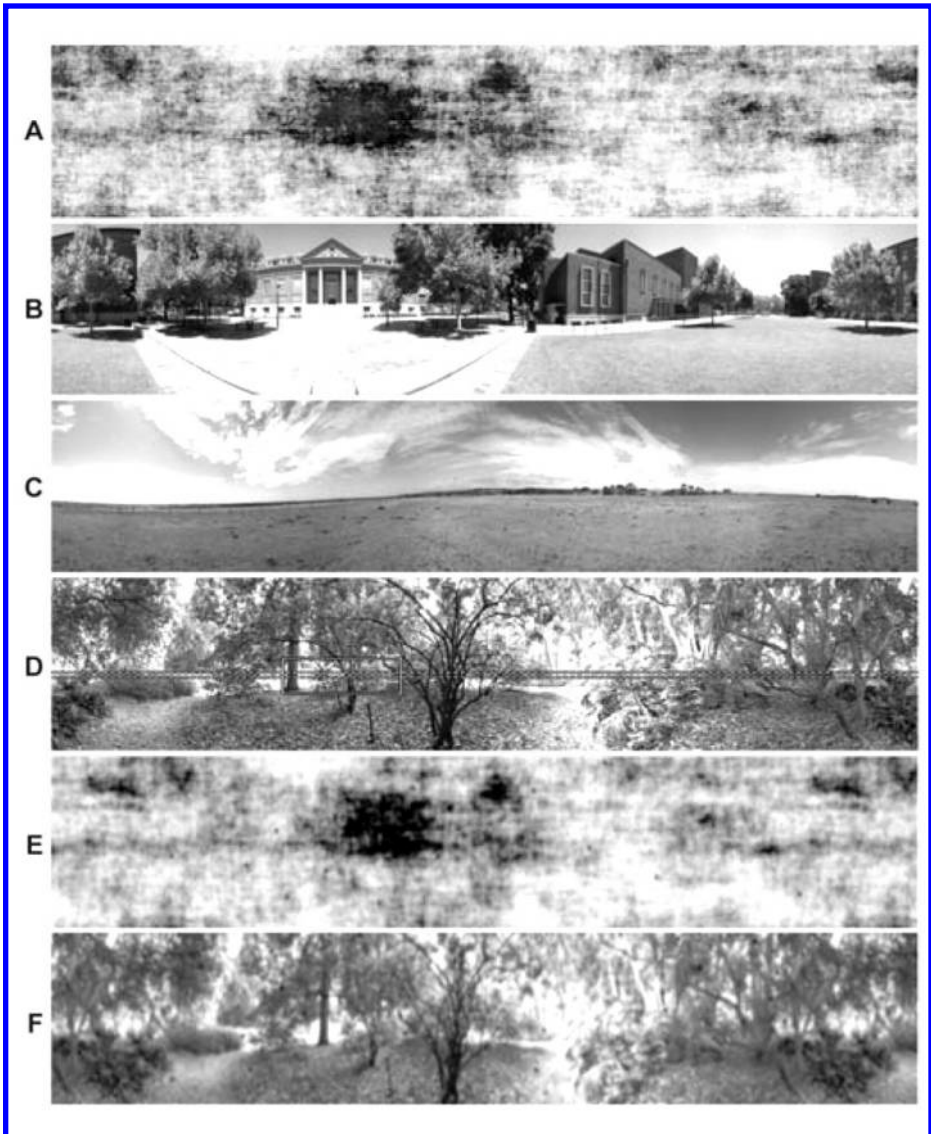


Figure 2: Input images and optical blurring. Four panoramic images are used as model inputs to test target discrimination. The images display natural statistics with luminance intensity inversely proportional to spatial frequency [24]. Image (A) is composed of the average magnitude and phase of 13 natural images [22]. Image (B) includes several man-made structural elements. Image (C) is relatively sparse, while (D) is a highly cluttered scene. The images are panoramic and extend 72° vertically. They have a resolution of 2048×410 pixels, with the “A” channel of the RGB image (depicted here in grayscale) retained for further processing, approximating the spectral sensitivity of motion detection mechanisms in the fly visual system [23]. The row section highlighted in image (D) corresponds to the data traces of Fig. 9. Images (E) and (F) are the optically blurred versions of images (A) and (D), including 20 pseudo-randomly scattered targets ($1.6^\circ \times 1.6^\circ$) in each image.

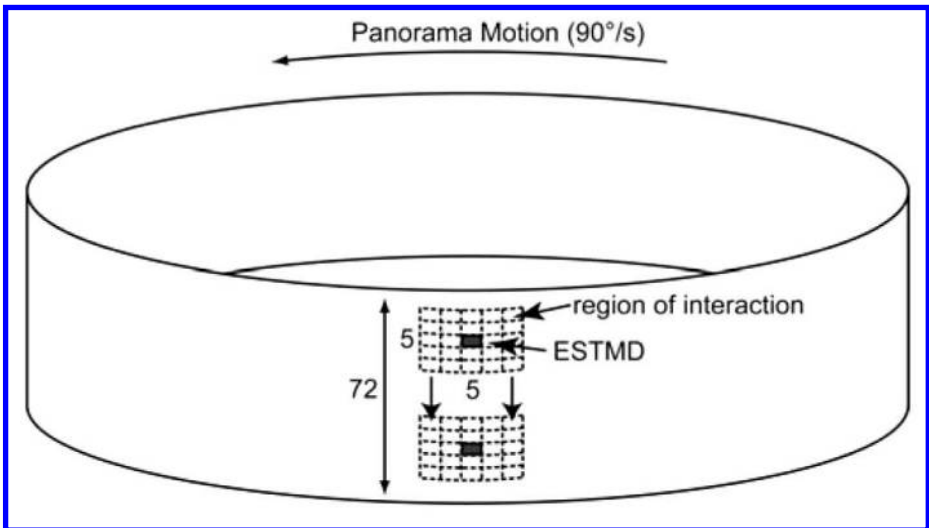


Figure 3: Panorama rotation. A single model output has 25 “photoreceptors” as inputs, each with 1° sampling separation (inter-ommatidial angle), thus representing a $5^\circ \times 5^\circ$ grid. The values representing luminance intensities at these locations vary over time as the panorama image is rotated past the ESTMD at $90^\circ/\text{s}$. Linear interpolation between pixels in the horizontal spatial domain results in higher temporal resolution (sampling at 5 kHz). There is an ESTMD at each degree separation down the vertical column, therefore 72 in all, each with overlapping, feed-forward, receptive fields.

Input Imagery

To test for robustness of the model for discriminating targets embedded in visual clutter, a series of three panoramic images (Fig. 2B–D), with a 72° vertical extent, were acquired from natural habitats [22]. The 8-bit images were 2048×410 pixels. Although original panoramas were sampled as RGB, all simulations used the green channel only in order to approximate the spectral sensitivity of the fly photoreceptors that sub-serve motion processing [23]. A fourth image (Fig. 2A) was obtained by combining the three natural images with ten others and averaging their phase and magnitude in the frequency domain [22]. This combined image, while displaying a typical power spectrum, lacks hard edge-like contours found in many (but not all) natural images. This image acts as a control with respect to potential phase congruency components underlying the motion detection mechanisms. The first stage of modeling emulates fly optics via spatial blurring (see Results: Photoreceptors), therefore reducing hard edges, including those of the targets. The Gaussian blurring is shown for two images (Fig. 2E, 2F) with 20 scattered $1.6^\circ \times 1.6^\circ$ targets embedded. The targets effectively have varying contrasts, and are difficult to discern, revealing the challenging nature of this target discrimination task. All of the four images had power spectra showing an approximately $1/f$ dependence on spatial frequency f , which is typical of natural images [24, 25].

We created a second set of images, identical to the first, but into which black targets ($1.6^\circ \times 1.6^\circ$) were pseudo-randomly distributed, with each target centered on an ommatidial row. To improve computational efficiency, we inserted twenty such targets into each image. We maintain a 70° horizontal separation between the targets and a

6° vertical separation. This limits spatiotemporal interactions between the targets at any stage of modeling, with a larger (in effect longer) horizontal separation required, as this becomes the resultant temporal domain due to the panorama being rotated horizontally (influences are of longer-term adaptive components, e.g. photoreceptor dynamics). Because these targets become a feature of the image (i.e. there is no relative motion between targets and background) these simulations test the most demanding condition observed in physiological STMD experiments [9].

Model simulation was run with a single control trial using the original panoramas without targets and 26 trials (for each image) in which different pseudo-random target distributions were used, allowing us to evaluate responses from a total of 26×20 target locations, across four images.

To analyze how effectively the targets are discriminated a spatial image of the model output, at varying stages of processing, was reconstructed from the vertical columnar units, and binning of the horizontal time dimension (back into an equivalent 1° spatial domain). Target locations are determined taking the non-uniform lag into account. We determine “hits” (above threshold output corresponding to target location) and “false positives” (above threshold outputs not corresponding to target locations). This categorization is done for each image (Fig. 2), at each processing stage, and across varying model output thresholds. By varying this threshold and plotting the “hit” rate (relative to total targets present in the scene) versus number of “false positives,” we constructed Receiver Operating Characteristic (ROC) curves.

In addition to the experiments using natural images, basic characteristics of the ESTMD were evaluated using a similar stimulus paradigm into which targets of varying contrast, height and velocity were animated against bright or mean luminance backgrounds.

Physiology

Flies (*Calliphora*) were either caught in the wild or reared in the laboratory under a natural day/night cycle. Insects were immobilized with wax. The back of the head was shaved, and a small hole was removed in the cuticle. Air sacs and other tissue were removed to provide clear access to the medulla. The brain was immersed with a Ringer solution: NaCl (130 mM), KCl (6 mM), $MgCl_2$ (4 mM), $CaCl_2$ (5 mM), with HEPES buffer at pH 7.0. Osmolarity was adjusted to 450 mM with the addition of sucrose. The fly was positioned to view a 200 Hz CRT monitor, mean luminance of 100 cd m^{-2} . The visual stimuli were programmed in Python, using the VisionEgg stimulus software (www.visionegg.org).

Micro-pipettes were pulled from 1 mm (O.D.) thick walled alumina-silicate glass capillaries (SM100F-10, Harvard Apparatus Ltd.), on a Sutter Instruments P-97 puller, and filled with 2 M KCl or 2 M potassium acetate. Electrode resistances were typically 120–150 M Ω .

A wide-field, square-wave, flicker stimulus (1 Hz) was induced opposing polarity potentials within the extracellular space. Intracellular recording from the RTC was identifiable by: a) by a drop to resting membrane potential of approximately -60 mV ; b) the full-wave rectification of the signal; c) depolarizing responses of 10–15 mV

(graded), with ~ 10 mV spikelets. The data was sampled at 5 kHz during acquisition, using a National Instruments 16-bit ADC. Data analysis was performed offline with Matlab.

DISCUSSION

By recording from a cell in the fly medulla (the RTC) we have been able to determine their quick temporal responsiveness to transient stimuli. This has provided parameters, such as adaptation time constants, that form the basis of our target detection model. We have compared responses of the model, e.g. contrast sensitivity, height tuning, and velocity tuning, to those observed in STMD physiological recordings and found that they are well matched.

We have shown that linear systems analysis of steady-state responses is not an appropriate method for characterization of the relevant neural responses (Fig. 5). In this case, when we consider the quickly adapting transient component of the RTC signal, we find the temporal responsiveness is well matched to the presumed early components of the visual system (the LMC). We also observe that apparent contrast insensitivity of a neural system may be the result of wide-field antagonistic interaction. In our modeling, due to a neural delay in the surround interactions, the naturally “unrealistic” wide-field flicker can transiently pass through the system, however with low contrast sensitivity the result. In comparison, the response to the limited spatial extent of a small target is quite contrast sensitive.

Larger wide-field STMD neurons display a position invariant receptive field that typically spans many ommatidia [8]. This presumably requires a pooling of the outputs of many sub-units from earlier stages of processing. In fact, because some STMD neurons are weakly direction-selective [8-10], rather than a summative pooling of “non-directional” sub-units, some type of higher-order spatial facilitation may take place. Weak direction selectivity could be built into our modeling via asymmetry in the inhibitory surrounds or via a higher order spatial facilitation during this pooling stage.

Unfortunately, RTC neurons are small and intracellular recording times are limited in duration. We have, to date, neither been able to establish the morphology of the neuron via dye-filling techniques nor can we examine more time intensive spatial characterization stimuli. Nevertheless, we are confident from our dissection technique and precise control of the location of the pipette that our regular recordings from the RTC are from the medulla. However, we cannot be certain if they are intrinsic to the medulla, or if they reside elsewhere and project to, from, or via the medulla. There is a possibility that they may be the termination of the fibers identified by Arnett [15-16] or a later post-synaptic element that has inherited the properties as seen in the projections from the lamina. Although our biological investigation of the RTC is limited, the aspects of computation that form the basis for our small target modeling has been well established in the work of Jansonius and van Hateren [17], Osorio [19] and now again in this present research.

RESULTS

We consider here in detail both the major stages of our model, and compare their outputs with known biological counterparts.

PHOTORECEPTORS

After target insertion we low-pass filter input images (Gaussian, half-width 1.4°) to mimic the spatial blur of fly optics (Fig. 1C, LPF1) [26]. Luminance values sampled by “photoreceptors” at 1° spatial separation approximately match the resolution of *Eristalis* [27] and *Calliphora* [3]. For computational efficiency, we use rectangular sampling in a $5^\circ \times 5^\circ$ receptor patch, rather than emulating the hexagonal distribution of ommatidia (Fig. 3). Photoreceptor transduction transforms the input luminance to membrane potential in a roughly logarithmic manner around an operating point determined by stimulus history [20, 28,29]. Our model mimics this effect by transforming luminance values with a Lipetz function (Eq. 1), with the exponent u set at 0.7, as in our earlier modeling of fly motion detection [30]

$$\frac{x^u}{x^u + x_o^u} \quad (1)$$

To elaborate this Lipetz non-linearity we include an “adaptation state” with the mid-level parameter x_0 set as a first-order low-pass filtered version of x (time constant (τ) of 750 ms). Fly photoreceptor responses are temporally limited, with a corner frequency of 40–70 Hz [31]. To capture this, our modeling employs a static low-pass filter with corner frequency of 60 Hz (Fig. 1C, LPF2) following the Lipetz transform.

Large Monopolar Cells

While the role of LMCs in motion processing has been controversial, most research suggests that they are the ideal input to this pathway [32–34]. The LMCs have been shown to remove redundancy [20] and maximize information transmission [35] and they work as spatiotemporal contrast detectors, suitable for feature detection. Therefore, we implement an LMC-like spatiotemporal band-pass filtering on the photoreceptor output (Fig. 1C). Spatial antagonism can be modeled as a recurrent inhibitory network (direct LMC to LMC inhibition), however, surround inhibition in a feed-forward manner, via a proposed surround “amacrine cell” is equally plausible and is in accordance with recent research on fly retina-lamina circuitry [36]. Our modeling comprises an amacrine cell that samples the surrounding nine photoreceptor outputs and subtractively inhibits the central LMC (leaving a 30% DC spatial component). The LMC spatial filtering dynamics is variable, dependent on overall light adaptation levels [37]; however, our model parameters remain constant for computational efficiency. The inhibitory signal is delayed prior to the subtraction by application of a first-order low-pass filter (LPF3, $\tau = 2$ ms), representing the time course of the amacrine cell signal spread [38]. The LMC has band-pass temporal characteristics, with low frequency roll-off below a few hertz and high frequency at ~ 80 – 100 Hz, in light adapted conditions [39]. For our model, the LMC signal is temporally filtered (R-HPF1) with a “relaxed” first-order high-pass filter (one that passes a small DC component of 10%). This filter is characterized in the Laplace domain by the transfer function:

$$\frac{0.1 * (10\tau s + 1)}{(\tau s + 1)} \quad (2)$$

where s is the Laplace variable and $\tau = 40$ ms. The LMC signal is inverted, to replicate the hyper-polarizing response to luminance increments observed in intracellular recordings [40].

Rectifying Transient Cell

Because electrophysiological data suggests that RTCs give little sustained response, unlike LMCs (Fig. 4A), the signal is passed through an additional first-order HPF3, $\tau = 40$ ms. A half-wave rectification is performed to segregate ON and OFF channels of the input waveform, with the negative phase inverted in sign.

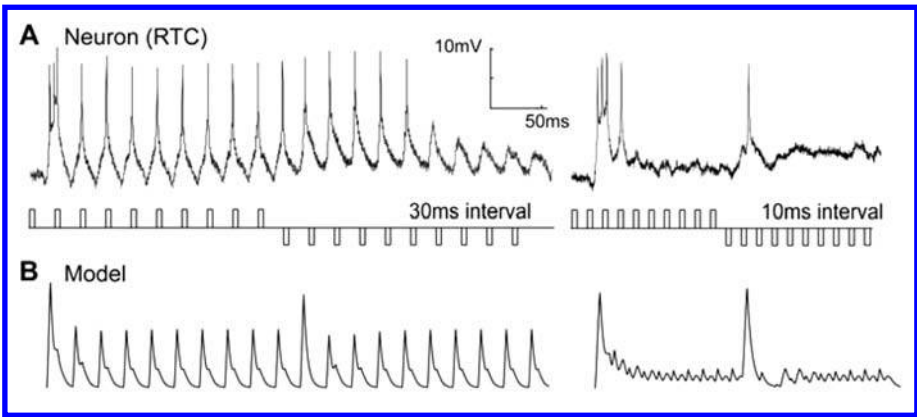


Figure 4: Rectifying transient cells (Independent Adaptation). (A) Intracellular recording from a rectifying transient cell shows independent adaptation to “ON” and “OFF” contrast changes. Pulses of equal, but opposite, contrast polarity are of 5 ms duration and separated by varying intervals. At a pulse interval of 30 ms (left trace), little adaptation can be seen (but the response to the first pulse is strongest). At 10 ms interval, temporal adaptation limits the response until the polarity of the contrast reverses, which then produces an unadapted response. A single electrophysiological recording is shown for clarity (from $N = 5$). The model version (B) output is similar, capturing the important functional characteristics of the RTC.

For each independent channel of the RTC, a signal representing an “adaptation state” is formed by applying a non-linear low-pass filter to the input signal with a fast onset, slow decay characteristic (Eq 3).

$$\begin{aligned} d / dt\{NLF\} &= (X - NLF) / \tau_1 \quad (X - NLF \geq 0) \\ &= (X - NLF) / \tau_2 \quad (X - NLF < 0), \end{aligned} \quad (3)$$

X designates the input, NLF the filter output, and τ_1 is set to 1 ms (LPFfast) and τ_2 to 100 ms (LPFslow). Such a filter is an approximation to plausible biophysical mechanisms, such as an interneuron with a long intrinsic membrane time constant and strong, “bursty” inputs. This fast depolarizing, slow repolarizing signal is subtracted from the unaltered, pass-through version of the input signal.

In addition to this step, a second subtractive inhibition is applied based on the average of the surrounding input signals of the same channel polarity (surrounding ON

subtractively inhibit the centre ON channel and similarly for the OFF channels). This is based on the surround inhibitory effect found in the “on-off” cells [21]. Unlike the previous parameters in our model, we do not have a physiologically derived estimate for the strength of this inhibitory effect, and consider the scaling of the inhibitory signal a free parameter (INH) in our modeling and simulations. Alteration of this value can be used to tune the model to different size image features. We include a neural delay, modeled by a first-order low-pass filter (LPF4, $\tau = 2$ ms), which is applied to the averaged and scaled surround inhibitory pathways.

The channels are then half-wave rectified to mimic a thresholded response (a non-linearity seen in many spiking neurons). The resultant channel signals are passed through a “neural delay” smoothing filter ($\tau = 2$ ms). This smoothing better represents the temporal response dynamics seen in the physiological RTC.

The final stage of processing is a recombination of the ON and OFF channels to form a single output corresponding to the ESTMD response. The simplest operation to achieve this would be a straightforward sum of the two output signals. However, we consider an operation that enhances the selectivity for small, dark targets. A delay operator D [*], consisting of a low-pass filter (LPF5), is applied to the OFF channel prior to recombination with the undelayed ON channel. For generality, we took a phenomenological approach to this recombination allowing second-order as well as linear interactions:

$$\text{Output} = a \cdot \text{ON} + b \cdot D[\text{OFF}] + c \cdot \text{ON} \cdot D[\text{OFF}]. \quad (4)$$

In our simulations, we consider primarily the purely linear case ($c = 0$), which we refer to as “RTC”, and the second-order case ($a = b = 0$), referred to as “ESTMD”. Note the formal similarity of the second-order structure to the correlational or Hassenstein-Reichardt elementary motion detector [41]. However, in this case the correlation operates on rectified signals of the opposite polarity from the same spatial location, rather than signals from spatially neighboring locations. In this form, although tuned primarily to small contrasting features, this rectification of polarities resembles models proposed to explain selectivity for expanding edges in “looming” motion detectors such as in the locust LGMD/DCMD [42, 43].

Although STMDs respond better to black targets [9] and light target sensitivity is not modeled here, a symmetric correlation operation could be established for a white target detector by interchange of the signal roles in Eq. 4. This would provide white target sensitivity by correlating a delayed ON channel with an undelayed OFF channel. A detection mechanism for targets of both contrast polarities (light and dark) would involve summing these two versions or having any weighted combination of the above terms (both linear and second-order).

Comparison of Model Responses to Fly RTCs

We compare our recordings of the RTC in the medulla of the blowfly to our modeled responses. The intracellular recordings (Fig. 4A) show independent adaptation to contrast increments and decrements, as seen in “on-off” type cells [17, 19]. Fig. 4A shows an experiment with a train of contrast pulses at two different frequencies. At

30 ms separation, the neuron recovers to produce graded depolarization in response to each pulse. When the separation is reduced to 10 ms, the adaptation suppresses the response to the stimulus. However, when the contrast polarity is reversed (from contrast increments to decrements), an unadapted response is observed before the neuron again rapidly adapts to the new polarity stimulus.

Temporal Responsiveness

Although our model captures the basic behavior of the biological RTC, the incorporation of an LMC-like input stage is somewhat contradicted by earlier work suggesting the frequency response (to sinusoidal stimuli) of “on-off” units rolls off above 12 Hz [17], while the LMCs have a much higher corner frequency [39]. Jansonius and van Hateren [17] suggested that this apparent low-pass characteristic is simply a result of the rapid adaptation that occurs at higher stimulus frequencies (as seen in Fig. 4A); it is possible that the unadapted system has a much higher temporal acuity than this result would suggest.

To test this hypothesis we used a “doublet” stimulus consisting of a pair of pulses (“ON” followed by “OFF”). While not strictly containing energy at a single frequency, this stimulus allowed us to construct transfer functions for the RTC to a single stimulus cycle, thus avoiding the influence of adaptation. The response power is calculated as the mean-square value until the neuron returns to within five percent of the resting membrane potential. As can be seen in our physiological data (Fig. 5A, dashed line, squares), the response of the medulla RTC to the doublet stimulus has a peak at high frequency (~50 Hz). The RTC still responds with 85 percent maximum at 100 Hz, the highest frequency doublet that we could generate on our 200 Hz stimulus display. The model RTC (Fig. 5A, dashed line) gives a similar temporal responsiveness. The RTC frequency response is a good match for that obtained by Fourier transforming the linear kernel for fly LMCs using white noise stimuli (Fig. 5A, solid line) [38]. Interestingly, if we simulate the earlier experiments of Jansonius and van Hateren [17] with a wide-field sinusoidal stimulus (Fig. 5B, dashed line), we obtain a curve that rolls off at a much lower frequency, consistent with their experimental data (reproduced in Fig. 5B, solid line). Our model rolls off more sharply at low frequency, likely due to the pure nature of our HPF3 and because the non-linearity introduced into their extracellular recordings by the thresholding mechanism for spike generation may lead to over-estimation of weak responses. We conclude that the apparent low-pass nature of the “on-off” cell frequency response was, as hypothesized, a result of adaptation [17], and that the response to transient as opposed to stationary stimuli reflects a much more rapid temporal response capability. Also, the inclusion of an LMC-like input stage in our model is supported by the very similar temporal characteristics of the LMC to the fly RTC.

Contrast Sensitivity Function

Due to the high-pass nature of the RTC data (and as captured by our model) we expect to form an ideal basis for a neural pathway for small target detection as the signal from

the passing target boundaries provides a near optimal transient stimulus, with no spatial antagonistic suppression that would occur with larger features.

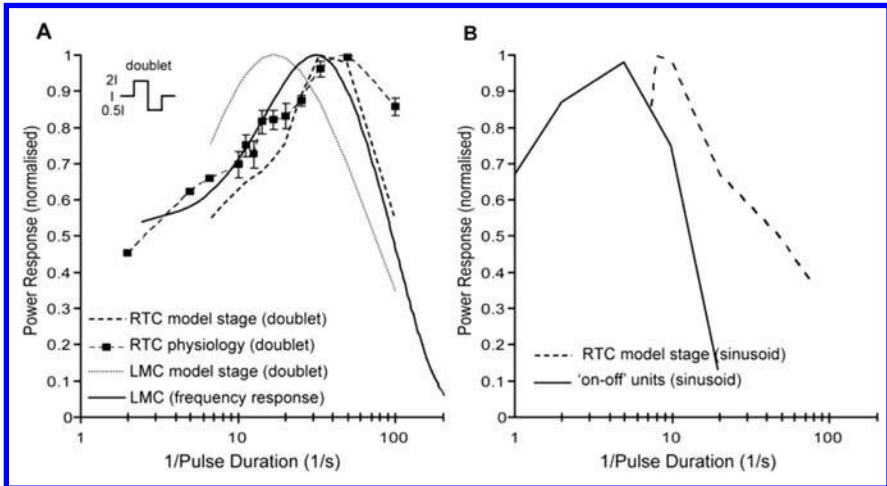


Figure 5: Temporal responsiveness. (A) The response of the physiological RTC to a stimulus doublet (2, 5, 6.6 Hz $N = 2$, no error bars; others $N = 6$ (flies) mean \pm SEM). This RTC transfer function peaks at ~ 50 Hz (dashed line, squares) and is still responsive at the highest stimulus frequencies, which are limited by the CRT refresh rate. We simulate doublet input and show that the model RTC frequency response is comparable to the physiological correlate (dashed line). The response to the doublet at the LMC stage of the model is also shown (dotted line). Frequency response properties of fly LMCs obtained via white noise analysis [38] is also plotted for comparison (solid line). It should be noted that the RTC and LMC response characteristics show a similar temporal responsiveness. (B) Previous analysis of “on-off” units in the fly lamina [17] showed poor temporal responsiveness (peak at ~ 6 Hz) (reproduced here, solid line) and our model shows a similar shift in response to the non-optimal sinusoidal stimulus (dashed line).

We determine the model response to a small target ($0.8^\circ \times 0.8^\circ$) as a function of target contrast and compare it with that induced by wide-field flicker stimuli (Fig. 6). As the target is below the size of a single ommatidium, an effective neural contrast is calculated by the convolution of the target with the optical blurring filter (half-width 1.4°) [9]. Even very low contrast discrete targets induce a model response over 10 times higher than that of the wide-field flicker stimulus (compare at equivalent contrast Fig. 6A with 6B, dashed lines). We also plot reproduced STMD responses to targets of varying contrast (Fig. 6A, squares). However, it is important to note that these responses were to $0.8^\circ \times 0.8^\circ$ targets ($50^\circ/\text{s}$) moving on complex moving backgrounds ($45^\circ/\text{s}$) [9].

Physiological data for the low contrast sensitivity of “on-off” cell responses to wide-field flicker [21] is well explained by the model (Fig. 6B). The divergence seen between the model and neuron recordings at higher negative contrast is expected, since we make no attempt to account for saturating non-linearities in neural components that would be expected in the biological system. Interestingly, the RTC model stage also produces a reasonable explanation for the near threshold contrast sensitivity of higher order STMD neurons (Fig. 6A, squares) [9].

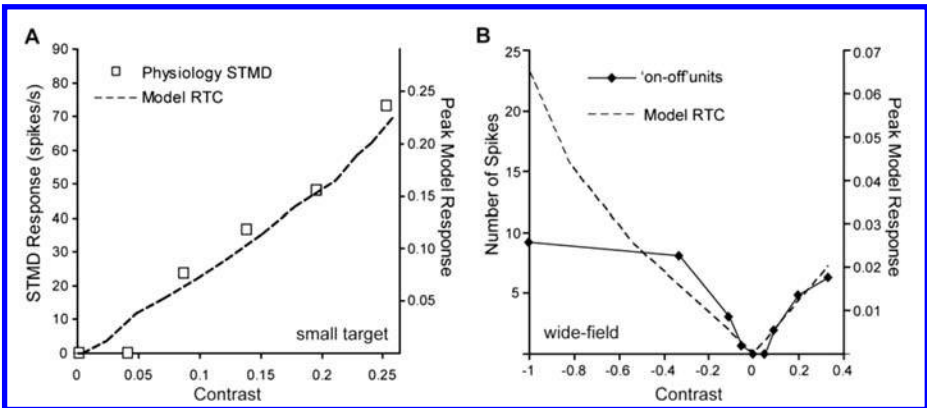


Figure 6: Contrast sensitivity function (Small Target and Wide-field). (A) The contrast sensitivity function is calculated from the peak model responses to varying contrasts of small targets ($0.8^\circ \times 0.8^\circ$) moving at $50^\circ/\text{s}$ on a mean background (RGB 0.5) (dashed line). Also plotted (squares) are physiological STMD responses to a $0.8^\circ \times 0.8^\circ$ target, moving at $50^\circ/\text{s}$. However, this stimuli included a complex moving background (mean luminance 150 cd m^{-2} , $45^\circ/\text{s}$) [9]. For the model we measure contrast as the effective neural contrast. For the physiological data the contrast values represent average Michelson contrasts as the targets traverses a complex moving background [9]. (B) Reproduced responses of “on-off” units to wide-field contrast steps of 500 ms duration (solid line) [17]. For comparison, we plot the model RTC responses to a simulation of this wide-field visual input (dashed line). We note that low contrast sensitivity is observed in the model output due to spatial antagonistic interactions and this could be a plausible explanation for low contrast sensitivity in the “on-off” units. The model responses in (B) are less than 1/10 to those seen in response to small targets of equivalent contrast (A).

Target Height Tuning

A feature of our ESTMD model is the inclusion of second-order spatial (lateral) inhibition by neighboring RTCs and a temporal cross correlation of the outputs of local ON and OFF pathways which form a “matched filter” for both the spatial and temporal characteristics of small, moving features.

By analogy to models for direction-selective motion detectors where wide-field optic flow can be deduced by summing output of local elementary motion detectors, we use the term “elementary small target motion detector” (ESTMD) for this stage. Responses of higher-order STMDs should be easily explained by simply summing across a weighted array of such ESTMDs to produce receptive fields of varying size (as observed in electrophysiological recordings from the lobula) [9, 10] while retaining position invariant selectivity for small features [8]. To confirm whether our model displays size selectivity, we estimate responses to discrete moving targets of different length (i.e. extended orthogonal to the direction of motion). Fig. 7 shows that the ESTMD stage of our model provides an excellent fit to the data published for lobula STMD neurons [10]. Note that while LMCs act to maximize information to the higher order pathways by enhancing edge-like features, the very sharp suppression of responses to targets above a few degrees in size that characterizes both model and neuron responses cannot be explained by the simpler spatial antagonism of LMCs (Fig. 7, dashed line).

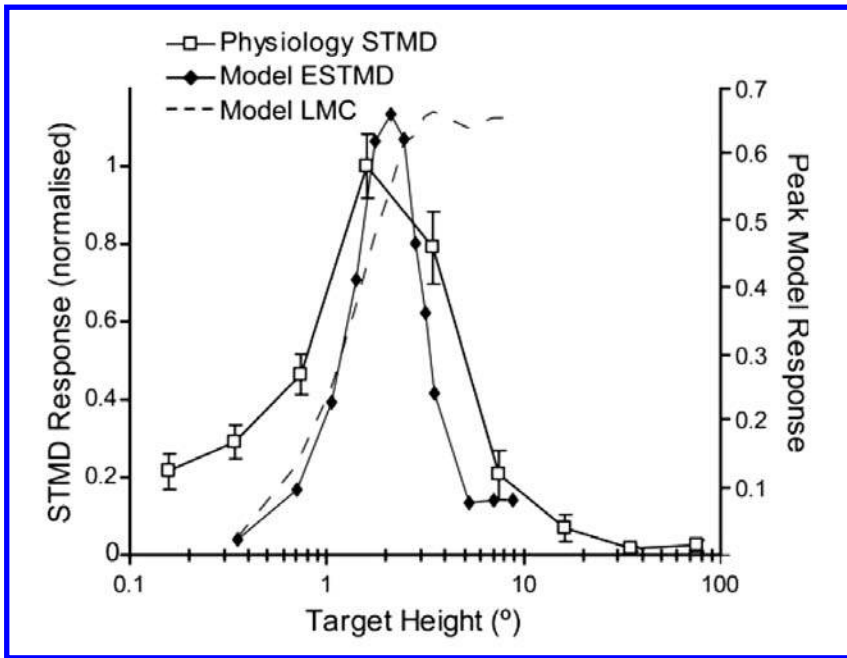


Figure 7: Target height tuning. The curve shows model ESTMD responses to targets of varying height (0.8° wide G targets on white background, moving at $50^\circ/\text{s}$). Physiological data from STMD neurons in the hoverfly for the equivalent target parameters and background is reproduced [10]. The model is selective for targets of less than a few degrees height with the suppression to the right of the peak determined by the strength of the lateral inhibition between channels. The model response to targets at the LMC stage (no units) shows that the responses remain maximum as the target is extended vertically (max height shown of 10°), i.e. the LMC is not target selective. This highlights that a second-order spatial antagonism is required for target selectivity.

Velocity Tuning

An important aspect of the second-order configuration of our model is its inherent similarity to a Reichardt correlator [41] such that the velocity dependence in response to small moving targets is essentially the same. The responses to a $0.8^\circ \times 0.8^\circ$ moving target (Fig. 8) represents a typical velocity tuning curve as obtained from a delay-and-correlate-type model. The position of the peak response is dependent on the time constant of the delay filter D [*] (LPF5). For comparison, we plot the velocity tuning curve seen in STMD neurons [8]. We have not attempted to specifically fit this data (nor in the target height tuning), and note that differences in the broadness of the tuning curves could reflect additional compressive non-linearities which we have not attempted to account for in this model.

Although the ESTMD model provides a good account for the basic tuning properties of STMDs, it is not unique in this respect. Other STMD models [11, 12] should also be able to explain both contrast sensitivity and velocity tuning. However, our key finding is that the unique adaptive component of the RTC inputs to our STMD can also explain the otherwise enigmatic finding that STMDs can respond to features embedded in clutter, but without relative motion cues [9].

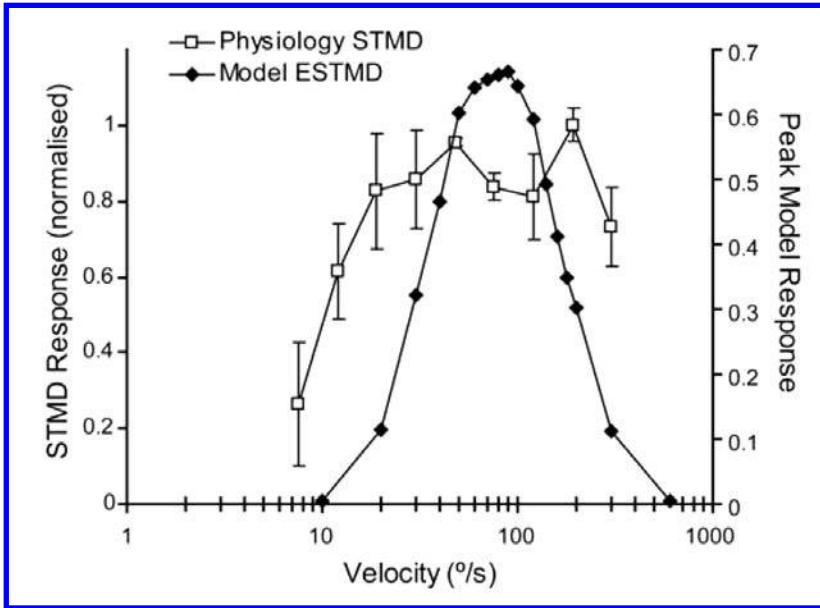


Figure 8: Velocity tuning. Model ESTMD responses to G moving targets ($0.8^\circ \times 0.8^\circ$) on a white background at varied velocities is shown in comparison to the physiological data of STMD neurons to the same visual stimulus from hoverflies [8]. The model output exhibits typical velocity tuning as observed in correlation-type motion detection mechanisms. The tuning of the model parameters (particularly, the OFF delay filter time constant) determines at which point the velocity response peaks. The broadness of the tuning curve may be extended and shaped via the addition of a final saturating non-linearity, not included in this model.

Responses to Targets in Clutter

Figure 9 shows a single output row at each stage of the model, in response to a panoramic image in which a small target is inserted (the image row is delineated in Fig. 2D). We selected this row to illustrate the effect of the key stages of the model in enhancing target responses, while rejecting other high contrast features.

Photoreceptor dynamics encodes a large luminance range into the limited dynamic range of the neuron [29, 44]. Our inputs have already emulated a similar process via a form of global gain control inherent in digital camera processing (Fig. 9A-B). The LMC output (Fig. 9C) with spatiotemporal high-pass filtering, enhances contrast boundaries in both space and time. The OFF fast temporal adaptation (Fig. 9D, solid line) suppresses textures and signals larger “breakthrough” contrast changes. The surround inhibition ensures that this effect is spatially localized. Note that the response to the tree trunk ($t = 1.1$ s), which also has a novel “OFF” shortly followed by an “ON” contrast boundary is suppressed as a consequence of second-order spatial inhibition (Fig. 9E, solid line). The ON channels (not shown) show similar characteristics. Finally, the OFF channel (Fig. 9F, solid line) is temporally delayed and correlated with the undelayed ON channel (Fig. 9F, dashed line) to signal target-like events (Fig. 9G).

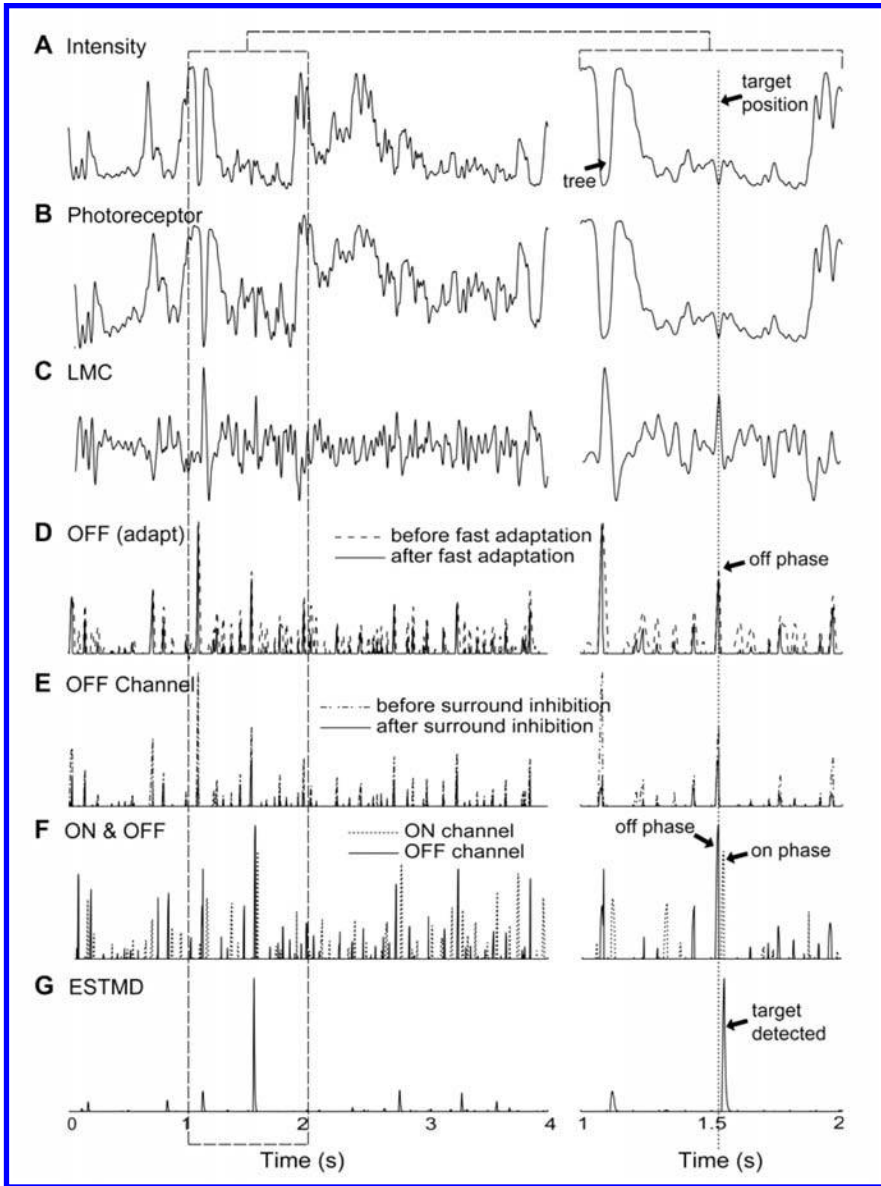


Figure 9: Sample data traces. The traces show the model outputs at various stages of processing over the second complete revolution of the scene (at $90^\circ/\text{s}$). The right hand trace shows a magnified version of the period between 1 and 2 sec. The y-axes are unit-less model outputs. The input intensity (A) is delineated in Fig. 2D. Photoreceptor dynamics (B) encodes a large luminance range into the limited dynamic range of the neuron. The LMC (C) exhibits spatiotemporal high-pass filtering, enhancing contrast boundaries. The temporal adaptive mechanisms within the independent channels suppress rapid texture variations but signal a novel contrast change (D). Surround antagonistic interactions limit the spatial extent of this type of signaling (E) and a final linear or quadratic re-combination of the channels (F) signal the presence of a dark moving target (G).

Figure 10 shows ROCs for the four panoramic images, at a velocity of $90^\circ/s$. During the pseudo-random distribution, some targets are scattered onto backgrounds of the same luminance (as the target) such that they lose all defining characteristics. In image D (Fig. 2), the most highly textured scene, it is difficult for the human observer to detect the scattered targets. Image C is extremely sparse and LMC filtering is enough for successful target discrimination (Fig. 10C). Across the varied scenes, both linear (RTC) and quadratic (STMD) processing have improved the discrimination of targets as revealed by the shift to the upper left corner of the ROC curve (Fig. 10 A–D). The limited number of false positives in the final model output suggests that target-like structures are rare in these natural image scenes.

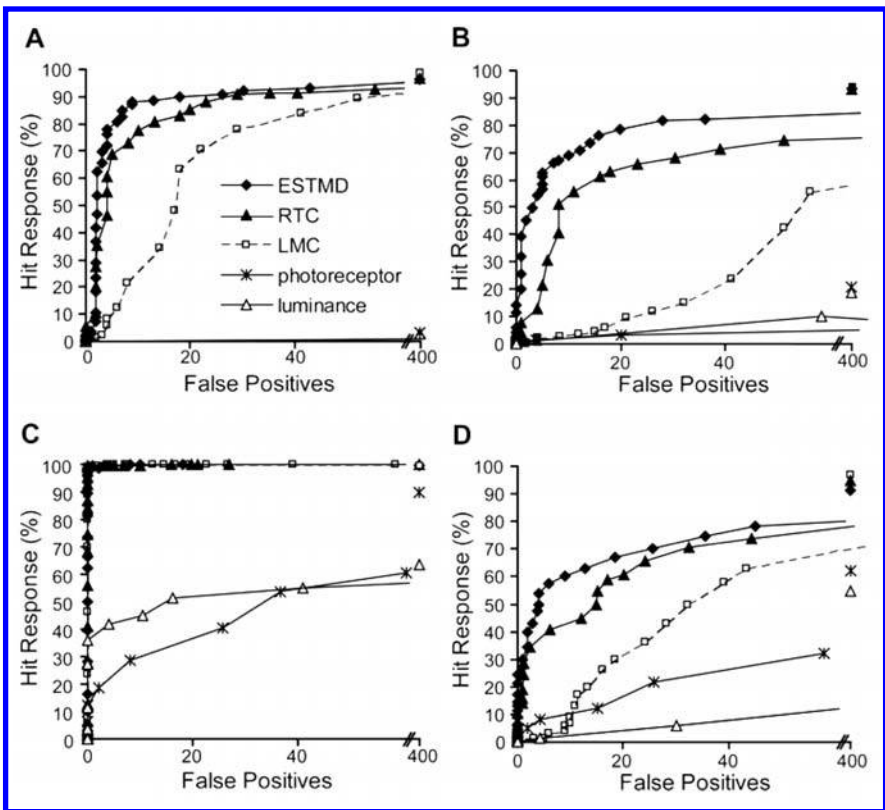


Figure 10: Natural image panoramas. Twenty targets ($1.6^\circ \times 1.6^\circ$) pseudo-randomly scattered (26 trials) on four panoramic images with the simulation run at a velocity of $90^\circ/s$. (A) ROC curves are shown for a scene with averaged natural statistics. The addition of RTC-type processing (solid line, triangle) to the LMC (dashed line, square) shifts the ROC curve to the upper left, revealing enhanced target discrimination. The quadratic (ESTMD) version of the model (solid line, diamond) shows further improvement via the multiplicative interaction of the delayed OFF and undelayed ON channels. (B) The LMC stage has a large number of false positives, due to high contrast, man-made features (which the RTC-type processing can discriminate). (C) This image is sparse so the targets can be readily discriminated by the LMC processing alone. (D) A highly textured scene, with many scattered targets losing defining characteristics, however, the target discrimination is still improved. Error bars are within symbol representation, therefore removed for clarity.

These results show that a highly non-linear filter (derived from the plausible biological components) exploits the spatiotemporal statistics of the moving target within its immediate surround. The statistics required is as follows: 1) A small duration of time (~ 50 ms) in which contrast changes do not exceed that of the upcoming target, therefore providing an unadapted “OFF” phase. This provides “distinctiveness” to the start of the dark feature. 2) An unadapted “ON” phase, which is inherent in the non-changing texture of the dark target 3). These same characteristics, i.e., unadapted phase, opposite polarity, contrast changes, not to be present in the immediate surrounds. If this third characteristic was relaxed, the detector would be sensitive to a similar width/velocity profile as the target, though not suppressed by the height of the feature, i.e. the detector would also be stimulated by a vertical “bar” stimulus.

Relative Motion

Intuitively, the ESTMD model is responsive to the motion of the contrast boundaries across the detector inputs. Relative motion between the target and background will have an effect on ESTMD responses, as it alters the temporal statistics (dependent on background velocity) that establishes the adaptation states of the independent channels. We tested this by varying the background motion with a constant target velocity of $90^\circ/\text{s}$ (Fig. 11).

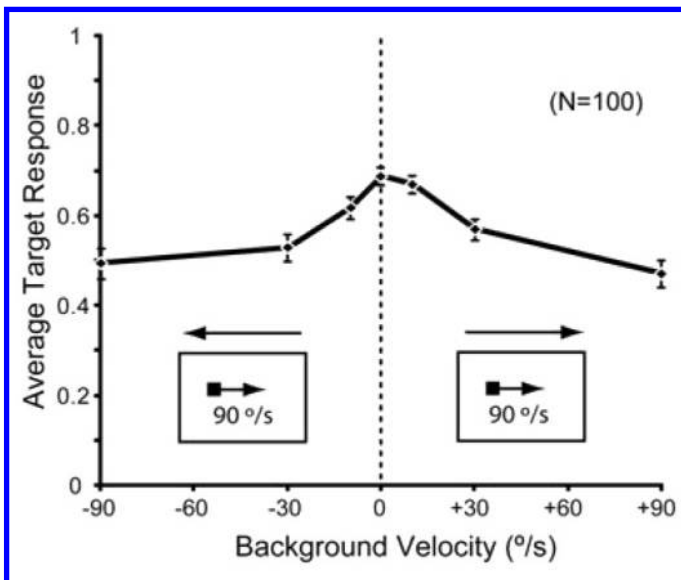


Figure 11: Relative motion. Results of simulations carried out for 25 targets in each of the four images, where background speed and direction was varied. Target speed was constant at $90^\circ/\text{s}$ (left to right, as indicated by pictograms). Data are mean \pm SEM, N = 100.

Depending on the background speed, we varied initial background position so that we could analyze target response at the same spatial juxtaposition of target and background

(target size of $1.6^\circ \times 1.6^\circ$). Hence, data for a background speed of $+90^\circ/\text{s}$ effectively represents the scenario in the other “no relative motion” panorama simulations. We repeated this test in 100 distributed locations across the four panoramic images. We showed that the ESTMD target responses are robust across the tested range of relative motions and the results confirm that the response improves when there is some relative motion, reaching a peak when the background speed is close to zero.

CONCLUSION

Our approach to modeling has provided a solution to the initially perplexing issue of how the STMD neuron responds robustly to target motion, even when there is no relative motion cue of the target to the background [9]. We have seen that this problem is solved by incorporating properties of the rectifying transient cell in the target detection pathway. This is an attractive solution, as our highly non-linear matched filter is computationally less intensive than complex segregation of transparent motion fields, required for relative motion calculations.

KEY WORDS

- **Amacrine cell**
- **Breakthrough response**
- **Elementary small target motion detector (ESTMD)**
- **Input imagery**
- **Large monopolar cells (LMC)**
- **Neural delay**
- **Photoreceptors**
- **Rectifying transient cell (RTC)**
- **Small target motion detectors (STMD)**

ACKNOWLEDGMENTS

Panoramic Images courtesy of Dr Russell Brinkworth. We thank the manager of the Botanic Gardens of Adelaide for allowing us to collect insects. We also thank past and present members of the O’Carroll lab for contributing discussions, especially Dr Russell Brinkworth, Dr Karin Nordström and Paul Barnett.

AUTHORS’ CONTRIBUTIONS

Conceived and designed the experiments: Steven D. Wiederman, Patrick A. Shoemaker, and David C. O’Carroll. Performed the experiments: Steven D. Wiederman. Analyzed the data: Steven D. Wiederman. Contributed reagents/materials/analysis tools: Steven D. Wiederman and David C. O’Carroll. Wrote the paper: Steven D. Wiederman, Patrick A. Shoemaker, and David C. O’Carroll.

Chapter 12

Honey Bee Queen Physiology and Insemination

Freddie-Jeanne Richard, David R. Tarpy, and Christina M. Grozinger

INTRODUCTION

Mating has profound effects on the physiology and behavior of female insects, and in honey bee (*Apis mellifera*) queens, these changes are permanent. Queens mate with multiple males during a brief period in their early adult lives, and shortly thereafter they initiate egg-laying. Furthermore, the pheromone profiles of mated queens differ from those of virgins, and these pheromones regulate many different aspects of worker behavior and colony organization. Because it is not possible to control the natural mating behavior of queens, we used instrumental insemination and compared the queens inseminated with semen from a single drone (single-drone inseminated (SDI)) to 10 drones (multi-drone inseminated, (MDI)). The chemical profiles of the mandibular glands of virgin, SDI, and MDI queens were characterized using GC-MS. Finally, we measured brain expression levels in SDI and MDI queens of a gene associated with phototaxis in worker honey bees (*Amfor*). Further research will be necessary to elucidate the mechanistic bases for these effects: insemination volume, sperm and seminal protein quantity, and genetic diversity of the sperm may all be important factors contributing to this profound change in honey bee queen physiology, queen behavior, and social interactions in the colony.

While many previous studies have considered the effects of mating on the physiology and behavior of female insects (i.e., reference 1), the effects of mating number and semen quantity have not been broadly considered. Honey bees are an excellent system in which to study this process. The colonies typically consist of a single reproductive queen and thousands of sterile worker bees, and the queen mates with several males (12 males on an average; reviewed in reference 2) during a brief period in her early adult life. However, studies of the effects of mating number have focused almost exclusively on the consequences of worker genetic diversity on overall colony health [3-5] and social interactions [6]. Relatively little is known about how queen mating number may alter queen physiology and thereby alter intracolony social interactions. Understanding the physiological effects of multiple mating could offer insights into the mechanisms that govern mating behavior and how the process is regulated in honey bees and female insects in general, as well as what consequences this may have for colony organization in bees and other social insects.

Virgin honey bee queens initiate mating very early in their lives, when they are approximately 1–2 weeks old, by taking multiple mating flights and mating with numerous males (drones) on each flight. On an average, queens are successfully inseminated by 12 males (based on molecular genotyping of workers [2]), but mating number is highly variable among queens (ranges from 128). The factors that determine mating

frequency are not fully understood [7, 8]. Mating has profound and permanent effects on queen's behavior, physiology, and resultant queen-worker interactions. Once they begin to oviposit, mated queens will never mate again and will remain in the colony for the rest of their lives (unless they depart during colony swarming). Mating stimulates vitellogenesis and oocyte-maturation in the ovaries [9], which prompts the initiation of egg-laying of up to 1500 eggs/day [10]. There are also profound changes in a queen's brain after mating, where the levels of dopamine significantly decrease [11], and the ratio of the neuropil/cell body volume in the mushroom bodies significantly increases [12].

Finally, mated and virgin queens differ dramatically in their pheromone profiles, and these pheromones are important for regulating colony organization and worker behavior [13, 14]. Queens produce pheromones from a variety of glands, and the complete "queen pheromone" has not been fully characterized [15-17]. However, five components in particular, termed "queen mandibular pheromone" (QMP), are produced by the mandibular gland and elicit many similar worker behavioral and physiological responses as a live queen. QMP consists of 9-oxo-(E)-2-decenoic acid (ODA), (R) - and (S)-9-hydroxy-(E)-2-decenoic acid (9-HDA), methyl p-hydroxybenzoate (HOB), and 4-hydroxy-3-methoxyphenylethanol (HVA) [18]. QMP has both primer (long-term) and releaser (short-term) effects on worker behavior and physiology. It elicits a "retinue response," in which workers are attracted from a distance (several cm) and then antennate and groom the queen [18-21]. QMP also inhibits worker ovary activation [22, 23], inhibits queen cell production by workers [24, 25], stimulates pollen foraging and brood rearing in small, newly founded colonies [26], increases nectar foraging [27, 28], and delays the age-at-onset of foraging and reduces juvenile hormone secretion [27]. Some components of QMP are involved in drone attraction and mating [29, 30]. However, while the five component QMP blend is a potent modulator of worker behavior and physiology, it is still not as potent as a live queen, suggesting that additional pheromonal components may exist. Indeed, four additional compounds were identified that synergize with QMP to increase the retinue response, but even those nine compounds do not elicit as robust a response as a live queen [17].

Although it is clear that mandibular gland pheromone profiles differ dramatically between young virgins and naturally mated, laying queens, the short-term effects of mating on pheromone profiles are largely unknown. Plettner *et al.* [14] compared the quantities of the QMP components between 6-day-old virgins and 1-year-old mated laying queens, and found that mated queens had significantly higher levels of 9-ODA, 9-HDA, HOB, and HVA than did virgins. However, a similar study by Slessor *et al.* [13], which compared 6 and 12-day-old virgins with mated queens that had been laying for 1 day, 5 weeks, or 2 years, found different results. In that study, levels of 9-ODA were not significantly different between any of these groups. 9-HDA levels were significantly higher in mated versus virgin queens, the HOB levels were significantly higher in the 2-year-old mated queens than in both the virgins and 1-day laying queens, and intermediate in the 5-week laying queens, and HVA levels were significantly higher in the 2-year mated queens compared to all the other groups. Thus, pheromone profiles are strongly affected by mating, age (or perhaps time since mating), and potentially by egg-laying. Finally, Apsegaite and Skirkevicius [31] found

slight differences in the quantity of 9-ODA between different strains of honey bees, suggesting that genotypic differences might also alter pheromone profiles.

Given the highly variable mating number and the profound effects mating has on queens, we hypothesize that mating number could modulate queen physiology, behavior, and pheromone production. However, “mating number” comprises of a host of factors, including the number and duration of mating flights, the physical act of insemination, the volume of ejaculate, the quantity and viability of sperm and seminal proteins in the ejaculate, and the genetic diversity of sperm and seminal proteins. Furthermore, given that queens mate during flights several meters above the ground, it is not possible to control natural mating behavior. However, the number of males that inseminate a queen can be precisely controlled by using instrumental insemination [32]. Previous studies have demonstrated that queens inseminated with lower quantities of semen (less than 8 μ l) are more likely to continue to take mating flights [33], but the effects of insemination quantity on other aspects of queen physiology have not been considered. To begin to address these questions, we focused on SDI (total semen from one drone) and MDI (total semen from 10 drones) queens. We monitored attraction of the workers to SDI or MDI queens in observation hive colonies, as well as the attraction of workers to virgin, SDI, and MDI queen mandibular gland extracts in cages. The chemical profiles of the mandibular glands of virgin, SDI, and MDI queens were characterized using GC-MS. Finally, since fully inseminated queens cease to be phototactic and no longer take mating flights, we measured brain expression levels in SDI and MDI queens of a gene that is associated with phototaxis in worker honey bees (Amfor, the foraging gene; [34]).

MATERIALS AND METHODS

Bee Rearing

Colonies headed by single-drone inseminated queens (*Apis mellifera carnica*, Glenn Apiaries, CA) were maintained at the NCSU Lake Wheeler Honey Bee Research Facility (Raleigh, NC). These colonies were used as genetic sources for producing supersister queens for the experiments. Due to the haplodiploid genome of the hymenoptera, the progeny of SDI-queens has a genetic relatedness of $G = 0.75$. Additionally, colonies headed by naturally mated *Apis mellifera ligustica* or Buckfast-SMR queens (B. Weaver, TX) were used to provide workers for the observation-hive and cage experiments. Note that while worker bees were derived from different source colonies for convenience, each individual experiment used workers from a single colony when testing differential responses to SDI or MDI queens and/or pheromone extract. Thus, though there might be differences between the colonies in worker responses to queen pheromones (i.e., reference 65), this should not be a factor in our results.

Queen Rearing

Supersister Queens were produced by grafting young larvae (<24 hr) from a single source colony and reared as queens in a queenless colony [32]. Once all queen cells were capped, they were transferred to a dark incubator at 33°C and 40 percent relative humidity. One or two days prior to emergence, each capped queen cell was placed into

an individual Plexiglas cage (10×10×7 cm). Frames of brood were removed from a hive and incubated at 33°C. Day-old workers were collected from the brood frames and 100 adult worker bees were placed in the cages with the capped queen cell. Bees were provided with water, food (45% honey/45% pollen/10% water), and a solution of 50% sucrose, and all cages were maintained in an incubator (at 33°C and 40 percent RH). The food was changed every 2 days. 5 days after emergence, the queens destined for insemination were treated with CO₂ for 4.0 min [66], while virgins were handled but left untreated, since we wanted a baseline non-reproductive control group and CO₂ treatment accelerates the transition to egg-laying [66]. Seven days after emergence, queens were again treated with CO₂ for 4.0 min, during which time they were inseminated with semen from either one drone (SDI) or 10 brother drones (MDI) by following standard insemination protocols which readily produce laying queens [32], though in our experiments queens were reared in cages without honeycomb, so there was no opportunity for them to lay eggs. The average drone produces approximately 1 µl of semen, thus SDI queens were inseminated with approximately 1 µl and MDI queens were inseminated with approximately 10 µl. Queens were then returned to their respective cages and collected 5 days after insemination onto dry ice and stored at 80°C. A total of 12 virgin, 15 SDI and 11 MDI queens were collected. Queens were reared in three separate cohorts (Cohorts 1: 5 SDI and 4 MDI; Cohorts 2: 5 SDI and 2 MDI, and Cohorts 3: 12 virgin, 5 SDI and 5 MDI), but queens from different cohorts were combined for the subsequent chemical analysis and behavioral assays.

Prior to dissection, queen heads were removed and partially lyophilized to facilitate dissection [67], after which their mandibular glands and brains were dissected out on dry ice and stored for future processing. In order to verify insemination success, we counted the number of sperms in each spermatheca (SDI, N = 15 and MDI, N = 8). As would be expected, spermathecae of MDI queens ($65 \times 10^4 \pm 25 \times 10^4$ sperm) contained significantly more sperm than those of SDI queens ($15 \times 10^4 \pm 8 \times 10^4$ sperm; $U = 20.0$, $p = 0.0098$). Note that these quantities of sperms are lower than typical for inseminated queens, but the lack of comb, the presence of a small number of workers, and the small size of the cages may have minimized sperm storage [38].

Behavioral Assays

Observation Hives

Supersister Queens were produced as described above. Capped queen cells were removed from the queen-rearing colony and individually placed into 1.5 frame observation hives (34"×5"×21.5" LxWxH). The entrance to each hive was blocked with queen excluder material so the queens could not exit the hives to take mating flights. Observation hives were stocked with ~1000 one-day-old bees and a half-frame of honey/pollen. The observation hives were stored in a 33°C incubator for 3 days (to ensure that workers were old enough to properly thermoregulate) prior to being placed in a room with access to the outside via a window. As the queens emerged, individual plastic numbered tags (Thorne Ltd, UK) were glued to their thoraxes. Approximately 5 days after emergence, queens were captured and treated with carbon dioxide for 4.0 min. Two days later, queens were captured again and treated with carbon dioxide

for 4.0 min during their insemination procedure. As outlined above, queens were inseminated with semen from either a single drone (SDI) or 10 brother drones (MDI). Queens were then released back into their respective hives. One hour later, the number of worker bees in the queen's retinue (surrounding the queen, licking and antennating her) was counted every minute over a period of 5.0 min [17, 18]. One hour later, the number of workers contacting the queen was counted again. The retinue size was calculated by summing across all of the observations, as in previous studies [17, 68]. The retinue was monitored every day, twice a day, for 5 days. In total, 2 SDI and 2 MDI queens were assayed in 2005 and 5 SDI and 3 MDI in 2006.

Differences in the retinue size for SDI and MDI queens in observation hives were analyzed using a mixed-model ANOVA (PROC mixed in SAS, Cary, NC), with treatment and day viewed as fixed factors, while trial, trial*treatment and replicate (trial*treatment) were random effects. Thus "day" was treated as a split plot factor.

Cage Assays

Next we compared worker responses to mandibular gland extracts of virgin, SDI, and MDI queens. The glands were extracted from each supersister queen produced as outlined above.

Frames of brood were removed from a hive and incubated at 33°C. Day-old workers were collected from the brood frames and 35 bees were placed in Plexiglas cages (10×10×7 cm). Bees were provisioned as described above. The cages were kept in a 33°C incubator with 40% relative humidity, and manipulations and observations were performed under red light to negate any potential behavioral effects. Cages were maintained for 5 days.

Experiment 1: Retinue Response

The retinue response was monitored as described previously [17, 21, 68, 69]. Extracts of mandibular glands of individual queens were produced as described below (see chemical analysis section). 0.05 queen equivalents (Qeq) of queen mandibular gland extract from individual queens (Virgin: n = 3; SDI: n = 8; MDI: n = 7) was placed onto a glass coverslip, the solvent was allowed to evaporate, and the coverslip was then placed inside the cage at the same time every day for 5 days. The number of bees, antennating and licking the coverslip was counted in each cage ("retinue"). The retinue was recorded 5, 10, and 15 min after pheromone introduction each day of the 5-day time course. A single trial was performed.

Experiment 2: Preference Assay

This experiment was repeated twice (Trial 1: Fall 2005 and Trial 2: Spring 2006). Bees were exposed to 0.1 Qeq of synthetic QMP (Pherotech, Canada). Every day, 10 µl of QMP was placed on a microscope slide and allowed to evaporate before being placed in the cage. This amount of QMP mimics a live queen in assays of worker behavior and physiology [70]. Since worker maturation is altered in the absence of queen pheromone [67, 68, 71], we reared these workers with QMP to mimic natural colony conditions. On the fifth day of the experiment, workers were presented with two slides containing equal quantities of extract (0.05 Qeq) from either a virgin and SDI queen

(Trial 1: $n = 9$ and Trial 2: $n = 10$), a virgin and MDI queen (Trial 1: $n = 10$ and Trial 2: $n = 10$), or an SDI and MDI queen (Trial 1: $n = 11$ and Trial 2: $n = 10$). The number of workers contacting each slide was counted every 5.0 min for 15 min after slide presentation. Note that a total of 6 virgin, 6 SDI, and 6 MDI queens were used in this analysis. Queens were derived from 2 cohorts. Trial 1 and trial 2 were not significantly different, so the data was pooled for the subsequent analysis.

Data was presented as mean \pm SEM. The effect of the mated number was evaluated with a non-parametric Kruskal-Wallis ANOVA on ranks for global comparison. The worker preferences between two slides were evaluated with a parametric t-test.

Chemical Analysis

The mandibular glands were dissected and immersed in 50 μ l of diethyl ether containing 0.4 μ g/ μ l of undec-10-enoic acid (as an internal standard) for minimum of 24 hr. A 5 μ l portion (approximately 0.1 bee equivalents) of an extract was placed in a small glass insert and the solvent gently evaporated. The residue was silylated overnight at room temperature in the insert with 10 μ l of neat bistrimethylsilyltrifluoroacetamide (BSTFA) [17]. The derivatized sample was diluted with hexane (100 μ l) and a 2 μ l portion was analyzed using gas chromatography on a HP 5890 equipped with capillary column (30 m \times 0.25 mm ID. 0.5 μ m film thickness) DB-5 (5% diphenyl-95% dimethylsiloxane) column (J&W scientific, Folsom, CA) in splitless mode. Helium was used as the carrier gas at a head pressure of 18 psi (flow rate = 1.3 ml/min). The GC temperature was held at 100°C for 1 min and then increased at 5°C/min to 200°C (5 min), followed by an increase of 10°C/min to 250°C (15 min). Injector and FID temperatures were both set at 250°C. We extracted the mandibular gland of 12 virgin queens, 15 SDI queens and 10 MDI queens. All queens used for chemical analysis were raised from the same grafting source to reduce any genetic variation in their pheromone profiles. However, the queens were reared in three different cohorts.

Compound identification was achieved by splitless capillary gas-chromatography-mass spectrometry using an HP 6890 GC and a model 5973A msd with an electron impact ion source and an HP-5ms capillary column (30 m \times 0.25 mm ID \times 0.25 μ m film thicknesses).

To examine differences in profiles related to number of inseminations based on the relative proportion of the chemical compounds, a stepwise discriminant analysis was employed, using all the chemical compounds (Statistica 6.0. Stat-Soft® Inc.). A MANOVA test was also used to compare treatment effects (queen insemination quantity). As the MANOVA test was significant, we compared each compound using a univariate analysis on the relative proportion for each compound. Both parametric and non-parametric tests were used for individual component comparisons, and both tests revealed comparable statistic p value. Here, we present the results from the MannWhitney test.

The following abbreviations are used for chemicals found in the analysis: HOB, 8-hydroxyoctanoic acid (8-HOAA), HVA, (E)-9- ODA, (E) 9-HDA, 10-hydroxydecanoic acid (10-HDAA), (E)-10-hydroxydec-2-enoic acid (10-HDA), decanedioic acid (C10:0 DA) and (E)-dec-2-enedioic acid (C10:1 DA).

Brain Gene Expression Levels of Amfor

Total RNA was isolated from dissected brains using a RNeasy RNA extraction kit (Qiagen, Valencia CA), yielding 0.6-1.5 $\mu\text{g}/\text{brain}$. cDNA was synthesized from 150 ng RNA using Arrayscript reverse transcriptase (Ambion, CA). Expression levels of Amfor were measured using quantitative real-time RT-PCR (qRT-PCR) with an ABI Prism 7900 sequence detector and the SYBR green detection method (Applied Biosystems, Foster City, CA). The eIF3-S8 housekeeping gene, which did not vary in expression levels in previous bee brain microarray studies [67, 72], was used as a loading control. For each sample, triplicate qRT-PCR reactions were performed and averaged. A standard curve was generated for each primer using dilutions of genomic DNA to calculate the relative quantities of mRNA levels for each sample. A dissociation curve and negative control (cDNA reaction without RT-enzyme) was used to ensure primer specificity and lack of contamination.

The sequences for the primers (5'3') used are as follows:

Amfor -F: AATATAACTTCCGGTGCAACGTATT;

Amfor -R: CGTTTGGATCACGGAAGAAAG;

eIFS8-F: TGAGTGTCTGCTATGGATTGCAA;

eIFS8-R: TCGCGGCTCGTGGTAAA;

We evaluated the brain gene-expression levels of 9 SDI queens and 9 MDI queens (derived from two cohorts). For each individual brain sample, the ratio of the expression level of Amfor to that of the control gene (eIF3-S8) was calculated.

DISCUSSION

In this study, we instrumentally inseminated the queen honey bees to determine if insemination quantity alters their physiology and social interactions under controlled environmental conditions. Our results clearly demonstrate that insemination quantity alters queen physiology, queen pheromone profiles, and queen-worker interactions. The MDI queens elicited a stronger retinue than SDI queens in natural colony conditions, and their mandibular gland extracts were more attractive in preference assays with caged worker bees. Moreover, GC-MS analysis of the mandibular gland chemical profiles revealed significant differences between the SDI and MDI queens. Finally, brain-expression levels of a behaviorally relevant gene were significantly different between the SDI and MDI queens. All of these results suggest that insemination quantity can have profound effects on queen physiology and behavior.

Comparisons of the mandibular gland profiles between MDI and SDI queens may lead to the identification of new components of queen pheromone. Previously, studies focusing on compounds that elicited a retinue response identified the five-component QMP blend [18]. Another study identified four additional compounds that did not elicit a retinue on their own, but synergized with QMP to produce a stronger retinue response [17]. However, the retinue response was still not as strong as that elicited by the live queens, suggesting that additional active compounds may still exist. In this study, we found that the MDI queens elicited a larger retinue than SDI queens in observation hive colonies. Since the mandibular glands are the main source of QMP,

we tested the mandibular gland extracts of virgin, SDI, and MDI queens on worker retinue responses in cages. When tested individually, the glands were equally attractive, though all glands are qualitatively comparable and contained the main QMP compounds [18]. However, when the glands were compared in a choice test, there were clear differences. Indeed, the glands of the inseminated queens were more attractive than the glands of virgins, while the gland extracts of MDI queens were more attractive than the glands of SDI queens. This suggests that MDI queen mandibular gland extracts have additional compounds that synergize with 9-ODA and 9-HDA to make these extracts more attractive in a preference assay, and that the relative proportions of the entire gland chemical profile affect the retinue response. Indeed, when the extracts were analyzed with GC-MS, the chemical profiles of the mandibular glands of the inseminated queens were significantly different from those of the virgins, and those of the MDI queens were significantly different from those of the SDI queens.

Our results suggest that these changes in pheromone profiles occur within days after insemination, and that additional changes occur over a long period of time. Previous studies have compared the queen mandibular gland compounds between 6-day-old virgin and 1-year-old mated laying queens, and mated queens had higher levels of 9-ODA, 9-HDA, HOB, HVA, and 10-HDAA, and lower levels of 10-HDA [14]. However, when virgins and mated queens of more similar ages were compared, the differences were less robust [13]. In particular, 12-day-old virgins and mated queens that were laying eggs for only 1 day did not differ significantly between levels of 9-ODA, 9-HDA, HOB, or HVA. In our study, virgins and inseminated queens were age-matched, and all queens were collected 5 days after insemination and were not laying eggs. However, we still observed significant differences in the overall chemical profiles and in several individual compounds, suggesting that insemination quantity causes changes in pheromone production within days. Thus, our results suggest that changes in mandibular gland profiles occur immediately or shortly after insemination, but additional modifications occur over time that may be associated with age, egg laying or both. Furthermore, the observation hives assays with live queens and the cage studies with queen mandibular gland extract demonstrate that workers can detect these differences in pheromone profiles and respond differently to virgins versus newly inseminated queens, and singly versus multiply inseminated queens.

The expression levels of a gene associated with phototaxis are also significantly altered by insemination quantity, suggesting that insemination quantity exerts effects of neuronal properties in the brain and possibly behavior. We focused our analysis on brain expression levels of the foraging gene (*Amfor*; GenBank Accession AF469010). Previous studies found that expression of *Amfor* is significantly higher in forager bees than in-hive bees [35]. Moreover, *Amfor* encodes a cGMP-dependent protein kinase (PKG) and treatment with a cGMP analog stimulates foraging behavior [35] and increases phototaxis [36]. Our results demonstrate that there are significant differences in gene expression levels in the brains of SDI and MDI queens, and these differences may be associated with changes in flight and phototaxis, though behavioral studies are clearly necessary to determine if this is the case. However, previous work demonstrates that queens inseminated with lower quantities of semen (<8 μ l) have an increased likelihood to attempt mating flights [37].

Clearly, insemination quantity has profound effects on queens, but what are the mechanisms by which insemination quantity triggers these changes in queen honey bees? As noted previously, a number of factors might play a role. The number of stored sperm may modulate the queen's post-mating physiology and behavior [38]. It is highly unlikely that the queens can directly assess the number of sperm in their spermathecae since there is no nerve enervation into the spermathecae and the membranes of their spermathecae are rigid [39, 40], so there is likely to be some other mechanism—one that is possibly correlated with the stored sperm number—that serves as the basis for these physiological and behavioral changes. One possible explanation is that insemination volume may be the cue that triggers these changes. As queens are inseminated with numerous drones, the large quantity of semen is temporarily stored in their lateral and median oviducts for several hours before a proportion (5–10%) of each male's sperm migrates into the spermathecae and the excess semen is excreted. Indeed, preliminary studies (Richard, Tarp, Grozinger, unpublished data) suggest insemination volume may be a key contributor to the observed post-insemination changes. One possible mechanism to induce these changes is that queens may have stretch receptors in their oviducts that provide a negative stimulus for additional mating behavior. Similar mechanisms exist in other insect systems [41–43], and abdomen distension has been tested in honey bees [44], but it remains unclear if abdominal enlargement is a physiological mechanism for reproductive senescence in queen bees. Alternatively, queens may use a substance in their mates' ejaculate, such as a hormonal precursor or seminal protein that causes physiological changes and decreases their subsequent reproductive behavior. Male seminal proteins have shown to have significant inhibitory effects on mating in female *Drosophila* [45–52] and possibly bumble bees [53, 54], and several substances in drone honey bee ejaculate have been identified, including sugars, metal ions, and proteins [55–57]. Further studies will be necessary to determine which factor(s) is involved in causing the differences in queen pheromone profile and brain gene expression that we have observed between SDI and MDI queens.

Previous studies have demonstrated that there may be colony-level adaptive benefits for genetically diverse workers, in terms of increased resistance to disease [5, 58], homozygosity at the sex determination locus [59], or better regulation of colony division of labor [60, 61]. Here, we demonstrate that insemination quantity, and thereby potentially mating number, could also affect different aspects of queen physiology or quality that could affect colony fitness. Additional research will be necessary to see if the physiological and pheromonal differences of differentially inseminated or mated queens are used by the workers as honest signals of their insemination quality or fertility [62–64].

RESULTS

Behavioral Assays

Observation Hives

One of the most measurable effects of queen pheromone is the induced retinue response, in which workers are attracted to the queen from a short distance, and lick and antennate her. Following insemination, the retinue response to SDI and MDI queens

was monitored in observation hives, twice a day, for 5 days. The MDI queens attracted significantly more worker bees in their retinue than the SDI queens ($F = 6.73$, $p = 0.02$; Fig. 1). There was no significant effect of day ($F = 0.46$, $p = 0.76$) or day*treatment interaction ($F = 0.68$, $p = 0.61$).

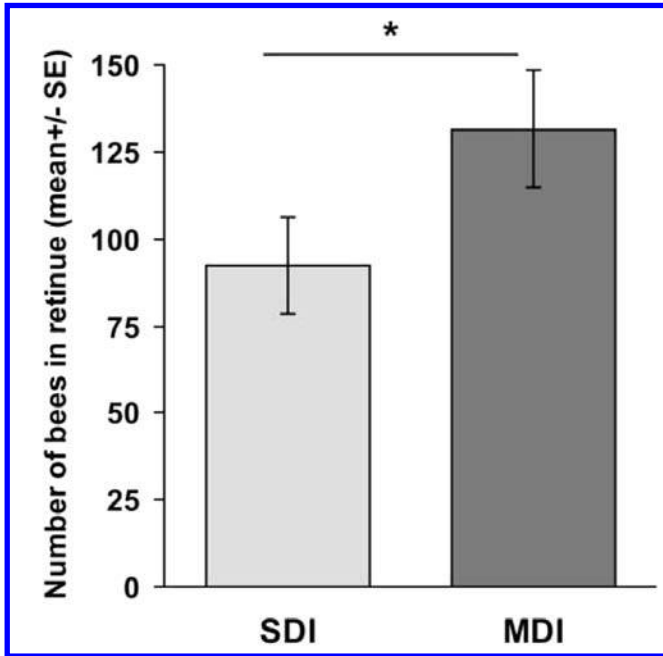


Figure 1: Workers are more attracted to MDI than to SDI queens in observation hives.

Following insemination, the retinue response to SDI and MDI queens was monitored in observation hives, twice a day, for 5 days. MDI queens attracted significantly more worker bees in their retinue than the SDI queens ($F = 6.73$, $p = 0.02$). (SDI: 7 queens; MDI: 5 queens).

Cage Assays

Worker retinue responses to the mandibular gland extracts of virgin, SDI, and MDI queens were tested in cages containing 4-day-old bees. The retinue size was equivalent whether workers were exposed to virgin, SDI, or MDI queen mandibular gland extracts ($H(2, 18) = 0.615$, $p = 0.735$; data not shown). However, worker bees exposed to two different mandibular gland extracts at the same time preferred gland extracts from SDI and MDI queens to virgins (respectively: $t = 4.2$, $df = 36$, $p < 0.001$ and $t = 3.1$, $df = 38$, $p < 0.01$, Fig. 2), and preferred MDI extracts to SDI extracts ($t = 2.7$, $df = 40$, $p < 0.01$). Data for the preference assay represent two trials which were not significantly different and were pooled for the subsequent analysis.

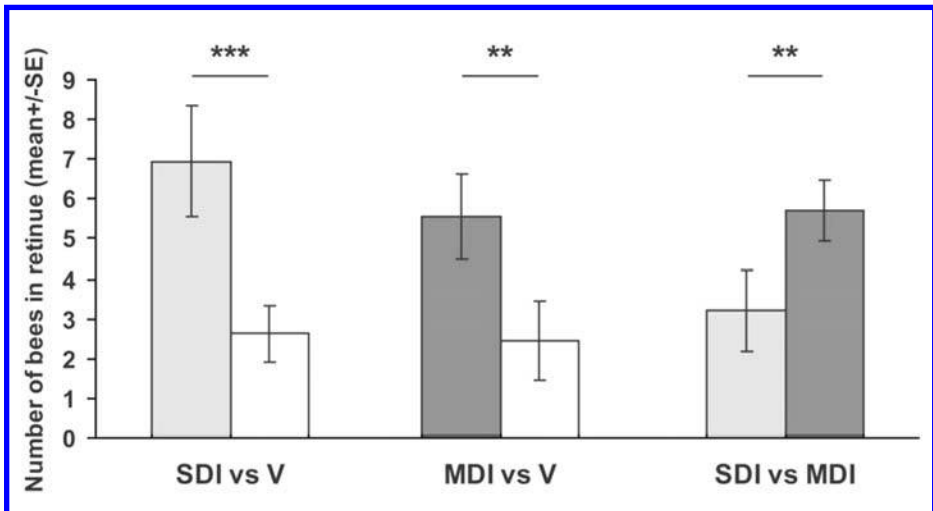


Figure 2: Workers are more attracted to the mandibular gland extracts of the MDI than SDI queens.

Caged workers were exposed to mandibular gland extract of two different queens simultaneously, and the retinue response to each extract was monitored. Workers were significantly more attracted to the extracts of inseminated versus virgin queens, and significantly more attracted to the extracts of MDI versus SDI queens (0.05 queen equivalents: Virgin versus SDI queens ($n = 19$); Virgin versus MDI ($n = 20$). MDI versus SDI ($n = 21$); all comparison with t-test: $t < 2.7$, $p < 0.01$). ** $p < 0.01$ and *** $p < 0.001$.

Chemical Analysis of Queen Mandibular Gland Profile

The chemical composition of the mandibular gland extract of virgin, SDI, and MDI queens were analyzed using gas chromatography. A total of 27 compounds were apparent in the GC analysis and used in the subsequent comparisons. There were significant differences in the overall chemical profiles between the three groups of queens, as revealed by a discriminant analysis ($F(33, 36) = 9.33$, $p < 10^{-4}$; Fig. 3). Two discriminant variables explained 100 percent of the variation. The chemical profiles of the virgin queen mandibular glands were mostly different from the two groups of mated queens (85 percent of the variation), and the other 15 percent of the variation could be attributed to insemination quantity.

Chemical composition of the mandibular gland extracts of Virgin, SDI, and MDI queens were analyzed using gas-chromatography. Discriminant analysis of mandibular extract of virgin, SDI, and MDI queens was based on the relative proportion of the chemical compounds ($F(33, 36) = 9.33$, $p < 10^{-4}$; All group distances < 0.005). Ellipses have been drawn to emphasize the categories, but have no specific statistical meaning.

Next, when the actual quantities of the compounds are analyzed (Table 1), the mated queens had significantly lower levels of 18 compounds relative to virgins, and

higher levels of one compound. MDI queens had significantly lower levels of seven compounds than SDI queens, and significantly higher levels of two compounds. Of the five QMP components, the quantities of 9-ODA, 9-HDA, and HVA were all significantly lower in mated queens compared to virgins. Levels of 9-ODA and 9-HDA were also significantly lower in the MDI queens than in the SDI queens.

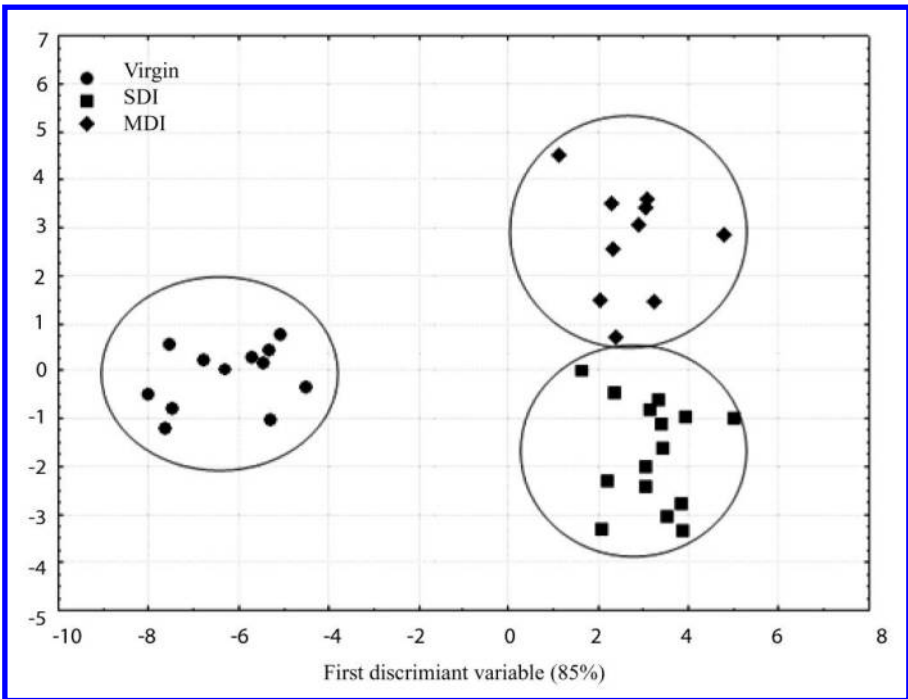


Figure 3: Insemination quantity significantly alters the chemical profile of mandibular glands.

Finally, we compared the relative proportions (compared to the total gland quantity) of the 27 individual compounds between virgin and mated queens, and between SDI and MDI queens (Table 2). The relative proportion of 13 compounds was significantly different between virgins and mated queens, and 10 of these compounds were significantly higher in mated queen mandibular glands. There were fewer compounds with significantly different relative proportions between SDI and MDI queens. Two compounds (8-hydroxyoctanoic acid and unidentified 5) were present in significantly higher proportions in SDI queens than in MDI queens (Table 2), while six compounds (4-hydroxybenzoic acid, unidentified 2, (E)-dec-2-enedioic acid, palmitic acid, alkane 2, and stearic acid) were significantly higher in MDI than in SDI queens mandibular glands (Table 2). Of the QMP components, relative levels of 9-ODA were significantly lower in mated queens compared to virgins, while HOB levels were significantly higher. None of the QMP components differed between SDI and MDI queens.

Table 1: Absolute Quantity of the Mandibular Gland Compounds (mean±STD) in µg of the Virgin, SDI and MDI Queens.

	Retention Index	Virgin (N = 12)		Inseminated (n = 25)		Mann Whitney (Virgin vs Inseminated)		SDI (n = 15)		MDI (n = 10)		Mann Whitney (SDI vs MDI)	
		mean	STD	mean	STD	U	p	mean	STD	mean	STD	U	p
Unidentified 1	1408	0.70	± 0.09	0.70	± 0.04	143	0.835	0.69	± 0.04	0.71	± 0.09	69	0.765
HOB	1499	0.20	± 0.01	0.20	± 0.02	126	0.451	0.22	± 0.03	0.16	± 0.04	49	0.160
4-hydroxy-3methoxybenzoic acid	1512	4.58	± 0.44	2.32	± 0.20	31	0.000	2.70	± 0.21	1.74	± 0.33	34	0.023
8-HOAA	1627	12.12	± 1.08	6.19	± 0.80	42	0.000	7.71	± 0.96	3.92	± 1.06	35	0.026
4-hydroxybenzoic acid	1635	8.09	± 0.64	3.77	± 0.28	14	0.000	3.92	± 0.29	3.55	± 0.55	63	0.531
3-HDAA	1658	1.07	± 0.07	0.53	± 0.05	18	0.000	0.59	± 0.05	0.43	± 0.08	42	0.071
4-hydroxydi-hydrocinnamyl alcohol	1687	0.07	± 0.02	0.22	± 0.04	89	0.049	0.22	± 0.05	0.22	± 0.09	61	0.461
9-ODA	1714	252.45	± 20.15	125.16	± 1130	23	0.000	144.70	± 13.18	95.84	± 16.94	35	0.026
HVA	1716	0.51	± 0.04	0.29	± 0.02	24	0.000	0.32	± 0.02	0.24	± 0.03	46	0.115
9-oxodecanoic acid	1750	0.77	± 0.09	0.44	± 0.04	53	0.001	0.51	± 0.05	0.34	± 0.04	32	0.016
4-hydroxy-3methoxybenzoic acid	1785	2.66	± 0.21	1.48	± 0.13	33	0.000	1.73	± 0.14	1.12	± 0.19	33	0.019
9-HDA	1798	37.65	± 3.87	19.56	± 1.68	35	0.000	22.91	± 2.04	14.54	± 2.12	32	0.016
Unidentified 2	1817	0.91	± 0.09	0.63	± 0.05	66	0.006	0.66	± 0.07	0.58	± 0.09	63	0.531
10-HDAA	1820	2.84	± 0.23	1.57	± 0.13	28	0.000	1.75	± 0.15	1.30	± 0.21	47	0.129
10-HDA	1873	34.87	± 3.95	23.90	± 2.63	79	0.021	24.64	± 3.57	22.81	± 4.04	73	0.935
Unidentified 3	1885	0.49	± 0.04	0.32	± 0.03	45	0.000	0.33	± 0.02	0.29	± 0.07	56	0.311
C10:0 DA	19.07	0.17	± 0.01	0.16	± 0.02	130	0.532	0.19	± 0.02	0.13	± 0.02	47	0.129
Dihydroferulic acid	1907	0.30	± 0.02	0.16	± 0.01	19	0.000	0.18	± 0.01	0.13	± 0.02	41	0.062
Alkane 1	1918	2.17	± 0.15	1.22	± 0.10	31	0.000	1.40	± 0.11	0.95	± 0.17	65	0.605
C10:1 DA	1957	3.29	± 0.32	2.35	± 0.20	71	0.009	2.48	± 0.23	2.16	± 0.36	40	0.055
Unidentified 4	1986	2.86	± 0.31	1.36	± 0.16	43	0.000	1.59	± 0.21	1.03	± 0.24	28	0.008
Unidentified 5	2023	6.88	± 0.68	4.31	± 0.45	62	0.003	5.23	± 0.52	2.92	± 0.61	64	0.567
Palmitic acid	2052	0.79	± 0.04	0.42	± 0.03	14	0.000	0.39	± 0.03	0.45	± 0.06	45	0.103
Unidentified 6	2068	4.74	± 0.40	3.48	± 0.33	74	0.013	3.91	± 0.43	2.83	± 0.45	59	0.397
Alkane 2	2119	0.36	± 0.03	0.27	± 0.02	60	0.003	0.25	± 0.02	0.29	± 0.05	66	0.643
Octadecenoic acid C18:1	2022	7.55	± 0.34	2.60	± 0.35	10	0.000	2.94	± 0.52	2.08	± 0.35	69	0.765

All significant differences with $p < 0.05$ are marked in bold.

Table 2: Chemical Identity and Relative Proportion (mean±STD) of the Queen Mandibular Gland of Honey Bees *Apis Mellifera* Belonging to Different Queen Group: Virgin, SDI, and MDI Queens.

	Retention Index	Virgin (N = 12)		Inseminated (n = 25)		Mann Whitney (Virgin vs Inseminated)		SDI (n = 15)		MDI (n = 10)		Mann Whitney (SDI vs MDI)	
		mean	STD	mean	STD	U	p	mean	STD	mean	STD	U	p
Unidentified 1	1408	0.21	± 0.05	0.42	± 0.06	41	0.000	0.33	± 0.03	0.57	± 0.13	49	0.149
HOB	1499	0.06	± 0.01	0.10	± 0.01	50	0.001	0.10	± 0.01	0.10	± 0.02	74	0.956
4-hydroxy-3methoxybenzoic acid	1512	1.19	± 0.07	1.15	± 0.08	124	0.399	1.24	± 0.12	1.05	± 0.09	62	0.471
8-HOAA	1627	3.08	± 1.12	2.79	± 0.26	113	0.230	3.39	± 0.29	2.01	± 0.36	31	0.015
4-hydroxybenzoic acid	1635	2.11	± 0.10	1.97	± 0.12	110	0.194	1.78	± 0.10	2.31	± 0.21	35	0.027
3-HDAA	1658	0.28	± 0.02	0.28	± 0.02	113	0.230	0.26	± 0.03	0.29	± 0.04	72	0.868
4-hydroxydi-hydrocinnamyl alcohol	1687	0.02	± 0.00	0.12	± 0.03	37	0.000	0.10	± 0.02	0.16	± 0.07	70	0.782
9-ODA	1714	64.77	± 0.63	60.38	± 0.96	73	0.012	61.19	± 1.27	58.65	± 1.36	49	0.149
HVA	1716	0.13	± 0.01	0.15	± 0.01	106	0.153	0.14	± 0.00	0.16	± 0.01	50	0.166
9-oxodecanoic acid	1750	0.19	± 0.01	0.23	± 0.01	84	0.032	0.22	± 0.01	0.24	± 0.03	71	0.824
4-hydroxy-3methoxybenzoic acid	1785	0.68	± 0.01	0.72	± 0.02	104	0.136	0.76	± 0.02	0.68	± 0.03	47	0.120
9-HDA	1798	9.41	± 0.40	9.70	± 0.28	136	0.650	9.85	± 0.34	9.43	± 0.50	63	0.506
Unidentified 2	1817	0.23	± 0.01	0.32	± 0.02	52	0.001	0.29	± 0.02	0.37	± 0.03	31	0.015
10-HDAA	1820	0.72	± 0.02	0.77	± 0.03	128	0.475	0.77	± 0.04	0.80	± 0.06	63	0.506
10-HDA	1873	8.62	± 0.56	12.04	± 1.01	95	0.074	10.96	± 1.28	14.11	± 1.48	41	0.059
Unidentified 3	1885	0.13	± 0.00	0.16	± 0.02	67	0.007	0.15	± 0.00	0.19	± 0.04	60	0.405
C10:0 DA	1907	0.04	± 0.00	0.08	± 0.01	38	0.000	0.09	± 0.01	0.08	± 0.01	74	0.956
Dihydroferulic acid	1907	0.08	± 0.00	0.08	± 0.00	114	0.243	0.08	± 0.00	0.08	± 0.00	53	0.222
Alkane 1	1918	0.57	± 0.02	0.60	± 0.01	113	0.230	0.61	± 0.02	0.57	± 0.02	54	0.244
C10:1 DA	1957	0.84	± 0.03	1.17	± 0.06	32	0.000	1.09	± 0.06	1.32	± 0.10	37	0.035
Unidentified 4	1986	0.71	± 0.04	0.68	± 0.06	118	0.299	0.69	± 0.09	0.63	± 0.06	73	0.912
Unidentified 5	2023	1.75	± 0.07	2.05	± 0.11	99	0.098	2.31	± 0.15	1.72	± 0.11	30	0.013
Palmitic acid	2052	0.22	± 0.02	0.26	± 0.04	130	0.516	0.18	± 0.02	0.37	± 0.09	39	0.046
Unidentified 6	2068	1.21	± 0.04	1.78	± 0.11	59	0.003	1.76	± 0.16	1.86	± 0.16	62	0.471
Alkane 2	2119	0.10	± 0.01	0.15	± 0.03	72	0.011	0.12	± 0.01	0.21	± 0.06	35	0.027
Octadecenoic acid C18:1	2022	2.11	± 0.23	1.42	± 0.19	64	0.005	1.20	± 0.26	1.50	± 0.29	58	0.346
Stearic acid	2249	0.54	± 0.05	0.45	± 0.05	85	0.035	0.34	± 0.06	0.56	± 0.09	33	0.020

All significant differences with $p < 0.05$ are marked in bold. (E)-4-hydroxycinnamic acid (1948), (E)-coniferyl alcohol (1957), traces.

Brain Gene Expression Levels of Amfor

We used quantitative real-time PCR to measure Amfor expression levels in the queens' brains to determine if insemination treatment altered brain gene expression and therefore presumably altered the neuronal properties in the brain. Amfor expression was significantly higher in SDI queens than in MDI queens ($U = 10$, $p = 0.02$; Fig. 4).

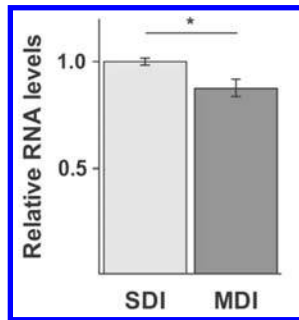


Figure 4: Brain gene expression levels are affected by insemination quantity.

Expression levels of *Amfor* were monitored using quantitative real-time PCR using individual brains (SDI: N = 9; MDI: N = 9). The SDI queens have significantly higher levels of *Amfor* than MDI queens ($U = 10$, $p = 0.022$). The data represent mean values, \pm standard error (converted to the same arbitrary scale as the mean), relative to the SDI brains.

KEY WORDS

- Bee rearings
- Cage assays
- 2-Decenoic acid (ODA)
- 9-Hydroxy-(E)-2-decenoic acid (9-HDA)
- Hydroxy-3-methoxyphenylethanol (HVA)
- Queen mandibular pheromone (QMP)
- Queen rearing
- Mating number
- Methyl p-hydroxybenzoate (HOB)
- Multi-drone inseminated (MDI)
- Retinue response
- Single-drone inseminated (SDI)

ACKNOWLEDGMENTS

We would like to thank Coby Schal and Michael Roe for use of their GC and GC/MS instruments, Cavell Brownie for her advice on the statistical analyses, Josh Summers, Jennifer Keller, and Joe Flowers for their beekeeping assistance, Kelly Hutcherson and Cynthia Rouf for their assistance in the field. This experiment complies with the laws of the USA.

AUTHORS' CONTRIBUTIONS

Conceived and designed the experiments: Christina M. Grozinger, Freddie-Jeanne Richard, and David R. Tarp. Performed the experiments: Freddie-Jeanne Richard and David R. Tarp. Analyzed the data: Christina M. Grozinger and Freddie-Jeanne Richard. Contributed reagents/materials/analysis tools: Christina M. Grozinger and David R. Tarp. Wrote the paper: Christina M. Grozinger, Freddie-Jeanne Richard, and David R. Tarp.

Chapter 13

High Heat Effect on City Ants

Michael J. Angilletta, Jr. Robbie S. Wilson, Amanda C. Niehaus,
Michael W. Sears, Carlos A. Navas, and Pedro L. Ribeiro

INTRODUCTION

Urbanization has caused regional increase in temperatures that exceed those measured on a global scale, leading to urban heat islands, as much as 12°C hotter than their surroundings. Optimality models predict that ectotherms in urban areas should tolerate heat better and cold worse than ectotherms in rural areas. We tested these predications by measuring heat and cold tolerances of leaf-cutter ants from South America's largest city (São Paulo, Brazil). Specifically, we compared thermal tolerance of ants from inside and outside of the city. Knock-down resistance and chill-coma recovery were used as indicators of heat and cold tolerances, respectively. Ants from within the city took 20 percent longer to lose mobility at 42°C than ants from outside the city. Interestingly, greater heat tolerance came at no obvious expense of cold tolerance; hence, our observations support the current theory only partially. Our results indicate that thermal tolerances of some organisms can respond to rapid changes in climate. Predictive models should account for acclimatory and evolutionary responses during climate change.

Major cities are hotter than their surroundings for many reasons, including the greater radiation from surfaces, the greater emission of heat, the thermal mass of buildings, the reduced evapotranspiration from soil, and the unusual pattern of convection [1]. Urban heat islands—increased temperatures within urban areas—scale logarithmically with the population of a city [2]. In the world's largest cities, the difference between urban and rural temperatures reaches as much as 12°C. Urban warming likely has widespread biological consequences; after all, environmental temperature has been linked to everything from temporal patterns of growth, survival and reproduction [3-5] to spatial patterns of body size, population density, and species diversity [6-8]. Urban heat islands should not only concern ecologists who wish to manage urban populations, but they should also interest the physiologists who seek to test theories of thermal adaptation.

Optimality models predict acclimatory or evolutionary responses, such that ectotherms in warm environments should tolerate high temperatures better and low temperatures worse than ectotherms in cool environments [9-11]. Researchers usually test these predictions by comparing the indices of acute or chronic thermal tolerance, such as the duration of survival during exposure to an extremely high temperature (knock-down resistance), or the duration of recovery after exposure to an extremely low temperature (chill-coma recovery). For several species, researchers have shown

that genotypes from low latitudes or altitudes tolerate heat better but cold poorer, than do genotypes from high latitudes or altitudes [12-14]. Therefore, we suspected that similar differences in thermal tolerance would be associated with the more localized clines in temperature caused by urbanization. Specifically, ectotherms from warm, urban environments should tolerate heat better and cold worse than ectotherms from cool, rural environments [15].

To test our predictions, we compared the thermal tolerances of leaf-cutter ants (*Atta sexdens*) from colonies inside and outside of São Paulo, Brazil (Fig. 1). With a population exceeding 10 million people, São Paulo fuels one of the most intense urban heat islands in the world [16], with distinct peaks occurring during the night in winter and during the day in summer [17]. Surface temperatures of the urban heat island should determine the body temperatures of small, terrestrial organisms, such as leaf-cutter ants [18]. Although leaf-cutter ants emerge primarily at night, some ants also forage during the day when surface temperatures can exceed 45°C (Fig. 2). Tolerance of extreme heat would enable ants to evacuate a trail effectively as temperatures rise during mid-day.

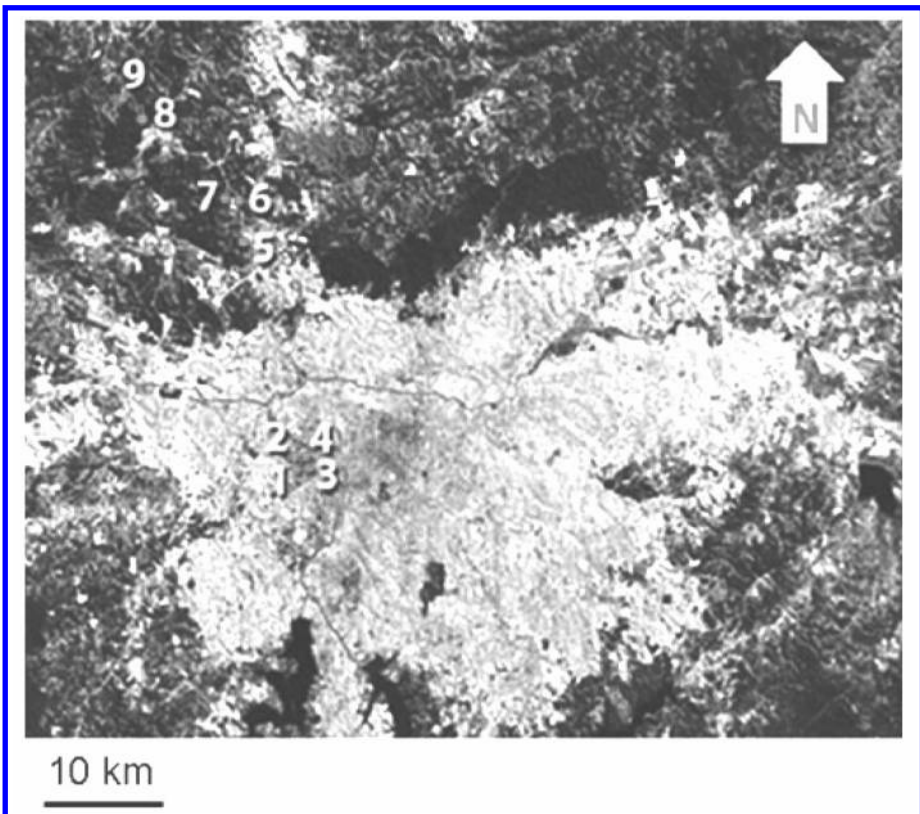


Figure 1: A satellite image of São Paulo showing the location of the colonies that we sampled for our study (image available from the United States Geological Survey, Sioux Falls, SD). Colonies 1–4 and 5–9 experienced urban and rural environments, respectively.

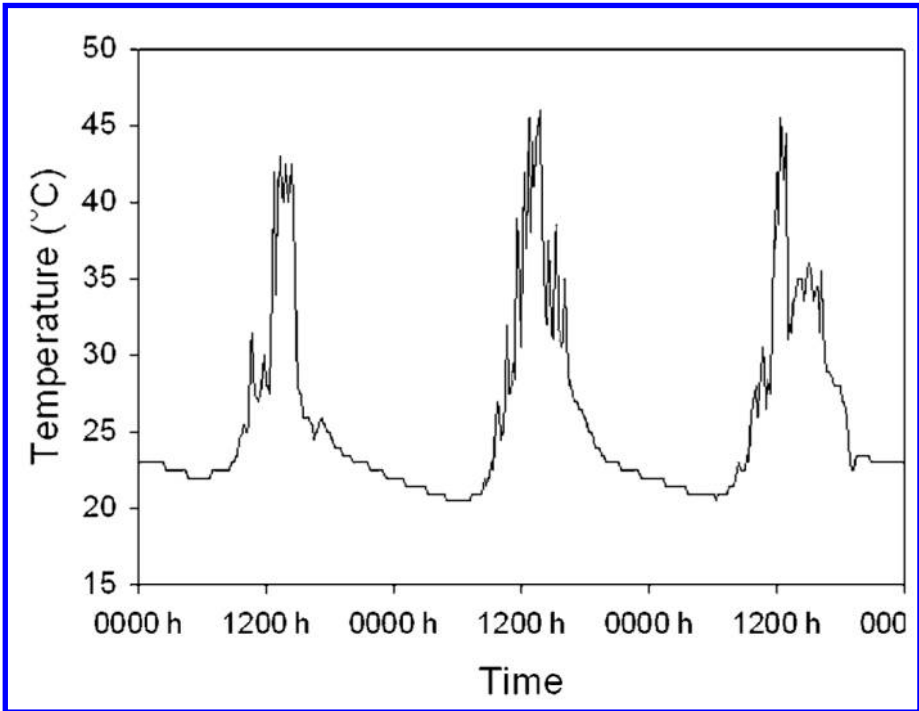


Figure 2: Trail temperatures exceed the critical thermal maximum for leaf-cutter ants for several hours per day. This data was recorded by an iButton Thermochron (Dallas Semiconductors) that was placed in full sun on the surface of an active trail. Data was collected during the week preceding our study (March 19–22, 2006); this same trail should be even hotter during the middle of summer.

MATERIALS AND METHODS

Sampling of Colonies

We sampled colonies of leaf-cutter ants (*Atta sexdens rubropilosa*) inside and outside of São Paulo. Our samples included four urban colonies near the University of São Paulo and five rural colonies distributed along a north-westerly transect (Fig. 1). We collected only those ants that were walking along trails, carrying leaves, or pieces of leaves. To minimize environmental and procedural effects, we collected all ants and measured their thermal tolerances on the same day (March 30, 2006). We collected ants between 1600 and 2200 h and began measures of thermotolerance by 2300 h. Logistically we were unable to collect ants from urban and rural colonies at the same time; therefore, urban ants were collected after rural ants to minimize the chance that high temperatures during collection would cause urban ants to tolerate heat better than rural ants. Between the time of collection and the time of the experiment, we held ants in large plastic jars containing a piece of saturated cotton as a source of water.

Heat Tolerance

We defined heat tolerance as the time required for the ants to lose mobility at a stressful temperature, usually referred to as knock-down resistance [19]. This common measure

of heat tolerance seems to correlate well with other measures of heat tolerance when comparing species [20]. During a preliminary study, we determined that ants from urban colonies were immediately immobilized at 44°C (= critical thermal maximum). We also noted that ant trails in the city approached these temperatures during mid-day (Fig. 2). Therefore, we assessed knock-down resistance at 42°C, a temperature slightly below the critical thermal maximum and within the range of temperatures experienced in nature.

To compare knock-down resistances of urban and rural ants, we used ants from four urban colonies ($n = 24\text{--}30$ per colony) and five rural colonies ($n = 30$ per colony). Ants from each colony were divided into groups of six; each group was placed in a Petri dish (150×10 mm) with a small piece of water-saturated cotton. The water was provided to ensure that ants did not succumb to heat due to dehydration. During the trials, some ants were observed drinking from the cotton and sharing fluids with neighboring ants. Furthermore, heat tolerances of urban and rural ants were unrelated to body mass in either urban or rural colonies, suggesting that variations in water stores and dehydration rates were unimportant; this conclusion was based on ANCOVA, in which colony was used as a random factor to control for pseudoreplication (urban ants: $\beta = 4.6 \pm 4.0$, $F_1, 5.9 = 1.66$, $P = 0.10$; rural ants: $\beta = 0.41 \pm 1.19$, $F_1, 8.2 = 1.15$, $P = 0.31$).

Knock-down resistance was measured in a walk-in environmental chamber that maintained a constant temperature during the experiment. All Petri dishes were brought into the room at the same time and were placed on a table for observation. Surface temperature of the table ($42 \pm 1^\circ\text{C}$) was monitored with data loggers (i-Button ThermoChron, Dallas Semiconductors) and an infrared thermal gun (Raynger ST30, Raytek). To minimize artifacts caused by thermal gradients, we created five zones along the length of the table; one Petri dish of ants from each colony was placed in each zone. Urban and rural ants within each zone were stratified to further reduce the chance of spatial artifacts.

During the experiment, at least four people scanned the dishes to identify the time that each ant lost mobility. Although ants clearly became disoriented before losing mobility, we found the loss of mobility to be a more objective criterion for scoring heat tolerance. Because ants can assume a curled position during heat stress, we tapped the dishes periodically to assess whether ants were truly immobilized or were merely exhibiting signs of stress. Tapping of dishes was performed in a systematic manner such that all the ants were disturbed similarly.

We compared the knock-down resistances of urban and rural ants with a Cox proportional hazards model, from the survival library of the R Statistical Package (R Development Core Team 2006). Because knock-down resistances of ants within colonies and within Petri dishes were likely correlated, we used a robust sandwich estimate of the variance, which accounted for correlated responses of individuals within colonies and dishes [21, 22]. This procedure enabled us to generalize our findings without pseudoreplication.

Cold Tolerance

We defined cold tolerance as the time required to recover from exposure to 0°C, usually referred to as chill-coma recovery. To compare chill-coma recoveries of urban and rural ants, we used ants from four urban colonies ($n = 19\text{--}31$ per colony) and four rural colonies ($n = 20\text{--}30$ per colony). Ants were sorted into Petri dishes (150×10 mm), which were entombed in ice for a period of 20 min. After this exposure, dishes were removed from ice and ants were transferred to sheets of paper at room temperature ($25 \pm 1^\circ\text{C}$). Using forceps, we positioned each ant on its back in the center of a printed circle (diameter = 32 mm). We recorded the time that elapsed between the removal of dishes from ice and the recovery of each ant. Recovery was scored when an ant assumed an upright position and broke the plane of the circle; this simple, objective measure of recovery reflected the onset of motor coordination because ants generally began exploring their environment immediately after assuming an upright position. As each ant left its circle, we covered it with a small plastic cup to prevent the ant from interfering with other ants on the same sheet.

Our experimental design controlled for many sources of variation. Because ants had to be assayed in successive trials, each trial involved ants from one urban and one rural colony. To ensure accurate detection or recovery, not more than thirty ants from each colony were assayed at a time, and at least three people watched the ants at all times. Petri dishes containing urban and rural ants were chilled together, and the position of urban and rural dishes was rotated between trials. To control for thermal heterogeneity within the room, we switched the positions of the papers for urban and rural ants between each trial. To minimize delays during data collection, we used event-recording software (ETHOM) to record the time of each observation [23]. We compared the time required to recover from chill coma using the same proportional hazards model that we used to compare knock-down resistances.

DISCUSSION

The difference in heat tolerance between urban and rural ants resembles differences documented within species that span latitudinal and altitudinal clines [reviewed by 24]. In *Drosophila melanogaster*, flies from northern Australia resisted heat longer but recovered from cold slower than flies from southern Australia [14]. In other species, either heat or cold tolerance varies geographically. For example, Sorensen and colleagues [25] observed an altitudinal cline in heat tolerance among populations of *Drosophila buzzatii*, without observing a cline in cold tolerance. This macrogeographic pattern observed among flies parallels the microgeographic pattern we observed among ants.

Currently, we do not know whether the difference between the heat tolerances of urban and rural ants has a genetic basis or simply results from plastic responses to environmental conditions. Studies of *Drosophila* have generally focused on offspring raised in a common environment to reduce environmental sources of variation in thermal tolerance. Unfortunately, we could not perform such studies with

ants. Therefore, some or all of the difference in heat tolerance could have resulted from acclimatization of urban ants (i.e., heat hardening). Nevertheless, plasticity in heat tolerance could also be an adaptation to the mean and variance of environmental temperature [10, 11]. Whether genetic effects, environmental effects, or both caused the greater heat tolerance of urban ants, our finding suggests that urbanization has influenced the phenotypes of ants in São Paulo.

The ecological significance of variations in knock-down resistance and chill-coma recovery remains controversial [19]. We believe these indices of thermal tolerance correlate with the thermal limits to survivorship under chronic exposure. Variation in these indices could also reflect variation in the shape of thermal performance curves, especially if performance at extreme temperature trades off with performance at intermediate temperatures [26]. Heat tolerance should directly benefit ants during activity because trails attain stressful temperatures for several hours per day (see Fig. 2). Indeed, many ants became disoriented and assumed defensive postures well before losing mobility, suggesting high heat tolerance would enable ants to evacuate a trail effectively as temperatures rise during mid-day. Observations of urban and rural ants in outdoor enclosures would help to define the ecological significance of the thermal tolerances that we observed.

Urban environments serve as excellent natural experiments for quantifying the impact of climate change on organisms. Although urbanization affects more than just the temperature of the environment, large cities arguably provide a timely model for understanding ecological and evolutionary responses to regional and global climate change. We expect researchers will find variations in thermal tolerance within other species that encounter urban heat islands. By studying such phenomena, scientists can better gauge the potential for acclimatization or adaptation during global climate change. Ultimately, studies of urban physiology could alter our current perspective, especially since most documented responses to climate change involve shifts in behavior and phenology rather than shifts in physiological tolerance [27].

RESULTS

When exposed to the stressful temperature of 42°C, ants from colonies within São Paulo survived 20 percent longer than ants from colonies surrounding São Paulo (mean \pm standard error = 216 \pm 4.8 and 179 \pm 4.2 min for urban and rural ants, respectively). A Cox proportional hazards model indicated that rates of mortality differed significantly between urban and rural colonies (β = -0.535 \pm 0.237; P = 0.02; Fig. 3.A). This greater heat tolerance came at no obvious expense of cold tolerance; mean times for urban and rural ants to recover from chill coma were nearly identical (6.6 \pm 0.2 and 6.7 \pm 0.2 min for urban and rural ants, respectively). A Cox proportional hazards model indicated no significant difference between the rates at which urban and rural ants recovered from cold exposure (β = -0.124 \pm 0.288; P = 0.67; Fig. 3B). Hence, our observations support the current theory only partially.

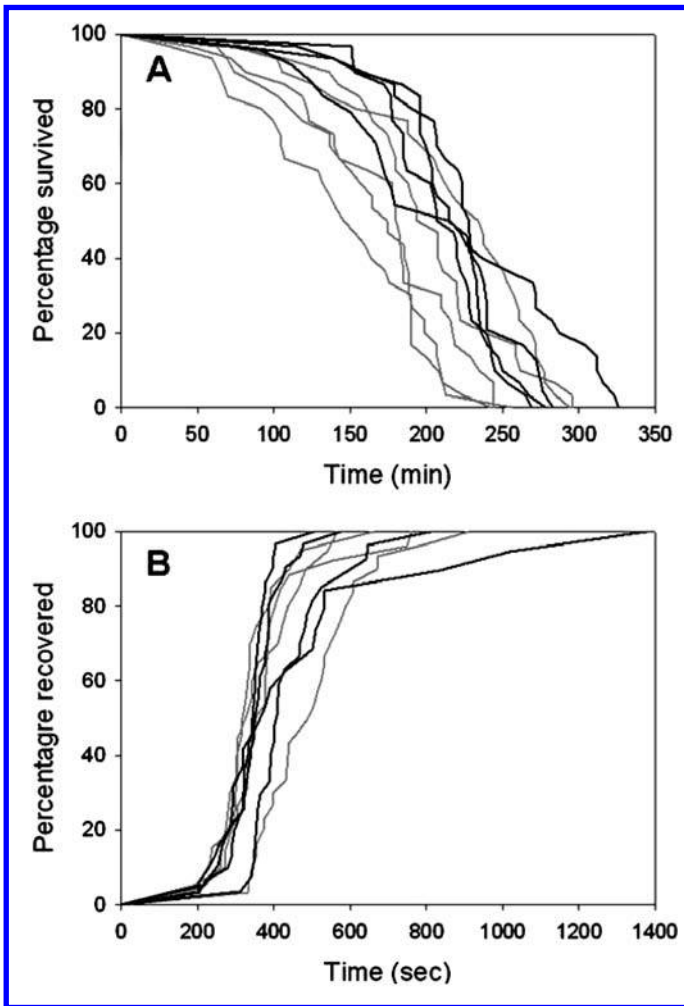


Figure 3: A) Ants from urban colonies (G lines) tolerated extreme heat (42°C) for a longer time than did ants from rural colonies (gray lines). Each line represents the survivorship curve of ants from a single colony. B) Ants from urban and rural colonies recovered from chill coma within a similar period of time. Each line represents the recovery curve of ants from a single colony.

KEY WORDS

- Chill-coma recovery
- Cold tolerance
- Ectotherms
- Event-recording software (ETHOM)
- Knock-down resistance
- Urbanization

ACKNOWLEDGMENTS

We thank Ivan Prates for his tireless help in the lab.

AUTHORS' CONTRIBUTIONS

Conceived and designed the experiments: Michael J. Angilletta, Jr., Robbie S. Wilson, Amanda C. Niehaus, and Pedro L. Ribeiro. Performed the experiments: Michael J. Angilletta, Jr., Robbie S. Wilson, Amanda C. Niehaus, and Pedro L. Ribeiro. Analyzed the data: Michael J. Angilletta, Jr., Amanda C. Niehaus, and Michael W. Sears. Contributed reagents/materials/analysis tools: Michael J. Angilletta, Jr., Robbie S. Wilson, Pedro L. Ribeiro, Carlos A. Navas, and Michael W. Sears. Wrote the paper: Michael J. Angilletta, Jr. and Michael W. Sears.

Chapter 14

Hemolymph Flow in Grasshoppers' (*Schistocerca americana*) Hearts

Wah-Keat Lee and John J. Socha

INTRODUCTION

Hemolymph flow patterns in opaque insects have never been directly visualized due to the lack of an appropriate imaging technique. The required spatial and temporal resolutions, together with the lack of contrast between the hemolymph and the surrounding soft tissue, are major challenges. Previously, indirect techniques have been used to infer insect heart motion and hemolymph flow, but such methods fail to reveal fine-scale kinematics of heartbeat and details of intra-heart flow patterns. Synchrotron X-ray phase contrast imaging is the only generally applicable technique that has the necessary spatial, temporal resolutions and the sensitivity to directly visualize heart dynamics and flow patterns inside opaque animals. This technique has the potential to illuminate many long-standing questions regarding small animal circulation, encompassing topics such as retrograde heart flow in some insects, and the development of flow in embryonic vertebrates.

Direct visualization of blood flow in small (millimeter-centimeter scale) animals remains a major challenge. Generally, spatial and temporal resolutions better than 50 μm and 0.1 s are required for studies in insect physiology. Current techniques, including X-ray, Magnetic resonance imaging (MRI), and ultrasound or visible light probes, suffer from insufficient spatial or temporal resolutions, lack of sensitivity, or inability to penetrate the animal's opaque body. For example, MRI has recently been used to visualize the internal dynamics of circulation, respiration, and digestion in tobacco hornworm pupae, but the temporal resolution (~ 300 ms) and spatial resolution (~ 150 μm , laterally) of MRI are insufficient to distinguish fine kinematic details of motion [1]. Consequently, internal movements in small animals such as insects remain poorly understood. One prominent example is the movement of hemolymph in the insect circulatory system. Real-time synchrotron X-ray phase-contrast imaging [2] has recently been demonstrated to be an excellent technique, for the study of the respiratory and digestive systems in small animals, and it has the necessary resolution to study blood flow as well. This technique is capable of spatial and temporal resolutions of ~ 1 μm and ~ 100 ps, respectively, although these parameters have to be weighed against the detrimental effects on the animal because higher temporal resolutions require higher beam intensities. Despite the capabilities of synchrotron X-ray imaging, this imaging technique alone cannot distinguish blood from the rest of the soft tissue because density differences are minimal. Here, we demonstrate a new method of visualizing

blood flow at the micrometer scale in intact small animals, using microbubble injection combined with synchrotron X-ray imaging.

For transparent or semi-transparent animals, visible light imaging techniques have been used successfully to study gross patterns of heart activity and blood flow in small animals. Movement of hemolymph, the insect “blood,” from the abdomen to the wings of a butterfly has been visualized by introducing a visible-light dye into the hemolymph [3]. Confocal microscopy has shed new light on the heart activity and blood flow in a zebra fish embryo, showing that pumping is not peristaltic, as was previously thought [4]. Optical coherence tomography (OCT) has been used to image heartbeat in *Drosophila melanogaster* [5], and Doppler OCT has been used to visualize blood flow in frog embryos [6]. Although these recent developments are promising, they remain ultimately limited by the transmission of light: many small animals have opaque exteriors and/or the heart is located sufficiently deep that there is insufficient visible light transmission to form an image. More importantly, none of these visible light techniques have demonstrated the ability to measure intra-heart flow patterns in animals with millimeter-centimeter-scale body size.

For animals with opaque bodies, a variety of indirect, non-imaging methods have been devised to deduce heart activity and circulation patterns. To study heart activity, researchers have implanted electrodes near the heart and used the impedance between them as a proxy for heart pulsations [7, 8]. This electrocardiogram technique is invasive and requires considerable skill in the implantation of the electrodes; moreover, it is not feasible for millimeter-sized animals. Alternatively, visible or infrared light transmission or reflected intensity has been used to detect heart pulsations [9, 10], and by using multiple probes, it is possible to deduce the temporal relationship between different heart segments [11]. Broad patterns of hemolymph flow have been inferred using “thermography” in which thermistors are attached to the exterior dorsal surface near the heart [12], and the flow is deduced by small temperature fluctuations in the thermistor. Indirect techniques have also provided inferential evidence for the relationship between the hemolymph flow and CO₂ exchange [13-15], the retrograde flow through the insect heart [10, 11], and for the function of accessory pulsatile organs that are hypothesized to help circulation [16]. Although these non-imaging techniques provide evidence of bulk flow, they do not provide quantitative structural information involved in heartbeat (e.g., amount of compression or shape change) or circulation (e.g., flow patterns). Furthermore, because they are inferential, these indirect techniques face common challenges involving data interpretation. For example, insects can telescope the abdomen, compress internal air sacs, and contract the gut, and these movements may occur independently from the heartbeat, making it difficult to distinguish the “true” signal from artifact with certainty (however, see [11]). Lastly, because these are “point” techniques, they cannot provide the contextual spatial information provided by direct imaging techniques. For example, using thermography, it is not possible to differentiate between hemolymph flows in an insect’s heart, versus flow in the surrounding pericardial sinus [17].

The insect circulatory system is profoundly different than its mammalian counterpart. Instead of flow occurring in a closed system of tubes and produced by a large

central pump, the insect system is open, consisting of a single, open-ended tube (the heart and aorta) that runs dorsally from the abdomen to the thorax or head [18]. The tube contains slit-like incurrent and excurrent valves (ostia) that run laterally along the length of the heart. Circumferential muscles ring the heart, and fan-like alary muscles connect it laterally to the body wall. Insects pump hemolymph through the heart toward the head (anterograde flow), and, in some species, reverse the flow toward the abdomen (retrograde flow) [10, 11]. However, the detailed flow patterns that result, both within the heart and the body, and how exactly they are produced are almost entirely unknown. Thus the detailed mechanics of the circulatory system of perhaps the most speciose and abundant animal group on earth remains largely unknown. The ability to directly visualize the fundamental physiological functions of microfluid flow *in situ* will be extremely valuable in advancing our understanding of the circulatory system in insects and other small animals.

In this study, we visualized heart flow directly with synchrotron X-ray phase-contrast imaging combined with the use of microbubbles as high-contrast tracer particles. Microbubbles are used in clinical environments as contrast agents for ultrasound imaging [19, 20]; however, the spatial resolution for *in-vivo* ultrasound imaging is wavelength limited to about 100 μm [21]. Our technique allows for direct simultaneous visualization of hemolymph flow and heart and tracheal activity, with micrometer-level spatial resolution and excellent image contrast. Although MRI [1] and OCT [5] have been used to study the structural dynamics of internal heart activity in insects, these techniques do not measure the actual flow rates. As far as we know, this is the first measurement of intra-heart flow rates, patterns and dynamics with micrometer-level spatial resolution in an insect. Although the results presented here are taken with video rate (30 Hz) acquisition, much faster exposure times and frame rates are possible at the cost of increased damage to the animal [2]. This technique extends the capability of synchrotron X-ray phase-contrast imaging to study all three essential fluid transport systems in insects: respiration (air), feeding (liquid food), and circulation (hemolymph).

MATERIALS AND METHODS

Schistocerca americana grasshoppers (mass, 1.3–1.7 g) were obtained from the laboratory colony of Prof. Jon Harrison (Arizona State University), and were supplied with food and water *ad libitum* prior to the experiment. Only males were used. We used clinical grade microbubbles (lipid/octafluoropropane bubbles; Definity, Bristol-Meyers Squibb) as the contrast agent. The average size of the microbubbles in the contrast agent (98% < 10 μm , 2.4–3.1 μm median) was near the spatial resolution of our system, and therefore was at the limit of visibility. These clinical grade microbubbles could indeed be seen in the grasshopper, but they did not provide the degree of flow visualization that we were seeking. To achieve larger, more easily tracked bubbles in the animal, we purposely left air (roughly the same volume as the Definity solution) in the tip of the needle when loading the syringe with the microbubble solution; during injection, both air and solution were then transferred into the grasshopper, creating additional 10–150 μm sized bubbles in the hemolymph. For the creation of the larger

bubbles, the Definity solution merely acted as a non-toxic surfactant to reduce surface tension, and it is likely that other cheaper alternatives may work as well. We experimented with different injection protocols; for the data presented in this chapter, we injected the animal both on the dorsal and ventral sides of the abdomen, near the third to last segment. On the dorsal side, we attempted to inject into the pericardial sinus, but were unable to verify placement due to hemolymph circulation between the time of injection and the start of imaging. Bubbles appeared stable over the course of the measurements (20 min to 1 hr), and disappeared within 24 hr.

Animals were held in place with a clip attached to the wings, with the abdomen oriented parallel to the ground and orthogonal to the X-ray beam, providing a lateral view image (Fig. 1). The legs and abdomen were inserted into separate Kapton (DuPont) tubes with slightly larger diameters, permitting small movements, but precluding large-scale movements for stable imaging. The tubes were arranged to position the legs out of view. The animal was mounted on a translation stage, allowing movement relative to the X-ray beam, and translation was controlled remotely.

For X-ray imaging, the X-ray energy was 25 keV and the incident power density was 80 W mm, similar to that used in our previous work [2]. The X-rays passing through the insect were converted to a visible light image using a cerium doped Y3A-15O12 scintillator, which was then imaged onto a video camera (Cohu 2700) using a Mitutoyo 5 × microscope objective together with a tube lens. The field of view was approximately 1.3 mm × 0.9 mm. Video images were recorded onto miniDV tapes. iMovie (Apple, OSX) was used to convert movie clips into still image stacks (30 frames per second) and then analyzed using MATLAB (Mathworks, MA, USA). A 400-mesh transmission electron microscope grid was used for image calibration. The data was collected at the X-ray Operations and Research beamline 32-ID-C at the Advanced Photon Source, Argonne National Laboratory.

For image analysis, the following protocol was used. To quantify pericardial compression, we identified locations along the heart with the most pronounced movement and digitized two points: one on the dorsal diaphragm, which moved dorsoventrally during compression, and one near the dorsal cuticle, which was static relative to compression. We defined pericardial depth as the vertical distance between these points; decreasing pericardial depth indicates compression. For tracheal compression analyses, we measured the diameter of the trachea by digitizing the dorsal and ventral edges of the tube. For some sequences, we scored flow discretely as forward (bubbles moving anteriorly), backward (bubbles moving posteriorly) or none (no overall translation of bubbles). Due to bubble buoyancy, our flow quantification was restricted to the dorsal regions of the heart.

DISCUSSION

Prior work on grasshopper hearts consists of optical cardiography (*Schistocerca gregaria*, [9]), electrocardiography and mechanography (*Melanoplus differentialis*, [23]), and direct observation through live dissection (multiple species, [22]). These studies quantified heart activity, but did not measure the hemolymph flow patterns within the heart. One valid comparison that can be made among studies is between mechanography

(pulsations detected using an electromechanical setup) and our measured pericardial compressions. Among the studies, measured pulsation frequencies (0.8–1.0 Hz) and waveform shapes are similar. Additionally, Jahn and colleagues [24] showed that the shapes and frequencies of the optical, electrical and mechano cardiography signals can vary greatly, from individual to individual, and show large dependence on temperature, further reinforcing the need for understanding the link between electrocardiography and actual flow.

More generally, we can compare this X-ray imaging method with other techniques that have recently been used to study small animal circulation. Confocal microscopy provides 2D depth-resolved images with micrometer-level spatial resolution, with depth of focus usually no more than a few micrometers, and high speed confocal microscopy has been demonstrated at 1000 frames per second (fps) [25]. Microscopic flow patterns can be quantified through the use of fluorescent tags, although the depth of focus can be a limitation if the flow is not parallel to the focal plane. OCT provides cross-sectional images of the sample with spatial resolution in the tens of micrometers [26], and framing rates of 1000 fps have also been demonstrated [6]. Doppler OCT can provide information on bulk flow, but it is not quantitative [6]. Both confocal microscopy and OCT are visible light techniques, and therefore, are limited by light transmission. Recently, MRI has been used to image the cross-sectional structure and flow in the pupae of the tobacco hornworm caterpillar (*Manduca sexta*) [1]. However, the spatial resolutions (156 μm with a slice thickness of 500 μm) are still not comparable to synchrotron X-ray phase contrast imaging or visible light techniques. MRI cross-sectional images can be obtained at a frequency of about 3 Hz [1]. In contrast, the X-ray technique described in this chapter has spatial resolution that is comparable to visible light techniques (μm -level), and high-speed X-ray imaging is possible as well. Compared to visible light techniques, X-ray imaging has the advantage of high penetration and can be used for opaque samples. X-ray images are 2D transmission projections and therefore depth information is lost, but this has the advantage that one can see through the entire animal without the need to adjust a “depth of focus.” Transverse flow (perpendicular to X-ray direction), when imaged with tracer particles, can be quantified at the micrometer-level, which cannot be done with MRI or OCT. Two disadvantages of this technique compared to visible light or MRI are that (1) the X-rays can have a detrimental effect on the animal [2] and (2) the need for contrast agents or tracer particles.

Several challenges and improvements need to be addressed to make this technique more accessible. First, it is necessary to tailor the contrast agent to the animal or species. In particular, it is important to limit the amount of bubbles within the volume of interest; otherwise, the projected overlapping bubbles will overwhelm specific features of interest. Second, it is important to generate bubbles of the proper size; obviously, for the visualization of internal heart flow, the sizes should be substantially smaller than the cross-sectional heart dimensions. Third, different species may require different injection protocols depending on anatomy and physiology. Finally, there is the question of bubble buoyancy and differences between bubble and fluid motion, which may be a major limitation on the quantification of flow. In our experiments, we oriented the insect's abdomen horizontally so that any observed posterior-to-anterior bubble flow

could be definitively attributed to fluid flow, rather than to buoyancy. The buoyancy issue can be addressed in future studies by using tracer particles that have a more comparable density with the hemolymph, such as metal-coated hollow glass spheres. Differences between actual fluid motion and bubble/tracer particle motion, and the effects of the bubbles themselves on the fluid motion, are complex questions that are beyond the scope of this chapter, especially in the realm of non-uniform pulsating flow that we see here. Nonetheless, for the parameters used here, the speed of the bubble should reflect the speed of the fluid, although there may be a phase difference between the two [27, 28]. The use of neutrally buoyant and smaller tracer particles should solve this problem. Finally, although we were able to quantify representative instances of individual bubble speed, the frame rate (30 fps) of our camera was not fast enough for a more complete velocity map. Planned future work includes the use of a high speed video camera (>500 fps), which should enable us to directly measure peak hemolymph flow velocities; the addition of flow-through respirometry, which would allow further insight into circulation-respiration coupling; and combination of this technique with available indirect techniques (e.g., thermography, light transmission), for purposes of verification and for generating complementary data.

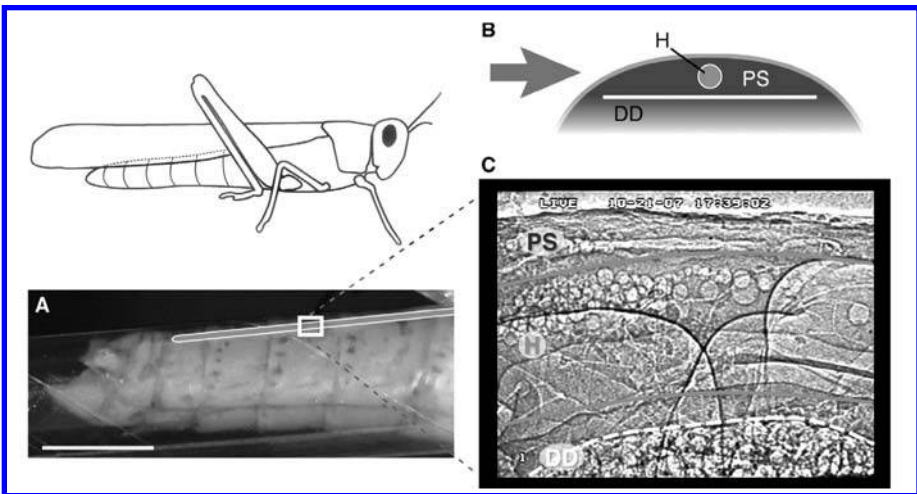


Figure 1: Flow visualization in the heart of a grasshopper (*Schistocerca americana*) using synchrotron X-ray phase-contrast imaging. (A) Side view of the grasshopper abdomen showing the approximate location of the heart (C), and the relative size of the imaging window (E rectangle, 1.3×0.9 mm). The abdomen is encapsulated in an X-ray transparent Kapton tube. Scale bar, 5 mm. (B), Cross-sectional schematic of the dorsal abdomen showing the relative sizes and locations of the heart (H), dorsal diaphragm (DD), and pericardial sinus (PS). The B arrow indicates the orientation of the X-ray beam. (C) X-ray video still of a region in the dorsal third abdominal segment in lateral view. Round structures are air bubbles used to visualize patterns of heartbeat and hemolymph flow.

RESULTS

Microbubbles ranging from 10–150 μm in diameter were clearly visualized, as were air sacs and numerous tracheae, including a main longitudinal tracheal trunk that runs adjacent to the heart (Fig. 1C). The buoyant bubbles accumulated along the ventral edge of the dorsal diaphragm, which partially compartmentalizes the dorsal heart region.

Within the heart, the buoyant bubbles demarcated the dorsal edge of the heart lumen. The ventral edge of the heart lumen could not be clearly identified, but the paths of microbubbles during flow within the heart suggested its ventral extent. Microbubble flow, compression of the pericardial sinus and changes in the tracheal diameters were all clearly visualized.

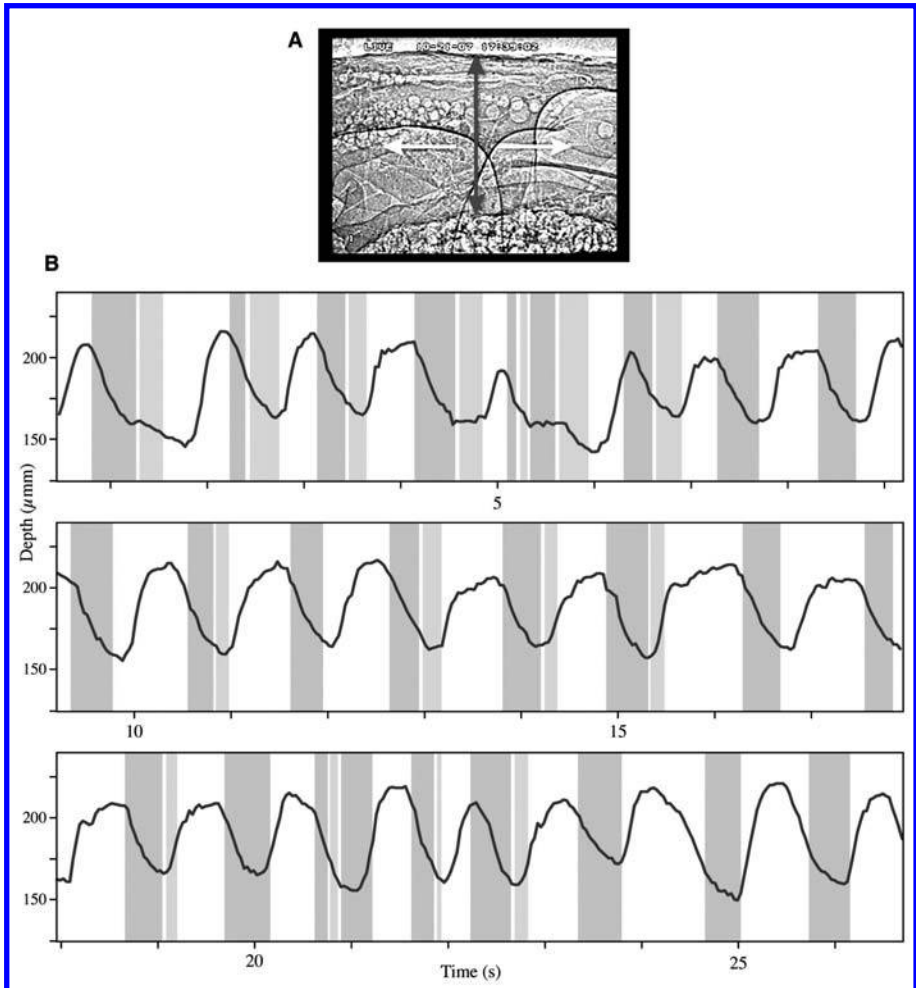


Figure 2: Relationship between the heart movements and hemolymph flow (third abdominal segment) in the grasshopper *Schistocerca americana*. (A) Side view X-ray video image indicating the color conventions used in (B). Anterior is to the right; dorsal is to the top. (B) Time series from one video sequence showing the relationship between pericardial sinus depth (C) and hemolymph flow direction (A, F, and E). Decrease in pericardial sinus depth corresponds to compression. A represents net forward (anterograde) flow, (F) represents backflow, and E indicates zero flow. Average compression frequency was 55 cycles/min (0.92 Hz). In most instances, forward flow occurred only during compressive movements of the pericardial sinus, and presumably of the heart itself. Backflow did not occur with each forward flow event, but when it did, it occurred directly after the forward flow event. Note that there was no observable hemolymph movement for roughly half the time.

As seen within the field of view ($1.3 \text{ H} \times 0.9 \text{ V mm}$), the flow patterns were complex and dependent on location. At any particular location along the heart, general flow patterns were repetitive, but not strictly time-periodic, over the course of the measurement (10 sec of seconds). For most pulsations (e.g., Fig. 2), forward flows coincided with the local pericardial compressions (see Methods). Interestingly, back flows, when they occurred, began during pericardial compression, and ended at or after the end of the compression. However, this could be due to a phase lag between the hemolymph and the bubble (see Discussion). The amplitude of pericardial sinus compression varied locally. Compressions of the longitudinal tracheal trunk were not synchronized with the pericardial sinus compressions (e.g., Fig. 3); however, their frequencies were similar (0.8–1.0 Hz). Air sac compressions also appeared to be independent of the pericardial sinus compressions. Flow within the heart was pulsatile, but did not appear to be bolus-like. Unlike previously observed peristaltic transport in the gut [2] in which the bolus-like transport of food and gut peristaltic waves were readily apparent, the hemolymph transport mechanism within the heart remains unknown from this preliminary study.

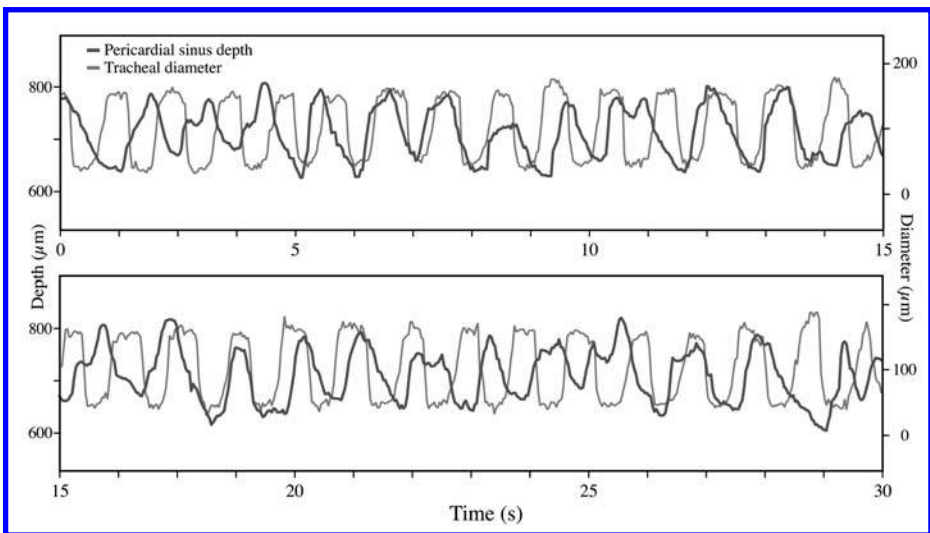


Figure 3: Relative timing of compression of the pericardial sinus (C) and a main longitudinal trachea (B) in the dorsal abdomen (fourth segment) of the grasshopper *Schistocerca americana*. This sequence shows that the movements of the pericardial sinus and the trachea are not phase locked.

The power of this technique is exemplified in the ability to track small-scale flow patterns. For example, bubbles can apparently be seen to enter the heart by moving through incurrent ostia (Fig. 4). However, it was not possible to differentiate if the incurrent ostia were opening actively or passively, nor were we able to positively identify the movement of bubbles out of the heart through the excurrent ostia [22]. The local flow patterns near the ostia, but external to the heart, were complex. In general, bubbles were observed to enter the ostia, originating both posteriorly (e.g.,

Fig. 4a) and anteriorly (e.g., Fig. 4b). In either case, once they entered the heart, the bubbles were swept anteriorly with the heartflow. Another example shows the complexity of flow within the heart. In Fig 5, four microbubbles are tracked over the course of 25 frames (~0.83 sec) in one section of the heart. This sequence suggests that the bubbles were pulled towards the middle of the image during diaphragm dilation, and upon compression, hemolymph was transported towards the head. The ability to image individual microbubbles allowed us to quantify instantaneous velocities, and potentially to map complex flow fields. Such detailed flow information cannot be obtained from any other technique.

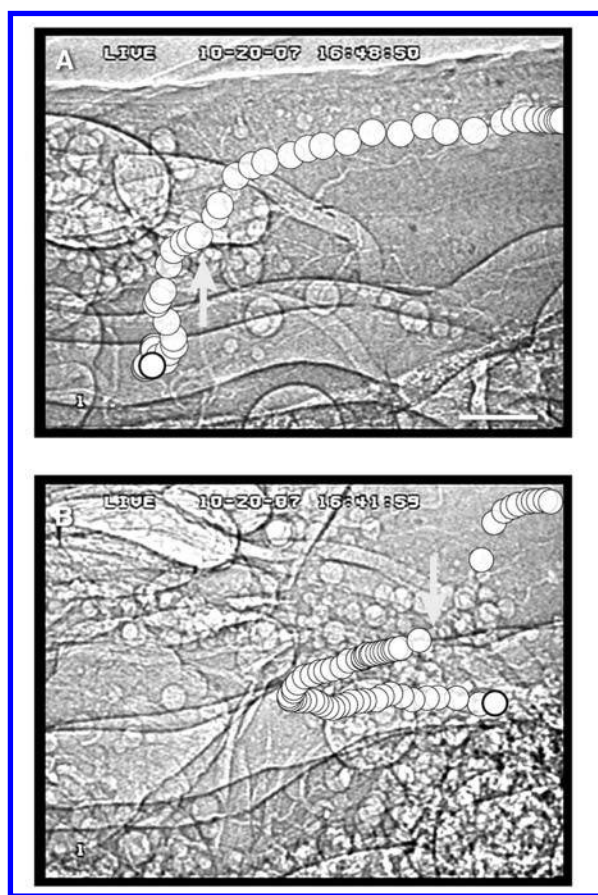


Figure 4: Examples of bubble movement through presumed ostial openings in the heart wall of the grasshopper *Schistocerca americana*. (F) bubbles represent single bubbles tracked through one video sequence (30 Hz), with the start of the sequence indicated in (E) and bubble positions corrected for whole-body movement. The (C) arrows represent the apparent locations of ostia, inferred from the movements of the bubbles. (A) Heart entrance event in which the bubble traveled dorsally and anteriorly in the pericardial sinus, moved through the ostium, and then was transported anteriorly within the heart (fifth abdominal segment). Scale bar, 200 μ m. (B) Entrance event in which the bubble moved posteriorly in the pericardial sinus, dorsally through the ostium, and anteriorly after entering the heart (sixth abdominal segment, same individual as above).

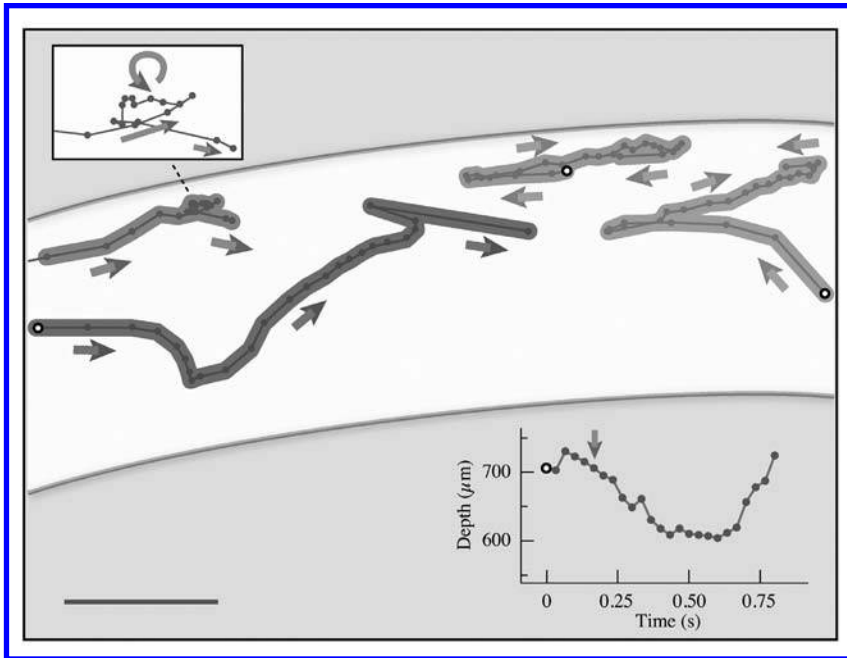


Figure 5: Examples of non-uniform flow patterns in the heart of the grasshopper *Schistocerca americana*. This schematically depicts the path of four bubbles digitized in one video sequence (duration, 0.83 sec) moving within the heart (white background, sixth abdominal segment). Each color represents a different bubble. The time between points is 0.033 sec; the start of the sequence is indicated with black and white circles. The overall motion of the flow is from left to right (anterograde; toward the head), but the microscale flow is non-uniform. For example, the (B) and (A) bubbles begin moving to the left while the (C) bubble was moving to the right; these bubbles also reverse the direction to the left at the end of their sequences. Note that the (D) bubble displays a counterclockwise vertical movement (shown with greater detail, inset box). The corresponding movement of the pericardial sinus is depicted in the graph (lower right). Note that the (D) bubble enters the frame from the left at $t = 0.20$ sec, 5 frames later than the other bubbles. Scale bar, 200 μm .

Although the main purpose of this chapter is to present this new technique, our measurements allow us to make a few preliminary observations on the hemolymph flow in the heart of the grasshopper *Schistocerca americana*.

1. In general, flow patterns are complex, and are time and location dependent. Furthermore, some flows appear to be three-dimensional. In some observations, there appeared to be no overall transport, but simply a back-and-forth oscillation of the hemolymph. This preliminary study suggests, that the origin of hemolymph transport may be more complicated than the commonly assumed peristaltic motion [10, 11, 14].
2. The maximum speed of bubbles that could be tracked was 9.5 mm/sec; faster moving bubbles were observed but could not be reliably measured due to motion blur (exposure, 16 ms). Based on this maximum speed, a heart diameter of 0.5 mm, and using the viscosity of water as an estimate of that of the hemolymph,

we calculate a Reynolds number of 4.8, suggesting that flows are in the laminar regime.

3. For two individuals that were imaged for 20–30 min each, there was no evidence of a sustained retrograde fluid transport. The microbubble motion was either pulsatile with overall forward transport, or oscillatory with no net transport.
4. Respiratory structures (tracheae and/or air sacs) were compressed in patterns both synchronous and asynchronous to the local heartbeat.
5. No immediate detrimental effects on the animal were observed, either from the X-rays or from the microbubbles. The animals that were injected with microbubbles and under X-ray irradiation of the heart for up to an hour were alive 24 hr later. This is consistent with our previous results [2] which showed that there were no observable negative effects in insects at similar X-ray intensities under irradiation of the abdomen. Local X-ray damage must have occurred, but effects on the heart, tracheal, or abdominal movements and behavior were not apparent within this time frame.

CONCLUSION

For the first time, detailed fluid flow patterns in small animals can be imaged at the micrometer scale. In addition to insects, this technique should find applications in areas including vertebrate development (in such model systems as zebrafish or chick), and any other field in which the understanding of moving fluids behind opaque anatomy, at small scales, is key to answering outstanding questions of physiology. The potential applications of this technique are very broad.

KEY WORDS

- *Drosophila melanogaster*
- Hemolymph flow
- Magnetic resonance imaging (MRI)
- Optical coherence tomography (OCT)
- Synchrotron X-ray phase contrast imaging
- Transparent animals
- Thermography
- Ultrasound
- Visible light probes

AUTHORS' CONTRIBUTIONS

Wah-Keat Lee and John J. Socha contributed equally to the conception, data collection, analysis, and writing of this work, and have read and approved the final manuscript.

ACKNOWLEDGEMENTS

We thank Jon F. Harrison of Arizona State University for providing the grasshoppers used in this study, and Mark Stremler for discussion. Use of the Advanced Photon Source was supported by the U. S. Department of Energy, Office of Science, Office of Basic Energy Sciences, under Contract No. DE-AC02-06CH11357.

Chapter 15

Sexual Maturity and Swimming in Male Silver Eels

Arjan P. Palstra, Denhi Schnabel, Maaike C. Nieveen,
Herman P. Spaink, and Guido E.E.J.M. van den Thillart

INTRODUCTION

If European silver eels are prevented from reproductive migration, they remain in a pre-pubertal stage by dopaminergic inhibition of pituitary activity. Because this inhibition is a likely requirement for an extended female growth stage, we tested if it is sex-specific by subjecting both the sexes to stimulation by Gonadotropin-Releasing Hormone agonist (GnRH_a) injection or 3-months swimming in seawater. In contrast to females, males showed a two- to three-fold higher LH β (luteinising hormone β sub-unit)—expression, a three- to five-fold higher Gonadosomatic index (GSI) and induced spermatogenesis when compared with the untreated control group. Dopaminergic inhibition is thus not effective in males and swimming results in natural maturation, probably via GnRH-release.

When European silver eels (*Anguilla anguilla*) venture in the ocean for their 5,500 km semelparous spawning run to the Sargasso Sea [1], they are still in a pre-pubertal stage. Sexual maturation has thus to occur during or after this long distance journey. Maturation in eels, as in other vertebrates, is regulated by the gonadotropic follicle-stimulating hormone (FSH) and luteinising hormone (LH) that are produced by the pituitary. If prevented from undertaking their oceanic migration, gonad development remains blocked by dopaminergic inhibition of pituitary activity as well as the absence of stimulation by GnRH [2]. Information about natural maturation is lacking, because migrating and spawning eels have never been caught near the spawning grounds. There is however an urgent need for an understanding of eel reproduction, because populations are collapsing on a global scale [3].

Investigations on eel reproduction have been mainly focused on females. They stay for 7–30 years in the freshwater before migration, in contrast to 4–9 years for males. As a consequence, females reach a ten-fold larger size than males at the onset of migration. The long female growth stage is likely required for a successful production of more than one million eggs, which at spawning time accounts for 40–60% of the body weight [4]. As the energy requirements for males are far less than those for females, it is possible that the observed dopaminergic inhibition is sex-specific. We have tested this hypothesis by subjecting male and female eels to a GnRH-agonist (GnRH_a), specifically the commercial product Gonazon for Fish (Intervet), as well as to stimulation by long-term swimming in seawater (SW) that is supposed to stimulate GnRH excretion by the hypothalamus. Recently we found that swimming in freshwater (FW) triggers the enlargement of the eyes and development of oocytes in female

eels [5, 6]; all signs of early maturation, suggesting that swimming could be a natural trigger for sexual maturation. However, further maturation (e.g. vitellogenesis) was not stimulated by FW-swimming, and may only be stimulated by SW-swimming during natural migration.

MATERIALS AND METHODS

Migratory male ($n = 28$; 40 ± 0.5 cm, 96 ± 3 g) and female silver eels ($n = 24$; 75 ± 1 cm, 719 ± 38 g) were anaesthetized, PIT-tagged (TROVAN) and randomly divided over four groups of $n = 6$. Starters were immediately dissected ($n = 10$ for males). Other eels either swam or rested in natural SW (35 ppt, 20°C) during the experimental period of three months. Resting eels were IP injected with GnRHa (32 µg/kg Gonazon) or left untreated (“resters”) in a 1,500-l tank. An oval shaped stream-gutter (6.0*4.0*0.8 m; 6,000-l) was constructed to enable a 3 months swimming trial. Female eels swam 1,420 km while the smaller males swam 912 km. Pituitaries were stored in RNAlater (Ambion), mRNA was purified from these samples to quantify gene expression.

Oligonucleotides were designed from the reported sequences of *A. anguilla* for the specific β -subunits of LH and FSH, and of the Japanese eel *A. japonica* for housekeeping gene β -actin. A specific RT-PCR was performed using RNA extracts from pituitaries from artificially matured *A. anguilla* [4]. RT-PCR was performed using the Superscript II one step RT-PCR system with platinum Taq (Invitrogen), run on the Biometra T1 Thermocycler (Westburg). The PCR products were cloned in pCRII-TOPO vector (Invitrogen), digested with restriction enzymes to identify the correct direction, and sequenced (Base Clear lab services) to verify that the final products correspond to the genes of interest by aligning them to genes previously described using the VectorNTI program.

Quantitative reverse transcriptase (Q-RT)—PCR using the MasterMix for SYBR® Green I (Eurogenetec) and the Chromo4™ Detector (Bio-Rad laboratories) was performed to quantify the expression of LH β , FSH β , and of the internal control β -actin in the pituitaries. DNA and deduced mRNA amounts were calculated from Ct values of standard curves generated from the plasmids containing each of the specific genes, after which amounts were normalized to the expression level of the housekeeping gene β -actin.

Experiments complied with the current laws of the Netherlands and were approved by the animal experimental commission (DEC nr. 6059).

DISCUSSION

The results show an obvious difference between male and female eels in their response to both SW-swimming and GnRHa-injection. In female eels, GnRHa is not effective which confirms the conclusions by Dufour *et al.* [7] about pre-pubertal inhibition.

In contrast to the response of the females, we observed sexual maturation in males upon GnRHa-injection, indicating that dopaminergic inhibition is not effective in males. In addition we observed stimulation of sexual maturation in male eels after three months SW-swimming, suggesting that swimming acts via a similar mechanism. Swimming may up-regulate GnRH-levels (in silver eels the mammalian-type

GnRH–mGnRH) that subsequently leads to positive effects on LH β -production in the pituitary [8]. This action may be exerted through swimming-induced alterations in cortisol that bind to glucocorticoid receptor expressing neurons [9]. However, in our study stimulation of LH β -expression in the pituitary occurred only in male eels. Since LH β -expression was not enhanced in females that either swam or received a GnRHa-injection, their pituitaries were considered as not sensitized and still under dopaminergic control.

RESULTS

Males that were either stimulated by three months SW-swimming or by GnRHa-injection showed a two- to three-fold higher LH β expression level than the male starters and resters (Fig. 1a). Both treatments also caused a three- to five-fold increase in GSI (Fig. 1b) and an induced spermatogenesis (>80 percent presence of spermatogonia late type b; Fig. 2). One male swimmer even showed the formation of spermatocytes (Fig. 2). In contrast, females were neither stimulated by SW-swimming nor by GnRHa, and even showed regression of maturation over time as demonstrated by lower LH β expression (Fig. 1c), GSI (Fig. 1d) and oocyte diameters in all groups after 3 months (Fig. 2). The expression of FSH β did not significantly change under different treatments in both males and females.

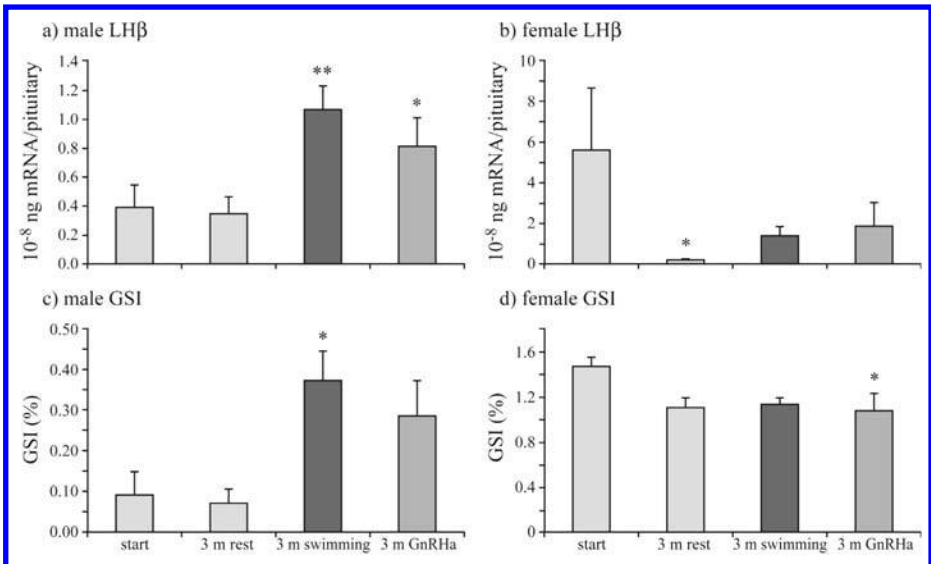


Figure 1: Expression (Q-RT-PCR) of LH β in the pituitary and the GSI in male and female eels. Eels were sampled at the start, after 3 months rest, after 3 months of SW-swimming and 3 months after a single GnRHa injection (Gonazon For Fish, Intervet). In females, regression occurs during the experimental period, an effect which is more pronounced in the resting group than those stimulated by SW-swimming and GnRHa. In males however, SW-swimming and GnRHa activate maturation (student t-tests with * = $P < 0.05$; ** = $P < 0.01$; 3 months rest versus start, 3 months swimming or 3 months GnRHa versus 3 months rest).

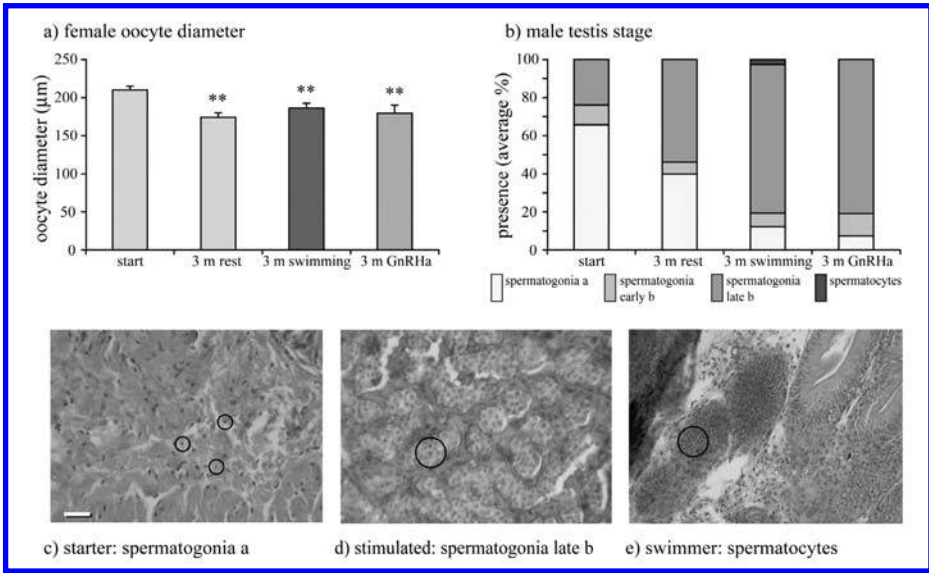


Figure 2: Gonad development parameters in males and females. a) oocyte diameters at the start, after 3 months of rest, after 3 months of SW-swimming and 3 months after GnRH injection; b) male testis stage with frequency distribution of spermatogonia type a, spermatogonia early type b, spermatogonia late type b and spermatocytes; c) testis in starter containing mainly spermatogonia type a (encircled), d) GnRH-stimulated testis containing spermatogonia late type b (encircled), e) testis of swimmer containing spermatocytes (encircled). The scale bar represents 100 µm. Asterisks indicate significant differences (student t-test with ** = $P < 0.01$; 3 months rest, 3 months swimming or 3 months GnRH versus start).

CONCLUSION

As long-term swimming is required for reaching the spawning site, we conclude that swimming results in natural maturation in males, probably via the release of GnRH. Males swam in this experiment for about one-sixth of their normal migration distance, so full spermiation can be expected after longer swimming trials. As naturally induced spermiation may result in improved sperm quality, we expect that swimming trials will improve the success of eel breeding.

KEY WORDS

- Follicle-Stimulating Hormone β subunit (FSH β)
- Freshwater(FW)
- Gonadotropin-Releasing Hormone agonist (GnRH α)
- Gonadosomatic index (GSI)
- Luteinising hormone subunit (LH β)
- Quantitative reverse transcriptase (Q-RT)

AUTHORS' CONTRIBUTIONS

Arjan P. Palstra and Guido E.E.J.M. van den Thillart conceived and designed the project and the experiments. Arjan P. Palstra performed the experiments, measurements, dissection and histology. Denhi Schnabel and Herman P. Spaik cloned β -actin and the LH β and FSH β subunits and tested the right conditions for Quantitative RT-PCR. Maaïke C. Nieveen performed Quantitative RT-PCR. Arjan P. Palstra and Guido E.E.J.M. van den Thillart wrote the paper.

ACKNOWLEDGEMENTS

The authors wish to express their thanks to Dr. W. Enright (Aquatic Animal Health Division, Intervet International BV) for providing Gonazon For Fish, to E. de Kuyper, J. Bij and P. Niemantsverdriet for their help in constructing a functional stream-gutter and the latter mentioned also for animal care, and to M. de Bakker, J. van Rijssel, V. Jacobson and R. Snepvangers for assistance with histology. M. Brittijn is acknowledged for his help with the lay-out of the figures and Dr. J. Jeffery is acknowledged for his help with the correct use of the English language. Supported by the Dutch Ministry of Agriculture, Nature and Food Quality (LNV) contract #3201817 to GvdT.

Permissions

Chapter 1: Animal Physiology and Circadian Photoresponses was originally published as “A Constant Light-Genetic Screen Identifies KISMET as a Regulator of Circadian Photoresponses” in *PLoS Genetics*, 5:12, 2009. Reprinted with permission under the Creative Commons Attribution License or equivalent.

Chapter 2: Complications in High Caloric Diet-Fed Rats was originally published as “Exercise Training Improves Relaxation Response and SOD-1 Expression in Aortic and Mesenteric Rings from High Caloric Diet-Fed Rats” in *BMC Physiology* 8:12, 2008. Reprinted with permission under the Creative Commons Attribution License or equivalent.

Chapter 3: Young Wild-Type Mice and Serotonin-Related Variables was originally published as “Relationships Among Body Mass, Brain Size, Gut Length, and Blood Tryptophan and Serotonin in Young Wild-Type Mice” in *BMC Physiology* 9:4, 2009. Reprinted with permission under the Creative Commons Attribution License or equivalent.

Chapter 4: Neurogenesis of Peripuberal and Adult Rabbits was originally published as “Genesis of Neuronal and Glial Progenitors in the Cerebellar Cortex of Peripuberal and Adult Rabbits” in *PLoS ONE*. 3:6, 2008. Reprinted with permission under the Creative Commons Attribution License or equivalent.

Chapter 5: Monkeys and Taste Development was originally published as “The Sweet Taste Quality Is Linked to a Cluster of Taste Fibers in Primates: Lactisole Diminishes Preference and Responses to Sweet in S fibers (Sweet Best) Chorda Tympani Fibers of *M. fascicularis* Monkey” in *BMC Physiology* 9:1, 2009. Reprinted with permission under the Creative Commons Attribution License or equivalent.

Chapter 6: Intermittent Claudication in Canines was originally published as “Metabolic Adaptations to Repeated Periods of Contraction with Reduced Blood Flow in Canine Skeletal Muscle” in *BMC Physiology* 5:11, 2005. Reprinted with permission under the Creative Commons Attribution License or equivalent.

Chapter 7: Body Mechanics of Moving Cats was originally published as “Whole Body Mechanics of Stealthy Walking in Cats” in *PLoS ONE* 3(11), 2008. Reprinted with permission under the Creative Commons Attribution License or equivalent.

Chapter 8: “Wound Repair on Horses with Equine CPNNB1 and PECAM1” was originally published as “Equine CTNNB1 and PECAM1 Nucleotide Structure and Expression Analyses in an Experimental Model of Normal and Pathological Wound Repair” in *BMC Physiology* 8:1, 2008. Reprinted with permission under the Creative Commons Attribution License or equivalent.

Chapter 9: Genetic Factors of Scrotal Hernia in Commercial Pigs was originally published as “Association and Haplotype Analyses of Positional Candidate Genes in Five Genomic Regions Linked to Scrotal Hernia in Commercial Pig Lines” in *PLoS ONE*. 4:3, 2009. Reprinted with permission under the Creative Commons Attribution License or equivalent.

Chapter 10: Acute Heat Stress Effect on Milk Serotonin of Cows was originally published as “Acute Heat Stress Brings Down Milk Secretion in Dairy Cows by Up-Regulating the Activity of the Milk-Borne Negative Feedback Regulatory System” in *BMC Physiology* 9:3, 2009. Reprinted with permission under the Creative Commons Attribution License or equivalent.

Chapter 11: Insect Physiology and Detection of Moving Targets was originally published as “A Model for the Detection of Moving Targets in Visual Clutter Inspired by Insect Physiology” in *PLoS ONE*. 3:7, 2008. Reprinted with permission under the Creative Commons Attribution License or equivalent.

Chapter 12: Honey Bee Queen Physiology and Insemination was originally published as “Effects of Insemination Quantity on Honey Bee Queen Physiology” in *PLoS ONE* 2:10, 2007. Reprinted with permission under the Creative Commons Attribution License or equivalent.

Chapter 13: High Heat Effect on City Ants was originally published as “Urban Physiology: City Ants Possess High Heat Tolerance” in *PLoS ONE* 2:2, 2007. Reprinted with permission under the Creative Commons Attribution License or equivalent.

Chapter 14: Hemolymph Flow in Grasshoppers’ (*Schistocerca americana*) Hearts was originally published as “Direct Visualization of Hemolymph Flow in the Heart of a Grasshopper (*Schistocerca americana*)” in *BMC Physiology* 9:2, 2009. Reprinted with permission under the Creative Commons Attribution License or equivalent.

Chapter 15: Sexual Maturity and Swimming in Male Silver Eels was originally published as “Male Silver Eels Mature by Swimming” in *BMC Physiology* 8:14, 2008. Reprinted with permission under the Creative Commons Attribution License or equivalent.

References

1

1. Hardin, P. E. (2005). The circadian time-keeping system of *Drosophila*, *Curr. Biol.*, **15**, R714–722.
2. Darlington, T. K., Wager-Smith, K., Ceriani, M. F., Staknis, D., and Gekakis, N., et al. (1998). Closing the Circadian Loop: CLOCK-induced Transcription of Its Own Inhibitors per and TIM, *Science*, **280**, 1599–1603.
3. Allada, R., White, N. E., So, W. V., Hall, J. C., and Rosbash, M. (1998). A mutant *Drosophila* homolog of mammalian Clock disrupts circadian rhythms and transcription of period and timeless, *Cell*, **93**, 791–804.
4. Rutila, J. E., Suri, V., Le, M., So, W. V., and Rosbash, M., et al. (1998). CYCLE is a second bHLH-PAS protein essential for circadian transcription of *Drosophila* period and timeless, *Cell*, **93**, 805–814.
5. Kloss, B., Price, J. L., Saez, L., Blau, J., and Rothenfluh-Hilfiker, A., et al. (1998). The *Drosophila* clock gene double-time encodes a protein closely related to human casein kinase I ϵ , *Cell*, **94**, 97–107.
6. Price, J. L., Blau, J., Rothenfluh-Hilfiker, A., Abodeely, M., and Kloss, B., et al. (1998). double-time is a novel *Drosophila* clock gene that regulates PERIOD protein accumulation, *Cell*, **94**, 83–95.
7. Martinek, S., Inonog, S., Manoukian, A. S., and Young, M. W. (2001). A role for the segment polarity gene shaggy/GSK-3 in the *Drosophila* circadian clock, *Cell*, **105**, 769–779.
8. Lin, J. M., Kilman, V. L., Keegan, K., Paddock, B., and Emery-Le, M., et al. (2002). A role for casein kinase 2 α in the *Drosophila* circadian clock, *Nature* **420**, 816–820.
9. Akten, B., Jauch, E., Genova, G. K., Kim, E. Y., and Edery, I., et al. (2003). A role for CK2 in the *Drosophila* circadian oscillator, *Nat. Neurosci.*, **6**, 251–257.
10. Fang, Y., Sathyanarayanan, S., and Sehgal, A. (2007). Post-translational regulation of the *Drosophila* circadian clock requires protein phosphatase 1 (PP1), *Genes. Dev.*, **21**, 1506–1518.
11. Sathyanarayanan, S., Zheng, X., Xiao, R., and Sehgal, A. (2004). Posttranslational regulation of *Drosophila* PERIOD protein by protein phosphatase 2A, *Cell*, **116**, 603–615.
12. Nawathean, P., and Rosbash, M. (2004). The doubletime and CKII kinases collaborate to potentiate *Drosophila* PER transcriptional repressor activity, *Mol. Cell.*, **13**, 213–223.
13. Yu, W., Zheng, H., Houl, J. H., Dauwalder, B., and Hardin, P. E. (2006). PER-dependent rhythms in CLK phosphorylation and E-box binding regulate circadian transcription, *Genes Dev.*, **20**, 723–733.
14. Kim, E. Y., and Edery, I. (2006). Balance between DBT/CKIepsilon kinase and protein phosphatase activities regulate phosphorylation and stability of *Drosophila* CLOCK protein, *Proc. Natl. Acad. Sci. U S A*, **103**, 6178–6183.
15. Emery, P., Stanewsky, R., Hall, J. C., and Rosbash, M. (2000). A unique circadian-rhythm photoreceptor, *Nature*, **404**, 456–457.
16. Stanewsky, R., Kaneko, M., Emery, P., Beretta, M., and Wager-Smith, K., et al. (1998). The cry^b mutation identifies cryptochrome as a circadian photoreceptor in *Drosophila*, *Cell*, **95**, 681–692.
17. Emery, P., So, W. V., Kaneko, M., Hall, J. C., and Rosbash, M. (1998). CRY, a *Drosophila* clock and light-regulated cryptochrome, is a major contributor to circadian rhythm resetting and photosensitivity, *Cell*, **95**, 669–679.
18. Busza, A., Emery-Le, M., Rosbash, M., and Emery, P. (2004). Roles of the two *Drosophila* CRYPTOCHROME structural domains in circadian photoreception, *Science*, **304**, 1503–1506.
19. Ceriani, M. F., Darlington, T. K., Staknis, D., Mas, P., and Petti, A. A., et al. (1999). Light-dependent sequestration of TIMELESS by CRYPTOCHROME, *Science*, **285**, 553–556.

20. Naidoo, N., Song, W., Hunter-Ensor, M., and Sehgal, A. (1999). A role for the proteasome in the light response of the timeless clock protein, *Science*, **285**, 1737–1741.
21. Lin, F. J., Song, W., Meyer-Bernstein, E., Naidoo, N., and Sehgal, A. (2001). Photic signaling by cryptochrome in the *Drosophila* circadian system, *Mol. Cell Biol.*, **21**, 7287–7294.
22. Peschel, N., Veleri, S., and Stanewsky, R. (2006). Veela defines a molecular link between Cryptochrome and Timeless in the light-input pathway to *Drosophila*'s circadian clock, *Proc. Natl. Acad. Sci. U S A*, **103**, 17313–17318.
23. Koh, K., Zheng, X., and Sehgal, A. (2006). JETLAG resets the *Drosophila* circadian clock by promoting light-induced degradation of TIMELESS, *Science*, **312**, 1809–1812.
24. Peschel, N., Chen, K. F., Szabo, G., and Stanewsky, R. (2009). Light-dependent interactions between the *Drosophila* circadian clock factors cryptochrome, jetlag, and timeless, *Curr. Biol.*, **19**, 241–247.
25. Knowles, A., Koh, K., Wu, J. T., Chien, C. T., and Chamovitz, D. A., et al. (2009). The COP9 signalosome is required for light-dependent timeless degradation and *Drosophila* clock resetting, *J. Neurosci.*, **29**, 1152–1162.
26. Stoleru, D., Nawathean, P., Fernandez, Mde, L., Menet, J. S., and Ceriani, M. F., et al. (2007). The *Drosophila* circadian network is a seasonal timer, *Cell*, **129**, 207–219.
27. Konopka, R. J., Pittendrigh, C., and Orr, D. (1989). Reciprocal behavior associated with altered homeostasis and photosensitivity of *Drosophila* clock mutants, *Journal of Neurogenetics*, **6**, 1–10.
28. Rørth, P., Szabo, K., Bailey, A., Laverty, T., and Rehm, J., et al. (1998). Systematic gain-of-function genetics in *Drosophila*, *Development*, **125**, 1049–1057.
29. Murad, A., Emery-Le, M., and Emery, P. (2007). A subset of dorsal neurons modulates circadian behavior and light responses in *Drosophila*, *Neuron*, **53**, 689–701.
30. Abdelilah-Seyfried, S., Chan, Y. M., Zeng, C., Justice, N. J., and Younger-Shepherd, S., et al. (2000). A gain-of-function screen for genes that affect the development of the *Drosophila* adult external sensory organ, *Genetics*, **155**, 733–752.
31. Helfrich-Förster, C., Winter, C., Hofbauer, A., Hall, J. C., and Stanewsky, R. (2001). The circadian clock of fruit flies is blind after elimination of all known photoreceptors, *Neuron*, **30**, 249–261.
32. Dolezelova, E., Dolezel, D., and Hall, J. C. (2007). Rhythm defects caused by newly engineered null mutations in *Drosophila*'s cryptochrome gene, *Genetics*, **177**, 329–345.
33. Rieger, D., Shafer, O. T., Tomioka, K., and Helfrich-Förster, C. (2006). Functional analysis of circadian pacemaker neurons in *Drosophila melanogaster*, *J. Neurosci.*, **26**, 2531–2543.
34. Yoshii, T., Funada, Y., Ibuki-Ishibashi, T., Matsumoto, A., and Tanimura, T., et al. (2004). *Drosophila* cryb mutation reveals two circadian clocks that drive locomotor rhythm and have different responsiveness to light, *J. Insect Physiol.*, **50**, 479–488.
35. Weihe, U., Dorfman, R., Wernet, M. F., Cohen, S. M., and Milan, M. (2004). Proximodistal subdivision of *Drosophila* legs and wings: the elbow-no ocelli gene complex, *Development*, **131**, 767–774.
36. Dorfman, R., Glazer, L., Weihe, U., Wernet, M. F., and Shilo, B. Z. (2002). Elbow and Noc define a family of zinc finger proteins controlling morphogenesis of specific tracheal branches, *Development*, **129**, 3585–3596.
37. Ciapponi, L. and Bohmann, D. (2002). An essential function of AP-1 heterodimers in *Drosophila* development, *Mech. Dev.*, **115**, 35–40.
38. Riesgo-Escovar, J. R. and Hafen, E. (1997). Common and distinct roles of DFos and DJun during *Drosophila* development, *Science*, **278**, 669–672.
39. Zeitlinger, J., Kockel, L., Peverali, F. A., Jackson, D. B., and Mlodzik, M., et al. (1997). Defective dorsal closure and loss of epidermal decapentaplegic expression in *Drosophila* fos mutants, *Embo. J.*, **16**, 7393–7401.
40. Weber, U., Pataki, C., Mihaly, J., and Mlodzik, M. (2008). Combinatorial signaling

- by the Frizzled/PCP and Egfr pathways during planar cell polarity establishment in the *Drosophila* eye, *Dev. Biol.*, **316**, 110–123.
41. Kim, T., Yoon, J., Cho, H., Lee, W. B., and Kim, J., et al. (2005). Downregulation of lipopolysaccharide response in *Drosophila* by negative crosstalk between the AP1 and NF-kappaB signaling modules, *Nat. Immunol.*, **6**, 211–218.
 42. Szuts, D. and Bienz, M. (2000). An auto-regulatory function of Dfos during *Drosophila* endoderm induction, *Mech. Dev.*, **98**, 71–76.
 43. Srinivasan, S., Armstrong, J. A., Deuring, R., Dahlsveen, I. K., and McNeill, H., et al. (2005). The *Drosophila* trithorax group protein KISMET facilitates an early step in transcriptional elongation by RNA Polymerase II, *Development*, **132**, 1623–1635.
 44. Daubresse, G., Deuring, R., Moore, L., Papoulas, O., and Zakrajsek, I., et al. (1999). The *Drosophila* KISMET gene is related to chromatin-remodeling factors and is required for both segmentation and segment identity, *Development*, **126**, 1175–1187.
 45. Bellen, H. J., Vaessin, H., Bier, E., Kolodkin, A., and D'Evelyn D, et al. (1992). The *Drosophila* couch potato gene: an essential gene required for normal adult behavior, *Genetics*, **131**, 365–375.
 46. Wing, J. P., Schreuder, B. A., Yokokura, T., Wang, Y., and Andrews, P. S., et al. (2002). *Drosophila* Morgue is an F box/ubiquitin conjugase domain protein important for grim-reaper mediated apoptosis, *Nat. Cell Biol.*, **4**, 451–456.
 47. Jiang, J. and Struhl, G. (1998). Regulation of the Hedgehog and Wingless signalling pathways by the F-box/WD40-repeat protein Slimb, *Nature*, **291**, 493–496.
 48. Grima, B., Lamouroux, A., Chelot, E., Papin, C., and Limbourg-Bouchon, B., et al. (2002). The F-box protein slimb controls the levels of clock proteins period and timeless, *Nature*, **420**, 178–182.
 49. Ko, H. W., Jiang, J., and Edery, I. (2002). Role for Slimb in the degradation of *Drosophila* Period protein phosphorylated by Doubletime, *Nature*, **420**, 673–678.
 50. Jekely, G. and Friedrich, P. (1999). Characterization of two recombinant *Drosophila* calpains. CALPA and a novel homolog, CALPB, *J. Biol. Chem.*, **274**, 23893–23900.
 51. Zhang, H., Tan, J., Reynolds, E., Kuebler, D., and Faulhaber, S., et al. (2002). The *Drosophila* slamdance gene: a mutation in an aminopeptidase can cause seizure, paralysis and neuronal failure, *Genetics*, **162**, 1283–1299.
 52. Arquier, N., Bourouis, M., Colombani, J., and Leopold, P. (2005). *Drosophila* Lk6 kinase controls phosphorylation of eukaryotic translation initiation factor 4E and promotes normal growth and development, *Curr. Biol.*, **15**, 19–23.
 53. Kidd, D. and Raff, J. (1997). LK6, a short lived protein kinase in *Drosophila* that can associate with microtubules and centrosomes, *J. Cell Sci.*, **110**, 209–219.
 54. Suri, V., Qian, Z., Hall, J. C., and Rosbash, M. (1998). Evidence that the TIM light response is relevant to light-induced phase shifts in *Drosophila melanogaster*, *Neuron*, **21**, 225–234.
 55. Levine, J. D., Casey, C. I., Kalderon, D. D., and Jackson, F. R. (1994). Altered circadian pacemaker functions and cyclic AMP rhythms in the *Drosophila* learning mutant dunce, *Neuron*, **13**, 967–974.
 56. Dietzl, G., Chen, D., Schnorrer, F., Su, K. C., and Barinova, Y., et al. (2007). A genome-wide transgenic RNAi library for conditional gene inactivation in *Drosophila*, *Nature*, **448**, 151–156.
 57. Zeng, H., Qian, Z., Myers, M. P., and Rosbash, M. (1996). A light-entrainment mechanism for the *Drosophila* circadian clock, *Nature*, **380**, 129–135.
 58. Shafer, O. T., Helfrich-Förster, C., Renn, S. C., and Taghert, P. H. (2006). Reevaluation of *Drosophila melanogaster*'s neuronal circadian pacemakers reveals new neuronal classes, *J. Comp. Neurol.*, **498**, 180–193.
 59. Shang, Y., Griffith, L. C., and Rosbash, M. (2008). Feature Article: Light-arousal and circadian photoreception circuits intersect at the large PDF cells of the *Drosophila* brain, *Proc. Natl. Acad. Sci. USA*.
 60. Emery, P., Stanewsky, R., Helfrich-Förster, C., Emery-Le, M., and Hall, J. C., et al. (2000). *Drosophila* CRY is a deep-brain

- circadian photoreceptor, *Neuron*, **26**, 493–504.
61. Picot, M., Cusumano, P., Klarsfeld, A., Ueda, R., and Rouyer, F. (2007). Light activates output from evening neurons and inhibits output from morning neurons in the *Drosophila* circadian clock. *PLoS Biol* **5**: e315. doi:10.1371/journal.pbio.0050315.
 62. Sheeba, V., Gu, H., Sharma, V. K., O'Dowd, D. K., and Holmes, T. C. (2008). Circadian- and light-dependent regulation of resting membrane potential and spontaneous action potential firing of *Drosophila* circadian pacemaker neurons, *J. Neurophysiol.*, **99**, 976–988.
 63. Klarsfeld, A., Malpel, S., Michard-Vanhee, C., Picot, M., and Chelot, E., et al. (2004). Novel features of cryptochrome-mediated photoreception in the brain circadian clock of *Drosophila*, *J. Neurosci.*, **24**, 1468–1477.
 64. Veleri, S., Brandes, C., Helfrich-Förster, C., Hall, J. C., and Stanewsky, R. (2003). A self-sustaining, light-entrainable circadian oscillator in the *Drosophila* brain, *Curr. Biol.*, **13**, 1758–1767.
 65. Mazzoni, E. O., Desplan, C., and Blau, J. (2005). Circadian pacemaker neurons transmit and modulate visual information to control a rapid behavioral response, *Neuron*, **45**, 293–300.
 66. Renn, S. C. P., Park, J. H., Rosbash, M., Hall, J. C., and Taghert, P. H. (1999). A pdf Neuropeptide Gene Mutation and Ablation of PDF Neurons Each Cause Severe Abnormalities of Behavioral Circadian Rhythms in *Drosophila*, *Cell*, **99**, 791–802.
 67. Stoleru, D., Peng, Y., Agosto, J., Rosbash, M. (2004). Coupled oscillators control morning and evening locomotor behaviour of *Drosophila*, *Nature*, **431**, 862–868.
 68. Okano, S., Kanno, S., Takao, M., Eker, A. P. M., and Isono, K., et al. (1999). A putative blue-light receptor from *Drosophila melanogaster*, *Photochem. Photobiol.*, **69**, 108–113.
 69. Yoshii, T., Todo, T., Wulbeck, C., Stanewsky, R., and Helfrich-Förster, C. (2008). Cryptochrome is present in the compound eyes and a subset of *Drosophila*'s clock neurons, *J. Comp. Neurol.* **508**, 952–966.
 70. Benito, J., Houl, J. H., Roman, G. W., Hardin, P. E. (2008). The blue-light photoreceptor CRYPTOCHROME is expressed in a subset of circadian oscillator neurons in the *Drosophila* CNS, *J. Biol. Rhythms*, **23**, 296–307.
 71. Kennison, J. A. and Tamkun, J. W. (1988). Dosage-dependent modifiers of polycomb and antennapedia mutations in *Drosophila*, *Proc. Natl. Acad. Sci. U S A*, **85**, 8136–8140.
 72. Srinivasan, S., Dorigi, K. M., and Tamkun, J. W. (2008). *Drosophila* KISMET regulates histone H3 lysine 27 methylation and early elongation by RNA polymerase II. *PLoS Genet* **4**: e1000217. doi:10.1371/journal.pgen.1000217.
 73. Melicharek, D., Shah, A., Distefano, G., Gangemi, A. J., and Orapallo, A., et al. (2008). Identification of Novel Regulators of atonal Expression in the Developing *Drosophila* Retina, *Genetics*, **180**, 2095–2110.
 74. Claridge-Chang, A., Wijnen, H., Naef, F., Boothroyd, C., and Rajewsky, N., et al. (2001). Circadian regulation of gene expression systems in the *Drosophila* head, *Neuron*, **32**, 657–671.
 75. Ceriani, M. F., Hogenesch, J. B., Yanovsky, M., Panda, S., and Straume, M., et al. (2002). Genome-wide expression analysis in *Drosophila* reveals genes controlling circadian behavior, *J. Neurosci.*, **22**, 9305–9319.
 76. Cheng, H. Y., Papp, J. W., Varlamova, O., Dziema, H., and Russell, B., et al. (2007). microRNA modulation of circadian-clock period and entrainment, *Neuron*, **54**, 813–829.
 77. Kadener, S., Menet, J. S., Sugino, K., Horwich, M. D., and Weissbein, U., et al. (2009). A role for microRNAs in the *Drosophila* circadian clock, *Genes Dev.*, **23**, 2179–2191.
 78. Yang, M., Lee, J. E., Padgett, R. W., and Edery, I. (2008). Circadian regulation of a limited set of conserved microRNAs in *Drosophila*, *BMC Genomics*, **9**, 83.
 79. Sanlaville, D. and Verloes, A. (2007). CHARGE syndrome: an update, *Eur. J. Hum. Genet.* **15**, 389–399.
 80. Vissers, L. E., van Ravenswaaij, C. M., Admiraal, R., Hurst, J. A., and de Vries, B. B.,

- et al. (2004). Mutations in a new member of the chromodomain gene family cause CHARGE syndrome, *Nat. Genet.*, **36**, 955–957.
81. Jackson, S. M. and Berg, C. A. (2002). An A-kinase anchoring protein is required for protein kinase A regulatory subunit localization and morphology of actin structures during oogenesis in *Drosophila*, *Development*, **129**, 4423–4433.
 82. Ryoo, H. D., Bergmann, A., Gonen, H., Ciechanover, A., and Steller, H. (2002). Regulation of *Drosophila* IAP1 degradation and apoptosis by reaper and ubcD1, *Nat. Cell Biol.*, **4**, 432–438.
 83. Ewer, J., Frisch, B., Hamblen-Coyle, M. J., Rosbash, M., and Hall, J. C. (1992). Expression of the period clock gene within different cell types in the brain of *Drosophila* adults and mosaic analysis of these cells' influence on circadian behavioral rhythms, *Journal of Neuroscience*, **12**, 3321–3349.
 84. Levine, J. D., Funes, P., Dowse, H. B., and Hall, J. C. (2002). Signal analysis of behavioral and molecular cycles, *BMC Neurosci.*, **3**, electronic publication.
 85. Park, J. H., Helfrich-Förster, C., Lee, G., Liu, L., and Rosbash, M., et al. (2000). Differential regulation of circadian pacemaker output by separate clock genes in *Drosophila*, **97**, 3608–3613.
 86. Rosato, E., Trevisan, A., Sandrelli, F., Zordan, M., and Kyriacou, C. P., et al. (1997). Conceptual translation of timeless reveals alternative initiating methionines in *Drosophila*, *Nucleic Acids Res.* **25**, 455–458.
 87. Sandrelli, F., Tauber, E., Pegoraro, M., Mazzotta, G., and Cisotto, P., et al. (2007). A molecular basis for natural selection at the timeless locus in *Drosophila melanogaster*, *Science*, **316**, 1898–1900.
 3. Diaz, M. N., Frei, B., Vita, J. A., and Keaney, J. F. Jr. (1997). Antioxidants and atherosclerotic heart disease, *N. Engl. J. Med.*, **337**(6), 408–416.
 4. Rush, J. W., Denniss, S. G., and Graham, D. A. (2005). Vascular nitric oxide and oxidative stress: determinants of endothelial adaptations to cardiovascular disease and to physical activity, *Can. J. Appl. Physiol.*, **30**(4), 442–474.
 5. Luz, P. L., Favarato, D., and Laurindo, F. R. M. (2006). Oxidative theory of atherosclerosis: why did large trials not show benefits? *Int. J. Atheroscler.*, **1**(2), 124–136.
 6. Naderali, E. K., Brown, M. J., Pickavance, L. C., Wilding, J. P. H., Doyle, P. J., and Williams, G. (2001). Dietary obesity in the rat induces endothelial dysfunction without cause insulin resistance: a possible role for triacylglycerols, *Clin. Sci.*, **101**(5), 499–506.
 7. Naderali, E. K., Fatani, S., and Williams, G. (2004). Chronic withdrawal of a high-palatable obesity-inducing diet completely reverses metabolic and vascular abnormalities associated with dietary-obesity in the rat, *Atherosclerosis*, **172**(1), 63–69.
 8. Woodman, C.R., Thompson, M. A., Turk, J. R., and Laughlin, M. H. (2005). Endurance exercise training improves endothelium-dependent relaxation in brachial arteries from hypercholesterolemic male pigs, *J Appl. Physiol.*, **99**(4), 1412–1421.
 9. Turk, J. R., Henderson, K. K., Vanvickle, G. D., Watkins, J., and Laughlin, M. H. (2005). Arterial endothelial function in a porcine model of early stage atherosclerotic vascular disease, *Int. J. Exp. Pathol.*, **86**(5), 335–345.
 10. Halverstadt, A., Phares, D. A., Wilund, K. R., Goldberg, A. P., and Hagberg, J. M. (2007). Endurance exercise training raises high-density lipoprotein cholesterol and lowers small low-density lipoprotein and very low-density lipoprotein independent of body fat phenotypes in older men and women, *Metabolism*, **56**(4), 444–450.
 11. Delp, M. D., McAllister, R. M., and Laughlin, M. H. (1993). Exercise training alters endothelium-dependent vasoreactivity of

2

- rat abdominal aorta, *J. Appl. Physiol.*, **75**(3), 1354–1363.
12. Sessa, W. C., Pritchard, K., Seyedi, N., Wang, J., and Hintze, T. H. (1994). Chronic exercise in dogs increases coronary vascular nitric oxide production and endothelial cell nitric oxide synthase gene expression, *Circ. Res.*, **74**(2), 349–353.
 13. Shen, W., Lundborg, M., Wang, J., Stewart, J. M., Xu, X., Ochoa, M., and Hintze, T. H. (1994). Role of EDRF in the regulation of regional blood flow and vascular resistance at rest and during exercise in conscious dogs, *J. Appl. Physiol.*, **77**(1), 165–172.
 14. Woodman, C. R., Muller, J. M., Laughlin, M. H., and Price, E. M. (1997). Induction of nitric oxide synthase mRNA in coronary resistance arteries isolated from exercise-trained pigs, *Am. J. Physiol.*, **273**(6), H2575–2579.
 15. Kingwell, B. A. (2000). Nitric oxide-mediated metabolic regulation during exercise: effects of training in health and cardiovascular disease, *FASEB J.*, **14**(12), 1685–1696.
 16. Maeda, S., Miyauchi, T., Kakiyama, T., Sugawara, J., Iemitsu, M., Irukayama-Tomobe, Y., Murakami, H., Kumagai, Y., Kuno, S., and Matsuda, M. (2001). Effects of exercise training of 8 weeks and detraining on plasma levels of endothelium-derived factors, endothelin-1 and nitric oxide, in healthy young humans, *Life Sci.*, **69**(9), 1005–1016.
 17. Maiorana, A., O'Driscoll, G., Taylor, R., and Green, D. (2003). Exercise and the nitric oxide vasodilator system, *Sports Med.*, **33**(14), 1013–1035.
 18. Dobrian, A. D., Davies, M. J., Prewitt, R. L., and Lauterio, T. J. (2000). Development of hypertension in a rat model of diet-induced obesity, *Hypertension*, **35**(4), 1009–1015.
 19. Herbert, V., Lau, K. S., Gottlieb, C. W., and Bleicher, S. J. (1965). Coated charcoal immunoassay of insulin, *J. Clin. Endocrinol. Metab.*, **25**(10), 1375–1384.
 20. Matthews, D. R., Hosker, J. P., Rudenski, A. S., Naylor, B. A., Treacher, D. F., and Turner, R. C. (1985). Homeostasis model assessment: insulin resistance and beta-cell function from fasting plasma glucose and insulin concentrations in man, *Diabetologia*, **28**(7), 412–419.
 21. Bradford, M. M. (1976). A rapid and sensitive method for the quantitation of microgram quantities of protein utilizing the principle of protein-dye binding, *Anal. Biochem.*, **7**(72), 248–254.
 22. Tschöp, M. and Heiman, M. L. (2001). Rodent obesity models: an overview, *Exp. Clin. Endocrinol. & Diabetes*, **109**(6), 307–319.
 23. Naderali, E. K. and Williams, G. (2003). Prolonged endothelial-dependent and -independent arterial dysfunction induced in the rat by short-term feeding with a high-fat, high-sucrose diet, *Atherosclerosis*, **166**(2), 253–259.
 24. Kougiyas, P., Chai, H., Lin, P. H., Yao, Q., Lumsden, A. B., and Chen, C. (2005). Effects of adipocyte-derived cytokines on endothelial functions: implication of vascular disease, *J. Surg. Res.*, **126**(1), 121–129.
 25. Galili, O., Versari, D., Sattler, K. J., Olson, M. L., Mannheim, D., McConnell, J. P., Chade, A. R., Lerman, L. O., and Lerman, A. (2007). Early experimental obesity is associated with coronary endothelial dysfunction and oxidative stress, *Am. J. Physiol. Heart. Circ. Physiol.*, **292**(2), H904–911.
 26. Fortuño, A., San José, G., Moreno, M. U., Díez, J., and Zalba, G. (2005). Oxidative stress and vascular remodeling, *Exp. Physiol.*, **90**(4), 457–462.
 27. Oscai, L. B., Essig, D. A., and Palmer, W. K. (1990). Lipase regulation of muscle triglyceride hydrolysis, *J. Appl. Physiol.*, **69**(5), 1571–1577.
 28. Hennig, B., Toborek, M., and McClain, C. J. (2001). High-energy diets, fatty acids and endothelial cell function: implications for atherosclerosis, *J. Am. Coll. Nutr.*, **20**(2 suppl), 97–105.
 29. Barnard, R. J., Roberts, C. K., Varon, S. M., and Berger, J. J. (1998). Diet-induced insulin resistance precedes other aspects of the metabolic syndrome, *J. Appl. Physiol.*, **84**(4), 1311–1315.
 30. Straczkowski, M., Kowalska, I., Dzienis-Straczkowska, S., Kinalski, M., Górski, J., and Kinalska, I. (2001). The effect of exercise training on glucose tolerance and skeletal muscle triacylglycerol content in rats fed with a high-fat diet, *Diabetes Metab.*, **27**(1), 19–23.

31. Krebs, M. and Roden, M. (2005). Molecular mechanisms of lipid-induced insulin resistance in muscle, liver and vasculature, *Diabetes Obes. Metab.*, **7**(6), 621–632.
32. López, I. P., Marti, A., Milagro, F. I., Zulet Md Mde, L., Moreno-Aliaga, M. J., Martinez, J. A., and De Miguel, C. (2003). DNA microarray analysis of genes differentially expressed in diet-induced (cafeteria) obese rats, *Obes. Res.*, **11**(2), 188–194.
33. Estadella, D., Oyama, L. M., Dâmaso, A. R., Ribeiro, E. B., and Oller Do Nascimento, C. M. (2004). Effect of palatable hyperlipidic diet on lipid metabolism of sedentary and exercised rats, *Nutrition*, **20**(2), 218–224.
34. Higashi, Y. and Yoshizumi, M. (2004). Exercise and endothelial function: role of endothelium-derived nitric oxide and oxidative stress in healthy subjects and hypertensive patients, *Pharmacol. Ther.*, **102**(1), 87–96.
35. Zanesco, A. and Antunes, E. (2007). Effects of exercise training on the cardiovascular system: Pharmacological approaches, *Pharmacol. Ther.*, **114**(3), 307–317.
36. Droge, W. (2002). Free radicals in the physiological control of cell function, *Physiol. Rev.*, **82**(1), 47–95.
37. Dimmeler, S., Fleming, I., Fisslthaler, B., Hermann, C., Busse, R., and Zeiher, A. M. (1999). Activation of nitric oxide synthase in endothelial cells by Akt-dependent phosphorylation, *Nature*, **399**(6736), 601–605.
38. Davis, K.L., Martin, E., Turko, I. V., and Murad, F. (2001). Novel effects of nitric oxide, *Annu. Rev. Pharmacol. Toxicol.*, **41**, 203–236.
39. Davis, M.E., Cai, H., McCann, L., Fukai, T., and Harrison, D. G. (2003). Role of c-Src in regulation of endothelial nitric oxide synthase expression during exercise training, *Am. J. Physiol. Heart Circ. Physiol.*, **284**(4), H1449–1453.
40. Inoue, N., Ramasamy, S., Fukai, T., Nerem, R. M., and Harrison, D. G. (1996). Shear stress modulates expression of Cu/Zn superoxide dismutase in human aortic endothelial cells, *Circ. Res.*, **79**(1), 32–37.
41. Fukai, T., Folz, R. J., Landmesser, U., and Harrison, D. G. (2002). Extracellular superoxide dismutase and cardiovascular disease, *Cardiovasc. Res.*, **55**(2), 239–249.
42. Rush, J. W., Turk, J. R., and Laughlin, M. H. (2003). Exercise training regulates SOD-1 and oxidative stress in porcine aortic endothelium, *Am. J. Physiol. Heart Circ. Physiol.*, **284**(4), H1378–1387.
43. Thompson, M. A., Henderson, K. K., Woodman, C. R., Turk, J. R., Rush, J. W., Price, E., and Laughlin, M. H. (2004). Exercise preserves endothelium-dependent relaxation in coronary arteries of hypercholesterolemic male pigs, *J. Appl. Physiol.*, **96**(3), 1114–1126.
44. Oltman, C. L., Parker, J. L., Adams, H. R., and Laughlin, M. H. (1992). Effects of exercise training on vasomotor reactivity of porcine coronary arteries, *Am. J. Physiol.*, **263**(2 Pt 2), H372–382.
45. McAllister, R. M., Kimani, J. K., Webster, J. L., Parker, J. L., and Laughlin, M. H. (1996). Effects of exercise training on responses of peripheral and visceral arteries in swine, *J. Appl. Physiol.*, **80**(1), 216–225.
46. Jasperse, J. L. and Laughlin, M. H. (1999). Vasomotor responses of soleus feed arteries from sedentary and exercise-trained rats, *J. Appl. Physiol.*, **86**(2), 441–449.
47. Henderson, K. K., Turk, J. R., Rush, J. W., and Laughlin, M. H. (2004). Endothelial function in coronary arterioles from pigs with early-stage coronary disease induced by high-fat, high-cholesterol diet: effect of exercise, *J. Appl. Physiol.*, **97**(3), 1159–1168.
48. De Moraes, C., Camargo, E. A., Antunes, E., De Nucci, G., and Zanesco, A. (2007). Reactivity of mesenteric and aortic rings from trained rats feed with high caloric diet, *Comp. Biochem. Physiol. A*, **147**(3), 788–792.

3

1. Janušonis, S., Anderson, G. M., Shifrovich, I., and Rakic, P. (2006). Ontogeny of brain and blood serotonin levels in 5-HT1A receptor knockout mice: potential relevance to the neurobiology of autism, *J. Neurochem.*, **99**, 1019–1031.

2. Janušonis, S. (2008). Origin of the blood hyperserotonemia of autism, *Theor. Biol. Med. Model*, **5**, 10.
3. Janušonis, S. (2009). Autism as a theoretical problem and the significance of blood hyperserotonemia, In *Causes and Risks for Autism*, A. C. Giordano and V. A. Lombardi (Eds.), Nova Science Publishers, Hauppauge, NY.
4. Anderson, G. M., Horne, W. C., Chatterjee, D., and Cohen, D. J. (1990). The hyperserotonemia of autism, *Ann. N Y Acad. Sci.*, **600**, 331–340.
5. Anderson, G. M. (2002). Genetics of childhood disorders: XLV. Autism, part 4: serotonin in autism, *J. Am. Acad. Child. Adolesc. Psychiatry*, **41**, 1513–1516.
6. Cook, E. H. and Leventhal, B. L. (1996). The serotonin system in autism, *Curr. Opin. Pediatr.*, **8**, 348–354.
7. Hanley, H. G., Stahl, S. M., and Freedman, D. X. (1977). Hyperserotonemia and amine metabolites in autistic and retarded children, *Arch. Gen. Psychiatry*, **34**, 521–531.
8. Anderson, G. M., Freedman, D. X., Cohen, D. J., Volkmar, F. R., Hoder, E. L., McPhe-dran, P., sderaa, R. B., Hansen, C. R., and Young, J. G. (1987). Whole blood serotonin in autistic and normal subjects, *J. Child. Psychol. Psychiatry*, **28**, 885–900.
9. McBride, P. A., Anderson, G. M., Hertzog, M. E., Snow, M. E., Thompson, S. M., Khait, V. D., Shapiro, T., and Cohen, D. J. (1998). Effects of diagnosis, race, and puberty on platelet serotonin levels in autism and mental retardation, *J. Am. Acad. Child Adolesc. Psychiatry*, **37**, 767–776.
10. Coutinho, A. M., Oliveira, G., Morgadinho, T., Fesel, C., Macedo, T. R., Bento, C., Marques, C., Ataide, A., Miguel, T., and Borges, L., et al. (2004). Variants of the serotonin transporter gene (SLC6A4) significantly contribute to hyperserotonemia in autism, *Mol. Psychiatry*, **9**, 264–271.
11. Mulder, E. J., Anderson, G. M., Kema, I. P., De, B. A., Van Lang, N. D., Den Boer, J. A., and Minderaa, R. B. (2004). Platelet serotonin levels in pervasive developmental disorders and mental retardation: Diagnostic group differences, within-group distribution, and behavioral correlates, *J. Am. Acad. Child Adolesc. Psychiatry*, **43**, 491–499.
12. Hranilovic, D., Bujas-Petkovic, Z., Vragovic, R., Vuk, T., Hock, K., and Jernej, B. (2007). Hyperserotonemia in adults with autistic disorder, *J. Autism Dev. Disord.*, **37**, 1934–1940.
13. Melke, J., Goubran, B. H., Chaste, P., Bétantcur, C., Nygren, G., Anckarsater, H., Rastam, M., Stahlberg, O., Gillberg, I. C., and Delorme, R., et al. (2008). Abnormal melatonin synthesis in autism spectrum disorders, *Mol. Psychiatry*, **13**, 90–98.
14. Hranilovic, D., Novak, R., Babic, M., Novokmet, M., Bujas-Petkovic, Z., and Jernej, B. (2008). Hyperserotonemia in autism: the potential role of 5HT-related gene variants, *Coll. Antropol.*, **32**(Suppl 1), 75–80.
15. Schain, R. J., and Freedman, D. X. (1961). Studies on 5-hydroxyindole metabolism in autistic and other mentally retarded children, *J. Pediatr.*, **58**, 315–320.
16. Zhao, X., Leotta, A., Kustanovich, V., Lajonchere, C., Geschwind, D. H., Law, K., Law, P., Qiu, S., Lord, C., and Sebat, J., et al. (2007). A unified genetic theory for sporadic and inherited autism, *Proc. Natl. Acad. Sci. USA*, **104**, 12831–12836.
17. Szatmari, P., Paterson, A. D., Zwaigenbaum, L., Roberts, W., Brian, J., Liu, X. Q., Vincent, J. B., Skaug, J. L., Thompson, A. P., and Senman, L., et al. (2007). Mapping autism risk loci using genetic linkage and chromosomal rearrangements, *Nat. Genet.*, **39**, 319–328.
18. Abrahams, B. S., and Geschwind, D. H. (2008). Advances in autism genetics: on the threshold of a new neurobiology, *Nat. Rev. Genet.*, **9**, 341–355.
19. Christian, S. L., Brune, C. W., Sudi, J., Kumar, R. A., Liu, S., Karamohamed, S., Badner, J. A., Matsui, S., Conroy, J., and McQuaid, D., et al. (2008). Novel submicroscopic chromosomal abnormalities detected in autism spectrum disorder, *Biol. Psychiatry*, **63**, 1111–1117.
20. Sebat, J., Lakshmi, B., Malhotra, D., Troge, J., Lese-Martin, C., Walsh, T., Yamrom, B., Yoon, S., Krasnitz, A., and Kendall, J., et al. (2007). Strong association of de novo copy number mutations with autism, *Science*, **316**, 445–449.

21. Lintas, C., and Persico, A. M. (2009). Autistic phenotypes and genetic testing: state-of-the-art for the clinical geneticist, *J. Med. Genet.*, **46**, 1–8.
22. Geschwind, D. H. (2008). Autism: many genes, common pathways? *Cell*, **135**, 391–395.
23. Gershon, M. D. (2004). Review article: serotonin receptors and transporters – roles in normal and abnormal gastrointestinal motility, *Aliment. Pharmacol. Ther.*, **20**(Suppl 7), 3–14.
24. Walther, D. J., Peter, J. U., Bashammakh, S., Hortnagl, H., Voits, M., Fink, H., and Bader, M. (2003). Synthesis of serotonin by a second tryptophan hydroxylase isoform, *Science*, **299**, 76.
25. Anderson, G. M., Stevenson, J. M., and Cohen, D. J. (1987). Steady-state model for plasma free and platelet serotonin in man, *Life Sci.*, **41**, 1777–1785.
26. Thomas, D. P. and Vane, J. R. (1967). 5-hydroxytryptamine in the circulation of the dog, *Nature*, **216**, 335–338.
27. Cook, E. H. Jr., Courchesne, R., Lord, C., Cox, N. J., Yan, S., Lincoln, A., Haas, R., Courchesne, E., and Leventhal, B. L. (1997). Evidence of linkage between the serotonin transporter and autistic disorder, *Mol. Psychiatry*, **2**, 247–250.
28. Anderson, G. M., Gutknecht, L., Cohen, D. J., Brailly-Tabard, S., Cohen, J. H., Ferrari, P., Roubertoux, P. L., Tordjman, S. (2002). Serotonin transporter promoter variants in autism: functional effects and relationship to platelet hyperserotonemia, *Mol. Psychiatry*, **7**, 831–836.
29. Persico, A. M., Pascucci, T., Puglisi-Allegra, S., Militerni, R., Bravaccio, C., Schneider, C., Melmed, R., Trillo, S., Montecchi, F., and Palermo, M., et al. (2002). Serotonin transporter gene promoter variants do not explain the hyperserotonemia in autistic children, *Mol. Psychiatry*, **7**, 795–800.
30. Persico, A. M., Militerni, R., Bravaccio, C., Schneider, C., Melmed, R., Conciatori, M., Damiani, V., Baldi, A., and Keller, F. (2000). Lack of association between serotonin transporter gene promoter variants and autistic disorder in two ethnically distinct samples, *Am. J. Med. Genet.*, **96**, 123–127.
31. Wu, S., Guo, Y., Jia, M., Ruan, Y., Shuang, M., Liu, J., Gong, X., Zhang, Y., Yang, J., and Yang, X., et al. (2005). Lack of evidence for association between the serotonin transporter gene (SLC6A4) polymorphisms and autism in the Chinese trios, *Neurosci. Lett.*, **381**, 1–5.
32. Ramoz, N., Reichert, J. G., Corwin, T. E., Smith, C. J., Silverman, J. M., Hollander, E., and Buxbaum, J. D. (2006). Lack of evidence for association of the serotonin transporter gene SLC6A4 with autism, *Biol. Psychiatry*, **60**, 186–191.
33. Wendland, J. R., DeGuzman, T. B., McMahon, F., Rudnick, G., tera-Wadleigh, S. D., and Murphy, D. L. (2008). SERT Ileu-425Val in autism, Asperger syndrome and obsessive-compulsive disorder, *Psychiatr. Genet.*, **18**, 31–39.
34. Minderaa, R. B., Anderson, G. M., Volkmar, F. R., Akkerhuis, G. W., and Cohen, D. J. (1987). Urinary 5-hydroxyindoleacetic acid and whole blood serotonin and tryptophan in autistic and normal subjects, *Biol. Psychiatry*, **22**, 933–940.
35. Croonenberghs, J., Verkerk, R., Scharpe, S., Deboutte, D., and Maes, M. (2005). Serotonergic disturbances in autistic disorder: L-5-hydroxytryptophan administration to autistic youngsters increases the blood concentrations of serotonin in patients but not in controls, *Life Sci.*, **76**, 2171–2183.
36. Janušonis, S. (2005). Statistical distribution of blood serotonin as a predictor of early autistic brain abnormalities, *Theor. Biol. Med. Model*, **2**, 27.
37. Coutinho, A. M., Sousa, I., Martins, M., Correia, C., Morgadinho, T., Bento, C., Marques, C., Ataíde, A., Miguel, T. S., Moore, J. H., et al. (2007). Evidence for epistasis between SLC6A4 and ITGB3 in autism etiology and in the determination of platelet serotonin levels, *Hum. Genet.*, **121**, 243–256.
38. Kemperman, R. F., Muskiet, F. D., Boutier, A. I., Kema, I. P., and Muskiet, F. A. (2008). Brief report: normal intestinal permeability at elevated platelet serotonin levels in a subgroup of children with pervasive developmental disorders in Curacao (The Netherlands Antilles), *J. Autism Dev. Disord.*, **38**, 401–406.

39. Carneiro, A. M., Cook, E. H., Murphy, D. L., and Blakely, R. D. (2008). Interactions between integrin alphaIIb beta3 and the serotonin transporter regulate serotonin transport and platelet aggregation in mice and humans, *J. Clin. Invest.*, **118**, 1544–1552.
40. Nakatani, Y., Sato-Suzuki, I., Tsujino, N., Nakasato, A., Seki, Y., Fumoto, M., and Arita, H. (2008). Augmented brain 5-HT crosses the blood-brain barrier through the 5-HT transporter in rat, *Eur. J. Neurosci.*, **27**, 2466–2472.
41. Lesch, K. P., Wolozin, B. L., Murphy, D. L., and Reiderer, P. (1993). Primary structure of the human platelet serotonin uptake site: identity with the brain serotonin transporter, *J. Neurochem.*, **60**, 2319–2322.
42. Brust, P., Friedrich, A., Krizbai, I. A., Bergmann, R., Roux, F., Ganapathy, V., and Johannsen, B. (2000). Functional expression of the serotonin transporter in immortalized rat brain microvessel endothelial cells, *J. Neurochem.*, **74**, 1241–1248.
43. Wakayama, K., Ohtsuki, S., Takayama, H., Hosoya, K., and Terasaki, T. (2002). Localization of norepinephrine and serotonin transporter in mouse brain capillary endothelial cells, *Neurosci. Res.*, **44**, 173–180.
44. Gershon, M. D. and Tack, J. (2007). The serotonin signaling system: From basic understanding to drug development for functional GI disorders, *Gastroenterology*, **132**, 397–414.
45. Aylward, E. H., Minshew, N. J., Goldstein, G., Honeycutt, N. A., Augustine, A. M., Yates, K. O., Barta, P. E., and Pearlson, G. D. (1999). MRI volumes of amygdala and hippocampus in non-mentally retarded autistic adolescents and adults, *Neurology*, **53**, 2145–2150.
46. Nicolson, R., DeVito, T. J., Vidal, C. N., Sui, Y., Hayashi, K. M., Drost, D. J., Williamson, P. C., Rajakumar, N., Toga, A. W., and Thompson, P. M. (2006) Detection and mapping of hippocampal abnormalities in autism, *Psychiatry Res.*, **148**, 11–21.
47. Sparks, B. F., Friedman, S. D., Shaw, D. W., Aylward, E. H., Echelard, D., Artru, A. A., Maravilla, K. R., Giedd, J. N., Munson, J., and Dawson, G., et al. (2002). Brain structural abnormalities in young children with autism spectrum disorder, *Neurology*, **59**, 184–192.
48. Kline, R. B. (2005). *Principles and practice of structural equation modeling*, 2nd ed., The Guilford Press, New York.
49. Cohen, J. (1994). The earth is round ($p < .05$), *Am. Psychologist*, **49**, 997–1003.
50. Miquel, M. C., Kia, H. K., Boni, C., Doucet, E., Daval, G., Matthiessen, L., Hamon, M., and Verge, D. (1994). Postnatal development and localization of 5-HT1A receptor mRNA in rat forebrain and cerebellum, *Brain Res. Dev. Brain Res.*, **80**, 149–157.
51. Patel, T.D. and Zhou, F. C. (2005). Ontogeny of 5-HT1A receptor expression in the developing hippocampus, *Brain Res. Dev. Brain Res.*, **157**, 42–57.
52. Waeber, C., Sebben, M., Nieoullon, A., Bocckaert, J., and Dumuis, A. (1994). Regional distribution and ontogeny of 5-HT4 binding sites in rodent brain, *Neuropharmacology*, **33**, 527–541.
53. del Olmo, E., Diaz, A., Guirao-Pineyro, M., del Arco, C., Pascual, J., and Pazos, A. (1994). Transient localization of 5-HT1A receptors in human cerebellum during development. *Neurosci. Lett.*, **166**, 149–152.
54. Blinkov, S. M. and Glezer, I. I. (1968). *The Human Brain in Figures and Tables: A Quantitative Handbook*, Plenum Press, New York.
55. Baker, J. R. (1958). *Principles of Biological Microtechnique*, Methuen & Co, Ltd, London.
56. Paxinos, G. and Franklin, K. B. J. (2001). *The Mouse Brain in Stereotaxic Coordinates: Deluxe Edition of the Atlas*. 2nd ed., Academic Press, San Diego, CA.
57. McClive, P. J. and Sinclair, A. H. (2001). Rapid DNA extraction and PCR-sexing of mouse embryos, *Mol. Reprod. Dev.*, **60**, 225–226.
58. Cohen, J., Cohen, P., West, S. G., and Aiken, L. S. (2003). *Applied Multiple Regression/Correlation Analysis for the Behavioral Sciences*, 3rd ed., Lawrence Erlbaum Associates, Mahwah, NJ.
59. Pham-Gia, T., Turkkan, N., and Marchand, E. (2006). Density of the ratio of two

- normal random variables and applications, *Comm. Stat. Theory Meth.*, **35**, 1569–1591.
60. Cote, F., Fligny, C., Bayard, E., Launay, J. M., Gershon, M. D., Mallet, J., and Vodjdani, G. (2007). Maternal serotonin is crucial for murine embryonic development, *Proc. Natl. Acad. Sci. USA.*, **104**, 329–334.
61. Fligny, C., Fromes, Y., Bonnin, P., Darmon, M., Bayard, E., Launay, J. M., Cote, F., Mallet, J., and Vodjdani, G. (2008). Maternal serotonin influences cardiac function in adult offspring, *FASEB J*, **22**, 2340–2349.
62. Salas, S. P., Giacaman, A., Romero, W., Downey, P., Aranda, E., Mezzano, D., and Vio, C. P. (2007). Pregnant rats treated with a serotonin precursor have reduced fetal weight and lower plasma volume and kalikrein levels, *Hypertension*, **50**, 773–779.
63. Schendel, D. and Bhasin, T. K. (2008). Birth weight and gestational age characteristics of children with autism, including a comparison with other developmental disabilities, *Pediatrics*, **121**, 1155–1164.
64. Sacco, R., Militeri, R., Frolli, A., Bravaccio, C., Gritti, A., Elia, M., Curatolo, P., Manzi, B., Trillo, S., and Lenti, C., et al. (2007). Clinical, morphological, and biochemical correlates of head circumference in autism, *Biol. Psychiatry*, **62**, 1038–1047.
65. Hoerder-Suabedissen, A., Paulsen, O., and Molnar, Z. (2008). Thalamocortical maturation in mice is influenced by body weight, *J. Comp. Neurol.*, **511**, 415–420.
66. Whitaker-Azmitia, P. M. (2001). Serotonin and brain development: role in human developmental diseases, *Brain Res. Bull.*, **56**, 479–485.
67. Wobber, V., Hare, B., and Wrangham, R. (2008). Great apes prefer cooked food, *J. Hum. Evol.*, **55**, 340–348.
68. Gibbons, A. (2007). Paleoanthropology, Food for thought, *Science*, **316**, 1558–1560.
69. Olivier, J. D., Jans, L.A., Korte-Bouws, G. A., Korte, S. M., Deen, P. M., Cools, A. R., Ellenbroek, B. A., and Blokland, A. (2008). Acute tryptophan depletion dose dependently impairs object memory in serotonin transporter knockout rats, *Psychopharmacology (Berl.)*, **200**, 243–254.
70. Uchida, S., Umeeda, H., Kitamoto, A., Masushige, S., and Kida, S. (2007). Chronic reduction in dietary tryptophan leads to a selective impairment of contextual fear memory in mice, *Brain Res.*, **1149**, 149–156.
71. Feria-Velasco, A., del Angel, A. R., and Gonzalez-Burgos, I. (2002). Modification of dendritic development, *Prog. Brain Res.*, **136**, 135–143.
72. Gross, C., Zhuang, X., Stark, K., Ramboz, S., Oosting, R., Kirby, L., Santarelli, L., Beck, S., and Hen, R. (2002). Serotonin1A receptor acts during development to establish normal anxiety-like behaviour in the adult, *Nature*, **416**, 396–400.
73. Adell, A., Celada, P., Abellan, M. T., and Artigas, F. (2002). Origin and functional role of the extracellular serotonin in the midbrain raphe nuclei, *Brain Res. Rev.*, **39**, 154–180.
74. Bar-Peled, O., Gross-Isseroff, R., Ben Hur, H., Hoskins, I., Groner, Y., and Biegon, A. (1991). Fetal human brain exhibits a prenatal peak in the density of serotonin 5-HT1A receptors, *Neurosci. Lett.*, **127**, 173–176.
75. Kirchgessner, A. L., Liu, M. T., Raymond, J. R., and Gershon, M. D. (1996). Identification of cells that express 5-hydroxytryptamine1A receptors in the nervous systems of the bowel and pancreas, *J. Comp. Neurol.*, **364**, 439–455.
76. Manzke, T., Preusse, S., Hulsmann, S., and Richter, D. W. (2008). Developmental changes of serotonin 4(a) receptor expression in the rat pre-Botzinger complex, *J. Comp. Neurol.*, **506**, 775–790.
77. Waeber, C., Sebben, M., Bockaert, J., and Dumuis, A. (1996). Regional distribution and ontogeny of 5-HT4 binding sites in rat brain, *Behav. Brain Res.*, **73**, 259–262.
78. Liu, M., Geddis, M. S., Wen, Y., Setlik, W., and Gershon, M. D. (2005). Expression and function of 5-HT4 receptors in the mouse enteric nervous system, *Am. J. Physiol. Gastrointest. Liver Physiol.*, **289**, G1148–G1163.
79. Amisten, S., Braun, O., Bengtsson, A., and Erlinge, D. (2008). Gene expression profiling for the identification of G-protein coupled receptors in human platelets, *Thromb. Res.*, **122**, 47–57.

4

1. Zupanc, G. K. (2006). Neurogenesis and neuronal regeneration in the adult fish brain, *J. Comp. Physiol. A*, **192**, 649–670.
2. Altman, J. and Bayer, S. A. (1997). *Development of the cerebellar system*, CRC Press, Boca Raton.
3. Fujita, S., Shimada, M., and Nakamura, T. (1966). H3-Thymidine autoradiographic studies on the cell proliferation and differentiation in the external and internal granular layers of the mouse cerebellum, *J. Comp. Neurol.*, **128**, 191–208.
4. Altman, J. (1969). Autoradiographic and histological studies of postnatal neurogenesis. III. Dating the time of production and onset of differentiation of cerebellar microneurons in rats, *J. Comp. Neurol.*, **137**, 433–458.
5. Rakic, P. (1971). Neuron-glia relationship during cell migration in developing cerebellar cortex: A Golgi and electron microscopic study in Macacus Rhesus, *J. Comp. Neurol.*, **141**, 283–312.
6. Abraham, H., Tornoczky, T., Kosztolanyi, G., and Seress, L. (2001). Cell formation in the cortical layers of the developing human cerebellum, *Int. J. Dev. Neurosci.*, **19**, 53–62.
7. Leto, K., Carletti, B., Williams, I. M., Magrassi, L., and Rossi, F. (2006). Different types of cerebellar GABAergic interneurons originate from a common pool of multipotent progenitor cells, *J. Neurosci.*, **26**, 11682–11694.
8. Maricich, S. M. and Herrup, K. (1999). Pax-2 expression defines a subset of GABAergic interneurons and their precursors in the developing murine cerebellum, *J. Neurobiol.*, **41**, 281–294.
9. Ponti, G., Peretto, P., and Bonfanti, L. (2006). A subpial, transitory germinal zone forms chains of neuronal precursors in the rabbit cerebellum, *Dev. Biol.*, **294**, 168–180.
10. Doetsch, F. and Alvarez-Buylla, A. (1996). Network of tangential pathways for neuronal migration in adult mammalian brain, *Proc. Natl. Acad. Sci. U S A*, **93**, 14895–14900.
11. Bonfanti, L. (2006). PSA-NCAM in mammalian structural plasticity and neurogenesis, *Prog. Neurobiol.*, **80**, 129–164.
12. Butt, A. M., Kiff, J., Hubbard, P., and Berry, M. (2002). Synantocytes: new functions for novel NG2 expressing glia, *J. Neurocytol.*, **31**, 551–565.
13. Butt, A. M., Hamilton, N., Hubbard, P., Pugh, M., and Ibrahim, M. (2005). Synantocytes: the fifth element, *J. Anat.*, **207**, 695–706.
14. Gordon-Weeks, P. R. and Fischer, I. (2000). MAP1B expression and microtubule stability in growing and regenerating axons, *Microsc. Res. Tech.*, **48**, 63–74.
15. Wu, H. Y., Dawson, M. R., Reynolds, R., and Hardy, R. J. (2001). Expression of QKI proteins and MAP1B identifies actively myelinating oligodendrocytes in adult rat brain, *Mol. Cell Neurosci.*, **17**, 292–302.
16. Brown, J. P., Couillard-Despres, S., Cooper-Kuhn, C. M., Winkler, J., and Aigner, L., et al. (2003). Transient expression of doublecortin during adult neurogenesis, *J. Comp. Neurol.*, **467**, 1–10.
17. Weisheit, G., Gliem, M., Endl, E., Pfeffer, P. L., and Busslinger, M., et al. (2006). Postnatal development of the murine cerebellar cortex: formation and early dispersal of basket, stellate and Golgi neurons, *Eur. J. Neurosci.*, **24**, 466–478.
18. Takayama, C. and Inoue, Y. (2004). Extrasynaptic localization of GABA in the developing mouse cerebellum, *Neurosci. Res.*, **50**, 447–458.
19. Zhou, Q. and Anderson, D. J. (2002). The bHLH transcription factors OLIG2 and OLIG1 couple neuronal and glial subtype specification, *Cell*, **109**, 61–73.
20. Takebayashi, H., Nabeshima, Y., Yoshida, S., Chisaka, O., and Ikenaka, K., et al. (2002). The basic helix-loop-helix factor olig2 is essential for the development of motoneuron and oligodendrocyte lineages, *Curr. Biol.*, **12**, 1157–1163.
21. Weyer, A. and Schilling, K. (2003). Developmental and cell type-specific expression of the neuronal marker NeuN in the murine cerebellum, *J. Neurosci. Res.*, **73**, 400–409.
22. Engelkamp, D., Rashbass, P., Seawright, A., and van Heyningen, V. (1999). Role of Pax6

- in development of the cerebellar system, *Development*, **126**, 3585–3596.
23. Yamasaki, T., Kawaji, K., Ono, K., Bito, H., and Hirano, T., et al. (2001). Pax6 regulates granule cell polarization during parallel fiber formation in the developing cerebellum, *Development*, **128**, 3133–3144.
 24. Jones, A., Bahn, S., Grant, A. L., Kohler, M., and Wisden, W. (1996). Characterization of a cerebellar granule cell-specific gene encoding the γ -aminobutyric acid type A receptor $\alpha 6$ subunit, *J. Neurochem.*, **67**, 907–916.
 25. Menezes, J. R. and Luskin, M. B. (1994). Expression of neuron-specific tubulin defines a novel population in the proliferative layers of the developing telencephalon, *J. Neurosci.*, **14**, 5399–5416.
 26. Stottmann, R. W. and Rivas, R. J. (1998). Distribution of TAG-1 and synaptophysin in the developing cerebellar cortex: relationship to Purkinje cell dendritic development, *J. Comp. Neurol.*, **395**, 121–135.
 27. Kornack, D. R. and Rakic, P. (1999). Continuation of neurogenesis in the hippocampus of the adult macaque monkey, *Proc. Natl. Acad. Sci. U S A*, **96**, 5768–5773.
 28. Sottile, V., Li, M., and Scotting, P. J. (2006). Stem cell marker expression in the Bergmann glia population of the adult mouse brain, *Brain Res.*, **1099**, 8–17.
 29. Lindsey, B. W. and Tropepe, V. (2007). A comparative framework for understanding the biological principles of adult neurogenesis, *Prog. Neurobiol.*, **80**, 281–307.
 30. Gage, F. H. (2000). Mammalian neural stem cells, *Science*, **287**, 1433–1438.
 31. Peretto, P., Merighi, A., Fasolo, A., and Bonfanti, L. (1999). The subependymal layer in rodents: a site of structural plasticity and cell migration in the adult mammalian brain, *Brain Res. Bull.*, **49**, 221–243.
 32. Alvarez-Buylla, A. and Garcia-Verdugo, J. M. (2002). Neurogenesis in adult subventricular zone, *J. Neurosci.*, **22**, 629–634.
 33. Bonfanti, L. and Ponti, G. (2008). Adult neurogenesis and the New Zealand white rabbit, *Vet. J.*, **175**, 310–331.
 34. Gould, E. (2007). How widespread is adult neurogenesis in mammals? *Nat. Rev. Neurosci.*, **8**, 481–488.
 35. Luzzati, F., Peretto, P., Aimar, P., Ponti, G., and Fasolo, A., et al. (2003). Glia independent chains of neuroblasts through the subcortical parenchyma of the adult rabbit brain, *Proc. Natl. Acad. Sci. U S A*, **100**, 13036–13041.
 36. Luzzati, F., De Marchis, S., Fasolo, A., and Peretto, P. (2006). Neurogenesis in the caudate nucleus of the adult rabbit, *J. Neurosci.*, **26**, 609–621.
 37. Ito, M. (2006). Cerebellar circuitry as a neuronal machine, *Prog. Neurobiol.*, **78**, 272–303.
 38. Nacher, J., Crespo, C., and McEwen, B. S. (2001). Doublecortin expression in the adult rat telencephalon, *Eur. J. Neurosci.*, **14**, 629–644.
 39. Rosslenbroich, V., Dai, L., Baader, S. L., Noegel, A. A., and Gieselmann, V., et al. (2005). Collapsin response mediator protein-4 regulates F-actin bundling, *Exp. Cell Res.*, **310**, 434–444.
 40. Bonfanti, L., Olive, S., Poulain, D. A., and Theodosis, D. T. (1992). Mapping of the distribution of polysialylated neural cell adhesion molecule throughout the central nervous system of the adult rat: an immunohistochemical study, *Neurosci.*, **49**, 419–436.
 41. Dusart, I., Morel, M. P., Wehrle, R., and Sotelo, C. (1999). Late axonal sprouting of injured Purkinje cells and its temporal correlation with permissive changes in the glial scar, *J. Comp. Neurol.*, **408**, 399–418.
 42. Carleton, A., Petreanu, L., Lansford, R., Alvarez-Buylla, A., and Lledo, P. M. (2003). Becoming a new neuron in the adult olfactory bulb, *Nat. Neurosci.*, **6**, 507–518.
 43. Rao, M. S. and Shetty, A. K. (2004). Efficacy of doublecortin as a marker to analyse the absolute number and dendritic growth of newly generated neurons in the adult dentate gyrus, *Eur. J. Neurosci.*, **19**, 234–246.
 44. Spacek, J., Parizek, J., and Lieberman, A. R. (1973). Golgi cells, granule cells and synaptic glomeruli in the molecular layer of the rabbit cerebellar cortex, *J. Neurocytol.*, **2**, 407–28.
 45. Mellor, J. R., Merlo, D., Jones, A., Wisden, W., and Randall, A. D. (1998). Mouse cerebellar granule cell differentiation: electrical activity regulates the GABA_A

- receptor alpha 6 subunit gene, *J. Neurosci.*, **18**, 2822–2833.
46. Tucker, R. P. and Matus, A. I. (1988). Microtubule-associated proteins characteristic of embryonic brain are found in the adult mammalian retina, *Dev Biol.*, **130**, 423–434.
 47. Cheng, A., Krueger, B. K., and Bambrick, L. L. (1999). MAP5 expression in proliferating neuroblasts, *Brain Res. Dev Brain Res.*, **113**, 107–113.
 48. Vouyiouklis, D. A. and Brophy, P. J. (1993). Microtubule-associated protein MAP1B expression precedes the morphological differentiation of oligodendrocytes, *J. Neurosci. Res.*, **35**, 257–267.
 49. Safaei, R. and Fisher, I. (1989). Regulation of microtubule-associated protein 2 (MAP2) mRNA expression during rat brain development, *J. Mol. Neurosci.*, **1**, 189–198.
 50. Viereck, C., Tucker, R. P., and Matus, A. (1989). The adult rat olfactory system expresses microtubule-associated proteins found in the developing brain, *J. Neurosci.*, **9**, 3547–3557.
 51. Nothias, F., Fischer, I., Murray, M., Mirman, S., and Vincent, J. D. (1996). Expression of a phosphorylated isoform of MAP1B is maintained in adult central nervous system areas that retain capacity for structural plasticity, *J. Comp. Neurol.*, **368**, 317–334.
 52. Nishiyama, A. (2007). Polydendrocytes: NG2 cells with many roles in development and repair of the CNS, *Neuroscientist*, **13**, 62–76.
 53. Graham, V., Khudyakov, J., Ellis, P., and Pevny, L. (2003). SOX2 functions to maintain neural progenitor identity, *Neuron*, **39**, 749–765.
 54. Ferri, A. L., Cavallaro, M., Braidà, D., Di Cristofano, A., and Canta, A., et al. (2004). Sox2 deficiency causes neurodegeneration and impaired neurogenesis in the adult mouse brain, *Development*, **131**, 3805–3819.
 55. Episkopou, V. (2005). SOX2 functions in adult neural stem cells, *Trends Neurosci.*, **28**, 219–221.
 56. Avilion, A. A., Nicolis, S. K., Pevny, L. H., Perez, L., and Vivian, N., et al. (2003). Multipotent cell lineages in early mouse development depend on SOX2 function, *Genes Dev.*, **17**, 126–140.
 57. Ohyu, J., Yamanouchi, H., and Takashima, S. (1997). Immunohistochemical study of microtubule-associated protein 5 (MAP5) expression in the developing human brain, *Brain Dev.*, **19**, 541–546.
 58. Smith, K. R. Jr. (1963). The cerebellar cortex of the rabbit, An electron microscopic study, *J. Comp. Neurol.*, **121**, 459–483.
 59. Lossi, L., Ghidella, S., Marroni, P., and Merighi, A. (1995). The neurochemical maturation of the rabbit cerebellum, *J. Anat.*, **187**, 709–722.
 60. Komuro, H., Yacubova, E., Yacubova, E., and Rakic, P. (2001). Mode and tempo of tangential cell migration in the cerebellar external granule layer, *J. Neurosci.*, **21**, 527–540.
 61. Ngwenya, L. B., Peters, A., and Rosene, D. L. (2005). Light and electron microscopic immunohistochemical detection of bromodeoxyuridine-labeled cells in the Brain: different fixation and processing protocols, *J. Histochem. Cytochem.*, **53**, 821–832.
 62. Wegner, M. and Stolt, C. C. (2005). From stem cells to neurons and glia: a Soxist's view of neural development, *Trends Neurosci.*, **28**, 583–588.
 63. Luzzati, F., De Marchis, S., Fasolo, A., and Peretto, P. (2007). Adult neurogenesis and local neuronal progenitors in the striatum, *Neurodegener. Dis.*, **4**, 322–327.
 64. Aguirre, A. A., Chittajallu, R., Belachew, S., and Gallo, V. (2004). NG2-expressing cells in the subventricular zone are type C-like cells and contribute to interneuron generation in the postnatal hippocampus, *J. Cell Biol.*, **165**, 575–589.
 65. Ligon, K. L., Fancy, S. P., Franklin, R. J., and Rowitch, D. H. (2006). Olig gene function in CNS development and disease, *Glia*, **54**, 1–10.
 66. Sanai, N., Tramontin, A. D., Quinones-Hinojosa, A., Barbaro, N. M., Gupta, N., and Kunwar, S., et al. (2004). Unique astrocyte ribbon in adult human brain contains neural stem cells but lacks chain migration, *Nature*, **427**, 740–744.
 67. Curtis, M. A., Kam, M., Nannmark, U., Anderson, M. F., Axell, M. Z., et al. (2007).

- Human neuroblasts migrate to the olfactory bulb via a lateral ventricular extension, *Science*, **315**, 1243–1249.
68. Leuner, B., Kozorovitskiy, Y., Gross, C. G., and Gould, E. (2007). Diminished adult neurogenesis in the marmoset brain precedes old age, *Proc. Natl. Acad. Sci. U S A*, **104**, 17169–17173.
 69. Luo, J., Daniels, S. B., Lenington, J. B., Notti, R. Q., and Conover, J. C. (2006). The aging neurogenic subventricular zone, *Aging Cell*, **5**, 139–152.
 70. Rakic, P. (2004). Immigration denied, *Nature*, **427**, 685–686.
 71. Ponti, G., Aimar, P., and Bonfanti, L. (2006). Cellular composition and cytoarchitecture of the rabbit subventricular zone (SVZ) and its extensions in the forebrain, *J. Comp. Neurol.*, **498**, 491–507.
- ## 5
1. Chandrashekar, J., Mueller, K. L., Hoon, M. A., Adler, E., Feng, L., Guo, W., Zuker, C. S., and Ryba, N. J. (2000). T2Rs function as bitter taste receptors, *Cell*, **100**(6), 703–711.
 2. Nelson, G., Hoon, M. A., Chandrashekar, J., Zhang, Y., Ryba, N. J., and Zuker, C. S. (2001). Mammalian sweet taste receptors, *Cell*, **106**(3), 381–390.
 3. Zhang, Y., Hoon, M. A., Chandrashekar, J., Mueller, K. L., Cook, B., Wu, D., Zuker, C. S., and Ryba, N. J. (2003). Coding of sweet, bitter, and umami tastes: different receptor cells sharing similar signaling pathways, *Cell*, **112**(3), 293–301.
 4. Zhao, G. Q., Zhang, Y., Hoon, M. A., Chandrashekar, J., Erlenbach, I., Ryba, N. J., and Zuker, C. S. (2003). The receptors for mammalian sweet and umami taste, *Cell*, **115**(3), 255–266.
 5. Mueller, K. L., Hoon, M. A., Erlenbach, I., Chandrashekar, J., Zuker, C. S., and Ryba, N. J. (2005). The receptors and coding logic for bitter taste, *Nature*, **434**(7030), 225–229.
 6. Chandrashekar, J., Hoon, M., Ryba, N., and Zuker, C. (2006). The receptors and cells for mammalian taste, *Nature*, **444**, 288–294.
 7. Huang, A. L., Chen, X., Hoon, M. A., Chandrashekar, J., Guo, W., Trankner, D., Ryba, N. J., and Zuker, C. S. (2006). The cells and logic for mammalian sour taste detection, *Nature*, **442**(7105), 934–938.
 8. Zotterman, Y. (1935). Action potentials in the glossopharyngeal nerve and in the chorda tympani, *Skandinavisches Archiv für Physiologie*, **72**, 73–77.
 9. Li, X., Li, W., Wang, H., Cao, J., Maehashi, K., Huang, L., Bachmanov, A. A., Reed, D. R., LeGrand-Defretin, V., and Beauchamp, G. K., et al. (2005). Pseudogenization of a sweet-receptor gene accounts for cats indifference toward sugar, *PLoS genetics*, **1**(1), 27–35.
 10. Andersson, B., Landgren, S., Olsson, L., and Zotterman, Y. (1950). The sweet taste fibres of the dog, *Acta. Physiology Scand.*, **21**, 105–119.
 11. Zotterman, Y. (1959). Studies on the nervous mechanism of taste, *Exp. Cell Res.*, **14**(Suppl 5), 520–526.
 12. Gordon, G., Kitchell, R., Strom, L., and Zotterman, Y. (1959) The response pattern of taste fibres in the chorda tympani of the monkey, *Acta. Physiologica Scandinavica*, **46**, 119–132.
 13. Erickson, R. P. (1963) Sensory neural patterns and gustation, In *Olfaction and Taste*. 1, Y. Zotterman (Ed.), Pergamon Press, Oxford, London, New York, Paris, 205–213.
 14. Erickson, R. P. (2000). The evolution of neural coding ideas in the chemical senses, *Physiology & behavior*, **69**(1–2), 3–13.
 15. Scott, T. R. and Giza, B. K. (2000). Issues of gustatory neural coding: where they stand today, *Physiology & behavior*, **69**(1–2), 65–76.
 16. Lemon, C. H. and Katz, D. B. (2007). The neural processing of taste, *BMC neuroscience*, **8**(Suppl 3), S5.
 17. Schiffman, S. S., Booth, B. J., Sattely-Miller, E. A., Graham, B. G., and Gibes, K. M. (1999). Selective inhibition of sweetness by the sodium salt of +/-2-(4-methoxyphenoxy)propanoic acid, *Chem. Senses*, **24**(4), 439–447.
 18. Kinghorn, A. D. and Compadre, C. M. (2001) Less common high-potency sweeteners.

- In *Alternative Sweeteners*, L. O. B. Nabors (Ed.), 3rd ed., CRC Press, 209–234.
19. Galindo-Cuspinera, V. and Breslin, P. A. (2006). The liaison of sweet and savory, *Chem. Senses*, **31**(3), 221–225.
 20. Hellekant, G. and Roberts, T. W. (1995). Whole nerve and single fiber recordings in non-human primates, In *Experimental Cell Biology of Taste and Olfaction: Current Techniques and Protocols*, A. I. Spielman, J. G. Brand, Raton Boca (Eds.), CRC Press, New York, London, Tokyo, 277–290.
 21. Hellekant, G. and Wang, A. (2008). A method to measure taste qualities, taste intensity and temporal profile of compounds aimed at human consumption by taste nerve recordings in monkeys, In *Sweetness and Sweeteners: Biology, Chemistry and Psychophysics*, D. K. Weerasinghe and G. E. Dubois (Eds.), ACS Symposium Series 979 Oxford University Press, 185–201.
 22. Smith, D. V. and Travers, J. B. (1979). A metric for the breadth of turning of gustatory neurons, *Chem. Sens. Flavor*, **4**(3), 215–229.
 23. Danilova, V., Danilov, Y., Roberts, T., Elmer, D., and Hellekant, G. (2002). Electrophysiological recordings of mammalian taste nerves. In *Methods and Frontiers in Neuroscience*, S. A. Simon and M. A. L. Nicoletis (Eds.), Boca Raton, CRC Press, London, New York, Washington D.C., 239–264.
 24. Nowak, R. M. (1991). Order Primates, In *Walker's Mammals of the world*, Volume II. 5th ed. John Hopkins, Baltimore and London, 472.
 25. Sato, M., Ogawa, H., and Yamashita, S. (1994). Gustatory responsiveness of chorda tympany fibers in cynomolgus monkey, *Chem. Senses*, **19**(5), 381–400.
 26. Diamant, H., Hellekant, G., and Zotterman, Y. (1972). The effect of miraculin on the taste buds of man, monkey and rat. In *Olfaction and Taste IV*, D. Schneider (Ed.), Stuttgart: Wissenschaftliche Verlagsgesellschaft MB4 Stuttgart, 241–244.
 27. Hellekant, G., Hagstrom, E. C., Kasahara, Y., and Zotterman, Y. (1974). On the gustatory effects of miraculin and gymnemic acid in monkey, *Chem. Sens. Flavor*, **1**, 137–145.
 28. Hellekant, G., Glaser, D., Brouwer, J. N., and Wel, H. (1976). Gustatory effects of miraculin, monellin and thaumatin in the Saguinus midas tamarin monkey studied with electrophysiological and behavioural techniques, *Acta. Physiologica Scandinavica*, **97**(2), 241–250.
 29. Hellekant, G. (1977). Effects of Miraculin and Gymnemic acid in the Rhesus monkey (*Macaca mulatta*), In *Food Intake and Chemical Senses*, Y. Katsuki, M. Sato, S. F. Takagi, and Y. Oomura (Eds.), University of Tokyo Press, Tokyo, 201–210.
 30. Brouwer, J. N., Glaser, D., Hard, Af., Segerstad, C., Hellekant, G., Ninomiya, Y., and Wel, H. (1983). The sweetness-inducing effect of miraculin; behavioural and neurophysiological experiments in the rhesus monkey *Macaca mulatta*, *Journal of Physiology*, **337**, 221–240.
 31. Bartoshuk, L. M., Dateo, G. P., Vandenberg, D. J., Buttrick, R. L., and Long, L. Jr. (1969). Effects of *Gymnema sylvestre* and *Synsepalum dulcificum* on taste in man, *Olfaction and Taste*, **1**, 436–449.
 32. Edgeworth, P. (1847). *Gymnema sylvestre*, *Pharm. J.*, **48**, 351.
 33. Kurihara, K., Kurihara, Y., and Beidler, L. M. (1969). Isolation and mechanism of taste modifiers; taste-modifying protein and gymnemic acids, In *Olfaction & Taste III*. Volume 1. 1st ed., C. Pfaffmann (Ed.), The Rockefeller University Press, New York., 450–469.
 34. Kurihara, Y. (1969). Antisweet activity of gymnemic acid A1 and its derivatives, *Life sciences*, **8**(9), 537–543.
 35. Diamant, H., Oakley, B., Strom, L., Wells, C., and Zotterman, Y. (1965). A comparison of neural and psychophysical responses to taste stimuli in man, *Acta. Physiol. Scand.*, **64**, 67–74.
 36. Oakley, B. (1985). Taste responses of human Chorda tympani nerve, *Chem. Senses*, **10**(4), 469–481.
 37. Hellekant, G., Ninomiya, Y., DuBois, G. E., Danilova, V., and Roberts, T. W. (1996). Taste in chimpanzee: I, The summated response to sweeteners and the effect of gymnemic acid, *Physiology & behavior*, **60**(2), 469–479.

38. Hellekant, G., Ninomiya, Y., and Danilova, V. (1997). Taste in chimpanzees II: single chorda tympani fibers, *Physiol. Behav.*, **61**(6), 829–841.
39. Hellekant, G., Ninomiya, Y., and Danilova, V. (1998). Taste in chimpanzees III: Labeled line coding in sweet taste, *Physiol. Behav.*, **65**(2), 191–200.
40. Jin, Z., Danilova, V., Assadi-Porter, F., Zhao, Q., Aceti, D., Markley, J., and Hellekant, G. (2002). Monkey electrophysiological responses to Brazzein mutants—where are the critical regions for Brazzein’s sweet taste, *2nd International Symposium on Sweetener*, Hiroshima, Japan, **143**, 128.
41. Jin, Z., Danilova, V., Assadi-Porter, F. M., Markley, J. L., and Hellekant, G. (2003). Monkey electrophysiological and human psychophysical responses to mutants of the sweet protein Brazzein: delineating Brazzein sweetness, *Chem. Senses*, **28**(6), 491–498.
42. Danilova, V., Hellekant, G., and Jin, Z. (1998). Effect of miraculin on behavioral and single taste fibers responses in common marmoset, *Callithrix jacchus jacchus*, *Chem. Senses Sarasota FL* 550.
43. Danilova, V., Hellekant, G., Roberts, R., Tinti, J. M., and Nofre, C. (1998). Behavioral and single chorda tympani taste fiber responses in the common marmoset, *Callithrix jacchus jacchus*, *An NY Acad. Sci. Olfaction and Taste XII*, **855**, 160–164.
44. Danilova, V., Danilov, Y., Roberts, T., Tinti, J.-M., Nofre, C., and Hellekant, G. (2002). The sense of taste in a New World monkey, the common marmoset: recordings from the chorda tympani and glossopharyngeal nerves, *J. Neurophysiol.*, **88**, 579–594.
45. Danilova, V., and Hellekant, G. (2004). Sense of taste in a New World monkey, the common marmoset. II. Link between behavior and nerve activity, *J. Neurophysiol.*, **92**(2), 1067–1076.
46. Danilova, V. and Hellekant, G. (2006). Elucidating coding of taste qualities with the taste modifier miraculin in the common marmoset, *Brain research bulletin*, **68**(5), 315–321.
47. Li, X., Staszewski, L., Xu, H., Durick, K., Zoller, M., and Adler, E. (2002). Human receptors for sweet and umami taste, *Proceedings of the National Academy of Sciences of the United States of America*, **99**(7), 4692–4696.
48. Li, X., Li, W., Mascioli, K. J., Bachmanov, A. A., Tordoff, M. G., Epple, G., Beauchamp, G. K., Reed, and D. R. (2003). Comparative analysis of the T1R taste receptor genes in primates, *ACHEMS XXV*, Sarasota FL, **74**:abstract, 296.
49. Xu, H., Staszewski, L., Tang, H., Adler, E., Zoller, M., and Li, X. (2004). Different functional roles of T1R subunits in the heteromeric taste receptors, *Proceedings of the National Academy of Sciences of the United States of America*, **101**(39), 14258–14263.
50. Jiang, P., Cui, M., Zhao, B., Liu, Z., Snyder, L. A., Benard, L. M., Osman, R., Margolskee, R. F., and Max, M. (2005). Lactisole interacts with the transmembrane domains of human T1R3 to inhibit sweet taste, *J. Biol. Chem.*, **280**(15), 15238–15246.
51. Li, X. (2008). *T1R3 sequence pers*, Communication to Hellekant G.
52. Scalfani, A. and Perez, C. (1997). Cypha [propionic acid, 2-(4-methoxyphenol) salt] inhibits sweet taste in humans, but not in rats, *Physiology & behavior*, **61**(1), 25–29.
53. Winnig, M., Bufe, B., and Meyerhof, W. (2005). Valine 738 and lysine 735 in the fifth transmembrane domain of rTas1r3 mediate insensitivity towards lactisole of the rat sweet taste receptor, *BMC neuroscience*, **6**(1), 22.
54. Farbman, A. I. (1980) Renewal of taste bud cells in rat circumvallate papillae, *Cell Tissue Kinet.*, **13**(4), 349–357.
55. Hellekant, G., Segerstad, C. H., Roberts, T., Wel, H., Brouwer, J. N., Glaser, D., Haynes, R., and Eichberg, J. W. (1985). Effects of gymnemic acid on the chorda tympani proper nerve responses to sweet, sour, salty and bitter taste stimuli in the chimpanzee, *Acta. Physiologiae Scand.*, **124**(3), 399–408.
56. Ninomiya, Y. and Hellekant, G. (1991). Specific taste sensitivity of single chorda tympani fibers in chimpanzee, *Proc. Jpn. Symp. Taste and Smell*, 313–316.
57. Yee, C. L., Yang, R., Bottger, B., Finger, T. E., and Kinnamon, J. C. (2001). “Type III” cells of rat taste buds: immunohistochemical

- and ultrastructural studies of neuron-specific enolase, protein gene product 9.5, and serotonin, *The Journal of comparative neurology*, **440**(1), 97–108.
58. Clapp, T. R., Yang, R., Stoick, C. L., Kinnamon, S. C., and Kinnamon, J. C. (2004). Morphologic characterization of rat taste receptor cells that express components of the phospholipase C signaling pathway, *The Journal of comparative neurology*, **468**(3), 311–321.
 59. Yang, R., Stoick, C. L., and Kinnamon, J. C. (2004). Synaptobrevin-2-like immunoreactivity is associated with vesicles at synapses in rat circumvallate taste buds, *The Journal of comparative neurology*, **471**(1), 59–71.
 60. Farbman, A. I., Hellekant, G., and Nelson, A. (1985). Structure of taste buds in foliate papillae of the rhesus monkey, *Macaca mulatta*, *American Journal of Anatomy*, **172**(1), 41–56.
 61. Kinnamon, J. C., Taylor, B. J., Delay, R. J., and Roper, S. D. (1985). Ultrastructure of mouse vallate taste buds, I. Taste cells and their associated synapses, *Journal of Comparative Neurology*, **235**(1), 48–60.
 62. Delay, R. J., Kinnamon, J. C., and Roper, S. D. (1986). Ultrastructure of mouse vallate taste buds: II. Cell types and cell lineage, *Journal of Comparative Neurology*, **253**(2), 242–252.
 63. Henzler, D. M. and Kinnamon, J. C. (1987). Ultrastructure of Mouse Fungiform Taste Buds, *Olfaction and Taste IX*, 359–361.
 64. Royer, S. M. and Kinnamon, J. C. (1987). Interactions between Taste Cells and Nerve Fibers in Murine Foliate Taste Buds, *Olfaction and Taste IX*, 577–579.
 65. Kinnamon, J. C., Sherman, T. A., and Roper, S. D. (1988). Ultrastructure of mouse vallate taste buds: III. Patterns of synaptic connectivity, *Journal of Comparative Neurology*, **270**(1), 1–10.
 66. Royer, S. M. and Kinnamon, J. C. (1988). Ultrastructure of mouse foliate taste buds: synaptic and nonsynaptic interactions between taste cells and nerve fibers, *Journal of Comparative Neurology*, **270**(1), 11–24.
 67. Kinnamon, J. C., Henzler, D. M., and Royer, S. M. (1993). HVEM ultrastructural analysis of mouse fungiform taste buds, cell types, and associated synapses, *Microscopy Research and Technique*, **26**, 142–156.
 68. McPheeters, M., Barber, A. J., Kinnamon, S. C., and Kinnamon, J. C. (1994). Electrophysiological and morphological properties of light and dark cells isolated from mudpuppy taste buds, *The Journal of comparative neurology*, **346**(4), 601–612.
 69. Royer, S. M. and Kinnamon, J. C. (1994). Application of serial sectioning and three-dimensional reconstruction to the study of taste bud ultrastructure and organization, *Microsc. Res. Tech.*, **29**(5), 381–407.
 70. Yang, R., Crowley, H. H., Rock, M. E., and Kinnamon, J. C. (2000). Taste cells with synapses in rat circumvallate papillae display SNAP-25-like immunoreactivity, *The Journal of comparative neurology*, **424**(2), 205–215.
 71. Huang, Y. J., Maruyama, Y., Dvoryanchikov, G., Pereira, E., Chaudhari, N., and Roper, S. D. (2007). The role of pannexin 1 hemichannels in ATP release and cell-cell communication in mouse taste buds, *Proceedings of the National Academy of Sciences of the United States of America*, **104**(15), 6436–6441.
 72. Roper, S. D. (2007). Signal transduction and information processing in mammalian taste buds, *Pflügers Arch.*, **454**(5), 759–776.
 73. Tomchik, S. M., Berg, S., Kim, J. W., Chaudhari, N., and Roper, S. D. (2007). Breadth of tuning and taste coding in mammalian taste buds, *J. Neurosci.*, **27**(40), 10840–10848.
 74. Finger, T. E., Danilova, V., Barrows, J., Bartel, D. L., Vigers, A. J., Stone, L., Hellekant, G., and Kinnamon, S. C. (2005). ATP signaling is crucial for communication from taste buds to gustatory nerves, *Science*, **310**(5753), 1495–1499.
 75. Yoshida, R., Murata, Y., Yasuo, T., Yasumatsu, K., Shigemura, N., and Ninomiya, Y. (2008). Taste signal transmission from fungiform taste bud cells to chorda tympani nerve fibers in mice, In *ECRO*, University of Ljubljana and Slovenian Physiological Society, Portoroz Slovenia.
 76. Yoshida, R., Yasumatsu, K., Shigemura, N., and Ninomiya, Y. (2006). Coding channels for taste perception: information transmission from taste cells to gustatory nerve

fibers, *Archives of histology and cytology*, **69**(4), 233–242.

77. Geran, L. C. and Travers, S. P. (2006). Single neurons in the nucleus of the solitary tract respond selectively to bitter taste stimuli, *J. Neurophysiol.*, **96**(5), 2513–2527.
 78. Herness, M. S. (1989). Vasoactive intestinal peptide-like immunoreactivity in rodent taste cells, *Neuroscience*, **33**(2), 411–419.
 79. Kaya, N., Shen, T., Lu, S. G., Zhao, F. L., and Herness, S. (2004). A paracrine signaling role for serotonin in rat taste buds: expression and localization of serotonin receptor subtypes, *American journal of physiology*, **286**(4), R649–658.
 80. Huang, Y. J., Maruyama, Y., Lu, K.S., Pereira, E., Plonsky, I., Baur, J. E., Wu, D., and Roper, S. D. (2005). Mouse taste buds use serotonin as a neurotransmitter, *J. Neurosci.*, **25**(4), 843–847.
 81. Shen, T., Kaya, N., Zhao, F. L., Lu, S. G., Cao, Y., and Herness, S. (2005). Co-expression patterns of the neuropeptides vasoactive intestinal peptide and cholecystokinin with the transduction molecules alpha-gustducin and T1R2 in rat taste receptor cells, *Neuroscience*, **130**(1), 229–238.
- 6**
1. Addison, P. D., Neligan, P. C., Ashrafpour, H., Khan, A., Zhong, A., Moses, M., Forrest, C. R., and Pang, C. Y. (2003). Noninvasive remote ischemic preconditioning for global protection of skeletal muscle against infarction, *Am. J. Physiol. Heart Circ. Physiol.*, **285**(4), H14351–443.
 2. Lewis, T. (1932). Pain in muscular ischemia, (Its relation to anginal pain), *Arch. Intern. Med.*, **49**, 713–729.
 3. Albers, M., Fratezi, A. C., and De Luccia, N. (1992). Assessment of quality of life of patients with severe ischemia as a result of infrainguinal arterial occlusive disease, *J. Vasc. Surg.*, **16**(1), 54–59.
 4. Greenhaff, P. L., Campbell-O'Sullivan, S. P., Constantin-Teodosiu, D., Poucher, S. M., Roberts, P. A., and Timmons, J. A. (2004). Metabolic inertia in contracting skeletal muscle: a novel approach for pharmacological intervention in peripheral vascular disease, *Br. J. Clin. Pharmacol.*, **57**(3), 237–243.
 5. Isner, J.M. and Rosenfield, K. (1993). Redefining the treatment of peripheral artery disease, Role of percutaneous revascularization, *Circulation*, **88**(4 Pt 1), 1534–1557.
 6. Stewart, K. J., Hiatt, W. R., Regensteiner, J. G., and Hirsch, A. T. (2002). Exercise training for claudication, *N. Engl. J. Med.*, **347**(24), 1941–1951.
 7. Taivassalo, T., Fu, K., Johns, T., Arnold, D., Karpati, G., and Shoubridge, E. A. (1999). Gene shifting: a novel therapy for mitochondrial myopathy, *Hum Mol. Genet.*, **8**(6), 1047–1052.
 8. Timmons, J. A., Constantin-Teodosiu, D., Poucher, S. M., and Greenhaff, P. L. (2004). Acetyl group availability influences phosphocreatine degradation even during intense muscle contraction, *J. Physiol.*, **561**(Pt 3), 851–859.
 9. Timmons, J. A., Gustafsson, T., Sundberg, C. J., Jansson, E., Hultman, E., Kaijser, L., Chwalbinska-Moneta, J., Constantin-Teodosiu, D., Macdonald, I. A., and Greenhaff, P. L. (1998). Substrate availability limits human skeletal muscle oxidative ATP regeneration at the onset of ischemic exercise, *J. Clin. Invest.*, **101**(1), 79–85.
 10. Timmons, J. A., Poucher, S. M., Constantin-Teodosiu, D., Macdonald, I. A., and Greenhaff, P. L. (1997). Metabolic responses from rest to steady state determine contractile function in ischemic skeletal muscle, *Am. J. Physiol.*, **273**(2 Pt 1), E233–238.
 11. Timmons, J. A., Poucher, S. M., Constantin-Teodosiu, D., Worrall, V., Macdonald, I. A., and Greenhaff, P. L. (1996). Increased acetyl group availability enhances contractile function of canine skeletal muscle during ischemia, *J. Clin. Invest.*, **97**(3), 879–883.
 12. Hiatt, W. R., Wolfel, E. E., Regensteiner, J. G., and Brass, E. P. Skeletal muscle carnitine metabolism in patients with unilateral peripheral arterial disease, *J. Appl. Physiol.*, **73**(1), 346–353.
 13. Holm, J., Bjornorp, P., and Schersten, T. (1972). Metabolic activity in human skeletal muscle, Effect of peripheral arterial insufficiency, *Eur. J. Clin. Invest.*, **2**(5), 321–325.

14. Kaijser, L., Sundberg, C. J., Eiken, O., Nygren, A., Esbjornsson, M., Sylven, C., and Jansson, E. (1990). Muscle oxidative capacity and work performance after training under local leg ischemia, *J. Appl. Physiol.*, **69**(2), 785–787.
15. Hiatt, W. R., Regensteiner, J. G., Wolfel, E. E., Carry, M. R., and Brass, E. P. (1996). Effect of exercise training on skeletal muscle histology and metabolism in peripheral arterial disease, *J. Appl. Physiol.*, **81**(2), 780–788.
16. Teravainen, H. and Makitie, J. (1977). Striated muscle ultrastructure in intermittent claudication, *Arch. Pathol. Lab. Med.*, **101**(5), 230–235.
17. Addison, P., Neligan, P., Forrest, C., Zhong, A., Perri, L., and Pang, C. Y. (2003). Acute adenosine treatment is effective in augmentation of ischemic tolerance in muscle flaps in the pig: an update, *Plast. Reconstr. Surg.*, **111**(2), 842–845.
18. Timmons, J. A., Poucher, S. M., Constantin-Teodosiu, D., Worrall, V., MacDonald, I. A., and Greenhaff, P. L. (1996). Metabolic responses of canine gracilis muscle during contraction with partial ischemia, *Am. J. Physiol.*, **270**(3 Pt 1), E400–406.
19. Graham, T., Bangsbo, J., and Saltin, B. (1993). Skeletal muscle ammonia production and repeated, intense exercise in humans, *Can. J. Physiol. Pharmacol.*, **71**(7), 484–490.
20. Hogan, M. C., Gladden, L. B., Grassi, B., Stary, C. M., and Samaja, M. (1998). Bioenergetics of contracting skeletal muscle after partial reduction of blood flow, *J. Appl. Physiol.*, **84**(6), 1882–1888.
21. Hogan, M. C., Richardson, R. S., and Kurdak, S. S. (1994). Initial fall in skeletal muscle force development during ischemia is related to oxygen availability, *J. Appl. Physiol.*, **77**(5), 2380–2384.
22. Katz, A., Sahlin, K., and Henriksson, J. (1986). Muscle ammonia metabolism during isometric contraction in humans, *Am. J. Physiol.*, **250**(6 Pt 1), C834–840.
23. Casey, A., Constantin-Teodosiu, D., Howell, S., Hultman, E., and Greenhaff, P. L. (1996). Metabolic response of type I and II muscle fibers during repeated bouts of maximal exercise in humans, *Am. J. Physiol.*, **271**(1 Pt 1), E38–43.
24. Op't Eijnde, B., Van Leemputte, M., Brouns, F., Van Der Vusse, G. J., Labarque, V., Ramaekers, M., Van Schuylenberg, R., Verbessert, P., Wijnen, H., and Hespel, P. (2001). No effects of oral ribose supplementation on repeated maximal exercise and de novo ATP resynthesis, *J. Appl. Physiol.*, **91**(5), 2275–2281.
25. Graham, T. E., Bangsbo, J., Gollnick, P. D., Juel, C., and Saltin, B. (1990). Ammonia metabolism during intense dynamic exercise and recovery in humans, *Am. J. Physiol.*, **259**(2 Pt 1), E170–176.
26. Howlett, R. A. and Hogan, M. C. (2003). Dichloroacetate accelerates the fall in intracellular PO₂ at onset of contractions in *Xenopus* single muscle fibers, *Am. J. Physiol. Regul. Integr. Comp. Physiol.*, **284**(2), R481–485.
27. Sabina, R. L. and Mahnke-Zizelman, D. K. (2000). Towards an understanding of the functional significance of N-terminal domain divergence in human AMP deaminase isoforms, *Pharmacol. Ther.*, **87**(23), 279–283.
28. Rico-Sanz, J. (2003). Progressive decrease of intramyocellular accumulation of H⁺ and Pi in human skeletal muscle during repeated isotonic exercise, *Am. J. Physiol. Cell Physiol.*, **284**(6), C1490–1496.
29. Timmons, J. A., Gustafsson, T., Sundberg, C. J., Jansson, E., and Greenhaff, P. L. (1998). Muscle acetyl group availability is a major determinant of oxygen deficit in humans during submaximal exercise, *Am. J. Physiol.*, **274**(2 Pt 1), E377–380.
30. MacLean, D. A., Graham, T. E., and Saltin, B. (1996). Stimulation of muscle ammonia production during exercise following branched-chain amino acid supplementation in humans, *J. Physiol.*, **493**(Pt 3), 909–922.
31. Mourtzakis, M. and Graham, T. E. (2002). Glutamate ingestion and its effects at rest and during exercise in humans, *J. Appl. Physiol.*, **93**(4), 1251–1259.
32. Anderson, J. L., Habashi, J., Carlquist, J. F., Muhlestein, J. B., Horne, B. D., Bair, T. L., Pearson, R. R., and Hart, N. (2000). A common variant of the AMPD1 gene

predicts improved cardiovascular survival in patients with coronary artery disease, *J. Am. Coll. Cardiol.*, **36**(4), 1248–1252.

33. De Ruiter, C. J., Van EDEHAANBG, Wevers, R. A., and De Haan, A. (2000). Muscle function during fatigue in myoadenylate deaminase-deficient Dutch subjects, *Clin. Sci. (Lond.)*, **98**(5), 579–585.
34. Norman, B., Sabina, R. L., and Jansson, E. (2001). Regulation of skeletal muscle ATP catabolism by AMPD1 genotype during sprint exercise in asymptomatic subjects, *J. Appl. Physiol.*, **91**(1), 258–264.
35. Kasibhatla, S. R., Bookser, B. C., Xiao, W., and Erion, M. D. (2001). AMP deaminase inhibitors. 5. Design, synthesis, and SAR of a highly potent inhibitor series, *J. Med. Chem.*, **44**(4), 613–618.

7

1. Cavagna, G. A., Heglund, N. C., and Taylor, C. R. (1977). Mechanical work in terrestrial locomotion: two basic mechanisms for minimizing energy expenditure, *American Journal of Physiology*, **233**, R243–R261.
2. Biewener, A. A. (2006). Patterns of mechanical energy change in tetrapod gait: Pendula, springs and work, *Journal of Experimental Zoology*, **305A**, 899–911.
3. Griffin, T. M., Main, R. P., and Farley, C. T. (2004). Biomechanics of quadrupedal walking: how do four-legged animals achieve inverted pendulum-like movements? *Journal of Experimental Biology*, **207**, 3545–3558.
4. Reilly, S. M., McElroy, E. J., and Biknevicius, A. R. (2007). Posture, gait and the ecological relevance of locomotor costs and energy saving mechanisms in tetrapods, *Zoology*, **110**, 271–289.
5. Ahn, A. N., Furrow, E., and Biewener, A. A. (2004). Walking and running in the red-legged running frog, *Kassina maculata*, *Journal of Experimental Biology*, **207**, 399–410.
6. Farley, C. T. and Ko, T. C. (1997). Mechanics of locomotion in lizards, *Journal of Experimental Biology*, **200**, 2177–2188.
7. Zani, P. A., Gottschall, J. S., and Kram, R. (2005). Giant Galapagos tortoises walk without inverted pendulum mechanical-energy exchange, *Journal of Experimental Biology*, **208**, 1489–1494.
8. Usherwood, J. R., Williams, S. B., and Wilson, A. M. (2007). Mechanics of dog walking compared with a passive, stiff-limbed, 4-bar linkage model, and their collisional implications, *Journal of Experimental Biology*, **210**, 533–540.
9. Manter, J. T. (1938). The dynamics of quadrupedal walking, *Journal of Experimental Biology*, **15**, 522–540.
10. Geyer, H., Seyfarth, A., and Blickhan, R. (2006). Compliant leg behavior explains basic dynamics of walking and running, *Proc. Roy. Soc. London B*, **273**, 2861–2867.
11. Biknevicius, A. R., and Reilly, S. M. (2006). Correlation of symmetrical gaits and whole body mechanics: Debunking myths in locomotor biodynamics, *Journal of Experimental Zoology*, **305A**, 923–934.
12. Parchman, A. J., Reilly, S. M., and Biknevicius, A. R. (2003). Whole-body mechanics and gaits in the gray short-tailed opossum *Monodelphis domestica*: integrating patterns of locomotion in a semi-erect mammal, *Journal of Experimental Biology*, **206**, 1379–1388.
13. Biknevicius, A. R., Reilly, S. M., White, T. D., Hancock, J. A., and McElroy, E. J. (2007). Interpreting the significance of whole body mechanics in primitive mammals, *Journal of Morphology*, **12**, 1049.
14. Demes, B., Larson, S. G., Stern, J. T. J., Jungers, W. L., and Biknevicius, A. R., et al. (1994). The kinetics of primate quadrupedalism: “hindlimb drive” reconsidered, *Journal of Human Evolution*, **26**, 353–374.
15. Cartmill, M., Lemelin, P., and Schmitt, D. (2002). Support polygons and symmetrical gaits in mammals, *Zoological Journal of the Linnean Society*, **136**, 401–420.
16. Hedrick, T. L. (2005). “DLT Data Viewer 2”, Digitizing and DLT in MATLAB.

8

1. Jacobs, K. A., Leach, D. H., Fretz, P. B., and Townsend, H. G. G. (1984). Comparative aspects of the healing of excisional wounds on the leg and body of horses, *Vet. Surg.*, **13**, 83–90.

2. Knottenbelt, D. C. (1997). Equine wound management: are there significant differences in healing at different sites on the body? *Vet. Dermatol.*, **8**, 273–290.
3. Perkins, N. R., Reid, S. W., and Morris, R. S. (2005). Profiling the New Zealand Thoroughbred racing industry 2 Conditions interfering with training and racing, *N Z Vet. J.*, **53**(1), 69–76.
4. Lefebvre-Lavoie, J., Lussier, J. G., and Theoret, C. L. (2005). Profiling of differentially expressed genes in wound margin biopsies of horses, using suppression subtractive hybridization, *Physiol. Genomics.*, **22**, 157–170.
5. Cheon, S., Poon, R., Yu, C., Khoury, M., Shenker, R., Fish, J., and Alman, B. A. (2005). Prolonged beta-catenin stabilization and tcf-dependent transcriptional activation in hyperplastic cutaneous wounds. *Lab. Invest.*, **85**(3), 416–425.
6. Bowley, E., O’Gorman, D. B., and Gan, B. S. (2007). Beta-catenin signaling in fibroproliferative disease, *J. Surg. Res.*, **138**(1), 141–150.
7. Biswas, P., Canosa, S., Schoenfeld, J., Schoenfeld, D., Tucker, A., and Madri, J. A. (2003). PECAM-1 promotes beta-catenin accumulation and stimulates endothelial cell proliferation, *Biochem. Biophys. Res. Commun.*, **303**(1), 212–218.
8. Nelson, W. J. and Nusse, R. (2004). Convergence of Wnt, beta-catenin, and cadherin pathways, *Science*, **303**(5663), 1483–1487.
9. Behrens, J., von Kries, J. P., Kuhl, M., Bruhn, L., Wedlich, D., Grosschedl, R., and Birchmeier, W. (1996). Functional interaction of beta-catenin with the transcription factor LEF-1, *Nature*, **382**(6592), 638–642.
10. Soler, C., Grangeasse, C., Baggetto, L. G., and Damour, O. (1999). Dermal fibroblast proliferation is improved by beta-catenin overexpression and inhibited by E-cadherin expression, *FEBS Lett.*, **442**(2–3), 178–182.
11. Cheon, S. S., Cheah, A. Y., Turley, S., Nadesan, P., Poon, R., Clevers, H., and Alman, B. A. (2002). beta-Catenin stabilization dysregulates mesenchymal cell proliferation, motility, and invasiveness and causes aggressive fibromatosis and hyperplastic cutaneous wounds, *Proc. Natl. Acad. Sci. U S A*, **99**(10), 6973–6978.
12. Venkiteswaran, K., Xiao, K., Summers, S., Calkins, C. C., Vincent, P. A., Pumiglia, K., and Kowalczyk, A. P. (2002). Regulation of endothelial barrier function and growth by VE-cadherin, plakoglobin, and beta-catenin, *Am. J. Physiol. Cell Physiol.*, **283**(3), C811–821.
13. Stojadinovic, O., Brem, H., Vouthounis, C., Lee, B., Fallon, J., Stallcup, M., Merchant, A., Galiano, R. D., and Tomic-Canic, M. (2005). Molecular pathogenesis of chronic wounds: the role of beta-catenin and c-myc in the inhibition of epithelialization and wound healing, *Am. J. Pathol.*, **167**(1), 59–69.
14. Newman, P.J. (1999). Switched at birth: a new family for PECAM-1, *J. Clin. Invest.*, **103**(1), 5–9.
15. Albelda, S. M., Muller, W. A., Buck, C. A., and Newman, P. J. (1991). Molecular and cellular properties of PECAM-1 (endoCAM/CD31): a novel vascular cell-cell adhesion molecule, *J. Cell. Biol.*, **114**(5), 1059–1068.
16. Ilan, N., Mahooti, S., Rimm, D. L., and Madri, J. A. (1999). PECAM-1 (CD31) functions as a reservoir for and a modulator of tyrosine-phosphorylated beta-catenin, *J. Cell Sci.*, **112**(18), 3005–3014.
17. Ilan, N., Mohsenin, A., Cheung, L., and Madri, J. A. (2001). PECAM-1 shedding during apoptosis generates a membrane-anchored truncated molecule with unique signaling characteristics, *FASEB J.*, **15**(2), 362–372.
18. Berman, M. E., Xie, Y., and Muller, W. A. (1996). Roles of platelet/endothelial cell adhesion molecule-1 (PECAM-1, CD31) in natural killer cell transendothelial migration and beta 2 integrin activation, *J. Immunol.*, **156**(4), 1515–1524.
19. Cao, G., O’Brien, C. D., Zhou, Z., Sanders, S. M., Greenbaum, J. N., Makrigiannakis, A., and DeLisser, H. M. (2002). Involvement of human PECAM-1 in angiogenesis and *in vitro* endothelial cell migration, *Am. J. Physiol. Cell Physiol.*, **282**(5), C1181–1190.

20. Nakada, M. T., Amin, K., Christofidou-Solomidou, M., O'Brien, C. D., Sun, J., Gurubhagavatula, I., Heavner, G. A., Taylor, A. H., Paddock, C., Sun, Q. H., Zehnder, J. L., Newman, P. J., Albelda, S. M., and DeLisser, H. M. (2000). Antibodies against the first Ig-like domain of human platelet endothelial cell adhesion molecule-1 (PECAM-1) that inhibit PECAM-1-dependent homophilic adhesion block *in vivo* neutrophil recruitment, *J. Immunol.*, **164**(1), 452–462.
21. Thompson, R. D., Noble, K. E., Larbi, K. Y., Dewar, A., Duncan, G. S., Mak, T. W., and Nourshargh, S. (2001). Platelet-endothelial cell adhesion molecule-1 (PECAM-1)-deficient mice demonstrate a transient and cytokine-specific role for PECAM-1 in leukocyte migration through the perivascular basement membrane, *Blood*, **97**(6), 1854–1860.
22. Brown, S., Heinisch, I., Ross, E., Shaw, K., Buckley, C. D., and Savill, J. (2002). Apoptosis disables CD31-mediated cell detachment from phagocytes promoting binding and engulfment, *Nature*, **418**(6894), 200–203.
23. Lampugnani, M. G., Resnati, M., Raiteri, M., Pigott, R., Pisacane, A., Houen, G., Ruco, L. P., and Dejana, E. (1992). A novel endothelial-specific membrane protein is a marker of cell-cell contacts, *J. Cell Biol.*, **118**(6), 1511–1522.
24. DeLisser, H. M., Christofidou-Solomidou, M., Strieter, R. M., Burdick, M. D., Robinson, C. S., Wexler, R. S., Kerr, J. S., Garlanda, C., Merwin, J. R., Madri, J. A., and Albelda, S. M. (1997). Involvement of endothelial PECAM-1/CD31 in angiogenesis, *Am. J. Pathol.*, **151**(3), 671–677.
25. Williams, J. L., Weichert, A., Zakrzewicz, A., Da Silva-Azevedo, L., Pries, A. R., Baum, O., and Egginton, S. (2006). Differential gene and protein expression in abluminal sprouting and intraluminal splitting forms of angiogenesis, *Clin. Sci. (Lond.)*, **110**(5), 587–595.
26. Wang, Y., Su, X., Sorenson, C. M., and Sheibani, N. (2003). Modulation of PECAM-1 expression and alternative splicing during differentiation and activation of hematopoietic cells, *J. Cell Biochem.*, **88**(5), 1012–1024.
27. McCrea, P. D., Turck, C. W., and Gumbiner, B. (1991). A homolog of the armadillo protein in *Drosophila* (plakoglobin) associated with E-cadherin, *Science*, **254**(5036), 1359–1361.
28. Peifer, M., Berg, S., and Reynolds, A. B. (1994). A repeating amino acid motif shared by proteins with diverse cellular roles, *Cell*, **76**(5), 789–791.
29. Sheibani, N., Sorenson, C. M., and Frazier, W. A. (1999). Tissue specific expression of alternatively spliced murine PECAM-1 isoforms, *Dev. Dyn.*, **214**(1), 44–54.
30. Wilmink, J. M., van Weeren, P. R., Stolk, P. W., Van Mil, F. N., and Barneveld, A. (1999). Differences in second-intention wound healing between horses and ponies: histological aspects, *Equine Vet. J.*, **31**(1), 61–67.
31. Theoret, C. L., Barber, S. M., Moyana, T. N., and Gordon, J. R. (2001). Expression of transforming growth factor beta(1), beta(3), and basic fibroblast growth factor in full-thickness skin wounds of equine limbs and thorax, *Vet. Surg.*, **30**(3), 269–277.
32. Schwartz, A. J., Wilson, D. A., Keegan, K. G., Ganjam, V. K., Sun, Y., Weber, K. T., and Zhang, J. (2002). Factors regulating collagen synthesis and degradation during second-intention healing of wounds in the thoracic region and the distal aspect of the forelimb of horses, *Am. J. Vet. Res.*, **63**(11), 1564–1570.
33. Lepault, E., Céleste, C., Doré, M., Martineau, D., and Theoret, C. L. (2005). Comparative study on microvascular occlusion and apoptosis in body and limb wounds in the horse, *Wound Repair Regen.*, **13**, 520–529.
34. Biswas, P., Zhang, J., Schoenfeld, J. D., Schoenfeld, D., Gratzinger, D., Canosa, S., and Madri, J. A. (2005). Identification of the regions of PECAM-1 involved in beta- and gamma-catenin associations. *Biochem. Biophys. Res. Commun.*, **329**(4), 1225–1233.
35. Biswas, P., Canosa, S., Schoenfeld, D., Schoenfeld, J., Li, P., Cheas, L. C., Zhang, J., Cordova, A., Sumpio, B., and Madri, J. A. (2006). PECAM-1 affects GSK-3beta-mediated beta-catenin phosphorylation and degradation, *Am. J. Pathol.*, **169**(1), 314–324.

36. Tsuji, H., Ishida-Yamamoto, A., Takahashi, H., and Iizuka, H. (2001). Nuclear localization of beta-catenin in the hair matrix cells and differentiated keratinocytes, *J. Dermatol. Sci.*, **27**(3), 170–177.
37. Zhu, A. J. and Watt, F. M. (1999). beta-catenin signaling modulates proliferative potential of human epidermal keratinocytes independently of intercellular adhesion, *Development*, **126**(10), 2285–2298.
38. Fathke, C., Wilson, L., Shah, K., Kim, B., Hocking, A., Moon, R., and Isik, F. (2006). Wnt signaling induces epithelial differentiation during cutaneous wound healing, *BMC Cell Biol.*, **7**, 4.
39. Vaporciyan, A. A., DeLisser, H. M., Yan, H. C., Mendiguren, I. I., Thom, S. R., Jones, M. L., Ward, P.A., and Albelda, S. M. (1993). Involvement of platelet-endothelial cell adhesion molecule-1 in neutrophil recruitment *in vivo*, *Science*, **262**(5139), 1580–1582.
40. Galeano, M., Altavilla, D., Cucinotta, D., Russo, G. T., Calo, M., Bitto, A., Marini, H., Marini, R., Adamo, E. B., Seminara, P., Minutoli, L., Torre, V., and Squadrito, F. (2004). Recombinant human erythropoietin stimulates angiogenesis and wound healing in the genetically diabetic mouse, *Diabetes*, **53**(9), 2509–2517.
41. Lévesque, V., Fayad, T., Ndiaye, K., Nahe, Diouf, M., and Lussier, J. G. (2003). Size-selection of cDNA libraries for the cloning of cDNAs after suppression subtractive hybridization, *Biotechniques*, **35**, 72–78.
42. [<http://www.ncbi.nlm.nih.gov/BLAST/>].
43. Bédard, J., Brûlé, S., Price, C. A., Silversides, D. W., and Lussier, J. G. (2003). Serine protease inhibitor-E2 (SERPINE2) is differentially expressed in granulosa cells of dominant follicle in cattle, *Mol. Reprod. Dev.*, **64**, 152–165.
44. Ndiaye, K., Fayad, T., Silversides, D. W., Sirois, J., and Lussier, J. G. (2005). Identification of downregulated messenger RNAs in bovine granulosa cells of dominant follicles following stimulation with human chorionic gonadotropin, *Biol. Reprod.*, **73**, 324–333.
45. [<http://rsb.info.nih.gov/nih-image/>].
46. Bradford, M. M. (1976). A rapid and sensitive method for the quantitation of microgram quantities of protein utilizing the principle of protein-dye binding, *Anal. Biochem.*, **7**, 248–254.
47. Brûlé, S., Faure, R., Dore, M., Silversides, D. W., and Lussier, J. G. (2003). Immunolocalization of vacuolar system-associated protein-60 (VASAP-60), *Histochem Cell Biol.*, **119**, 371–381.

9

- Skandalakis, J. E., Colborn, L., and Skandalakis, L. J. (1997). The embryology of the inguino-femoral area, an overview, *Hernia*, **1**, 45–54.
- Bendavid, R. (2004). The unified theory of hernia formation, *Hernia*, **8**, 171–176.
- Diniz, G., Aktaş, S., Ortaç, R., and Yegane, S. (2004). A comparative histopathological evaluation of sacs from boys and girls with inguinal hernia, *Pathol. Res. Pract.*, **200**, 531–536.
- Jansen, P. L., Mertens, P., Pr., Klinge, U., and Schumpelick, V. (2004). The biology of hernia formation, *Surgery*, **136**, 1–4.
- Hutson, J. M. and Temelco, C. (2005). Could inguinal hernia be treated medically? *Med. Hypotheses*, **64**, 37–40.
- Mikami, H. and Fredeen, H. T. (1979). A genetic study of cryptorchidism and scrotal hernia in pigs, *Can. J. Gene.t Cytol.*, **21**, 9–19.
- Vogt, D. W. and Ellersieck, M. R. (1990). Heritability of susceptibility to scrotal herniation in swine, *Am. J. Vet. Res.*, **51**, 1501–1503.
- Thaller, G., Dempfle, L., and Hoeschele, I. (1996). Maximum likelihood analysis of rare binary traits under different modes of inheritance, *Genetics*, **143**, 1819–1829.
- McCarthy, M. I., Abecasis, G. R., Cardon, L. R., Goldstein, D. B., and Little, J., et al. (2008). Genome-wide association studies for complex traits: consensus, uncertainty and challenges, *Nat. Rev. Genet.*, **9**, 356–369.
- The International HapMap Consortium (2007). A second generation human haplotype map of over 3.1 million SNPs, *Nature*, **449**, 851–861.

11. The ENCODE Project Consortium (2007). Identification and analysis of functional elements in 1% of the human genome by the ENCODE pilot project, *Nature*, **447**, 799–816.
12. García-Closas, M., Malats, N., Real, F. X., Yeager, M., and Welch, R., et al. (2007). Large-scale evaluation of candidate genes identifies associations between VEGF polymorphisms and bladder cancer risk, *PLoS Genet.*, **3**, e29.
13. Puri, V., McQuillin, A., Choudhury, K., Datta, S., and Pimm, J., et al. (2007). Fine mapping by genetic association implicates the chromosome 1q23.3 gene UHMK1, encoding a serine/threonine protein kinase, as a novel schizophrenia susceptibility gene, *Biol. Psychiatry*, **61**, 873–879.
14. Dick, D. M., Aliev, F., Wang, J. C., Saccone, S., and Hinrichs, A., et al. (2008). A Systematic single nucleotide polymorphism screen to fine-map alcohol dependence genes on chromosome 7 identifies association with a novel susceptibility gene ACN9, *Biol. Psychiatry*, **63**, 1047–1053.
15. Morrison, A. C., Boerwinkle, E., Turner, S. T., and Ferrell, R. E. (2008). Regional association-based fine-mapping for sodium-lithium countertransport on chromosome 10, *Am. J. Hypertens.*, **21**, 117–121.
16. Verma, R., Holmans, P., Knowles, J. A., Grover, D., and Evgrafov, O. V., et al. (2008). Linkage Disequilibrium Mapping of a Chromosome 15q25-26 Major Depression Linkage Region and Sequencing of NTRK3, *Biol. Psychiatry*, **63**, 1185–1189.
17. Chen, Y., Zhu, J., Lum, P.Y., Yang, X., and Pinto, S., et al. (2008). Variations in DNA elucidate molecular networks that cause disease, *Nature*, **452**, 429–435.
18. Du, F., Mathialagan, N., Dyer, C. J., Grosz, M. D., and Messer, L. A., et al. (2004). Discovery and mapping of a QTL affecting scrotal hernia incidence on chromosome 2 in domestic pigs, *29th International Conference on Animal Genetics*, ISAG, Tokyo, 123.
19. Du, F. X., Mathialagan, N., Dyer, C. J., Grosz, M. D., and Messer, L. A., et al. (2004). Mapping genes affecting scrotal hernia condition in domestic pigs. *J. Anim. Sci.* Vol. **82**, Suppl. 1/*J Dairy Sci.* **87**, Suppl. 1/*Poult Sci.* **83**, 453.
20. Grindflek, E., Moe, M., Taubert, H., Simianer, H., and Lien, S., et al. (2006). Genome-wide linkage analysis of inguinal hernia in pigs using affected sib pairs, *BMC Genet.*, **3**, 25.
21. Chanock, S. J., Manolio, T., Boehnke, M., Boerwinkle, E., and Hunter, D. J., et al. (2007). Replicating genotype-phenotype associations, *Nature*, **447**, 655–660.
22. Zondervan, K. T. and Cardon, L. R. (2007). Designing candidate gene and genome-wide case-control association studies, *Nat. Protoc.*, **2**, 2492–2501.
23. Du, F. X., Clutter, A. C. and Lohuis, M. M. (2007). Characterizing linkage disequilibrium in pig populations, *Int J. Biol. Sci.*, **3**, 166–178.
24. Bellon, J. M., Bajo, A., Ga-Honduvilla, N., Gimeno, M. J., and Pascual, G., et al. (2001). Fibroblasts from the transversalis fascia of young patients with direct inguinal hernias show constitutive MMP-2 overexpression, *Ann. Surg.*, **233**, 287–291.
25. Klinge, U., Binnebosel, M., and Mertens, P. R. (2006). Are collagens the culprits in the development of incisional and inguinal hernia disease? *Hernia*, **10**, 472–477.
26. Lynen Jansen, P., Rosch, R., Rezvani, M., Mertens, P. R., and Junge, K., et al. (2006). Hernia fibroblasts lack beta-estradiol-induced alterations of collagen gene expression, *BMC Cell Biol.*, **29**, 36.
27. Szczesny, W., Cerkaska, K., Tretyn, A., Dabrowiecki, S. (2006). Etiology of inguinal hernia: ultrastructure of rectus sheath revisited, *Hernia*, **10**, 266–271.
28. Tanyel, F. C., Muftuoglu, S., Dagdeviren, A., Kaymaz, F. F., and Buyukpamukcu, N. (2001). Myofibroblasts defined by electron microscopy suggest the dedifferentiation of smooth muscle within the sac walls associated with congenital inguinal hernia, *BJU Int.*, **87**, 251–255.
29. Ulusu, N. N., Tandogan, B., and Tanyel, F. C. (2007). Sarco(end)plasmic reticulum and plasmalemmal Ca(2+)-ATPase activities in cremaster muscles and sacs differ according to the associated inguinal pathology, *Cell Biochem. Funct.*, **25**, 515–519.

30. Tanyel, F. C., Ulusu, N. N., Tezcan, E. F., and Buyukpamukcu, N. (2003). Total calcium content of sacs associated with inguinal hernia, hydrocele or undescended testis reflects differences dictated by programmed cell death, *Urol. Int.*, **70**, 211–215.
31. Tiranti, I. N., Genghini, R. N., Gonzalez Quintana, H., and Wittouck, P. (2002). Morphological and karyotypic characterization of intersex pigs with hernia inguinalis, *J. Agric. Sci.*, **138**, 333–340.
32. Koskimies, P., Suvanto, M., Nokkala, E., Huhtaniemi, I. T., and McLuskey, A., et al. (2003). Female mice carrying a ubiquitin promoter-Insl3 transgene have descended ovaries and inguinal hernias but normal fertility, *Mol. Cell. Endocrinol.*, **206**, 159–166.
33. Tanyel, F. C., Yüzbaşıoğlu, A., Kocaefe, C., Orhan, D., and Özgüç, M. (2006). Androgen receptor immunostaining and androgen receptor messenger ribonucleic acid expression are increased in cremaster muscles associated with undescended testis, *Urology*, **67**, 855–858.
34. Tez, M. and Kilic, Y. A. (2006). Stem cell origin theory of the inguinal hernia, *Med. Hypotheses.*, **66**, 1042–1043.
35. Bernardini, L., Castori, M., Capalbo, A., Mokini, V., and Mingarelli, R., et al. (2007). Syndromic craniosynostosis due to complex chromosome 5 rearrangement and MSX2 gene triplication, *Am J. Med. Genet. A*, **143A**, 2937–2943.
36. Hart, E. A., Caccamo, M., Harrow, J. L., Humphray, S. J., and Gilbert, J. G., et al. (2007). Lessons learned from the initial sequencing of the pig genome: comparative analysis of an 8 Mb region of pig chromosome 17, *Genome Biol.*, **8**, R168.
37. Zhu, X., Tang, H., and Risch, N. (2008). Admixture mapping and the role of population structure for localizing disease genes, *Adv. Genet.*, **60**, 547–569.
38. Luboshits, G. and Benayahu, D. (2007). MS-KIF18A, a kinesin, is associated with estrogen receptor, *J. Cell Biochem.*, **100**, 693–702.
39. Stumpff, J., von Dassow, G., Wagenbach, M., Asbury, C., and Wordeman, L. (2008). The kinesin-8 motor Kif18A suppresses kinetochore movements to control mitotic chromosome alignment, *Dev. Cell.*, **14**, 252–262.
40. Yasuhara, F., Gomes, G. R., Siu, E. R., Suenaga, C. I., and Maróstica, E., et al. (2008). Effects of the Antiestrogen Fulvestrant (ICI 182,780) on Gene Expression of the Rat Efferent Ductules, *Biol. Reprod.*, **79**, 432–441.
41. Zhao, X., Du, Z. Q., Vukasinovic, N., Rodriguez, F., and Clutter, A. C., et al. (2008). Biological Candidate Gene Analyses Identify that HOXA10 and MMP2 are Associated with Scrotal Hernias in Pigs, *Am J. Vet. Res.* (in press).
42. Koch, M., Veit, G., Stricker, S., Bhatt, P., and Kutsch, S., et al. (2006). Expression of type XXIII collagen mRNA and protein, *J. Biol. Chem.*, **281**, 21546–21557.
43. Banyard, J., Bao, L., Hofer, M. D., Zurakowski, D., and Spivey, K. A., et al. (2007). Collagen XXIII expression is associated with prostate cancer recurrence and distant metastases, *Clin. Cancer Res.*, **13**, 2634–2642.
44. Donnison, M., Beaton, A., Davey, H. W., Broadhurst, R., and L’Huillier, P., et al. (2005). Loss of the extraembryonic ectoderm in Elf5 mutants leads to defects in embryonic patterning, *Development*, **132**, 2299–2308.
45. Zhou, J., Chehab, R., Tkalcevic, J., Naylor, M. J., and Harris, J., et al. (2005). Elf5 is essential for early embryogenesis and mammary gland development during pregnancy and lactation, *EMBO J.*, **24**, 635–644.
46. Oakes, S. R., Naylor, M. J., Asselin-Labat, M. L., Blazek, K. D., and Gardiner-Garden, M., et al. (2008). The Ets transcription factor Elf5 specifies mammary alveolar cell fate, *Genes Dev.*, **22**, 581–586.
47. Metzger, D. E., Stahlman, M. T., and Shannon, J. M. (2008). Misexpression of ELF5 disrupts lung branching and inhibits epithelial differentiation, *Dev. Biol.*, **320**, 149–160.
48. Laird, N. M., Horvath, S., and Xu, X. (2000). Implementing a unified approach to family based tests of association, *Genetic Epi.*, **19**, S36–S42.

49. Barrett, J. C., Fry, B., Maller, J., and Daly, M. J. (2005). Haploview: analysis and visualization of LD and haplotype maps, *Bioinformatics*, **21**, 263–265.
 50. Purcell, S., Neale, B., Todd-Brown, K., Thomas L., and Ferreira, M. A., et al. (2007). PLINK: a tool set for whole-genome association and population-based linkage analyses, *Am. J. Hum. Genet.*, **81**, 559–575.
 51. Benjamini, Y. and Hochberg, Y. (1995). Controlling the False Discovery Rate: A Practical and Powerful Approach to Multiple Testing, *Journal of the Royal Statistical Society*, **57**, 289–300.
- ## 10
1. Silanikove, N. (2000). Effects of heat stress on the welfare of extensively managed domestic ruminants, *Livest Prod Sci.*, **67**, 1–18.
 2. Kadzere, C. T., Murphy, M. R., Silanikove, N., and Maltz, E. (2002). Heat stress in lactating dairy cows: a review, *Livest Prod Sci.*, **77**, 59–91.
 3. MacFarlane, W. V. and Howard, B. (1972). Comparative water and energy economy of wild and domestic mammals, *Proc Symp Zool Soc., London*, **31**, 261–296.
 4. Barash, H., Silanikove, N., Shamay, A., and Ezra, E. (2001). Interrelationships among ambient temperature, day length, and milk yield in dairy cows under a Mediterranean climate, *J. Dairy Sci.*, **84**, 2314–2320.
 5. Maltz, E., Kroll, O., Barash, H., Shamy, A., and Silanikove, N. (2000). Lactation and body weight of dairy cows, interrelationships among heat stress, calving season and milk yield, *J. Anim Feed Sci.*, **9**, 33–45.
 6. Collier, R. J., Dahl, G. E., and VanBaale, M. J. (2006). Major advances associated with environmental effects on dairy cattle, *J. Dairy Sci.*, **89**, 1244–1253.
 7. Horowitz, M. (2001). Heat acclimation: Phenotypic plasticity and cues to the underlying molecular mechanisms, *J. Thermal Biol.*, **26**, 357–363.
 8. Collier, R. J., Collier, J. L., Rhoads, R. P., and Baumgard, L. H. (2008). Invited Review: Genes involved in the bovine heat stress response. *J. Dairy Sci.*, **91**, 445–454.
 9. Rhoads, R. P., Sampson, J. D., Lucy, M. C., Spain, J. N., Spiers, D. E., Tempelman, R. J., and Coussens, P. M. (2005). Hepatic gene expression profiling during adaptation to a period of chronic heat stress in lactating dairy cows, *FASEB J.*, **19**, A1673.
 10. Silanikove, N. (1994). The struggle to maintain hydration and osmoregulation in animals experiencing severe dehydration and rapid rehydration, the story of ruminants, *Exp. Physiol.*, **79**(3), 281–300.
 11. Silanikove, N. and Tadmor, A. (1989). Rumen volume, saliva flow rate, and systemic fluid homeostasis in dehydrated cattle, *Am J. Physiol.*, **256**(4 Pt 2), R809–815.
 12. Maltz, E. and Silanikove, N. (1996). Kidney function and nitrogen balance of high yielding dairy cows at the onset of lactation, *J. Dairy Sci.*, **79**, 1621–1626.
 13. Maltz, E., Silanikove, N., Shalit, U., and Berman, A. (1994). Diurnal fluctuations in plasma ions and water intake of dairy cows as affected by lactation in warm weather, *J. Dairy Sci.*, **77**, 2630–2639.
 14. Daly, S. E. J., Owens, R. A., and Hartmann, P. E. (1993). The short-term synthesis and infant-regulated removal of milk in lactating women. *Exp Physiol.*, **78**:209–220.
 15. Wilde, C. J. and Peaker, M. (1990). Auto-crine control in milk secretion, *J Agric Sci, Camb.*, **114**, 235–238.
 16. Shennan, D. B. and McNeillie, S. A. (1994). Milk accumulation down-regulates amino-acid-uptake via system-A and system-L by lactating mammary tissue, *Hormone Metabol Res.*, **26**, 611.
 17. Li, M., Liu, X., Robinson, G., Bar-Peled, U., Wagner, K-U., Young, W. S., Hennighausen, L., and Furth, P. A. (1997). Mammary-derived signals activate programmed cell death during the first stage of mammary gland involution, *Proc National Acad Sci. USA*, **94**, 3425–3430.
 18. Quarrie, L. H., Addey, C. V. P., Wilde, C. J. (1998). Programmed cell death during mammary tissue involution induced by weaning, litter removal, and milk stasis, *J. Cell Physiol.*, **168**, 559–569.
 19. Silanikove, N., Shamay, A., Shinder, D., and Moran, A. (2000). Stress down-regulates milk yield in cows by plasmin induced

- beta-casein product that blocks K⁺ channels on the apical membranes. *Life Sci.*, **67**, 2201–2212.
20. Silanikove, N., Merin, U., and Leitner, G. (2006). Physiological role of indigenous milk enzymes: An overview of an evolving picture, *Intl Dairy J.*, **16**, 535–545.
 21. Shamay, A., Shapiro, F., Mabweesh, S. J., and Silanikove N. (2002). Casein-derived phosphopeptides disrupt tight junction integrity, and precipitously dry up milk secretion in goats, *Life Sci.*, **70**, 2707–2719.
 22. Shamay, A., Shapiro, F., Leitner, G., and Silanikove, N. (2003). Infusions of casein hydrolyzates into the mammary gland disrupt tight junction integrity and induce involution in cows, *J Dairy Sci.*, **86**, 1250–1258.
 23. Silanikove, N., Shapiro, F., Shamay, A., and Leitner, G. (2005). Role of xanthine oxidase, lactoperoxidase, and NO in the innate immune system of mammary secretion during active involution in dairy cows: manipulation with casein hydrolyzates, *Free Radic. Biol. Med.*, **38**, 1139–115.
 24. Leitner, G., Shamay, J., Maltz, E., and Silanikove, N. (2007). Casein hydrolyzate intramammary treatment improves the comfort behavior of cows induced into dry-of, *Livest Sci.* **110**, 292–297.
 25. Silanikove, N., Iscovich, J., and Leitner, G. (2005). Therapeutic treatment with casein hydrolyzate eradicate effectively bacterial infection in treated mammary quarters in cows, In *Mastitis in Dairy Production – Current Knowledge and Future Solutions*. H. Hogeveen (Eds.), Wageningen academic publishers, 327–332.
 26. Silanikove, N., Shamay, Y., and Leitner, G. (2008). Intra-mammary single infusion of casein hydrolyzate in dairy cows as alternative dry period treatment: Curing bacterial infection and increasing milk yield in the subsequent lactations, *Nature Precedings*.
 27. Shamay, A., Shapiro, F., Barash, H., Bruckental, I., and Silanikove, N. (2000). Effect of dexamethasone on milk yield and composition in dairy cows, *Annals Zootechniques*, **49**, 343–352.
 28. Flamenbaum, I., Wolfenson, D., Mamen, M., and Berman, A. (1986). Cooling dairy cattle by a combination of sprinkling and forced ventilation and its implementation in the shelter system, *J. Dairy Sci.*, **69**, 3140–3147.
 29. Shalit, U., Maltz, E., Silanikove, N., and Berman, A. (1991). Water, sodium, potassium, and chlorine metabolism of dairy cows at the onset of lactation in hot weather, *J. Dairy Sci.*, **74**, 1874–1883.
 30. Silanikove, N. and Shapiro, F. (2007). Distribution of xanthine oxidase and xanthine dehydrogenase activity in bovine milk: Physiological and technological implications, *Intl. Dairy J.*, **17**, 1188–1194.
 31. Shennan, D. B. (1992). K⁺ and Cl⁻ transport by mammary secretory-cell apical membrane-vesicles isolated from milk, *J Dairy Res.*, **59**, 339–348.
 32. Reynolds, E. C., Riley, P. F., and Adamson, N. J. (1994). A selective precipitation purification procedure for multiple phosphoserine-containing peptides and methods for their identification, *Anal. Biochem.*, **217**, 277–284.
 33. vanTol, B. L., Missan, S., Crack, J., Moser, S., Baldrige, W. H., Linsdell, P., and Cowley, E. A. (2007). Contribution of KCNQ1 to the regulatory volume decrease in the human mammary epithelial cell line MCF-7, *Am J Physiol:Cell Physiol.*, **293**, C1010–1019.
 34. Lund, L. R., Bjorn, S. F., Sternlicht, M. D., Nielsen, B. S., Solberg, H., Usher, P. A., Osterby, R., Christensen, I. J., Stephens, R. W., Bugge, T. H., Dano, K., and Werb, Z. (2000). Lactational competence and involution of the mouse mammary gland require plasminogen, *Development*, **127**(20), 4481–4492.
 35. Buffington, D. E., Collier, R., and Canton, G. H. (1983). Shade management systems to reduce heat stress for dairy cows in hot, humid climates, *Transactions Am. Soc. Agric. Eng. (ASAE)*, **26**, 1798–1802.
 36. Yamamoto, S., Young, B. A., Purwanto, B., Nakamasu, F., and Natsumoto, T. (1984). Effect of solar radiation on the heat load of dairy heifers, *Australian J. Agric. Res.*, **45**, 1741–1749.
 37. Moran, D. S., Shitzer, A., and Pandolf, K. B. (1998). A physiological strain index to

- evaluate heat stress, *Am. J. Physiol.*, **275**(1 Pt 2), R129–R134.
38. Igono, M. O., Bjotvedt, G., and Sanford-crane, H. T. (1992). Environmental profile and critical-temperature effects on milk-production of Holstein cows in desert climate, *Intl. J. Biometeorol.*, **36**, 77–87.
 39. Stelwagen, K., van Espen, D. C., Verkerk, G. A., McFadden, H. A., and Farr, V. C. (1998). Elevated plasma cortisol reduces permeability of mammary tight junctions in the lactating bovine mammary epithelium, *J. Endocrinol.*, **159**, 173–178.
 40. Boe, K. E. and Faerevik, G. (2003). Grouping and social preferences in calves, heifers and cows. *App. Anim. Behav. Sci.*, **80**175–190.
 41. Rucker, M., Schafer, T., Scheuer, C., Harder, Y., Vollmar, B., and Menger, M. D. (2006). Local heat shock priming promotes recanalization of thromboembolized microvasculature by upregulation of plasminogen activators, *Arteriosclerosis it Thrombosis Vascular. Biol.*, **26**, 1632–1639.
 42. Crane, A. and Aguilar-Bryan, L. (2004). Assembly, maturation and turnover of KATP channel subunits. *J. Biol. Chem.*, **279**, 9080–9090.
- ## 11
1. Wagner, H. (1986). Flight performance and visual control of flight of the free-flying housefly (*Musca domestica* L) 3. Interactions between angular movement induced by widefield and smallfield stimuli, *Philos T R Soc B.*, **312**, 581–595.
 2. Wehrhahn, C. (1979). Sex-specific differences in the chasing behavior of houseflies (*Musca*), *Biol Cybern.*, **32**, 239–241.
 3. Land, M. F. (1997). Visual acuity in insects, *Annu Rev Entomol*, **42**, 147–177.
 4. Collett, T. S. and King, A. J. (1975). Vision during flight, G. A. Horridge (Ed.), *The compound eye and vision of insects*, Clarendon Press, Oxford, 437–466.
 5. Gilbert .C. and Strausfeld, N. J. (1991). The functional organization of male-specific visual neurons in flies, *J. Comp. Physiol A.*, **169**, 395–411.
 6. O'Carroll, D. (1993). Feature-detecting neurons in dragonflies, *Nature*, **362**, 541–543.
 7. Wachenfeld, A. (1994). Elektrophysiologische untersuchungen und funktionelle charakterisierung männchenspezifischer visueller interneurone de schmeißfliege *Calliphore erythrocephala* [PhD Thesis], Köln, Universität zu Köln.
 8. Nordström, K. and O'Carroll, D. C. (2006). Small object detection neurons in female hoverflies, *P Roy Soc. B-Biol Sci.*, **273**, 1211–1216.
 9. Nordström, K., Barnett, P. D., and O'Carroll, D. C. (2006). Insect detection of small targets moving in visual clutter, *PLOS Biol.*, **4**, 378–386.
 10. Barnett, P. D., Nordström, K., O'Carroll, D. C. (2007). Retinotopic organization of small-field-target-detecting neurons in the insect visual system, *Curr. Biol.*, **17**, 569–578.
 11. Egelhaaf, M. (1985). On the neuronal basis of figure-ground discrimination by relative motion in the visual-system of the fly. 3. Possible input circuitries and behavioral significance of the FD-cells, *Biol. Cybern.*, **52**, 267–280.
 12. Higgins, C. M. and Pant, V. (2004). An elaborated model of fly small-target tracking, *Biol. Cybern.*, **91**, 417–428.
 13. Rowell, C. H., O'Shea M., Williams, J. L. (1977). The neuronal basis of a sensory analyser, the acridid movement detector system 4. The preference for small field stimuli, *J. Exp. Biol.*, **68**, s157–185.
 14. O'Carroll, D. C., Osorio, D., James, A. C., and Bush, T. (1992). Local feedback mediated via amacrine cells in the insect optic lobe, *J. Comp. Physiol. A.*, **171**, 447–455.
 15. Arnett, D. W. (1971). Receptive field organization of units in the first optic ganglion of Diptera, *Science*, **173**, 929–931.
 16. Arnett, D. W. (1972). Spatial and temporal integration properties of units in first optic ganglion of dipterans, *J. Neurophysiol.*, **35**, 429–444.
 17. Jansonius, N. M. and Van Hateren, J. H. (1991). Fast temporal adaptation of On-Off units in the 1st optic chiasm of the blowfly, *J. Comp. Physiol. A.*, **168**, 631–637.

18. Osorio, D. (1991). Mechanisms of early visual processing in the medulla of the locust optic lobe - How self-inhibition, spatial-pooling, and signal rectification contribute to the properties of transient cells, *Visual Neurosci*, **7**, 345–355.
19. Osorio, D. (1987). The temporal properties of nonlinear, transient cells in the locust medulla, *J. Comp. Physiol. A.*, **161**, 431–440.
20. Srinivasan, M. V., Laughlin, S. B., and Dubs, A. (1982). Predictive coding - a fresh view of inhibition in the retina, *P Roy Soc. B-Biol. Sci.*, **216**, 427–459.
21. Jansonius, N. M. and Van Hateren, J. H. (1993). On-Off units in the 1st optic chiasm of the blowfly 2 Spatial properties, *J. Comp. Physiol. A.*, **172**, 467–471.
22. Brinkworth, R. S. A. and O'Carroll, D. C. (2007). Biomimetic motion detection, *Proc. ISSNIP.*, 137–142.
23. Srinivasan, M. V. and Guy, R. G. (1990). Spectral properties of movement perception in the dronefly *Eristalis*, *J. Comp. Physiol. A.*, **166**, 287–295.
24. Tolhurst, D. J., Tadmor, Y., and Chao, T. (1992). Amplitude spectra of natural images, *Ophthalm. Physiol. Opt.*, **12**, 229–232.
25. Bex, P. J. and Makous, W. (2002). Spatial frequency, phase, and the contrast of natural images, *J. Opt. Soc. Am A.*, **19**, 1096–1106.
26. Stavenga, D. G. (2003). Angular and spectral sensitivity of fly photoreceptors I Integrated facet lens and rhabdomere optics, *J. Comp. Physiol. A.*, **189**, 1–17.
27. Straw, A. D., Warrant, E. J., and O'Carroll, D. C. (2006). A 'bright zone' in male hoverfly (*Eristalis tenax*) eyes and associated faster motion detection and increased contrast sensitivity, *J. Exp. Biol.*, **209**, 4339–4354.
28. Laughlin, S. (1981). A simple coding procedure enhances a neuron's information capacity, *Z Naturforsch C.*, **36**, 910–912.
29. van Hateren, J. H. and Snippe, H. P. (2001). Information theoretical evaluation of parametric models of gain control in blowfly photoreceptor cells. *Vision. Res.*, **41**, 1851–1865.
30. Shoemaker, P. A., O'Carroll, D. C., Straw, A. D. (2005). Velocity constancy and models for wide-field visual motion detection in insects, *Biol. Cybern.*, **93**, 275–287.
31. Laughlin, S. B. and Weckstrom, M. (1993). Fast and slow photoreceptors - a comparative study of the functional diversity of coding and conductances in the Diptera, *J. Comp. Physiol. A.*, **172**, 593–609.
32. Coombe, P. E., Srinivasan, M. V., Guy, R. G. (1989). Are the Large Monopolar Cells of the insect lamina on the optomotor pathway, *J Comp Physiol A.*, **166**, 23–35.
33. Douglass, J. K. and Strausfeld, N. J. (2003). Anatomical organization of retinotopic motion-sensitive pathways in the optic lobes of flies, *Microsc. Res. Techniq.*, **62**, 132–150.
34. Keller, A. (2002). *Genetic intervention in sensory systems of a fly [PhD Thesis]*, Bayerischen Julius-Maximilians-Universität, Würzburg.
35. van Hateren, J. H. (1992). Theoretical predictions of spatiotemporal receptive-fields of fly LMCs, and experimental validation, *J. Comp. Physiol. A.*, **171**, 157–170.
36. Zheng, L., de Polavieja, G. G., Wolfram, V., Asyali, M. H., and Hardie, R. C., et al. (2005). Feedback network controls photoreceptor output at the layer of first visual synapses in *Drosophila*. *J. Gen. Physiol.* **127**, 495–510.
37. Srinivasan, M. V., Pinter, R. B., and Osorio, D. (1990). Matched filtering in the visual system of the fly - Large Monopolar Cells of the lamina are optimized to detect moving edges and blobs, *P Roy. Soc. B-Biol. Sci.*, **240**, 279–293.
38. James, A. C. (1990). *White-noise studies in the fly lamina [PhD Thesis]*, Australian National University, Canberra.
39. Juusola, M., Uusitalo, R. O., Weckstrom, M. (1995). Transfer of graded potentials at the photoreceptor interneuron synapse, *J. Gen. Physiol.*, **105**, 117–148.
40. Järvilehto, M. and Zettler, F. (1970). Microlocalisation of lamina-located visual cell activities in the compound eye of the blowfly *Calliphora*, *J. Comp. Physiol. A.*, **69**, 134–138.
41. Hassenstein, B. and Reichardt, W. (1956). Systemtheoretische analyse der zeitreihenfolgen und vorzeichenbewertung bei der bewegungsperzeption des rüsselkafers *Chlorophanus*, *Z. Naturforsch.*, 513–524.

42. Rind, F. C. and Bramwell, D. I. (1996). Neural network based on the input organization of an identified neuron signaling impending collision, *J. Neurophysiol.*, **75**, 967–985.
43. Rind, F. C. and Simmons, P. J. (1992). Orthopteran DCMD neuron: a reevaluation of responses to moving objects. I. Selective responses to approaching objects, *J. Neurophysiol.*, **68**, 1654–1666.
44. Brinkworth, R. S. A., Mah, E. L., and O'Carroll, D. C. (2006). Bioinspired pixel-wise adaptive imaging, *Proc SPIE*, **3**, 641411–641418.

12

1. Gillott, C. (2003). Male accessory gland secretions: modulators of female reproductive physiology and behavior, *Annu. Rev. Entomol.*, **48**, 163–184.
2. Tarpy, D. R. and Nielsen, D. I. (2002). Sampling error, effective paternity and estimating the genetic structure of honey bee colonies (Hymenoptera: Apidae), *Ann. Entomol. Soc. Am.*, **95**, 513–528.
3. Oldroyd, B. P., Clifton, M. J., Parker, K., Wongsiri, S., and Rinderer, T. E., et al. (1998). Evolution of mating behavior in the genus *Apis* and an estimate of mating frequency in *A. cerana* (Hymenoptera: Apidae), *Ann. Entomol. Soc. Am.*, **91**, 700–709.
4. Oldroyd, B. P., Clifton, M. J., Wongsiri, S., Rinderer, T., and Sylvester, H. A., et al. (1997). Polyandry in the genus *Apis*, particularly *Apis andreniformis*, *Behav. Ecol. Sociobiol.*, **40**, 17–26.
5. Tarpy, D. R. and Seeley, T. D. (2006). Lower disease infections in honeybee (*Apis mellifera*) colonies headed by polyandrous vs monandrous queens, **93**, 195–199.
6. Crozier, R. H. and Pamilo, P. (1996). *Evolution of social insect colonies*, R. M. May and P. H. Harvey (Eds.), Oxford University Press, Oxford.
7. Tarpy, D. R. and Page, R. E. (2000). No behavioral control over mating frequency in queen honey bees (*Apis mellifera* L.): implications for the evolution of extreme polyandry, *Am. Nat.* **155**, 820–827.
8. Schlüns, H., Moritz, R. F. A., Neumann, P., Kryger, P., and Koeniger, G. (2005). Multiple nuptial flights, sperm transfer and the evolution of extreme polyandry in honeybee queens, *Anim. Behav.*, **70**, 125–131.
9. Tanaka, E. D. and Hartfelder, K. (2004). The initial stages of oogenesis and their relation to differential fertility in the honey bee (*Apis mellifera*) castes. *Arth. Struct. Dev.*, **33**, 431–442.
10. Winston, M. L. (1987). *The Biology of the Honey Bee*, Harvard University Press, Cambridge.
11. Harano, K., Sasaki, K., and Nagao, T. (2005). Depression of brain dopamine and its metabolite after mating in European honeybee (*Apis mellifera*) queens, *Naturwissenschaften*, **92**, 310–313.
12. Fahrenbach, S. E., Giray, T., and Robinson, G. E. (1995). Volume changes in the mushroom bodies of adult honey bee queens. *Neur. Learn. Mem.*, **63**, 181–191.
13. Slessor, K. N., Kaminski, L. A., King, G. G. S., and Winston, M. L. (1990). Semiochemicals of the honeybee queen mandibular glands, *J. Chem. Ecol.*, **16**, 851–860.
14. Plettner, E., Otis, G. W., Wimalaratne, P. D. C., Winston, M. L., and Slessor, K. N., et al. (1997). Species- and caste-determined mandibular gland signals in honeybees (*Apis*), *J. Chem. Ecol.*, **23**, 363–377.
15. Blum, M. S. (1992). *The hive and the honey bee*, J. M. Graham (Ed.), Dadant and Sons, Hamilton.
16. Free, J. B. (1987). *Pheromones of social bees*, Chapman and Hall (Eds.), University Press, London.
17. Keeling, C., Slessor, K. N., Higo, H. A., and Winston, M. L. (2003). New components of the honey bee (*Apis mellifera* L.) queen retinue pheromone. *Proc. Natl. Acad. Sci. U S A*, **100**, 4486–4491.
18. Slessor, K. N., Kaminski, L. A., King, G. G. S., Borden, J. H., and Winston, M. L. (1988). The semiochemical basis of the retinue response to queen honey bees, *Nature*, **332**, 354–356.
19. Pankiw, T., Winston, M., and Slessor, K. N. (1994). Variation in worker response to honey bee (*Apis mellifera* L.) queen mandibular pheromone (Hymenoptera: Apidae), *J. Ins. Behav.*, **7**, 1–15.

20. Pankiw, T., Winston, M., and Slessor, K. N. (1995). Queen attendance behaviour of worker honey bees (*Apis mellifera* L.) that are high and low responding to queen mandibular pheromone, *Insects Soc.*, **42**, 371–378.
21. Kaminski, L. A., Slessor, K. N., Winston, M. L., Hay, N. W., and Borden, J. H. (1990). Honeybee response to queen mandibular pheromone in laboratory bioassays, *J. Chem. Ecol.*, **16**, 841–850.
22. Butler, C. G., and Fairey, E. M. (1963). The role of the queen in preventing oogenesis in worker honey bees, *J. Apic. Res.*, **2**, 14–18.
23. Hoover, S. E. R., Keeling, C. I., Winston, M. L., and Slessor, K. N. (2003). The effect of queen pheromones on worker honey bee ovary development, *Naturwissenschaften*, **90**, 477–480.
24. Melathopoulos, A. P., Winston, M., Pettis, J. S., and Pankiw, T. (1996). Effect of queen mandibular pheromone on initiation and maintenance of queen cells in the honey bee (*Apis mellifera* L.), *Can. Entomol.*, **128**, 263–272.
25. Pettis, J. S., Winston, M., and Collins, A. M. (1995). Suppression of queen rearing in European and Africanized honey bees *Apis mellifera* L. by synthetic queen mandibular gland pheromone, *Insectes. Soc.*, **42**, 113–121.
26. Higo, H. A., Colley, S. J., Winston, M. L., and Slessor, K. N. (1992). Effects of honey bee (*Apis mellifera* L.) queen mandibular gland pheromone on foraging and brood rearing, *Can. Entomol.*, **124**, 409–418.
27. Pankiw, T., Huang, Z. Y., Winston, M. L., and Robinson, G. E. (1998). Queen mandibular gland pheromone influences worker honey bee (*Apis mellifera* L.) foraging ontogeny and juvenile hormone titers, *J. Ins. Physiol.*, **44**, 685–692.
28. Pettis, J. S., Winston, M., and Slessor, K. N. (1995). Behavior of queen and worker honey bees (Hymenoptera, Apidae) in response to exogenous queen mandibular gland pheromone, *Ann. Entomol. Soc. Amer.*, **88**, 580–588.
29. Gary, N. E. (1962). Chemical mating attractants in the queen honey bee, *Science*, **136**, 773–774.
30. Brockmann, A., Dietz, D., Spaethe, J., and Tautz, J. (2006). Beyond 9-ODA: sex pheromone communication in the european honey bee *Apis mellifera* L., *J. Chem. Ecol.*, **32**, 657–667.
31. Apsegaite, V. and Skirkevicus, A. (1999). Content of (E)-9-oxo-2-decenoic acid in pheromones of honeybee (*Apis mellifera* L.) queens, *Pheromones*, **9**, 27–32.
32. Laidlaw, H. H. J. (1977). *Instrumental insemination of honey bee queens: its origin and development*, IL: Dandant, Hamilton.
33. Woyke, J., Jasinski, A., and Fliszkiewicz, (1995). Further investigations on natural mating of instrumentally inseminated *Apis mellifera* queens. *J. Apic. Res.*, **32**, 105–106.
34. Ben-Shahar, Y. (2005). The foraging gene, behavioral plasticity, and honeybee division of labor, *J. Comp. Physiol. A*, **191**, 987–994.
35. Ben-Shahar, Y., Robichon, A., Sokolowski, M. B., and Robinson, G. E. (2002). Behavior influenced by gene actio across different time scales, *Science*, **296**, 742–744.
36. Ben-Shahar, Y., Leung, H. T., Pak, W. L., Sokolowski, M. B., and Robinson, G. E. (2003). cGMP-dependent changes in phototaxis: a possible role for the foraging gene in honey bee division of labor, *J. Exp. Biol.*, **14**, 2507–2515.
37. Woyke, J. (1966). Which is the most suitable volume of semen in artificial insemination of queen honey bees. *USDA Bee Cult. Lab. Warsaw*, 12–15.
38. Woyke, J. (1983). Dynamics of entry of spermatozoa into the spermatheca of instrumentally inseminated queen honeybees, *J. Apic. Res.*, **22**, 150–154.
39. Dade, H. A. (1978). *Anatomy and dissection of the honeybee*, International Bee Research Association, London.
40. Tomanek, B., Jasinski, A., Sulek, Z., Muszynska, J., and Kulinowski, Pea. (1996). Magnetic resonance microscopy of internal structure of drone and queen honey bees, *J. Apic. Res.*, **35**, 3–9.
41. Nijhout, H. F. (1984). Abdominal stretch reception in *Dipetalogaster-Maximus* (Hemiptera, Reduviidae). *J. Ins. Physiol.*, **30**, 629–633.

42. Ringo, J. (1996). Sexual receptivity in insects, *Annu. Rev. Entomol.*, **41**, 473–494.
43. Roth, L. M. (1962). Hypersexual activity induced in females of the cockroach *Nauphoeta cinerea*, *Science*, **138**, 1267–1269.
44. Kaftanoglu, O. and Peng, Y. S. (1982). Effects of insemination on the initiation of oviposition in the queen honey bee, *J. Apic. Res.*, **21**, 3–6.
45. Chapman, T. and Davies, S. J. (2004). Functions and analysis of the seminal fluid proteins of male *Drosophila melanogaster* fruit flies, *Peptides*, **25**, 1477–1490.
46. Heifetz, Y., Lung, O., Frongillo, E. A., and Wolfner, M. F. (2000). The drosophila seminal fluid protein Acp26Aa stimulates release of oocytes by the ovary, *Current Biology*, **10**, 99–102.
47. Mueller, J. L., Ripoll, D. R., Aquadro, C. F., and Wolfner, M. F. (2004). Comparative structural modeling and inference of conserved protein classes in *Drosophila* seminal fluid, *PNAS*, **101**, 13542–13547.
48. Riddiford, L. M. and Ashenurst, J. B. (1973). The switchover from virgin to mated behavior in female *Cecropia* moths: the role of the Bursa copulatrix, *Biol. Bull.*, **144**, 162–171.
49. Sugawara, T. (1986). Oviposition behavior of the cricket *Teleogryllus commodus*: the site of action of an oviposition-stimulating factor and the role of the nervous system, *J. Ins. Physiol.*, **32**, 485–492.
50. Tram, U. and Wolfner, M. F. (1998). Seminal fluid regulation of female sexual attractiveness in *Drosophila melanogaster*, *PNAS*, **95**, 4051–4054.
51. Wolfner, M. F. (1997). Tokens of love: functions and regulation of *Drosophila* male accessory gland products, *Insect Biochem. Molec. Biol.*, **27**, 179–192.
52. Wolfner, M. F. (2002). The gifts that keep on giving: physiological functions and evolutionary dynamics of male seminal proteins in *Drosophila*, *Heredity*, **88**, 85–93.
53. Baer, B., Maile, R., Schmid-Hempel, P., Morgan, E. D., and Jones, G. R. (2000). Chemistry of a mating plug in bumblebees, *J. Chem. Ecol.*, **26**, 1869–1875.
54. Baer, B., Morgan, E. D., and Schmid-Hempel, P. (2001). A nonspecific fatty acid within the bumblebee mating plug prevents females from remating, *PNAS*, **98**, 3926–3928.
55. Blum, M. S., Glowska, Z. S., and Taber, I. (1962). Chemistry of the drone honey bee reproductive system. II. Carbohydrates in the reproductive organs and semen, *Ann. Entomol. Soc. Am.*, **55**, 135–139.
56. Collins, A.M., Williams, V., and Evans, J. D. (2004). Sperm storage and antioxidative enzyme expression in the honey bee, *Apis mellifera*, *Ins. Molec. Biol.*, **13**, 141–146.
57. Klenk, M., Koeniger, G., Koeniger, N., and Fasold, H. (2004). Proteins in spermathecal gland secretion and spermathecal fluid and the properties of a 29 kDa protein in queens of *Apis mellifera*, *Apidologie*, **35**, 371–381.
58. Seeley, T. D. and Tarpy, D. R. (2007). Queen promiscuity lowers disease within honeybee colonies, *Proc. R. Soc. B.*, **274**, 67–72.
59. Tarpy, D. R. and Page, R. E. (2002). Sex determination and the evolution of polyandry in honey bees (*Apis mellifera*), *Behav. Ecol. Sociobiol.*, **52**, 143–150.
60. Lobo, J. A. and Kerr, W. E. (1993). Estimation of the number of matings in *Apis mellifera*: extensions of the model and comparison of different estimates, *Ethol. Ecol. Evol.*, **5**, 337–345.
61. Oldroyd, B. P., Rinderer, T. E., Harbo, J. R., and Buco, S. M. (1992). Effects of intracolony genetic diversity on honey bee (Hymenoptera: Apidae) colony performance, *Ann. Entomol. Soc. Am.*, **85**, 335–343.
62. Keller, L. and Nonacs, P. (1993). The role of queen pheromones in social insects: queen control or queen signal? *Anim. Behav.*, **45**, 787–794.
63. Seeley, T. (1985). *Honeybee ecology: a study of adaptation in social life*, Princeton University Press, Princeton, New Jersey.
64. Woyciechowski, M. and Lomnicki, A. (1987). Multiple mating of queens and the sterility of workers among eusocial hymenoptera, *J. Theor. Biol.*, **128**, 317–328.
65. Pankiw, T., Winston, M. L., Fondrk, M. K., and Slessor, K. N. (2000). Selection on worker honeybee responses to queen pheromone (*Apis mellifera* L.), *Naturwissenschaften*, **87**, 487–490.

66. Laidlaw, H. H. J. and Page, R. E. J. (1997). Queen rearing and bee breeding, C. W. Chesshire (Ed.).
67. Grozinger, C. M., Sharabash, N. M., Whitfield, C. W., and Robinson, G. E. (2003). Pheromone-mediated gene expression in the honey bee brain, *Proc. Natl. Acad. Sci. U S A*, **100**, 14519–14525.
68. Grozinger, C. M., Fischer, P., and Hampton, J. E. (2006). Uncoupling primer and releaser responses to pheromone in honey bees, *Naturwissenschaften*, **94**, 375–379.
69. Hoover, S. E. R., Oldroyd, B. P., Wossler, T. C., and Winston, M. L. (2005). Anarchistic queen honey bees have normal queen mandibular pheromones, *Insectes Soc.*, **52**, 6–10.
70. Slessor, K. N., Winston, M., and Le Conte, Y. (2005). Pheromone communication in the honey bee (*Apis mellifera* L.), *J. Chem. Ecol.*, **31**, 2731–2745.
71. Morgan, S. M., Butz Huryn, V. M., Downes, S. R., and Mercer, A. R. (1998). The effects of queenlessness on the maturation of the honey bee olfactory system, *Behav. Brain Res.*, **91**, 115–126.
72. Whitfield, C. W., Cziko, A. M., and Robinson, G. (2003). Gene expression profiles in the brain predict behavior in individual Honey Bees, *Science*, **302**, 296–299.
6. Angilletta, M. J., Steury, T. D., and Sears, M. W. (2004). Temperature, growth rate, and body size in ectotherms: fitting pieces of a life-history puzzle, *Integrative and Comparative Biology*, **44**, 498–509.
7. Brown, J. H., Gillooly, J. F., Allen, A. P., Savage, V. M., and West, G. B. (2004). Toward a metabolic theory of ecology, *Ecology*, **85**, 1771–1789.
8. Wiens, J. J., Graham, C. H., Moen, D. S., Smith, S. A., and Reeder, T. W. (2006). Evolutionary and ecological causes of the latitudinal diversity gradient in hylid frogs: treefrog trees unearth the roots of high tropical diversity, *American Naturalist*, **168**, 579–596.
9. Lynch, M. and Gabriel, W. (1987). Environmental tolerance, *American Naturalist*, **129**, 283–303.
10. Gabriel, W. and Lynch, M. (1992). The selective advantage of reaction norms for environmental tolerance, *Journal of Evolutionary Biology*, **5**, 41–59.
11. Gabriel, W., Luttbeg, B., Sih, A., and Tollrian, R. (2005). Environmental tolerance, heterogeneity, and the evolution of reversible plastic responses, *American Naturalist*, **166**, 339–353.
12. Stillman, J. H. and Somero, G. N. (2000). A comparative analysis of the upper thermal tolerance limits of eastern Pacific porcelain crabs, genus *Petrolisthes*: Influences of latitude, vertical zonation, acclimation, and phylogeny, *Physiological and Biochemical Zoology*, **73**, 200–208.
13. Gibert, P. and Huey, R. B. (2001). Chilling temperature in *Drosophila*: Effects of developmental temperature, latitude, and phylogeny, *Physiological and Biochemical Zoology*, **74**, 429–434.
14. Hoffmann, A., Anderson, A., and Hallas, R. (2002). Opposing clines for high and low temperature resistance in *Drosophila melanogaster*, *Ecology Letters*, **5**, 614–618.
15. McLean, M. A., Angilletta, M. J., and Williams, K. S. (2005). If you can't stand the heat, stay out of the city: thermal reaction norms of chitinolytic fungi in an urban heat

13

1. Roth, M. (2002). *Effects of cities on local climates*, Arlington Institute for Global Environmental Strategies. 1–13.
2. Oke, T. R. (1973). City size and the urban heat island, *Atmospheric Environment*, **7**, 769–779.
3. Huey, R. B. and Stevenson, R. D. (1979). Integrating thermal physiology and ecology of ectotherms: discussion of approaches, *American Zoologist*, **19**, 357–366.
4. Angilletta, M. J., Niewiarowski, P. H., and Navas, C. A. (2002). The evolution of thermal physiology in ectotherms, *Journal of Thermal Biology*, **27**, 249–268.
5. Savage, V. M., Gillooly, J. F., Brown, J. H., West, G. B., and Charnov, E. L. (2004). Effects of body size and temperature on

island, *Journal of Thermal Biology*, **30**, 384–391.

16. Oke, T. R. (1997). Urban climates and global change, A. Perry and R. Thompson (Eds.), *Applied Climatology: Principles and Practice*, Routledge, London, 273–287.
17. Monteiro, C. A. F. (1986). Some aspects of the urban climates of tropical South America: the Brazilian contribution, T. R. Oke (Ed.), *Urban Climatology and its Applications with Special Regard to Tropical Areas*, World Meteorological Organization, Geneva, 166–198.
18. Gates, D. M. (1980). *Biophysical Ecology*, Springer-Verlag, New York.
19. Hoffmann, A. A., Sorensen, J. G., and Loeschcke, V. (2003). Adaptation of *Drosophila* to temperature extremes: bringing together quantitative and molecular approaches, *Journal of Thermal Biology*, **28**, 175–216.
20. Berrigan, D. (2000). Correlations between measures of thermal stress resistance within and between species, *Oikos*, **89**, 301–304.
21. Lin, D. Y. and Wei, L. J. (1989). The robust inference for the Cox proportional hazards model, *Journal of the American Statistical Association*, **84**, 1074–1078.
22. Therneau, T. M. and Grambsch, P. M. (2000). *Modeling Survival Data: Extending the Cox Model*, Springer, New York.
23. Shih, H. T. and Mok, H. K. (2000). ETHOM: event-recording computer software for the study of animal behavior, *Acta Zoologica Taiwanica*, **11**, 47–61.
24. Chown, S. L. and Nicolson, S. W. (2004). *Insect Physiological Ecology: Mechanisms and Patterns*, Oxford University Press, Oxford.
25. Sorensen, J. G., Norry, F. M., Scannapieco, A. C., and Loeschcke, V. (2005). Altitudinal variation for stress resistance traits and thermal adaptation in adult *Drosophila buzzatii* from the New World, *Journal of Evolutionary Biology*, **18**, 829–837.
26. Huey, R. B. and Kingsolver, J. G. (1989). Evolution of thermal sensitivity of ectotherm performance, *Trends in Ecology & Evolution*, **4**, 131–135.
27. Bradshaw, W. E., and Holzapfel, C. M. (2006). Climate change: evolutionary

response to rapid climate change, *Science*, **312**, 1477–1478.

14

1. Hallock, K. J. (2008). Magnetic resonance microscopy of flows and compressions of the circulatory, respiratory, and digestive systems in pupae of the tobacco hornworm, *Manduca sexta*, *Journal of Insect Science*, **8**, 10.
2. Socha, J. J., Westneat, M. W., Harrison, J. F., Waters, J.S., and Lee, W. K. (2007). Real-time phase-contrast X-ray imaging: a new technique for the study of animal form and function, *BMC Biology*, **5**, 6.
3. Wasserthal, L. T. (1983). Hemolymph flows in the wings of pierid butterflies visualized by vital staining (Insecta, Lepidoptera), *Zoomorphology*, **103**(3), 177–192.
4. Forouhar, A. S., Liebling, M., Hickerson, A., Nasiraei-Moghaddam, A., Tsai, H.J., Hove, J. R., Fraser, S. E., Dickinson, M. E., and Gharib, M. (2006). The embryonic vertebrate heart tube is a dynamic suction pump, *Science*, **312**(5774), 751–753.
5. Choma, M. A., Izatt, S. D., Wessells, R. J., Bodmer, R., and Izatt, J. A. (2006). *In vivo* imaging of the adult *Drosophila* melanogaster heart with real-time optical coherence tomography, *Circulation*, **114**(2), E35–36.
6. Mariampillai, A., Standish, B. A., Munce, N. R., Randall, C., Liu, G., Jiang, J. Y., Cable, A. E., Vitkin, I. A., and Yang, V. X. D. (2007). Doppler optical cardiogram gated 2D color flow imaging at 1000 fps and 4D *in vivo* visualization of embryonic heart at 45 fps on a swept source OCT system, *Optics Express*, **15**(4), 1627–1638.
7. Angioy, A. M. and Pietra, P. (1995). Mechanism of beat reversal in semi-intact heart preparations of the blowfly *Phormia regina* (Meigen), *Journal of Comparative Physiology B: Biochemical, Systemic, and Environmental Physiology*, **165**(3), 165–170.
8. Schwab, E. R., Chilson, R. A., and Eddleman, C. D. (1991). Heartbeat rate modulation mediated by the ventral nerve cord in the honey-bee, *Apis mellifera*, *Journal of Comparative Physiology B: Biochemical*,

- Systemic, and Environmental Physiology*, **161**(6), 602–610.
9. Lhotsky, S., Phaneuf, C., Langlois, J. M., Gagne, S., and Poussart, D. (1975). Op-tocardiography – *in vivo* measurements of insect cardiac activity with a new optical method, *Journal of Insect Physiology*, **21**(2), 237–248.
 10. Slama, K. (2003). Mechanical aspects of heartbeat reversal in pupae of *Manduca sexta*, *Journal of Insect Physiology*, **49**(7), 645–657.
 11. Wasserthal, L. T. (2007). *Drosophila* flies combine periodic heartbeat reversal with a circulation in the anterior body mediated by a newly discovered anterior pair of ostial valves and ‘venous’ channels, *J Exp. Biol.*, **210**(Pt 21), 3707–3719.
 12. Wasserthal, L. T. (1980). Oscillating hemolymph circulation in the butterfly *Papilio machaon* L. revealed by contact thermography and photocell measurements, *Journal of Comparative Physiology*, **139**(2), 145–163.
 13. Wasserthal, L. T. (1981). Oscillating haemolymph ‘circulation’ and discontinuous tracheal ventilation in the giant silk moth *Attacus atlas* L., *Journal of Comparative Physiology B: Biochemical, Systemic, and Environmental Physiology*, **145**(1), 1–15.
 14. Hetz, S. K., Psota, E., and Wasserthal, L. T. (1999). Roles of aorta, ostia and tracheae in heartbeat and respiratory gas exchange in pupae of *Troides rhadamantus* Staudinger 1888 and *Ornithoptera priamus* L. 1758 (Lepidoptera, Papilionidae), *International Journal of Insect Morphology and Embryology*, **28**(1–2), 131–144.
 15. Wasserthal, L. T. (1996). Interaction of circulation and tracheal ventilation in holometabolous insects, *Advances in Insect Physiology*, **26**, 297–351.
 16. Pass, G. (2000). Accessory pulsatile organs: Evolutionary innovations in insects, *Annual Review of Entomology*, **45**, 495–518.
 17. Slama, K. (2000). Extracardiac versus cardiac haemocoelic pulsations in pupae of the mealworm (*Tenebrio molitor* L.), *Journal of Insect Physiology*, **46**(6), 977–992.
 18. Chapman, R. F. (1998). *The Insects – Structure and Function*, 4th ed., Cambridge University Press, Cambridge.
 19. Klivanov, A. L. (2006). Microbubble contrast agents – Targeted ultrasound imaging and ultrasound-assisted drug-delivery applications, *Investigative Radiology*, **41**(3), 354–362.
 20. Lindner, J. R., Dayton, P. A., Coggins, M. P., Ley, K., Song, J., Ferrara, K., and Kaul, S. (2000). Noninvasive imaging of inflammation by ultrasound detection of phagocytosed microbubbles, *Circulation*, **102**(5), 531–538.
 21. Harris, R. A., Follett, D. H., Halliwell, M., and Wells, P. N. T. (1991). Ultimate limits in ultrasonic-imaging resolution, *Ultrasound in Medicine and Biology*, **17**(6), 547–558.
 22. Nutting, W. L. (1951). A comparative anatomical study of the heart and accessory structures of the orthopteroid insects, *Journal of Morphology*, **89**, 501–598.
 23. Crescitelli, F. and Jahn, T.L. (1938). Electrical and mechanical aspects of the grasshopper cardiac cycle, *Journal of Cellular and Comparative Physiology*, **11**, 359–376.
 24. Jahn, T. L., Crescitelli, F., and Taylor, A. B. (1937). The electrocardiogram of the grasshopper (*Melanoplus differentialis*), *Journal of Cellular and Comparative Physiology*, **10**(4), 439–460.
 25. Tanaami, T., Otsuki, S., Tomosada, N., Koguchi, Y., Shimizu, M., and Ishida, H. (2002). High-speed 1-frame/ms scanning confocal microscope with a microlens and Nipkow disks, *Applied Optics*, **41**(22), 4704–4708.
 26. Huang, D., Swanson, E. A., Lin, C. P., Schuman, J. S., Stinson, W. G., Chang, W., Hee, M. R., Flotte, T., Gregory, K., and Puliafito, C.A., et al. (1991). Optical coherence tomography, *Science*, **254**(5035), 1178–1181.
 27. Clift, R., Grace, J. R., and Weber, M. E. (1978). *Bubbles, Drops, and Particles*, Academic Press, Inc., New York.
 28. Hjelmfelt, A. T. Jr. and Mockros, L. F. (1966). Motion of discrete particles in a turbulent fluid, *Applied Scientific Research*, **16**(1), 149–161.

15

1. Schmidt, J. (1923). Breeding places and migration of the eel, *Nature*, **111**, 51–54.
2. Vidal, B., Pasqualini, C., Le Belle, N., Claire, M., Holland, H., Sbaihi, M., Vernier, P., Zohar, Y., and Dufour, S. (2004). Dopamine inhibits luteinizing hormone synthesis and release in the juvenile European eel: A neuroendocrine lock for the onset of puberty, *Biol. Reprod.*, **71**, 1491–1500.
3. Stone, R.: Freshwater eels are slip-sliding away, *Science*, **203**, 221–222.
4. Palstra, A. P., Cohen, E. G. H., Niemantsverdriet, P. R. W., van Ginneken, V. J. T., and Thillart, G. E. E. J. M. (2005). Artificial maturation and reproduction of European silver eel: Development of oocytes during final maturation, *Aquaculture*, **249**, 533–547.
5. van Ginneken, V., Dufour, S., Sbaihi, M., Balm, P., Noorlander, K., de Bakker, M., Doornbos, J., Palstra, A., Antonissen, E., Mayer, I., and Thillart, G. (2007). Does a 5,500-km swim trial stimulate early sexual maturation in the European eel (*Anguilla anguilla* L.)? *Comp. Biochem. Physiol. A*, **147**, 1095–1103.
6. Palstra, A., Curiel, D., Fekkes, M., de Bakker, M., Székely, C., van Ginneken, V., and Thillart, G. (2007). Swimming stimulates oocyte development in European eel, *Aquaculture*, **270**, 321–332.
7. Dufour, S., Lopez, E., Le Menn, F., Le Belle, N., Baloché, S., and Fontaine, Y. A. (1988). Stimulation of gonadotropin release and of ovarian development, by the administration of a gonadoliberin agonist and of dopamine antagonists, in female silver eel pretreated with estradiol, *Gen. Comp. Endocr.*, **70**, 20–30.
8. Montero, M., Le Belle, N., King, J. A., Millar, R. P., and Dufour, S. (1995). Differential regulation of the two forms of gonadotropin-releasing hormone (mGnRH and cGnRH-II) by sex steroids in the European female silver eel (*Anguilla anguilla* L.), *Neuroendocrinology*, **61**, 525–535.
9. Teitsma, C. A., Anglade, I., Lethimonier, C., Le Dréan, G., Saliguat, D., Ducouret, B., and Kah, O. (1999). Glucocorticoid receptor immunoreactivity in neurons and pituitary cells implicated in reproductive functions in rainbow trout: A double immunohistochemical study, *Biol. Reprod.*, **60**, 642–650.

Index

A

Acesulfame-K, 84
Acid-best fibers, 84
Adherens junction (AJ), 111
Albay, R., 33–46
Altered apoptosis pathway, 126
Anderson, G. M., 33–46
Angilletta, M. J., 183–190
Anti-KIS-L and anti-PDF antibodies, 4
Antunes, E., 23–31
Apismellifera ligustica, 170
ATP homeostasis, 90
Autism spectrum disorders (ASDs), 33

B

Bee rearing, 170
Behavioral assays
 brain gene expression levels of Amfor
 by insemination quantity, 182
 quantitative real-time PCR, 181–182
 standard curve, 174
 cage, 172, 177–178
 chemical analysis, 173
 Ep line screen, 3
 locomotor activity, 3
 mandibular gland extracts, 178
 observation hives, 171–172, 176
 MDI to SDI queens, 177
 phase-responses, 3
 preference, 172–173
 queen mandibular gland profile,
 178–181
 retinue response, 172
Bishop, K. L., 99–100
Bistrimethylsilyltrifluoroacetamide
 (BSTFA), 173
Blood brain barrier (BBB), 34
Blue-light photoreceptor cryptochrome
 (CRY), 1–2
Bonfanti, L., 47–70
BrdU injections and tissue preparation, 48
BSTFA. *See* Bistrimethylsilyltrifluoroacet-
 amide (BSTFA)

C

Candidate genes, 10–12
Canine intermittent claudication study in,
 89
 functional and biochemical characteris-
 tics, 91–92
 intramuscular metabolites, 95
 materials and methods
 metabolite analysis, 91
 muscle stimulation parameters and
 blood sampling, 91
 surgical procedures, 90–91
 model characteristics, 93–94
 muscle ammonia efflux, 96
 muscle contractile function, 94–95
 muscle lactate efflux, 96–97
 oxygen consumption, 94–95
 reduced ammonia production, 92–93
Canton-S, 13
Catalase gene (CAT), 132
Central nervous system (CNS), 47
Cercopithecus aethiops, study with mira-
 culin in, 77
CHARGE syndrome, 8
Chen, A., 33–46
Chill-coma recovery, 183, 187
Chorda tympani (CT) nerves, 72–73
Chromatin-remodeling enzyme KISMET
 (KIS), 1
 CRY and TIM degradation, 19–21
 and cry genetically interact, 20–21
 down regulation in flies expressing KIS
 dsRNAs, 17
 functions in circadian neurons, 18–19
 and functions in PDF negative circadian
 neurons, 18–19
 KIS-L levels, 17
 photosensitivity, 8
 protein expression in circadian neurons,
 4
 role as regulator of CRY input pathway,
 5–6

- Circadian mis-expression screen under constant light, 8–10
- Circadian photoresponses study
- behavioral analysis, 3
 - candidate genes functions, 10–13
 - Drosophila* stocks, 2–3
 - KISMET functions, 18–19
 - KIS role, 14–17
 - mis-expression screen under constant light, 8–10
 - phase responses, 13–14
 - real-time quantitative PCR, 4–5
 - regulators, 5–8
 - RNase protections, 5
 - TIM degradation, 19–21
 - Western Blot, 4
 - whole-mount brain immunostaining and quantification, 4
- City ants, heat effect study
- chill-coma recovery, 183
 - cold tolerance, 187
 - colonies sampling, 185
 - Cox proportional hazards model, 188
 - ectotherms, 183–184
 - ETHOM, 187
 - heat tolerance, 185–186
 - differences, 187
 - urban and rural, 189
 - knock-down resistance, 183
 - optimality models, 183
 - predictions test, 184
 - São Paulo, satellite image, 184
 - trail temperatures, 185
 - urban environments, 188
 - heat islands, 183–184
- Clock (CLK) transcription factors, 1
- Clutter, A. C., 125–134
- Cold tolerance
- chill-coma recovery, 187
 - petri dishes, 187
- Collagen metabolism (COL23A1), 128
- pathway, 125
- Colonies sampling, 185
- Commercial pigs, genetic effects study on scrotal in, 125
- admixture mapping, 128
 - association analysis results, 132–133
 - candidate gene analysis, 129–130, 133
 - case-control analysis, 128
 - COL23A1 in hernia development, 129
 - collagen metabolism, 129
 - family-based analysis, 128
 - family-based Pietrain lines, 131–132
 - Hardy–Weinberg equilibrium, 131
 - mapping of variants, 128
 - materials and methods
 - animals, 126
 - polymorphisms and genotyping, 126–127
 - statistical analysis, 127
 - regions linked with, 131
 - Sequenom platform, 131
 - sex hormone de-regulation, 128–129
- Complement regulatory protein CD59 molecule, 129
- Concentration-response curves
- data, 24
 - line, 24–25
 - nonlinear regression analyses, 24–25
- Confocal microscopy, 192, 195
- Congruity, 102
- Contrast decrements (OFF channel), 149
- Contrast increments (ON channel), 149
- Contrast sensitivity function, 159–161
- Cows, acute heat stress
- ambient conditions
 - air temperature and relative humidity, 137
 - diurnal and milk composition treatments, effect, 143
 - hourly milk secretion rates, 143
 - isolation and regrouping, 141
 - K⁺ uptake into SMV, 137
 - β-Cn F (1-28) and measurement channel blocking activity, 138
 - Inf, used, 138
 - in milk serum-derived vesicles, 146
 - and time of sampling, treatments effect, 144
 - into vesicles, effect, 145
 - lactation, 140
 - milk yield (MY), 135
 - and mammary function, 135–136

PA-PG-PL system, involvement, 139
 treatments effects, 142
 multiple regression analysis, 140
 negative-feedback regulatory system, 136
 plasminogen activator-plasminogen-plasmin system, 144
 rectal temperature and respiration rate, 137
 respiration rate per minute, 141–142
 statistical analysis
 data and model, 138
 treatments for period, 139
 study, 136–137, 139, 141
 THI parameter, 139–140
 Cox proportional hazards model, 188
 Cragin, T., 72–88
 Cryptochrome (CRY), 1
 input pathway, 6–7
 signaling, 7
 Cycle (CYC) transcription factors, 1

D

Danilova, V., 72–88
 Davel, A. P. C., 23–31
 de Moraes, C., 23–31
Drosophila brains, circadian neurons in, 16–17
Drosophila buzzatii, 187
Drosophila melanogaster, 187, 192
 Dubruille, R., 1–22
 DurbinWatson test, 39

E

EFEMP2. *See* Epidermal growth factor-containing fibulin-like extracellular matrix protein 2 (EFEMP2)
 EGT. *See* Exuberant granulation tissue (EGT)
 Electrocardiogram technique, 192
 Electrophysiology, 82–84
 Elementary small target motion detector (ESTMD) model, 150–151
 E74-like factor 5 (ELF5), 131
 Emery, P., 1–22
 EMT. *See* Epithelial-mesenchymal transition (EMT)

Epidermal growth factor-containing fibulin-like extracellular matrix protein 2 (EFEMP2), 131
 Epithelial-mesenchymal transition (EMT), 125–126, 128
 EP lines behavior, 10–11, 13
 Equine
 CTNNB1 and PECAM1, cloning
 cDNAs, 112
 full-length, size, 112
 oligos, 112
 RNA isolation, 112
 tissues and RNA extraction
 formalin fixed and FFPE, 113
 standardbred mares, 112–113
 thoracic and limb, 112
 ESTMD model. *See* Elementary small target motion detector (ESTMD) model
 Estrogen receptors (KIF18A and NPTX1), 128
 signaling pathway, 125
 Event-recording software (ETHOM), 187
 Experimental protocol, 24
 External granule cell layer (EGL), 47
 Exuberant granulation tissue (EGT), 110

F

FaasX software, 3
 Family-based analysis, 125
 Fast depolarization, slow repolarization (FDSR), 150
 FBAT software packages, 127
 Flies
 KISMET dsRNAs expression in constant light, 15–16
 miR-282 over expression, 14

G

Genome-wide association analyses (GWA), 125–126
 Genotyping, 38
 Glossopharyngeal (NG) nerves, 72–73
 Glutamine synthetase (GS), 93
 Gonadotropin-releasing hormone agonist (GnRH_a), 203
 Grozinger, C. M., 168–184

Guido, E. E. J. M., 203–206
Gymnemic acid (GA), 76

H

Haploview software packages, 127

HapMap and ENCODE projects, 125–126

Heat tolerance, knock-down resistance,
185–186

Hellekant, G., 72–88

Hemolymph flow in grasshopper's heart
study

bubble movement, example of, 199

challenges and improvements,
195–196

compressions, 198

confocal microscopy, 192, 195

Drosophila melanogaster, 192

electrocardiogram technique, 192

and heart movements, relationship
between, 197

local flow patterns, 198–199

magnetic resonance imaging (MRI),
191

materials and methods, 193–194

microbubbles, 193

non-uniform flow patterns, example
of, 200

optical coherence tomography
(OCT), 192

pericardial sinus, timing of, 198

purpose of, 200–201

synchrotron X-ray phase, 191

thermography, 192

transparent or semi-transparent
animals, 192

visualization of, 196

Hierarchical cluster analysis (SYSTAT), 76

High caloric fed rats study

ACh, 26

aim of, 23–24

antioxidant defense systems, 27

atherosclerosis, 23

cardiovascular benefits, 27

concentration-response curves, 23

condition, 26–27

drugs and solutions, 25

endothelium-dependent relaxation of
blood vessels, 26

evidences, 23

experimental models of obesity, 26

experimental protocol, 24

glucose concentration, 23

insulin concentration, 23, 26–27

IR phosphorylation, 26–27

isoforms of SOD, 27

lipid profile, 25

obesity, 23

oxidative stress, 23

plasma nitrite/nitrate (NOx) levels

determination, 25

plasma triglycerides concentration, 26

receptors and signaling pathways, 27

results

ACh, 30

aortic rings, 30

concentration response curves,
29–31

data from Western Blotting analysis,
31

effects of exercise training, 31

endothelium-dependent relaxation,
30

during experimental protocol, 28

Glucose concentration, 28–29

HOMA index, 29

maximal relaxation responses, 30

NOx concentration and levels, 29

SD and SDD groups, 28–30

TR and TRD groups, 28–30

triglycerides concentration, 30

statistical analysis, 25–26

Western Blotting assay for Cu/Zn su-
peroxide dismutase, 25

High-pass filtering (HPF3), 150

Histological procedures and immunohis-
tochemistry, 48

Homeodomain interacting protein kinase 3
(HIPK3), 129

Honey bee queen physiology and insemin-
ation

bee rearing, 170

behavioral assays, 171–174, 176–182

BSTFA, 173

- chemical profiles of, 170
 gene expression levels, 175
 male seminal proteins, 176
 mandibular gland
 MDI and SDI queens, comparisons, 174–175
 MANOVA test, 173
 mating
 number, 170
 stimulations, 169
 multi-drone inseminated (MDI), 168
 multiple mating, effects of, 168
 queen
 pheromone, 169
 rearing, 170–171
 queen mandibular pheromone (QMP), 169
 single-drone inseminated (SDI), 168
 Horses, wound healing
 acute inflammatory response, 117
 β -catenin, 110–111
 immunohistochemical localization of, 122
 PBS-buffered formalin-fixed tissues, 114
 and PECAM1, immunohistochemical localization, 114
 body and limb
 protein localization in, 121
 CTNNB1 and PECAM1 for, 110
 ectodomain mediates adhesion, 111
 EGT, 110
 epithelial cells, 116
 membrane staining of, 117
 equine CTNNB1 and PECAM1, cloning
 cDNAs, 112
 cloning and characterization, 118–119
 full-length, size, 112
 oligos, 112
 RNA isolation, 112
 equine tissues and RNA extraction
 formalin fixed and FFPE, 113
 standardbred mares, 112–113
 thoracic and limb, 112
 hyperplastic wounds in, 111
 immunoblot analyses
 protein extracts, 114
 samples, 113–114
 immunohistochemistry, 118
 limbs, repair of, 110
 PECAM1, 111, 117
 immunohistochemical localization of, 122
 SSH, 110
 statistical analysis
 repeated-measures (RM) linear model, 115
 study, 110, 111–112, 115–116
 temporal expression of mRNA
 CTNNB1 and PECAM1 in body and limb, 119
 semi-quantitative RT-PCR analysis, 113
 of thorax and limb skin
 equine CTNNB1 mRNA, 120
 equine PECAM1 mRNA, 120–121
 Wnt pathway, activation, 111
 HPF3. *See* High-pass filtering (HPF3)
 Human T1R3 receptor, 78–79
- ## I
- Image analysis, 194
 Input images and optical blurring, 152
 Insect circulatory system, 192–193
 Insect physiology and detection of moving targets, 148
 in clutter, 163–166
 computational models for target discrimination, 149
 contrast sensitivity function, 159–161
 detection pathway, 151
 full-wave rectifying transient neurons, 149–150
 large monopolar cells, 156–157
 linear systems analysis, 155
 materials and methods
 input imagery, 153–154
 modeling, 151
 natural day/night cycle, 154–155
 model responses, comparison of, 158–159
 photoreceptors, 156

rectifying transient cell, 157–158
 relative motion, 166–167
 RTC neurons, 155
 temporal responsiveness, 159
 velocity tuning, 162–163
 wide-field STMD neurons display, 155

Insulin receptor (IR), 26
 Intermittent claudication (IC), 89
 muscle metabolism in, 90
 Ischemia-reperfusion injury, 90
 Isometric force transducer, 90

J

Janušonis, S., 33–46
 Jetlag (JET), 2

K

Kinesin family member 18A (KIF18A),
 131
 Kinetic energy (KE), 100
 KIS. *See* Chromatin-remodeling enzyme
 KISMET (KIS)
 Knock-down resistance, 183, 185–186
 ecological significance of, 188
 Koposov, A., 72–88

L

Lactisole, 73
 effect on intake of non-sweet com-
 pounds, 74
 in *homo* and *M. fascicularis*, 78
 Laplace variable, 157
 Large monopolar cells (LMC), 149–150
 Laplace variable, 157
 like spatiotemporal band-pass filtering,
 156
 in motion processing, 156
 transfer function, 156
 Large-scale association analysis, 125
 Lee, W. K., 191–201
 Lefebvre-Lavoie, J., 110–123
 Linkage disequilibrium (LD) fine map-
 ping, 125–126
 Lipetz function, 150
 LL arrhythmicity, 5

LMC. *See* Large monopolar cells (LMC)
 LON peptidase 1 (LONP1), 129
 Loss-of-function mutations, 7
 Lussier, J. G., 110–123

M

MacInnes, A., 89–98
 Magnetic resonance imaging (MRI), 191,
 195
 Male silver eels
 sexual maturity and swimming in
 Anguilla anguilla, 203–204
 and female, difference, 204–205
 follicle stimulating hormone (FSH),
 203
 gonad development parameters, 206
 gonadosomatic index (GSI), 203
 LH β -expression, 205
 luteinising hormone (LH), 203
 materials and methods, 204
 Mandibular glands, 168, 170, 172–174,
 177–178
 Mann-Whitney test, 43
 MANOVA test, 173
 Minor allele frequency (MAF), 127
 Miraculin (MA), 77–78
 Miragliotta, V., 110–123
 miR-282 and miR-8 circadian tissues, 7–8
M. mulatta, single fiber study, 77
 Monkeys, taste development study, 72
 behavior, 81
 comparison in S-fibers, 76
 dendrogram, 85
 electrophysiology, 82–84
 error bars, 85
 lactisole effects, 85
 materials and methods
 animals and stimuli, 73
 behavioral experiments, 73–74
 electrophysiology, 75–76
 surgery, 74–75
 multidimensional scaling, 86–87
 nerve impulses in S fibers, 79
 S fibers and cell types in taste buds,
 80–81

sweet taste modifiers miraculin and GA, 77–78
 taste fiber types, 76–77
 temporal pattern/intensity, 85–86
 T1 receptors, lactisole and S fibers, 78–79
 Morgue E2 ubiquitin ligase, 12–13
 Moving cats, body mechanics
 animals and equipment
 force plate, 100–101
 full strides for, 101
 Kistler force sensors, 100
 and video records, 101
 curvilinear relationship, 107
 and dogs comparison with, 105
 energy calculations
 average forward velocity, 101
 congruity, 102
 diagonality, 104
 footfalls, timing, 104
 force measurements, accuracy, 101
 gravitational acceleration, 102
 potential energy, 101–102
 statistics, 102
 total mechanical energy (TME), 102
 trot, 104
 walking mechanics, studies, 103
 energy-saving mechanism, 103
 hip height, diagonality and mean, 107
 locomotor goals, balance, 100
 mechanical energy, percent recovery, 104, 105–106
 metabolic cost, 99
 novel study, 108
 PE and KE fluctuations, 100
 stealthy walking style, 99
 stiff-legged walking, 107
 studies, 99
 Multidimensional scaling, 86–87
 Multi-drone inseminated (MDI), 168, 170, 174
 Murad, A., 1–22
 Muscle ammonia efflux, 96
 Muscle contractile function, 94–95
 Muscle lactate efflux, 96–97
 Muscle stimulation parameters and blood sampling, 91

N

Natural image panoramas, 165
 Navas, C. A., 183–190
 NeuroExplorer, 75
 Neuronal pentraxin I (NPTX1), 133
 Neurons in solitary tracts (NTS), 80
 Niehaus, A. C., 183–190
 Nieveen, M. C., 203–206
 Northern Blot assays, 7

O

O'Carroll, D. C., 148–167
 OFF channel. *See* Contrast decrements (OFF channel)
 Offline Sorter, 75
 Oligonucleotides, 204
 ON channel. *See* Contrast increments (ON channel)
 “On-off” cell experiments, 149–150
 Open flow system, 75
 Optical coherence tomography (OCT), 192, 195
 Optimality models, 183

P

Pai, A. K., 99–100
 Paired t-test, 91
 Palstra, A. P., 203–206
 Panorama rotation, 153
 Paraffin-embedded (FFPE), 113
 “Peakphaseplot” function, 3
 Peretto, P., 47–70
 Period (PER) proteins, 1
 Peripuberal and adult rabbits neurogenesis
 brain neurogenic sites, 57
 BrdU injections and tissue preparation, 48
 cell proliferation markers, 70
 cerebellar neurons in mammals, 47–48
 CNS, 47
 dynamics of
 BrdU⁺, 55
 cell genesis and neurochemical maturation, 54
 CNS, 55
 GABA⁺, 55

- Map⁵⁺/Olig²⁺/Sox²⁺ multipolar cells, 55
- PSA-NCAM and DCX, 55
- steps of cell maturation, 55, 61
- EGL, 47–48
- GABA, 47
- histological procedures and immunohistochemistry, 48–49
- interneurons and synantocyte/polydendrocyte-like cells
- BrdU⁺ cells, 53–54
 - CRMP-4 and DCX, 53
 - GABA-ergic, 53
 - Ng²⁺ and Map⁵⁺ cells, 53–54
 - Pax⁶⁺ cells, 53
 - PSA-NCAM⁺/DCX⁺, 53
- mammalian cerebellum, 47, 51
- multipolar cells, 47
- neuroepithelial-derived interneuronal precursors, 60–64
- neuronal and glial progenitor cells
- astrocytic/oligodendrocytic shape, 52
 - BrdU⁺, 51–52
 - CRMP-4, and Map5, 51–53
 - PSA-NCAM and DCX, 51–53
- newly-formed cells, 57–60
- newly generated cells, 66–67
- newly generated neuronal and glial cell progenitors, 67–70
- permissive tissue for, 56
- plasticity, 51
- pre-embedding immunoelectron microscopy, 49
- quantitative analyses
- BrdU⁺ cells, 50–51
 - PSA-NCAM⁺ and Map⁵⁺ cells, 50–51
 - student's test T. A value, 50–51
 - Tukey HSD test, 50
- residual granule cell precursors, 64–65
- rodents and lagomorphs, 57
- SPL, 47–48
- subventricular zone (SVZ), 48, 51
- transcription factors and Blbp relationships, 70
- Photoreceptors
- fly motion detection, 156
 - Lipetz function, 156
 - transduction, 156
- Pig genome sequencing project, 127
- PLINK software packages, 127
- Polycomb negative regulators, 6
- Ponti, G., 47–70
- Potential energy (PE), 100
- Proteasome-dependent protein turnover, 7
- Pseudo-random distribution, 165
- Putative protein phosphates (cg9801), 13
- Pyrroline-5-carboxylate reductase 1 (PYCR1), 133
- ## Q
- Q Cluster fibers, 84
- Quadrupedal animals, 99
- Quantitative reverse transcriptase (Q-RT), 204
- Queen mandibular gland profile, chemical analysis
- absolute quantity of, 180
 - composition of, 178
 - identity and relative proportion, 181
 - insemination quantity, 179
- Queen mandibular pheromone (QMP) components, 169
- Queen rearing, 170–171
- ## R
- Radiometer ABL 625GL, 90
- Real-time PCR analysis, 4–5
- Recorder software, 75
- Rectifying transient cell (RTC)
- based target detection model, 148
 - channels, 158
 - electrophysiological data, 157
 - linear interactions, 158
 - slow decay characteristic, 157
 - STMD, 158
- Ribeiro, P. L., 183–190
- Richard, F. J., 168–184
- RNase protections, 5
- Roberts, T. W., 72–88
- Rodriguez, F., 125–134
- Rosbash, M., 1–22
- Rossoni, L. V., 23–31
- Rothschild, M. F., 125–134

S

- Saccharin, 84
Schistocerca americana grasshoppers, 193–194
 Schmitt, D., 99–100
 Schnabel, D., 203–206
 Scrotal hernia in pigs, 125
 SDI. *See* Single-drone inseminated (SDI)
 Sears, M. W., 183–190
 Sequenom MassARRAY® system, 127
 Serotonin transporter (SERT), 33
 Sex hormone de-regulation, 126
 S Fibers, 84
 Shapiro, F., 135–146
 ShapiroWilk test, 38–39
 Shinder, D., 135–146
 Shoemaker, P. A., 148–167
 Silanikove, N., 135–146
 Single CT taste fibers
 hierarchical cluster analysis, 83
 profiles by topographical method, 82
 Single-drone inseminated (SDI), 168, 170
 Skim-milk-derived vesicles (SMV)
 in cows, 137–138
 SLIMB, E3 ubiquitin ligase, 12–13
 “Small target motion detectors” (STMD), 148
 Socha, J. J., 191–201
 Spaink, H. P., 203–206
 SpectroChip®, 127
 Spectromax Plus, 91
 Spike trains and fiber responsiveness, 75–76
 SSH. *See* Suppression subtractive hybridization (SSH)
 Stevioside, 84
 Subpial layer (SPL), 47
 Suppression subtractive hybridization (SSH), 110
 Surgical procedures, 90–91
 Sus scrofa chromosomes (SSC), 126
 SYSTAT. *See* Hierarchical cluster analysis (SYSTAT)

T

- Target height tuning, 162
 Targets in clutter, 163–166

- Tarpy, D. R., 168–184
 Taste-O-Matic. *See* Open flow system
 Taste receptor cell (TRC), 72
 Tatevosyan, M., 33–46
 Temporal responsiveness, 160
 Theoret, C. L., 110–123
 Thermography, 192
 Time intensity (TI) of responses of fiber, 85–86
 Timeless (TIM) proteins, 1
 Timmons, J. A., 89–98
 Tissue harvesting, 35
 Total mechanical energy (TME), 102
 Transmission disequilibrium tests (TDT), 127
 Trithorax protein, 6
 T1R3 monomer, 72
 T1R2/R3 receptors, 72
 Two-bottle method (TBP), 73–74, 81
 Type III cells, 80–81

U

- Urban heat islands
 surface temperatures, 183–184

V

- van den Thillart, 203–206
 Velocity tuning, 162–163
 Vukasinovic, N., 125–134

W

- Whole-mount brain immunostaining, 8
 Wiederman, S. D., 148–167
 Wild type-mice and serotonin related variables study
 advantages, 34
 aim, 34
 animals, 35
 ASDs, 33–34, 40
 BBB, 34, 41
 blood and platelet hyperserotonemia of autism, 33–34
 body mass, 40
 brain/body mass ratio, 41, 44
 brain hippocampal complex, 35–36
 cardiac output, 40

cross-correlations
 brain mass/body mass and blood
 5-HT levels, 43–45
 Cook's distances (Cook's D), 44
 Mann-Whitney test, 43
 normality test, 43
 pups, 45
 ratio variables, 43
 samples, 43–44
 Spearman's correlation coefficient,
 43
data screening
 ANOVA, 42
 blood volume and 5-HT concentra-
 tion, 42
 objective criteria, 41–42
DurbinWatson test, 39
genotyping, 38
guts
 length of, 36–37, 40–41
 protocols, 36–37
 relaxation, 36–37, 42–43
hippocampal complex, 33–34, 41–42
5-HT_{1A} receptors, 34–35, 41
investigations, 33–34

Pearson's correlation, 39, 43
platelet and blood 5-HT levels, 33–34
 model, 40
SERT, 33–34
and sex-genotyping 3D-reconstruction,
35–36
statistical analysis
 general linear model (GLM), 38–39
 ShapiroWilk test, 38–39
tissue harvesting, 35
whole-blood tryptophan level and 5-HT,
37–38, 41
Wilson, R. S. Jr., 183–190

X

Xia Zhao, 125–134

Y

Yiwen Wang, 72–88

Z

Zanesco, A., 23–31

Zhi-Qiang Du, 125–134